NANO-GRAPHITE AS A FUNCTIONAL ADDITIVE FOR ROTATIONALLY MOULDABLE POLYMERS AND PHASE CHANGE MATERIALS FOR ENERGY STORAGE

By

Washington Mhike

Thesis submitted in partial fulfilment of the requirements for the degree of

Doctor of Philosophy

In

Chemical Technology

In the Faculty of Engineering, Built Environment and Information Technology
University of Pretoria

Pretoria

April 2016

Declaration

I, **Washington Mhike**, **student No. 29712573**, do hereby declare that this research is my original work and that to the best of my knowledge and belief, it has not previously in its entirety or in part been submitted and is not currently being submitted either in whole or in part at any university for a degree or diploma, and that all references are acknowledged.

SIGNED on this day _____of_____ 2016.

Washington Mhike

NANO-GRAPHITE AS A FUNCTIONAL ADDITIVE FOR ROTATIONALLY MOULDABLE POLYMERS AND PHASE CHANGE MATERIALS FOR ENERGY STORAGE

Author: Washington Mhike

Supervisor: Prof. Walter W. Focke

Department: Chemical Engineering

Degree: PhD (Chemical Technology)

Abstract

The overall aim of this study was to obtain a facile method of synthesizing graphite nanoplatelets from commercial expandable graphite and use these as functional fillers in rotational moulding applications and phase change materials for energy storage. Two commercial expandable graphites were evaluated as precursors for the synthesis of graphite nanoplatelets. Microwave radiation treatment was shown to be more efficient in exfoliating expandable graphite than furnace heating. The expandable graphite with better exfoliating characteristics was selected. XRD results of this graphite showed that it was a high stage graphite intercalation compound.

Graphite nanoplatelets with an average particle size of 13 μm and an estimated thickness of about 76 nm were prepared by microwave exfoliation and ultrasonication-assisted liquid phase exfoliation in isopropanol from the selected expandable graphite. Prior to the selection of isopropanol as the ultrasonication media, various exfoliation media that encompassed

different solvents and water with various surfactants had been evaluated, on the basis of their acoustic cavitation characteristics.

The graphite nanoplatelets were used as a functional additive to fabricate linear low density polyethylene (LLDPE) and poly(ethylene-co-vinyl acetate) (EVA) based nanocomposites using the rotational moulding (rotomoulding) process. The dry blending approach yielded surface resistivities within the static dissipation range (antistatic) at filler loadings as low as 0.25 wt.% (0.1 vol.%). However, even at this low graphite content, impact properties were significantly reduced compared to the neat polymers. Bilayer mouldings via the double dumping method proved to be a feasible approach to achieve both acceptable mechanical properties and antistatic properties. This was achieved by rotomoulding nanocomposites with a 1 mm outer layer containing the filler and a 2 mm inner layer of neat LLDPE. Excellent fire resistance, in terms of cone calorimeter testing, was achieved when the outer layer also contained 10 wt.% expandable graphite.

Pseudo binary mixtures of stearyl alcohol/commercial triple pressed stearic acid where prepared and characterized as a new phase change material (PCM) for energy storage. A facile method of preparing highly thermally conductive stearyl alcohol/stearic acid phase change material/graphite nanoplatelets (GNPs) nanocomposites was developed. Inclusion of the GNPs in the PCM matrix reduced the enthalpy of melting and crystallization marginally. However, the PCM/nanocomposite exhibited negligible super cooling. At 10 wt.% loading, the graphite nanoplatelets enhanced the thermal conductivity of the PCM by close to 600 % and 1200 % in the solid and molten states, respectively. Thermal conductivity modelling showed that the substantial thermal conductivity enhancement was as a result of relatively low interfacial thermal resistance between the PCM matrix and GNPs. The PCM/GNPs nanocomposites also showed excellent thermal reliability after being subjected to accelerated thermal cycling tests of 100 melting and freezing cycles. Settling tests showed the PCM/GNPs nanocomposite with 10 wt.% GNPs was stable after 60 days, with no apparent separation between the PCM matrix and the graphite nanoplatelets.

Key words: Graphite nanoplatelets, Rotational moulding, Antistatic, Impact strength, Stearyl alcohol, Stearic acid, Phase change material, Enthalpy, Thermal conductivity

Dedication

Dedicated to My Parents and Family

Acknowledgements

This work is based on the research supported by the South African Research Chairs Initiative of the Department of Science and Technology and National Research Foundation (NRF) of South Africa (Grant No. 97994), the African Laser Centre (ALC) and Xyris Technology CC. Any opinion, finding and conclusion or recommendation expressed in this material is that of the author(s) and the NRF does not accept any liability in this regard.

I wish to express my sincere gratitude to:

- My Supervisor Prof. Walter W. Focke, for his invaluable support, mentorship and guidance, as well as his contributions and the encouragement that he gave me throughout this study, especially during trying times.
- Prof. Ncholu I. Manyala, for the support, advice and invaluable discussions I had with him.
- Dr. Heinrich Badenhorst, for his advice.
- Andre de Lange, with the grinding of the rotomoulding polymers.
- Joseph Sebekedi and staff of Xyris Technology, for their technical assistance.
- Isbe van der Westhuizen, for the technical support.
- Centre for Microscopy, University of Pretoria, especially Allan Hall and Andre Botha.
- Suzette Seymore, for being there always.
- All my colleagues at the Institute for Applied Materials: Shepherd Tichapondwa, Mthokozisi Sibanda, Afonso Macheka, Hermínio Muiambo and Shatish Ramjee, for their thought-provoking suggestions, support and companionship.
- My parents, Boniface and Majorie, and brother Lawrence, for encouraging and tolerating me. Thank you for the faith you have shown in me.
- The love of my life, my wife, Theresa T. Mhike, thank you for your patience and understanding.
- My dearest son, Jeremy Lebohang Mhike, sorry for the time I stole from you!
- The Lord Our God, through Whom all things are possible.

Contents

List of figures

List of tables

Abbreviations

LLDPE	Linear low density polyethylene
HDPE	High density polyethylene
LHTES	Latent heat thermal energy storage
PCMs	Phase change materials
GNPs, xGnP^{TM}	Graphite nanoplatelets
a_o, c_o	Graphite unit cell parameters
A, B, C	Layers of carbon atoms in graphite
GICs	Graphite intercalation compounds
IUPAC	International Union of Pure and Applied Chemistry
M	Electropositive species
C_x	Electron in the π electron network of graphite
A	Electronegative species
XRD	X-Ray diffraction
DTA	Differential thermal analysis
TGA	Thermogravimetric analysis
THF	Tetrahydrofuran
NMP	1-methyl-2-pyrrolidinone
GBL	g-butyrolactone
DMA	N,N-dimethylacetamide
NVP	N-vinyl- 2-pyrrolidone
DMF	N,N-dimethylformamide
ODCB	Ortho-dichlorobenzene
SDBS	Sodium dodecyl benzene sulphonate
SDS	Sodium dodecyl sulphate
SC	Sodium chlorate
SWNTs	Single wall carbon nanotubes
D	Vessel diameter for an ultrasonication induced cavitation process
L	Liquid height for an ultrasonication induced cavitation process
FLG	Few layer graphene
BYK-163	High molecular weight dispersant
HR-STEM	High-resolution scanning transmission electron microscopy

IEC	International Electrotechnical Commission
FIGRA	Fire growth rate
MARHE	maximum average rate of heat emission
HRR	Heat release rate
pHRR	Peak heat release rate
tHR	Total Heat release
ARM	Association of Rotational Moulders
ASTM	ASTM International
FTIR	Fourier transform infrared spectroscopy
YIE	Yellowness index
PIAT	Peak internal air temperature
EVA	Ethylene vinyl acetate
PET	Polyethylene terephthalate
PLLA	Poly-lactic acid
UV	Ultraviolet radiation
HALS	Hindered amine light stabilizer
SEM	Scanning electron microscopy
UL	Underwriters Laboratories
DSC	Differential scanning calorimetry
ES 250 B5	Expandable graphite ES250 B5
ES170 300A	Expandable graphite ES170 300A
HR FESEM	High resolution field emission scanning electron microscopy
BET	Brunauer-Emmett-Teller
PSD	Particle size distribution
MFI	Melt flow index
L/D	Length to diameter ratio of the screws in the twin screw extruder
ATR	Attenuated total reflectance
C_{18}-OH	Stearyl alcohol
C_{18}-Acid	Stearic acid
XRF	X-ray fluorescence
Tween 20	Polyethylene glycol sorbitan monolaurate
I_D/I_G	Intensity ratio of the D to that of the G band in Raman spectra
EG	Expandable graphite

List of Symbols

Graphite, graphene and graphite nanoplatelets

σ	sigma orbitals [-]
π	pi orbitals [-]

Liquid phase exfoliation mechanism: thermodynamic approach in terms of enthalpy of mixing:

ΔH_{mix}	enthalpy of mixing [J]
V_{mix}	volume of mixture [m^3]
T_{flake}	thickness of a graphene flake [m]
$E_{S,S}$, $E_{S,G}$	surface energies of the solvent and graphene, respectively [J m^{-2}]
ϕ	volume fraction of graphene [-]

Liquid phase exfoliation mechanism: role of solubility parameters

δ_T	Hildebrand solubility parameter [$MPa^{1/2}$]
δ_D , δ_P , δ_H	Hansen solubility parameters [$MPa^{1/2}$]. The subscripts D, P, and H represent dispersive, polar and hydrogen-bonding interaction components between graphene and the solvent, respectively

Electrical resistivity of polymer composites: Statistical percolation model

σ_s	surface resistivity close to and above the percolation threshold [Ω or Ω $(square)^{-1}$ ($\Omega\ \square^{-1}$)]
σ_f	resistivity of the conductive additive [$\Omega\ \square^{-1}$]
V	volume fraction of the conductive additive [-]
t	a critical exponent of a universal character
V_c	percolation threshold [-]

Cone calorimeter tests

t	time [s]

Thermal conductivity modelling: Nan model

λ_m	matrix thermal conductivity [W m^{-1} K^{-1}]

λ_c	effective thermal conductivity for the nanocomposite [W m^{-1} K^{-1}]
β_{11}, β_{33}	calculated parameters [-]
λ_g	thermal conductivity of graphite nanoplatelets [W m^{-1} K^{-1}]
λ_{11}^g , λ_{33}^g	equivalent thermal conductivities along the transverse and longitudinal axes of a nanocomposite unit cell, which is defined as a graphite nanoplatelet coated with thin interfacial thermal barrier layer [W m^{-1} K^{-1}]
p	aspect ratio for graphite nanoplates, which is defined as the ratio of the shortest radii to that of the longest radii for oblate ellipsoids which in this case becomes the ratio of the thickness to the diameter of GNPs [-]
a_3, a_1	thickness and diameter of graphite nanoplatelets [m]
γ, α	calculated parameters [-]
a_k	Kapitza radius [m]
G_k	interfacial thermal conductance [W m^{-2} K^{-1}]
R_k	thermal resistance or Kapitza resistance, reciprocal of interfacial thermal conductance [m^2 K W^{-1}]

Phase change materials for energy storage: Energy stored

Q	amount of heat stored [J]
T	temperature [°C]
T_i, T_m, T_f	initial, melting and final temperatures, respectively [°C]
m	mass of the PCM [kg]
$C_\mathrm{p}, C_\mathrm{sp}, C_\mathrm{lp}$	specific heat capacity, average heat capacity between T_i and T_m and average specific heat capacity between T_m and T_f, respectively [kJ kg^{-1} °C^{-1}]
a_m	fraction of the PCM that actually melts [-]
Δh_m	specific heat of fusion of the PCM [kJ kg^{-1}]

Solid-liquid equilibrium: Schröeder-Van Laar equation

x_i	mole fraction [-]
ΔH_i	heat of fusion of pure compound i [kJ mol^{-1}]
T_i	melting temperature of pure compound i [°C]
R	universal gas constant [8.314 J mol^{-1} K^{-1}]
T	melting temperature of the mixture [°C]

Chapter 1 Introduction

1.1. Background

1.1.1 Rotational moulding

Rotational moulding, also referred to as rotomoulding or rotocasting, is a polymer forming process used to make hollow plastic products through biaxial rotation and heat. In a history of the process described by Beall (1998), it is noted that elements of the process were first documented in the 1850s. Rotational moulding evolved from a process developed to make metal ordnance shells and artillery shells in the 1850s, hollow wax objects and chocolate eggs in the 1900s, to a process for moulding plasticized polyvinyl chloride (plastisols) in the 1940s. The advent of polyethylene in the 1950s heralded a significant turning point for rotomoulding. The ability to pulverize polyethylene pellets into fine flowing powder was key to the development and growth of the process (Beall, 1998, Dodge and Perry, 2001).

Nowadays, rotomoulding competes with and complements other polymer forming processes such as injection moulding, thermoforming and blow moulding (Crawford et al., 1996, Crawford and Gibson, 2006). It is particularly suitable for large hollow parts and complex parts which cannot easily be fabricated by any other method (Cramez et al., 2003, Bellehumeur, 2005). It is also economic to run short production runs.

Traditionally, rotomoulding has been considered for the design of products with simple geometries and no load bearing capabilities. Crawford and Throne (2002) have given a comprehensive summary of such products which includes chemical storage and septic tanks, containers, automotive parts, marine industry components, toys and outdoor furniture. Crawford and Throne (2002) and Beall (1998) also gave a breakdown of rotomoulded products segments showing how the markets are different in America and Europe.

However, nowadays rotational moulding is also considered for more sophisticated products. For instance, Li et al. (2007) rotomoulded a truck fender using linear low density polyethylene. Barboza Neto et al. (2014) recently fabricated pressure vessel liner prototypes for use in compressed natural gas cylinders by rotomoulding blends of linear low density polyethylene (LLDPE) and high density polyethylene (HDPE).

In South Africa, rotomoulded products are exemplified by large (up to 5000 litres) water storage tanks commonly referred to as Jojo tanks, in reference to the name of the company that popularized them (Figure 1-1). However, there is a wide range of other rotomoulded products on the South African market that include roadside barriers for traffic control, refuse bins, septic tanks, cattle feeding troughs and temporary toilets. Rotomoulded products also find their way into underground mining applications. For instance, battery casings for locomotives used extensively in underground mines are rotomoulded. South Africa happens to be home to the world's deepest mines extending to beyond 4 km below the earth's surface.

Figure 1-1 Rotomoulded water tank 5000 litre water tank (JojoTanks, 2016).

By the end of the last millennium, rotomoulding was experiencing rapid growth rates of between 10-20 % per annum (Yan et al., 2006). Further growth has however been hindered by reliance of the process on polyethylene (Robert et al., 2000). Polyethylene is the major rotomoulding material, with over 85 % of all rotomoulded material being various grades of polyethylene (Yan et al., 2006, Liu and Peng, 2010).

Polyethylene is well suited to rotomoulding because of its low melting temperature, relative thermal stability hence wider processing window, favourable rheology and relatively low cost (Yuan et al., 2007, Chang et al., 2011, Sharifi et al., 2012). However, polyethylene has relatively low strength and stiffness, limited abrasion resistance and heat distortion

temperatures (Harkin-Jones and Crawford, 1996, Murphy et al., 2003, Yuan et al., 2007). Polyethylene is also highly flammable and a good electrical insulator (Sun et al., 1993). Build-up of static charge on polyethylene products presents a potential fire and explosion hazard in some situations (Wang et al., 2010a). This limits the use of polyethylene from emerging applications and new markets with demanding material characteristics. The development of new materials suitable for the rotomoulding process is necessary for its continued growth.

1.1.2 Phase change materials for energy storage

The ever increasing demand for energy can be alleviated by efficient utilization of presently available sources and availing new sources, particularly renewable energy. The depletion of fossil fuels and their environmental impact has resulted in the search for renewable energy sources and energy conservation. Energy storage plays a vital role in the efficient utilization and conservation of energy sources (Farid et al., 2004, Sharma et al., 2009).

Energy storage is also a solution for the disparity between energy demand and supply, enabling energy conservation through efficient utilization and energy supply security (Zalba et al., 2003, Sharma et al., 2009). The intermittent nature of energy availability, particularly from renewable sources, is a challenge which energy storage addresses (Farid et al., 2004, Cui et al., 2011). Latent heat thermal energy storage (LHTES) through phase change materials (PCMs) is an attractive method for energy storage due to their high energy storage densities and the storage/extraction of the energy at nearly constant temperatures (Sharma et al., 2009). Phase change materials store energy by virtue of them absorbing latent heat during phase change transitions. Various materials have been studied as phase change materials for energy storage for numerous applications (Zalba et al., 2003, Farid et al., 2004, Sharma et al., 2009).

Fatty acids and their mixtures have been widely studied as PCMs (Yuan et al., 2014). Most of the properties of fatty acids enable their exploitation as PCMs. Their latent heats of fusion and crystallization are relatively high (Yuan et al., 2014). Fatty acids also undergo consistent melting and freezing and do not exhibit super cooling (Sharma et al., 2009). Unlike salt hydrates, fatty acids melt congruently. Fatty acids also have a low vapour pressure in the melt, are non-toxic, have relatively good chemical and thermal stability and are relatively

inexpensive (Yuan et al., 2014). However, fatty acids are mildly corrosive and have bad odour (Sharma et al., 2009, Huang et al., 2013).

Several fatty alcohols or normal alkanols (*n*-alkanols) have also been studied as PCMs (Zeng et al., 2008, Yavari et al., 2011). These fatty alcohols qualify as phase change materials for energy storage due to their high latent heats of fusion and non-corrosiveness (van Miltenburg et al., 2001, Ventola et al., 2002). However, they exhibit polymorphism which can affect heat storage and extraction from them (Ventola et al., 2002).

Stearyl alcohol and stearic acid have relatively low thermal conductivities (0.38 W/mK at room temperature for stearyl alcohol and 0.172 W/mK at 70 °C) (Zalba et al., 2003, Yavari et al., 2011). Low thermal conductivities constrain the rate of heat transfer into and out of the PCM thereby limiting the heat storage and extraction rates and applicability of the LTHES system.

1.1.3 Nanocomposites

Nanofillers have attracted great interest recently due to their ability to produce polymer nanocomposites with improved mechanical, electrical, thermal and barrier properties and flame retardancy, amongst other properties at very low filler loadings (Chen et al., 2007, Haznedar et al., 2013). A nanocomposite is composed of one or more nanofillers with at least one dimension in the nanometre range (less than 100 nm) (Haznedar et al., 2013).

1.1.4 Graphite nanoplatelets

Graphite nanoplatelets (GNPs) are graphite crystals with thicknesses less than 100 nanometres, but with lateral dimensions which can extend into micrometres (Carotenuto et al., 2012). GNPs are composed of a several layers of graphene, making them alternative nanofillers closely similar to graphene. The lateral dimensions of GNPs (micrometres) are suitable for their exploitation as reinforcements with nanometre thicknesses and excellent thermal and electrical properties. The estimated properties of GNPs are given in Table 1-1.

Table 1-1 Properties of graphite nanoplatelets (Jang and Zhamu, 2008).

Property	Value	Unit
Density	1.8-2.2	g cm^{-1}
Modulus	1	TPa
Strength	100-400	GPa
Resistivity	50	μΩ cm
Thermal conductivity	5300	W m^{-1} K^{-1}
	6-30*	W m^{-1} K^{-1}
Specific surface area	Experimentally observed: 100-1000, theoretical >2600	m^2 g^{-1}

*Value in the c-axis

1.2 Aims and objectives

The overall aim of this study was to obtain a facile method of synthesizing graphite nanoplatelets from commercial expandable graphite and use these as functional fillers in rotational moulding applications and phase change materials for energy storage.

The first objective was to study the exfoliation and delamination characteristics of two commercial expandable graphites into graphite nanoplatelets. Having obtained a suitable expandable graphite and method to exfoliate and delaminate it, the next objectives were to use the obtained graphite nanoplatelets as a functional filler.

With respect to rotational moulding applications, the overall aim was to develop cost-effective, flame-retardant and antistatic polyethylene-graphite compounds suitable for rotational moulding for use in underground mining applications. A previous study considered antistatic polyethylene-graphite composites using micron-sized natural flake graphite (Mhike and Focke, 2013). The inclusion of the natural graphite in polyethylene also improved the ignition resistance in cone calorimeter fire tests (Mhike et al., 2015). However, the impact and tensile strengths of these composites were severely compromised at the graphite loadings required to achieve static dissipation (≥ 10 wt.%). In this present study it was hypothesized that antistatic and flame retarded rotomoulded polymer nanocomposites based on graphite nanoplatelets could overcome some of these limitations at low graphite contents. The

objectives were therefore to formulate and fabricate antistatic and flame retardant rotomoudable polymer nanocomposites with graphite nanoplatelets as the functional filler in an attempt to minimize the amount of filler and retain useful mechanical properties.

With respect to phase change materials for energy storage, the aims were twofold. The first aim was to fabricate a mixture of stearic stearyl alcohol and stearic acid which exhibits a single endotherm and exotherm at its melting and crystallization transitions for application as a novel PCM. The second aim was to enhance the thermal conductivity of this PCM using graphite nanoplatelets by utilizing a facile method to prepare PCM/graphite nanocomposites and characterize them as phase change material nanocomposites for thermal comfort applications. It was hypothesized that good interfacial interaction between graphite nanoplatelets and the PCM would result in superior thermal conductivity. The objectives were to evaluate the thermophysical properties (melting and crystallization enthalpies as a function of temperature, thermal conductivity, thermal stability and thermal cyclability).

1.3 Outline of the study

In Chapter one a background to the study is given. The background encompasses an overview of the rotational moulding process and highlights the limited material selection for this process. This has inhibited its further growth as rotomoulded polyethylene products find limited applicability. The background also includes phase change materials for energy storage, highlighting the advantages and limitations of stearyl alcohol and stearic acid as phase change materials for energy storage. The emergence of nanocomposites as materials with enhanced properties is also highlighted. Graphite nanoplatelets are introduced as a functional nanofiller with outstanding electrical, thermal and mechanical properties. The aims and objectives of the study are presented in this chapter.

The literature study is presented in four chapters. Chapter two focuses on graphite, graphene, and graphite nanoplatelets. The chapter gives an overview of the properties of graphite and its compounds. It also examines the properties of graphene and its synthesis, particularly through liquid phase exfoliation. Ultrasonication is studied in-depth. The chapter concludes with a study of the synthesis of graphite nanoplatelets using ultrasonication assisted liquid phase exfoliation. Chapter three focuses on polymer composites, highlighting the electrical,

mechanical, thermal and fire properties of polymer composites. The nanoscale effect of fillers on these properties is examined. In chapter four, attributes of the rotational moulding process were studied exhaustively. The use of functional additives and how they are included in rotomoulding polymers is one of the highlights of this chapter. In this chapter possible mixing techniques which can be exploited for rotomoulded nanocomposites and their effects on properties are reviewed. Chapter five is a study of phase change materials for energy storage, particularly their characterization. The nature of stearyl alcohol with respect to its polymorphism is examined in this chapter. Various ways in which the thermal conductivity of PCMs is enhanced are investigated in this chapter.

The experimental methodology is presented in chapter six. The chapter is divided into three sections; synthesis of graphite nanoplatelets, rotomoulded polymer/graphite nanocomposites and phase change material/graphite nanocomposites.

The results and discussions are presented in three chapters. Chapter seven focuses on the graphite nanoplatelets, chapter eight focuses on rotomoulded polymer/graphite nanocomposites and chapter nine focuses on phase change material/graphite nanocomposites.

Chapter ten presents the conclusions and recommendations for future work.

Chapter 2 Literature: Graphite, graphene and graphite nanoplatelets

2.1 Carbon polymorphs

The element carbon exists in the form of various allotropes or polymorphs depending on which electronic configuration it assumes during bonding. The most common polymorphs of carbon are diamond, graphite and fullerenes (Pierson, 1993, Chung, 2002).

Graphite and all other graphitic structures are formed from the covalent bonding of sp^2 hybridized carbon atoms (Pierson, 1993). Three sigma (σ) orbitals from an sp^2 hybridized carbon atom with a single electron each covalently bond with other sigma orbitals from three other sp^2 hybridized carbon atoms to form trigonal planar covalent sigma bonds at 120 ° to each other, resulting in a hexagonal planar structure. The forth valence electron is delocalised in a pi (π) orbital perpendicular to the plane. Graphene is composed of a single plane of sp^2 hybrid carbon atoms covalently bonded in an infinite two dimensional structure. Figure 2-1 shows the σ and π orbitals in the hexagonal planar structure of graphene (Jorio et al., 2011). As shown in Figure 2-2, all graphitic structures have graphene as their fundamental structure (Geim and Novoselov, 2007).

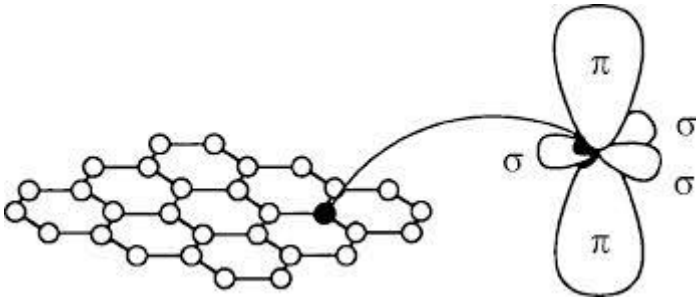

Figure 2-1 σ and π orbitals in the hexagonal planar structure of graphene (Jorio et al., 2011).

2.2 Graphite

Graphite is composed of a series of carbon planes staked together through weak van der Waals bonds emanating from interaction of the π electron orbitals (Pierson, 1993, Chung,

2002). The delocalized electrons in the π orbitals can move from one end of the plane to other but not cross one layer to another (Pierson, 1993).

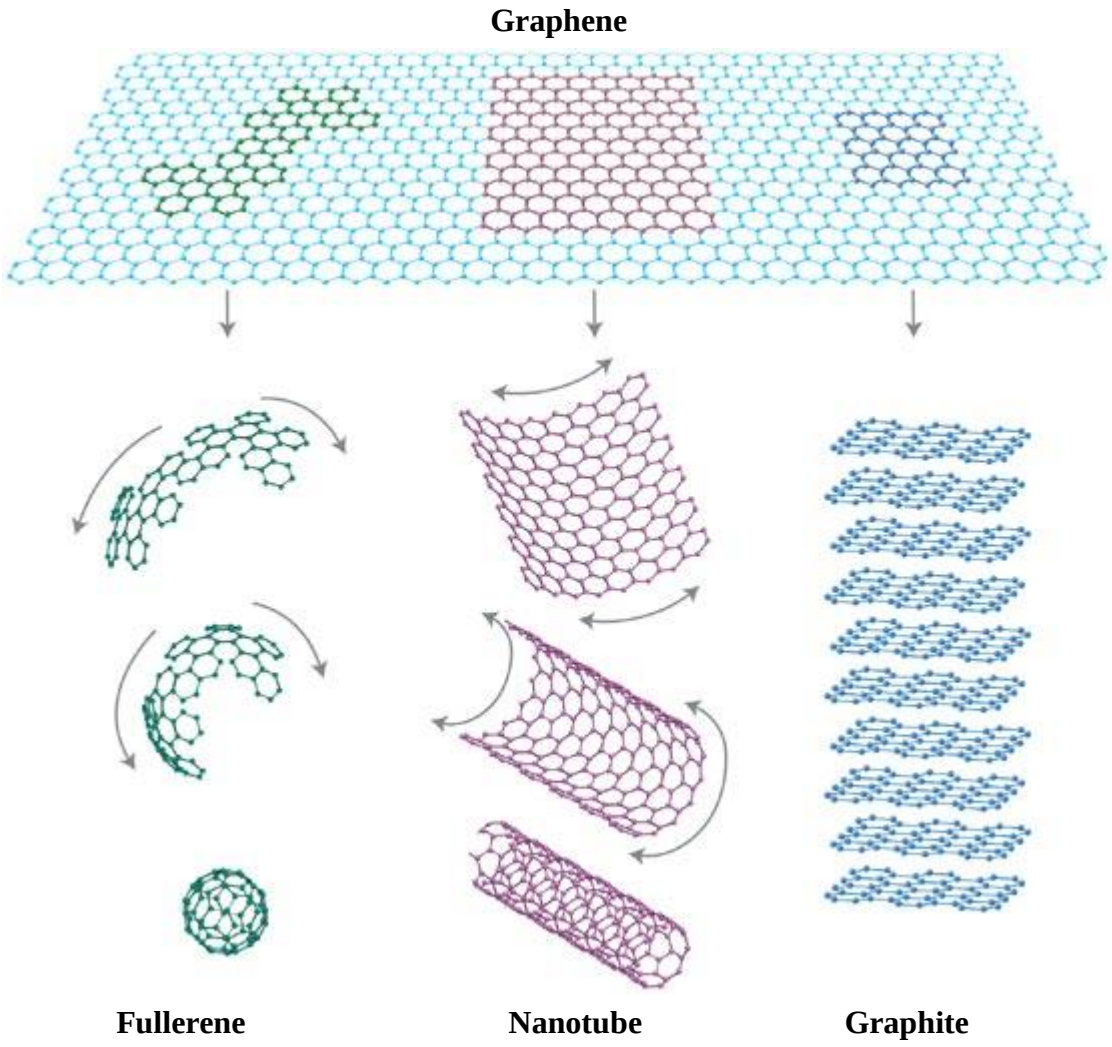

Figure 2-2 Graphitic structures with graphene as the fundamental structure (Geim and Novoselov, 2007).

2.2.1 Crystal structure

Within a graphite crystal, layers of carbon atoms can stack in an -ABABAB- or -ABCABC- sequence (Pierson, 1993, Chung, 2002). Hexagonal graphite results from the -ABABAB- stacking sequence. It is the most stable form. In hexagonal graphite, carbon atoms in each second layer superimposed are over each other. Figure 2-3 shows the stacking sequence in hexagonal graphite together with the unit cell outline and lattice parameters. The interlayer

spacing between successive carbon layers is 0.335 nm (Chung, 2002). Table 2-1 gives a summary of the properties of a hexagonal graphite crystal.

Rhombohedral graphite results from the -ABCABC- stacking of carbon layers. It is not thermodynamically stable. Rhombohedral graphite is always found in combination with hexagonal graphite. In rhombohedral graphite, carbon atoms in each third layer are superimposed over each other (Pierson, 1993). Table 2-1 also give a summary of the properties of a rhombohedral graphite structure.

Table 2-1 Graphite crystal structure (Pierson, 1993).

Characteristic	**Hexagonal**	**Rhombohedral**
Space group	D^4_{6H}-$P6_3/mmc$	D^5_{3d}-R3m
Crystal lattice parameters	a_o=0.245 nm	a_o=0.2256 nm
	c_o=0.6708 nm	c_o=1.006 nm
Colour	Black, black streak	-
Stability	Thermodynamically stable	-

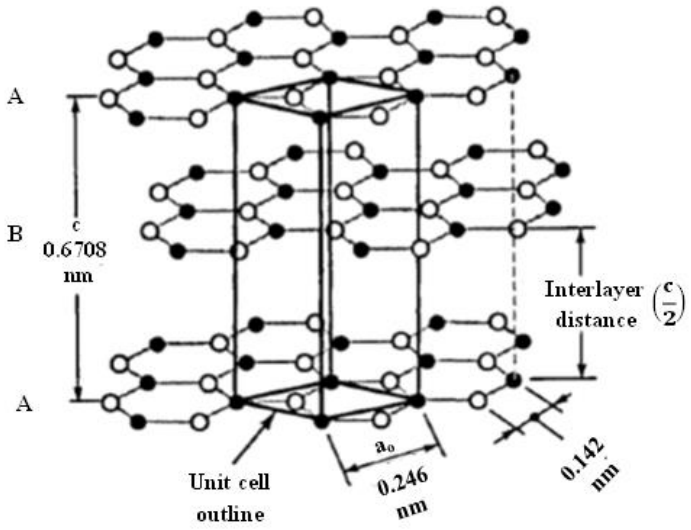

Figure 2-3 Hexagonal graphite (modified from Pierson (1993)).

2.2.2 Occurrence: Natural and synthetic graphite

Graphite is classified as natural or synthetic graphite depending on its source (Wissler, 2006). Graphite occurs naturally in metamorphic rocks in the Earth's crust (Kalyoncu et al., 2005). Natural graphite is further divided into macro-crystalline and micro-crystalline forms with reference to crystallite sizes (Wissler, 2006). Macro-crystalline graphite is either flake graphite or vein graphite flake. It is highly crystalline. Micro-crystalline graphite is also referred to as amorphous graphite (Wissler, 2006). Graphite is formed in igneous or metamorphic rocks. However, deposits of commercial importance are found in metamorphic rocks (Kalyoncu et al., 2005).

Flake graphite consists of large crystals oriented in lamella or scaly forms (Wissler, 2006). Froth flotation is used to extract flake graphite from its ore. Carbon contents of between 80-98% are obtained. Higher purity flake graphite is obtained by further chemical treatment. Several countries which include Brazil, Canada, China, Madagascar, Mozambique, and Zimbabwe have significant deposits of flake graphite (Kalyoncu et al., 2005).

Vein graphite is a naturally occurring form of pyrolytic graphite deposited from a fluid phase. Vein graphite occurs as deposits of veins of variable thickness with niddle-like, intergrown large crystals. Due to the process by which vein graphite is deposited viz. fluid to solid, the purity of deposits is usually high, typically above 90 %. Conventional surface or shaft methods are used to mine vein graphite. Sri Lanka is known to have commercially viable deposits of vein graphite (Kalyoncu et al., 2005).

Amorphous graphite has a low degree crystalline order. It has a microcrystalline structure and is formed by thermal metamorphism of coal seams. Conventional coal extracting techniques are used to extract amorphous graphite (Kalyoncu et al., 2005).

Heat treatment of unstructured carbons above 2500 °C orients disordered layers into graphitic structures (Wissler, 2006). Synthetic graphite differs in properties according to raw materials used and the particular heat treatment process applied. Synthetic graphite is divided into primary and secondary synthetic graphite. Conditions under which primary synthetic graphite is made are stringent, ensuring more consistent properties, compared to secondary synthetic graphite.

2.2.3 Physical properties

The unique properties of graphite that make it any interesting functional filler for polymers are given in Table 2-2. The properties of graphite are necessarily anisotropic due to the nature of its electronic configuration. The properties of natural graphite described by Pierson (1993) and other workers (Sengupta et al., 2011) are essentially those of single crystalline graphite although graphite is seldom found in single crystal form. Most of these properties are theoretical.

Table 2-2 Physical properties of graphite (Sengupta et al., 2011).

Property	**In-plane**	**C-axis**	**Unit**
Density	2.26	-	g cm^{-1}
Tensile modulus	1	-	TPa
Tensile strength	130	-	GPa
Resistivity	50	-	μΩ cm
Thermal conductivity	3000	6	W m^{-1} K^{-1}
Thermal stability	450-650 (in air)		°C

2.3 Graphite compounds

Several reviews and reports on empirical studies classify graphite compounds inconsistently (Hennig, 1952, Hennig, 1955, Rüdorff, 1959, Ebert, 1976, Chung, 2002). An attempt is made to present a classification of the compounds in a logical manner easy to follow.

Hennig (1955) classified compounds of graphite into surface, substitutional and interstitial compounds. Hennig (1955) suggested that the surface atoms on the periphery of the graphite crystal can interact with reacting species to form surface compounds. Hennig (1955) envisaged that the graphite edge atoms are more reactive due to their possession of residual valence bonds. The oxidation reaction was cited as an example of such a reaction. Hennig also hypothesized that reacting species such as boron, nitrogen or antimony could substitute carbon atoms in graphite, analogous to reactions of other group IV elements to form substitutional graphite compounds. There was however no experimental evidence of this type of graphite compounds except for the graphite compound with boron. The existence of

vacancies in the graphite lattice structure was also considered to be a form of graphite substitutional compounds.

According to the classification used by Hennig (1955), the majority of reactions of graphite with other species result in graphite interstitial compounds. Most workers have called these graphite intercalation compounds (Rüdorff, 1959, Ebert, 1976, Selig and Ebert, 1980, Chung, 2002) although other scholars have referred to them as insertion or inclusion compounds (Forsman et al., 1983). The common denominator in these compounds is the insertion or inclusion of the reacting species within the basal layers of the graphite lattice thereby increasing the interlayer spacing between the layers. However, the manner in which the reacting species interacts with the carbon atoms of graphite differs, leading to a further distinction of these compounds.

The graphite compounds which Hennig (1955) referred to as interstitial compounds of graphite can be classified into two groups, depending on how the reacting species interacts with graphite. The first group are the covalent compounds of graphite (Hennig, 1955, Rüdorff, 1959, Ebert, 1976, Selig and Ebert, 1980, Chung, 2002). In this type of graphite compounds, the interstitial species interacts with graphite by forming covalent bonds with the carbon atoms in the graphite lattice. The planar structure of carbon atoms in graphite reverts to a wavy or puckered structure due to the change from trigonal sp^2 hybridisation bonding in graphite to tetragonal sp^3 hybridization in these compounds (Selig and Ebert, 1980, Chung, 2002). These compounds are not electrically conducting because the delocalised fourth valence electron in graphite is no longer available but rather involved in bonding (Hennig, 1955, Rüdorff et al., 1963). Graphite oxide, carbon monofluoride, and tetracarbon monofluoride are examples of covalent interstitial compounds of graphite.

The second group of graphite interstitial compounds are to a greater extent ionic in nature (Hennig, 1955, Rüdorff, 1959, Chung, 2002). The delocalized π electrons in carbon atoms of graphite interact with reacting species and form polar bonds, retaining these species within the carbon layers. The interlayer spacing increases as a result, but the planar structure of the layers is maintained. This group of compounds includes graphite salts for instance graphite bisulphate and graphite nitrate, graphite-alkali metal compounds, graphite halogen compounds and graphite-metal chloride.

2.3.1 Graphite intercalation compounds

The International Union of Pure and Applied Chemistry (IUPAC) ascribed the term graphite intercalation compounds (GICs) to compounds of graphite formed as a result of charge transfer between graphite and the reacting species (Boehm et al., 1994). From the preceding section it is apparent that these compounds are a subgroup of graphite compounds that Hennig (1955) classified as interstitial compounds of graphite. However, in that group of compounds, the IUPAC regards only those which exhibit ionic character to be GICs. This is in contrast to the classification of graphite compounds by, for instance, Chung (2002). Chung (2002) also had surface and substitutional compounds as Hennig (1955) did, but additionally intercalation compounds which are interstitial compounds. In his classification all interstitial compounds of graphite are graphite intercalation compounds. It must thus be noted that in previous works the term graphite intercalation compound was used to refer to a wide range of graphite compounds (Rüdorff, 1959, Ebert, 1976, Selig and Ebert, 1980, Chung, 2002). The definition of graphite intercalation compounds as defined by IUPAC is used in subsequent discussions.

A comprehensive review on graphite intercalation compounds as defined by the IUPAC was published by Dresselhaus and Dresselhaus (1981). This review has proved to be so popular according to the number of its citations; it had to be republished in the year 2002. Noel and Santhanam (1998) gave a history of the synthesis of graphite intercalation compounds. The earliest report on GICs was on the synthesis of sulphuric acid based GICs by Schafhaut in 1841 (Noel and Santhanam, 1998, Dresselhaus and Dresselhaus, 1981). The reacting species is referred to as the intercalate (Boehm et al., 1994).

The various methods that can be used to synthesize graphite intercalation compounds have been discussed by Ebert (1976) and Dresselhaus and Dresselhaus (1981). These include vapour absorption, chemical intercalation, electrochemical methods and co-intercalation techniques.

2.3.1.1 Classification

Donor/Acceptor compounds

In the formation of graphite intercalation compounds, a reacting species can either donate electrons to graphite or accept electrons from graphite, hence a further subdivision into donor or acceptor type GICs compounds. Electropositive species (M) donate electrons to graphite to form donor compounds by reducing graphite as shown by the reaction (Noel and Santhanam, 1998):

$$C_x + M \leftrightarrow C_x^- \cdot M^+$$

where C_x represents electrons in the π network. Electronegative species (A) accept electrons from graphite and form an ionic bond with the π electron network (Noel and Santhanam, 1998):

$$C_x + A \leftrightarrow C_x^+ \cdot A^-$$

Ternary GICs can have a mixture of donor or acceptor species or more than one type of each (Noel and Santhanam, 1998). The intercalating species largely retain their molecular form in the graphite lattice due to low degrees of ionization (Dresselhaus and Dresselhaus, 1981, Chung, 2002).

The alkali metal GIGs compounds are the most common donor compounds (Dresselhaus and Dresselhaus, 1981). The valance electrons of these metals occupy the conduction band of graphite (Rüdorff et al., 1963). Acceptor compounds are largely based on Lewis acid and Brønsted acid intercalates (Dresselhaus and Dresselhaus, 1981). Strong oxidizing agents accept electrons from graphite to form acceptor compounds leaving positively charged carbon layers on the graphite lattice (Hennig, 1955, Rüdorff et al., 1963). The graphite salts, graphite halogen compounds and graphite-metal chloride are typical acceptor type compounds. The transfer of electrons in both cases results in increased conductivity of graphite intercalation compounds (Hennig, 1955).

2.3.1.2 Properties of GICs

Staging

Graphite intercalation compounds are characterized by the staging phenomenon (Dresselhaus and Dresselhaus, 1981). Staging relates to the periodicity or repeatability in which intercalate layers are inserted within graphite layers. The stage index number *n* is the number of graphite

layers in between adjacent intercalate layers. The stage index is determined through X-ray diffraction using (00*l*) reflections, where *l* is an integer (Dresselhaus and Dresselhaus, 1981).

The definition of staging assumes existence of the intercalate species as a continuous phase in between graphene layers of an ideal, defect free graphite lattice structure (Noel and Santhanam, 1998). Graphite seldom has the ideal lattice structure, exhibiting defects and grain boundaries within the lattice (Noel and Santhanam, 1998). The intercalating species can intercalate randomly into the layers forming different stages. It can also form islands of various sizes within the lattice instead of the idealised continuous phase.

Lamella/residue compounds

Graphite intercalation compounds can be further classified as lamellar or residue graphite intercalation compounds (Ebert, 1976, Chung, 1978). Lamellar compounds are formed when graphite intercalation compounds are exposed to excess intercalate (Chung, 1978). Lamellar compounds exhibit highly ordered layered structures (Ebert, 1976, Chung, 2002).

Residue compounds are formed when lamellar compounds are removed from an environment in which they were in equilibrium with excess intercalate (Chung, 1978, Dresselhaus and Dresselhaus, 1981). Removal of excess intercalate causes desorption of intercalate out of the GIC, forming a residue compound. Desorption continues until an equilibrium is established between the compound and partial pressure of the external intercalate (Chung, 1978). The intercalate concentration of the residue compound is influenced by the desorption temperature and concentration of the preceding lamellar compound. Residue compounds are relatively stable compared to lamellar compounds (Dresselhaus and Dresselhaus, 1981). Desorption is aided by thermal and vacuum treatment (Ebert, 1976, Selig and Ebert, 1980).

Washing of graphite intercalation compounds with water is used to obtain higher stage compounds with dilute intercalate concentration (Dresselhaus and Dresselhaus, 1981). These dilute compounds are not well staged. Washing with water apparently results in the formation of residue graphite intercalation compounds (Hennig, 1952).

The structure of residue compounds has remained largely controversial as they have not been extensively studied. The c-axis interlayer distance increases as a result of intercalation of

species into the graphite lattices. However, in X-ray diffraction (XRD) studies of the residue compounds of graphite-bisulphite and graphite-bromide, Hennig (1952) observed insignificant increases in the c-axis interlayer distances to be able to account for the intercalate. This led him to the conclusion that intercalates in residue graphite compounds were mostly trapped in crevices or faults (crystal imperfections) as an impurity. This conclusion is contrary to the subsequent observations of Inagaki et al. (1977) and Chung (1978) which suggested that intercalates in residue compounds also existed in ordered layers as in lamellar compounds.

2.3.2 Exfoliation of graphite intercalation compounds

Graphite intercalation compounds expand substantially along the c-axis when exposed to heat, due to vaporization of the intercalate (Chung, 1987). This phenomenon is known as exfoliation. Above a critical temperature exfoliation is irreversible. Exfoliation involves the delamination of layered materials such that all inter planar interaction in between the layers of a layered material is removed (Furdin, 1998). Exfoliated graphite is also known as expanded graphite.

The exfoliation of graphite intercalation compounds is exploited when they are used as intumescent flame retardants. The endothermic nature of the exfoliation process and formation of a barrier blanket of exfoliated graphite has been shown to be an effective flame retardant mechanism for some polymers which slows down heat transfer into the substrate (Qu and Xie, 2003, Weil and Levchik, 2008).

2.3.3.1 Exfoliation mechanisms

Anderson and Chung (1984) and Chung (1987) reviewed several mechanisms proposed for the exfoliation of graphite intercalation compounds. It is undisputed that exfoliation of graphite intercalation compounds occurs as a result of the explosion accompanying the vaporization or decomposition of pockets of intercalates (Anderson and Chung, 1984, Chung, 1987, Falcao et al., 2007). However, the origin of the vaporised pockets of intercalates is still a matter of much scientific debate (Anderson and Chung, 1984, Chung, 1987). It has been suggested that the vaporized intercalate is segregated to defects in the graphite lattice. However, experimental evidence points otherwise. Anderson and Chung (1984) proposed an

exfoliation mechanisms involving intercalate islands as originally proposed in the Dumas-Harold model.

Furdin (1998) proposed that during exfoliation of residue graphite intercalation compounds there is competition between boiling of the intercalate within the residue compound which leads to exfoliation and; desorption of the intercalate by evaporation through the graphite edges. These two are dependent on the rate of heat transfer to the compound. Furdin (1998) also interpreted the phenomena observed during exfoliation to be due to mostly endothermic reactions, although it was shown that exothermic reactions can also govern exfoliation. Furdin (1998) interpreted his differential thermal analysis (DTA) and thermogravimetric analysis (TGA) results of graphite nitrate compounds by suggesting that intercalates vaporize without boiling and desorbs to particle edges and defects during initial stages of exfoliation. The intercalate trapped within the defects then boils as desorption simultaneously continues. Boiling of the intercalate leads to exfoliation, and eventually complete desorption occurs.

2.3.2.2 Factors governing exfoliation of graphite

Several workers have investigated various aspects of the exfoliation of graphite intercalation compounds. The experimental results of Anderson and Chung (1984) suggested that the initial stage of a graphite compound was more influential on its exfoliation behaviour than the intercalate concentration in the compound. Exfoliation occurred to a greater extent in compounds which had a higher initial stage. The degree of exfoliation also increased with the temperature used to exfoliate the compound. The results of Furdin (1998) apparently contradict the observations of Anderson and Chung (1984). In the work by Furdin (1998), the surface area and co-efficient of expansion of the exfoliated graphite obtained from graphite nitrates of various stages showed that the stage of the precursor compound had no influence on the exfoliation propensity of the graphite compound. The pleated layer model was used to explain these results. The model assumes that the intercalate is found within all interlayers regardless of stage, with only the density of the intercalate varying per unit volume with stage.

Yoshida et al. (1991) explored the effect of various intercalates on the morphology of the exfoliated graphite. They observed that exfoliated graphite from acceptor type GICs had large collapsed balloons with the widths almost as that of the original particles. Donor type GICs

exfoliated by dividing into smaller balloons with smaller widths. Stacking of graphite layers was easily discernable in the acceptor compounds, in contrast to the donor type compounds.
The effect of various preparation conditions of graphite intercalation compounds on the exfoliation characteristics was investigated by Kang et al. (2002). They prepared residue compounds with H_2SO_4 using the electrochemical method. They observed exfoliated graphite with worm like structures consisting of large balloons similar to those observed by Yoshida et al. (1991) for acceptor compounds. The exfoliation volume, specific surface area and pore volume depended on the electrical energy consumed. Their results showed that the temperature at which exfoliation was conducted is a critical variable. However, the exfoliation volume, specific surface area and pore volume tended towards saturation beyond exfoliation temperatures of 800 °C. Inagaki et al. (2004) also showed that exfoliation volume increased with the temperature used to exfoliate the graphite whereas the bulk density decreases with increase in the temperature used to exfoliate the graphite compound for exfoliated graphite prepared from residue compounds of graphite and sulphuric acid. The results of Furdin (1998) also show that the temperature at which exfoliation occurs is independent of the heating rate used and the stage of precursor residue compound. The study by Murdie et al. (1985) showed that particles exfoliate if their diameter is more than 200 μm, otherwise the intercalate desorbs.

The type of graphite used in the synthesis of GICs influences their exfoliation characteristics (Furdin, 1998). Polycrystalline graphite intercalated with sulphate or nitrate exfoliates poorly due to the tendency of the smaller particles to desorb all the intercalate and not retain any intercalate as a result of their small domain sizes. Single crystalline graphite exfoliates better.

Various methods of heat treatment for exfoliation of graphite intercalation compounds have been mentioned in the literature, but the conventional heating method is rapid heating by passing the graphite through a flame (Chung, 1987). Alternative heating methods such as inductively coupled plasma, infrared, microwave and laser radiation have been suggested (Chung, 1987, Tryba et al., 2005). Furdin (1998) used the hypothesis that the heat transfer rate determines whether mostly exfoliation or desorption of the intercalate occurs to explain the results of an earlier study (Thomy et al., 1987). These results showed high surface area obtained through laser irradiation of graphite nitrate compared to that obtained by furnace heating at 600 °C of the same samples. Furdin (1998) also showed his own experimental evidence to support this hypothesis.

Tryba et al. (2005) demonstrated that exfoliated graphite with properties comparable to those of GICs exposed to rapid heating at 1000 °C in a furnace could be obtained through microwave radiation. The advantage of using microwave radiation over the traditional heating is fast exfoliation time which is less energy intensive at room temperature (Tryba et al., 2005). The major disadvantage they highlighted was that exfoliation preferentially occurs on the graphite intercalation compound on top, but this can be resolved by exfoliating thinner layers. Falcao et al. (2007) also demonstrated the effectiveness and simplicity of microwave-exfoliation of a potassium- tetrahydrofuran (THF) graphite co-intercalation compound. Wei et al. (2009b) proposed a rapid and efficient method of simultaneously intercalating and exfoliating using microwave radiation.

2.3.2.3 Industrial scale production of exfoliated graphite

Exfoliated graphite is produced from residue graphite intercalation compounds which are also called expandable graphite (Talanov et al., 1993, Inagaki et al., 2004). The expandable graphite is commonly synthesized through the chemical reaction of natural graphite flakes with sulphuric acid in the presence of strong oxidising agents such as HNO_3, CrO_3, $KMnO_4$, PbO_2 (Inagaki et al., 1990).

In the industrial synthesis of exfoliated graphite, a stage 1 or stage 2 GIC is first synthesized (Furdin, 1998). Following the work of Yaroshenko et al. (2002), the graphite salt graphite bisulphate is formed from the chemical oxidative intercalation of graphite with sulphuric acid in the presence of nitric acid according to the following reaction scheme:
Nitric acid is ionized resulting in nitronium cations:

$$HNO_3 + H_2SO_4 \rightarrow NO_2^+ + HSO_4^- + H_2O$$

The graphite crystal lattice is oxidized by nitronium cations, enabling the sulphate ions and molecules to be intercalated within the carbon layers:

$$C_{24n} + NO_2^+ \rightarrow C_{24n}^+ + NO_2$$

$$C_{24n}^+ + HSO_4^- + mH_2SO_4 \rightarrow C_{24n}^+ \cdot HSO_4^- \cdot mH_2SO_4$$

The stage number is denoted by n and m denotes the number of sulphuric acid molecules associated with each intercalated ion. For the stage 1 compound n is equal to one and m is equal to 2. The composition of the stage 1 graphite bisulphate compound which is deep blue in colour is $C_{24}^+ \cdot HSO_4^- \cdot 2H_2SO_4$ (Rüdorff, 1959). This is then is followed by washing to produce residue compounds (Furdin, 1998, Inagaki et al., 2004). Furdin (1998) termed these

washed compounds ‘complexes’, although in the literature lamellar GICs subjected to environments in which they have been desorbed or decomposed through processes such as washing with water have been termed residue compounds (Hennig, 1952). These residue compounds obtained contain mixtures of stages ranging from 10 and up to 25 (Furdin, 1998). The composition of the residue compounds can be approximated by $C_n^+ \cdot HSO_4^- \cdot 4H_2SO_4$ (Hennig, 1952). The residue compounds also contain graphite and completely desorbed compounds (Furdin, 1998).

Exfoliated graphite is subsequently obtained through thermally shocking the residue compound. Under the conditions in which the GIC is exfoliated, the intercalate instantaneous vaporises or decomposes before it desorbs. Exfoliation efficiency is characterized through the coefficient of expansion and surface area of the exfoliated particles, their bulk density and microscopy (Furdin, 1998).

In a recent study, Focke et al. (2014) found that commercial expandable graphite was not entirely composed of graphite intercalation compounds with sulphuric acid species intercalated as guest ions and molecules in between intact graphene layers. Focke et al. (2014) tested the hypothesis put across by Camino et al. (2001) that exfoliation of commercial expandable graphite was due to the generation of blowing gases through the redox reaction between H_2SO_4 and graphite:

$$C + 2H_2SO_4 \rightarrow CO_2 + 2H_2O + 2SO_2$$

However, the composition of evolved gases in the experimental work of Focke et al. (2014) on two commercial expandable graphites did not correspond to the reaction above. Elemental analysis also showed that expandable graphite contained a significant amount of oxygen. Focke et al. (2014) proposed a model in which expandable graphite contained ordered crystalline regions intercalated with sulphate ions and molecules, and highly disordered regions composed of graphite oxide. In the model oxidised graphite oxide layers were interstratified within the crystalline graphite layers intercalated with sulphate ions and molecules. XRD reflection patterns showed evidence of the presence of both an amorphous graphite oxide phase and a crystalline intercalated phase. Focke et al. (2014) concluded that the oxygen containing functional groups of the graphite oxide also decompose and volatilize upon heating, producing carbon monoxide and carbon dioxide during the exfoliation of expandable graphite.

2.4. Graphene

Graphene has been theoretically studied since the 1940s (Wallace, 1947, McClure, 1957, Slonczewski and Weiss, 1958). However, it was not until the year 2004 that Geim and co-workers reported on the successfully isolation of graphene through micromechanical cleavage and its unique properties (Novoselov et al., 2004). Andre Geim and Konstantin Novoselov were rewarded with the Nobel Prize for Physics for the year 2010 for their work on graphene (Singh et al., 2011). Since the report of its first isolation in 2004, graphene has drawn a surge of interest from scientists the world over due to its outstanding properties (Randviir et al., 2014). Table 2-3 lists some of them.

As alluded to in section 2.1, graphene is a carbon allotrope composed of a planar monolayer of carbon atoms in a two dimensional honeycomb lattice (Geim and Novoselov, 2007, Singh et al., 2011). It is the building block of all graphitic materials; the 0D fullerenes, 1D carbon nanotubes and the 3D graphite (Figure 2-2) (Geim and Novoselov, 2007).

Table 2-3 Graphene properties.

Property		**Value**	**References**
Charge carrier mobility	Experimental	$1x10^4$ cm^2 V^{-1}	Novoselov et al. (2004)
	Theoretical	$2x10^5$ cm^2 V^{-1}	Morozov et al. (2008)
Thermal conductivity	Theoretical	5000 W $m^{-1}K^{-1}$	Balandin (2011)
Young's modulus	Theoretical	1 TPa	Lee et al. (2008)
Tensile strength:	Experimental	130 GPa	Lee et al. (2008)
Surface area	Experimental	400–700 m^2 g^{-1}	Ciesielski &Samori (2014):
	Theoretical	2600 m^2 g^{-1}	Stoller et al. (2008)
			Chae et al. (2004)
Optical transparency		97.7%	Brownson et al. (2012)

The range of applications conceived for graphene is substantially wide (Novoselov et al., 2012). These include electronics and photonics, energy generation and storage, composite materials, sensors and metrology, and bioapplications. The major challenge in utilizing graphene is the absence of methods for large scale production of pristine, defect free

graphene at low cost, high yield and through put (Hernandez et al., 2008, Paton et al., 2014, Zhong et al., 2015).

2.4.1 Graphene synthesis

Several reviews discussed in-depth the methods currently used to produce graphene, for instance those by Ambrosi et al. (2014), Ren and Cheng (2014) and Zhong et al. (2015). These methods are classified into top-down and bottom-up approaches. Bottom-up approaches utilize molecular building blocks to assemble the two dimensional graphene structures though catalytic, thermal or chemical processes such as chemical vapour deposition, silicon carbide decomposition or organic synthesis, respectively. Top-down approaches utilize the exfoliation of a precursor graphite material to exfoliate graphene through mechanical, chemical or electrochemical processes such as scotch tape, liquid phase exfoliation or exfoliation oxidation/reduction and exfoliation, respectively. These methods weaken the van der Waals forces in between the staked graphene layers in graphite thereby delaminating them. The unzipping of carbon nanotubes to produce graphene nano ribbons is another top-down method.

A number of manufactures claim to produce graphene on an industrial scale by utilization of top-down bulk graphite exfoliation routes (Ren and Cheng, 2014). Oxidation-exfoliation-reduction, intercalation-exfoliation and liquid phase exfoliation have been typically exploited in the mass production of the graphene materials. The oxidation routes can produce large quantities of graphene like, defective reduced graphene oxide.

2.4.1.1 Oxidation-exfoliation-reduction method

In the oxidation-exfoliation-reduction method, graphite oxide is synthesized from graphite, and subsequently exfoliated into graphene oxide. Graphene is obtained by reducing the graphene oxide (Schniepp et al., 2006, Stankovich et al., 2007). Graphite oxide is obtained through the oxidation of graphite by strong oxidants in the presence of strong acids primarily through the Brodie, Staudenmaier or Hummers methods (Park and Ruoff, 2009). Graphite oxide consists of oxidized graphene sheets with epoxide and hydroxyl functional groups on their basal planes and carbonyl and carboxyl groups which are thought to be on their edges (Stankovich et al., 2007). Introduction of oxygen functionalities on the graphite structure

lattice disrupts the sp^2 planar structure in graphite and results in sp^3 hybridization of the carbon atoms (Ambrosi et al., 2014) (as discussed earlier on in section 2.3). The presence of oxygen functional groups within graphite oxide increases the interlayer spacing between carbon layers significantly (Ambrosi et al., 2014).

The oxygen functionalities on the oxidized graphene sheets render them hydrophilic (Park and Ruoff, 2009, Stankovich et al., 2007). Subsequently, the interlayer cohesion of the graphene oxide sheets is small and exfoliation and dispersion can be effected in aqueous media by sonication to form isolated sheets of graphene oxide (Stankovich et al., 2006, Stankovich et al., 2007). Graphene oxide sheets require thermal, chemical or electrochemical processes to reduce them to the planar sp^2-hybridized carbon structure of graphene. However, the oxygen functional groups are not fully eliminated during the reduction stage and the resulting graphene exhibits structural defects (Singh et al., 2011, Ambrosi et al., 2014). Hence the properties of the reduced graphene are not as good as those of pristine graphene.

2.4.1.2 Intercalation-exfoliation route

The intercalation-exfoliation route exploits either the electrochemical intercalation of ions into graphite and electrochemical reaction with the electrolyte to exfoliate the graphite (Ren and Cheng, 2014, Zhong et al., 2015) or the exfoliation of graphite intercalation compounds (Gu et al., 2009, Yoon et al., 2015). The nature of the graphene materials produced from the electrochemical route depends on the voltage and electrolyte used (Zhong et al., 2015). Electrochemical exfoliation of graphite is relatively fast and environmentally friendly, and it can be done in ambient conditions. However, when electrochemical exfoliation is performed using anodic potentials to intercalate ions, it leaves the graphite susceptible to unintended oxidation which disrupts the sp^2 hybridization thereby deteriorating the properties of graphene (Ambrosi et al., 2014). The graphene size and layer distribution is also difficult to control, with few layer graphene or multilayer graphite often being produced (Ambrosi et al., 2014, Zhong et al., 2015).

2.4.1.3 Liquid phase exfoliation

Liquid phase exfoliation of graphite has been touted and investigated as a possible way to produce defect free, large quantities of graphene (Coleman, 2012). Ultrasonication assisted

liquid phase exfoliation of graphite into graphene in various liquid media has been extensively studied by Coleman and co-workers and other groups (Hernandez et al., 2008, Blake et al., 2008, Lotya et al., 2009, Hernandez et al., 2009, Bourlinos et al., 2009a). Liquid phase exfoliation was developed from the experience of dispersing carbon nanotubes in solvents (Coleman, 2012). In solvent based systems the solvent-graphene interaction is strong enough to overcome the forces between graphene layers in graphite (Lotya et al., 2009, Bourlinos et al., 2009a). Experimental evidence from Coleman's work showed that liquid phase exfoliation resulted in monolayer and multi-layered graphene free from defects and residual oxides (Coleman, 2012).

Liquid phase exfoliation mechanism

Liquid phase exfoliation can be considered to be a quasi-dissolution process (Du et al., 2013). Coleman and co-workers (Hernandez et al., 2008, Coleman, 2012) explained the process using a thermodynamic approach in terms of the enthalpy of mixing and Bourlinos et al. (2009a) explained it in terms of charge transfer between solvent molecules and the graphene layers in graphite. The experimental work of Coleman and co-workers (Hernandez et al., 2008, Coleman, 2012) revealed that solvents with surface tensions of ~40 mJ m^{-2} (which is equivalent to surface energy of graphene (~70 mJ m^{-2})) had the highest propensity to effectively exfoliate graphite. They proposed the following model to account for these results:

$$\frac{\Delta H_{mix}}{V_{mix}} \approx \frac{2}{T_{flake}}\left(\sqrt{E_{S,S}} - \sqrt{E_{S,G}}\right)^2 \phi \qquad \textbf{(2-1)}$$

where ΔH_{mix} is the enthalpy of mixing, V_{mix} is the volume of mixture, T_{flake} is the thickness of a graphene flake, $E_{S,S}$ and $E_{S,G}$ are the surface energies of the solvent and graphene, respectively, and ϕ is the volume fraction of graphene.

From the above expression, the enthalpy of mixing is minimized when the surface tension of the liquid is close to or similar to that of graphene, meaning that the energy cost of exfoliation is minimised. Exfoliation occurs readily in such liquids through mild sonication. Based on this expression numerous organic solvents whose surface tensions match those of graphene have been classified as effective media for graphite exfoliation into graphene, for instance benzyl benzoate, 1-methyl-2-pyrrolidinone (NMP), g-butyrolactone (GBL), N,N-

dimethylacetamide (DMA), N-vinyl- 2-pyrrolidone (NVP), and N,N-dimethylformamide (DMF). Those solvents whose surface tensions are lower than that of graphene such as water, ethanol and acetone are classified as poor exfoliating media. The appropriate solvents for graphene exfoliation stabilize dispersed graphene sheets from re-agglomeration (Coleman, 2012).

Coleman and co-workers (Hernandez et al., 2009, Coleman, 2012) further investigated theoretically and experimentally the role of solubility parameters in the dispersion of graphene. They measured the dispersibility of graphene in 40 solvents and ranked them according to their effectiveness. Their work showed that good solvents for graphene dispersion are characterized by a Hildebrand solubility parameter of $\delta_T \sim 23$ MPa$^{1/2}$ and Hansen solubility parameters of $\delta_D \sim 18$ MPa$^{1/2}$, $\delta_P \sim 9.3$MPa$^{1/2}$, and $\delta_H \sim 7.7$ MPa$^{1/2}$, where the subscripts D, P, and H represent dispersive, polar and hydrogen-bonding interaction components between graphene and the solvent, respectively. Graphene was dispersed less effectively in solvents with Hansen solubility parameters far from these values.

Following the work of Coleman and co-workers, several other solvents have been suggested and evaluated by other groups. For instance, Hamilton et al. (2009) reported on the dispersion of non-oxidized graphene with concentrations of up to 0.03 mg mL^{-1} with no functional groups using sonication and centrifugation in ortho-dichlorobenzene (ODCB) (surface tension 36.6 mJ m^{-2}). The results of Behabtu et al. (2010) showed that graphite spontaneously exfoliates into high yield graphene in chlorosulphonic acid without any sonication, covalent functionalization or surfactant stabilization. Behabtu et al. (2010) suggested that protonation of the graphene resulted in repulsion between the layers thereby inducing spontaneous dispersion of graphene sheets. In an attempt to obtain a solvent which is easily and completely removed from graphene, Choi et al. (2011a) investigated the exfoliation of graphite in 1-propanol. Their results showed that the dispersion concentration of graphene in 1-propanol was higher than that reported for chloroform and isopropanol by Coleman and co-workers (Hernandez et al., 2009). Choi et al. (2011a) highlighted that although the surface tension of 1-propanol (23.4 mJ m^{-2}) is much lower than that suggested by Coleman's group (Hernandez et al., 2009) for good solvents for graphene, its solubility parameters are favourable.

In the charge transfer approach, it was found that some solvents with electron donating or electron withdrawing functional groups could affect exfoliation and stabilize graphene (Bourlinos et al., 2009a). It was postulated that charge transfer between solvent molecules and graphite sheets such as that which occurs during the intercalation of graphite effects exfoliation (Du et al., 2013). Liu et al. (2012) showed that graphene sheets are either negatively or positively charged when dispersed in solvents. They concluded that electrostatic repulsion is responsible for de-agglomeration and stability of graphene sheets. Charged carbon atoms do not participate in π bonding, thus weakening the van der Waals forces (Du et al., 2013).

The use of graphite intercalation compounds as precursors for synthesizing graphene through liquid phase exfoliation has been reported by various workers (Li et al., 2008, Fu et al., 2011, Zhou et al., 2014, Gu et al., 2009). Van der Waals bonding forces in-between carbon layers induce binding energies that scale to $1/r^6$, where r is the interlayer distance. By increasing the interlayer distances the binding energy between graphite layers is reduced thereby facilitating exfoliation (Du et al., 2013). Intercalation of various species within graphite layers can increase this interlayer distance. However, Stankovich et al. (2007) reported that despite several attempts using powerful sonication equipment they were not able to obtain pristine graphene using the graphite intercalation approach. In actual fact, the recent theoretical study of Yoon et al. (2015) suggested that intercalation of electronegative or electropositive intercalants results in an increased exfoliation energy compared to that required for exfoliating pristine graphite because of additional binding forces that emanates from charge transfer between intercalates and graphene layers.

The charge transfer mechanism could explain exfoliation efficiency of ionic liquids due to their strong interactions with the π electrons of graphite (Du et al., 2013). Ionic liquids are salts which remain in the liquid state at less than 100 °C (Ma et al., 2010). They have low vapour pressures, high ionicities, high thermal and chemical stabilities, they are compatible with a wide range of solvents and their surface tensions are close to that of graphite (Ma et al., 2010, Restolho et al., 2009). Several workers investigated and demonstrated the effective use of ionic liquids as exfoliation media for graphite (Liu et al., 2008, Wang et al., 2010b, Nuvoli et al., 2011). In one instance, a very high concentration of graphene was obtained using bath sonication (5.33 mg mL^{-1}) (Nuvoli et al., 2011).

Water is attractive as a medium for liquid phase exfoliation due to its non-toxicity, low boiling point and compatibility. However, graphite and graphene are hydrophobic. It is thus essential to add surfactants to water to enable the dispersion of graphite in water and to reduce the surface tension of water so that it matches that of graphene and exfoliation becomes feasible. The use of surfactants in water also results in the formation of even mixtures of the precursor graphite in water, facilitating sonication. Surfactants also play the key role of preventing re-agglomeration of graphene sheets through electrostatic stabilization or steric hindrance (Du et al., 2013).

Lotya et al. (2009) obtained a low concentration of graphene (<0.01 mg mL^{-1}) when they first reported the liquid phase exfoliation of graphite in aqueous sodium dodecyl benzene sulphonate (SDBS) surfactant solutions. However, they subsequently obtained higher graphene concentrations (0.3 mg mL^{-1}) by using sodium chlorate surfactant (Lotya et al., 2010). Green and Hersam (2009) had previously obtained a lower graphene concentration (0.09 mg mL^{-1}) by using the same sodium chlorate surfactant in water. Bourlinos et al. (2009b) have also shown that aqueous solutions of a polymeric surfactant, polyvinylpyrrolidone were able to effective exfoliate graphite to yield concentrations of up to 1 mg mL^{-1} under sonication.

Smith et al. (2010) investigated the effectiveness of 12 ionic and non-ionic surfactants in dispersing and stabilizing graphene in water. Their results showed that the degree of exfoliation was similar for all the solutions. The dispersed concentration varied for each surfactant/water solution, ranging from 0.011 mg mL^{-1} for sodium dodecyl sulphate (SDS) to 0.026 mg mL^{-1} for sodium chlorate (SC). However, the dispersed graphene concentration increased with square of the zeta potential of the surfactant coated flakes for ionic surfactants. It was inferred that the concentration of the dispersed graphene increased with an increase in the magnitude of the electrostatic potential barrier which is responsible for the stabilization of surfactant coated flakes against aggregation. The dispersed graphene concentration increased linearly with the steric potential barrier stabilizing the graphene flakes. Guardia et al. (2011) also prepared aqueous dispersions of graphene in the presence of several ionic and non-ionic surfactants and evaluated their effectiveness. Their study showed that non-ionic surfactants exfoliated graphite into single and few layer graphene with concentrations of up to 1 mg mL^{-1}.

The yields of graphene dispersions obtained from the liquid phase exfoliation of graphite are usually low. The yields can be improved by methods such as successive filtration and centrifugations or increasing sonication time as described by Khan et al. (2010). Increasing sonication time is however detrimental as it reduces the size of graphene due to sonication-induced scissions (Coleman, 2012).

The lateral dimensions of solvent dispersed graphene is less than a micrometre which makes its use as reinforcement rather unlikely (Coleman, 2012). Flake size can be controlled by centrifugation techniques. Longer sonication times reduce the flake sizes, although the concentration of dispersed graphene increases. Solvents with correct surface energies have high boiling points, they are also toxic, expensive and not biocompatible. Isopropanol and acetone dispersed graphene less than the solvents identified as excellent solvents for graphite exfoliation (Coleman, 2012).

2.5 Graphite nanoplatelets

2.5.1 Synthesis of graphite nanoplatelets

Graphite nanoplatelets can be synthesized through chemical vapour deposition and arc discharge bottom-up approaches (Wang et al., 2004, Subrahmanyam et al., 2009, Kim et al., 2010b). However, these methods suffer from low yields as in the case of graphene synthesis, they are highly complicated processes that require specialised equipment and are energy intensive (Kim et al., 2010b).

Graphite intercalation chemistry and mechanical delamination is a top-down approach to graphite nanoplatelets that has been frequently exploited due the abundance of graphite and ability to produce graphite nanoplatelets on a large scale (Viculis et al., 2005, Li and Zhong, 2011). The precursors to graphite nanoplatelets in this approach are usually acceptor type graphite intercalation compounds prepared with graphite and strong acids in the presence of strong oxidising agents (Chen et al., 2004, Viculis et al., 2005, Yu et al., 2007, Wei et al., 2009b). These graphite compounds are apparently residue graphite intercalation compounds (discussed in section 2.3.1.2) as the as-prepared graphite intercalation compounds used are frequently washed with water and dried. This suggests that these precursor compounds are higher stage compounds. It has been reported that these graphite compounds are not well

staged; the stage of these graphite intercalation compounds could be as high as 25 (Hennig, 1952, Furdin, 1998). These compounds also known as expandable graphite, are subjected to heat treatment which imparts a thermal shock through them, producing a porous, vermicular worm like structure which is frequently called expanded graphite or exfoliated graphite (section 2.3.2). Graphite nanoplatelets can be subsequently obtained by mechanical delamination through ball milling, vibratory milling or ultrasonication in liquid media.

2.5.2 Delamination of exfoliated graphite into graphite nanoplatelets

Delamination of exfoliated graphite into graphite nanoplatelets induced by ultrasonication in liquid media has been previously reported (Chen et al., 2004). Ball milling and vibratory milling have also been reported on (Cho et al., 2005). The work of Cho et al. (2005) showed that ball milling and vibratory milling of expanded graphite resulted in graphite nanoplatelets of smaller sizes.

2.6 Ultrasonication

Sound is a mechanical wave that is propagated through the oscillation of particles of the medium through which it is transmitted. Molecular oscillation in liquids occurs about an equilibrium position in the direction of wave propagation, thus producing longitudinal waves (Lorimer and Mason, 2002). Ultrasound waves are sound waves having frequencies above 20 kHz, the threshold of human hearing. Oscillation of the molecules of a liquid medium as a result of ultrasonication leads to acoustic cavitation, a phenomenon in which micro bubbles are formed, grow and collapse in the liquid (Figure 2-4) (Ashokkumar et al., 2007, Ashokkumar, 2011).

Molecular oscillations in a liquid due to transmission of ultrasound waves through it result in particles being compressed in some regions (compressions) and pulled apart in the other regions (expansions or rarefactions). The compressions and rarefactions are regions of high pressure and low pressure, respectively, which move through the medium periodically. Voids or cavities are formed when the negative pressure of the expansion cycle is more than the intermolecular cohesive forces of the liquid (Thompson and Doraiswamy, 1999, Leonelli and Mason, 2010). The voids are formed through nucleation processes at nucleation sites which contain gaseous impurities or pre-existing micro bubbles from prior cavitation events

(Suslick et al., 1990, Thompson and Doraiswamy, 1999, Santos et al., 2009). The voids or cavities are known as cavitation bubbles (Lorimer and Mason, 2002).

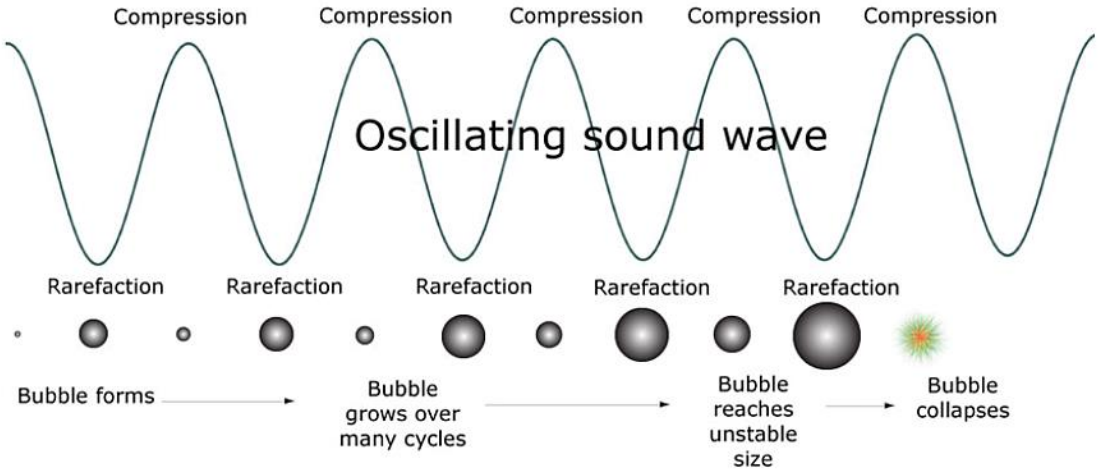

Figure 2-4 Bubble formation, growth and collapse in acoustic cavitation (Leong et al., 2011).

Acoustic cavitation bubbles can grow through rectified diffusion or coalescence mechanisms (Leighton, 1995b, Leong et al., 2011). Bubbles that grow large enough exit the system due to buoyance forces (degassing) (Leong et al., 2011). However, cavitation bubbles in an acoustic field under ultrasonic radiation can undergo inertial cavitation (also referred to as transient cavitation) and non-inertial cavitation. At sufficiently high acoustic pressure amplitudes above a certain threshold, the cavitation threshold, inertial cavitation occurs (Leighton, 1995a, Bader et al., 2012). In this instance, the cavitation bubbles grows rapidly within one or a few compression and expansion cycles, become unstable and collapse violently during compression (Leighton, 1995a). Non-inertial cavitation occurs at low pressure amplitudes. During non-inertial cavitation, the bubbles oscillate about an equilibrium size for numerous cycles (Leighton, 1995a). Figure 2-5 illustrates all phenomena which a bubble can experience in an acoustic field (Leong et al., 2011).

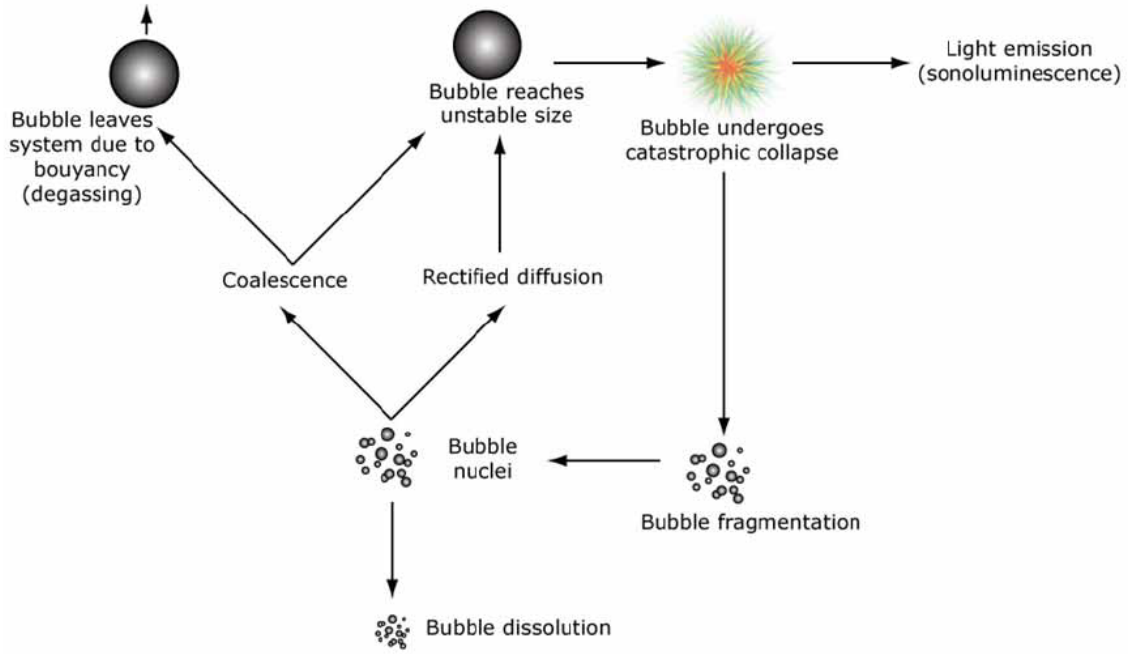

Figure 2-5 Bubble nuclei in an acoustic field (Leong et al., 2011).

Bubble collapse during inertial cavitation concentrates the diffuse energy of sound through compression of gas within the bubbles (Suslick et al., 1999). The collapse is nearly adiabatic, the temperature and pressure within cavitation bubbles rises rapidly to 5000 °C and 1000 atmospheres, respectively. This creates short lived localized hot spots with heating and cooling rates of up to 10^{10} °C s^{-1} (Suslick et al., 1999). The violent collapse of cavitation bubbles that occurs during inertial cavitation generates several physical and chemical effects such as shock waves, micro jets, turbulence and shear forces, emission of light (sonoluminescence) and chemical reactions (sonochemistry) (Suslick, 2003, Ashokkumar, 2011).

Suslick et al. (1999) outlined the manifestations of acoustic cavitation due to ultrasonic irradiation in liquid-solid systems. These include improvement of mass transport from turbulent mixing and acoustic streaming, surface erosion at liquid-solid interfaces by shock waves and micro-jets, high-velocity interparticle collisions in slurries and the fragmentation of friable solids.

2.6.1 Factors that influence acoustic cavitation from ultrasonic radiation

2.6.1.2 Cavitation threshold

The onset of cavitation in an ultrasonically irradiated liquid is governed by a cavitation threshold, which is the minimum applied acoustic pressure amplitude required for cavitation bubbles to be formed (Lorimer and Mason, 2002, Santos et al., 2009). The applied acoustic pressure is proportional to intensity of the ultrasound wave. The intensity of an ultrasound wave is the amount of kinetic energy per second per unit area carried by the wave, with units of W m^{-2}.

Several factors that influence the cavitation threshold and therefore the onset of acoustic cavitation due to ultrasound have been discussed analytically and qualitatively (Lorimer and Mason, 2002, Santos et al., 2009, Thompson and Doraiswamy, 1999). Liquids with high viscosities and surface tensions have stronger cohesive forces and therefore have a higher cavitation threshold. Another liquid property which affects the cavitation threshold is the vapour pressure. Liquids with high vapour pressures have lower cavitation thresholds. The use of high ultrasound frequencies has the effect of limiting the time in which bubbles can be formed during the rarefaction cycles. An increased ultrasound frequency requires higher intensities (pressure amplitudes) for cavitation bubbles to be formed, that is it increases the cavitation threshold. Increasing the liquid temperature decreases the cavitation threshold due to a decrease in the viscosity and surface tension and an increase in the vapour pressure of the liquid. An increased external pressure does increase the cohesive forces and reduces the vapour pressure and hence increases the cavitation threshold. However, bubbling gas into the liquid can promote nucleation of bubbles and enhance their formation.

2.6.1.3 Onset of inertial (transient) cavitation

The Blake threshold is the acoustic pressure amplitude beyond which a bubble above a critical radius will expand rapidly under quasi-static, low frequency (<20 kHz) conditions (Atchley, 1989). However, inertial cavitation will occur above a threshold governed by the initial bubble size, the frequency of the acoustic field and its amplitude (Leighton, 1995a). For inertial cavitation to occur the applied ultrasound must be of sufficient intensity and the bubbles must be above a critical, threshold size (Leighton, 1995a, Harvey et al., 2014). The bubble threshold size necessary for inertial cavitation determines the sufficient ultrasound

intensity (Harvey et al., 2014). This bubble threshold size is a function of the frequency of the applied ultrasound, the hydrostatic pressure, the liquid media properties temperature, viscosity, surface tension and vapour pressure (Harvey et al., 2014).

Although it is more difficult to form cavitation bubbles in liquids with high surface tensions and high viscosities, once they are formed these implode with higher temperatures and pressures (Lorimer and Mason, 2002).

As elucidated earlier on, increasing the liquid temperature reduces the cavitation threshold by reducing the surface tension and viscosity and increasing the vapour pressure. However, the magnitude of the implosions that occur during bubble collapse get less intense at elevated temperatures due to more vapour being contained in the bubbles formed (Thompson and Doraiswamy, 1999, Santos et al., 2009). The vapour reduces the energy produced in the bubble implosion by shielding it and also using part of it as enthalpy for condensation (Thompson and Doraiswamy, 1999). Santos et al. (2009) recommended a compromise temperature which allows bubble formation and yet still result in intense implosions. However, to derive maximum effect from ultrasound, Thompson and Doraiswamy (1999) and Lorimer and Mason (2002) recommended the use of the lowest temperatures possible and solvents with low vapour pressures.

Higher frequencies potentially result in shorter compression times than the time required for bubble implosion, thereby reducing the effect of the ultrasonication (Thompson and Doraiswamy, 1999, Lorimer and Mason, 2002). Decreasing the ambient pressure can result in more intense implosions due to decreased vapour pressure of the liquid. However, each system will have an optimum ambient pressure which does allow the formation of bubbles and their effective implosion (Thompson and Doraiswamy, 1999). Increased ultrasound intensity results in more violent bubble collapse (Lorimer and Mason, 2002). The intensity is directly proportional to the amplitude of the applied ultrasound and a minimum intensity is necessary for cavitation to occur (Santos et al., 2009). Very high amplitudes can lead to the premature damage of the ultrasound transducer. This could then result in liquid agitation instead of cavitation (Santos et al., 2009).

Lorimer and Mason (2002) discussed the four types of ultrasonic equipment available commercially. These are the whistle reactor, ultrasonic bath, probe and cup-horn.

The ultrasonic probe or sonic horn is directly immersed into a vessel and delivers intensities a 100 times higher compared to ultrasonic baths and cup horns (Santos et al., 2009). The ultrasonic intensity decreases rapidly radially and axially from the ultrasonic probe (Santos et al., 2009). The shape of the vessel used should minimize dead cavitation zones for maximum ultrasonication effect (Santos et al., 2009). As a result of temperature increases during use of an ultrasonic probe, ice baths are commonly used to control the temperature of the liquid medium when ultrasonic probes are used (Santos et al., 2009). The other strategies are the use of the pulse mode and specially designed vessels. The reaction diameter must be minimized and the vessel should have a conical shape to reduce dead zones. A low sonication volume allows more collisions between particles.

2.6.2 Ultrasonication of graphite

Ultrasonication assisted liquid phase exfoliation of pristine graphite into graphene has been extensively studied as a possible route to large scale synthesis of graphene. A significant number of studies were focused on the suitability of various solvents as effective graphite exfoliation media for dispersing and stabilizing graphene. It was shown that those solvents with surface tensions close to the surface energy of graphite (40 mJ m^{-1}) and suitable solubility parameters were effective exfoliation media (section 2.4.1.3). It was also shown that some surfactants can stabilize graphene in aqueous solutions. However, the science behind ultrasound in effecting graphite exfoliation is often overlooked (Cravotto and Cintas, 2010).

2.6.2.1 Mechanism of ultrasonic delamination of graphite

Cravotto and Cintas (2010) elucidated the interaction of acoustic waves with solid matter, including graphite. Yi and Shen (2015) gave a plausible explanation on how ultrasound induced cavitation can effect graphite exfoliation into graphene. In their assertion, during ultrasonication of graphite, cavitation bubbles are formed around graphite flakes. Micro-jets and shockwaves that emanate from the transient collapse of the bubbles impact on the graphite surfaces instantly. This induces compressive stress waves which propagate throughout the graphite lattice. The theory of stress waves dictates that when the compressive stress wave reaches a free graphite interface, a tensile stress is reflected back into the graphite lattice. Collapses of numerous bubbles will lead to intensive tensile stresses which effectively

exfoliates graphite. Unbalanced compressive stresses could also exfoliate adjacent layers through a shear processes. The micro-jets exfoliate graphite by splitting the interlayers. Ultrasound effects also break the basal structure of graphite into smaller fragments (Cravotto and Cintas, 2010).

Ultrasonication parameters influencing graphite exfoliation

Ultrasonication parameters in ultrasonication assisted exfoliation of graphite into graphene have been seldom studied, with the exception of the ultrasonication time and power applied. Cheng et al. (2010) studied the effects of ultrasonication parameters and solvent properties on the debundling (exfoliation) and dispersion of graphene analogues single wall carbon nanotubes (SWNTs) in various solvents. Exfoliation and dispersion of the SWNTs as characterized by a dispersion limit and aggregation fraction correlated with solvent properties which influence the sonication process.

The study of Cheng et al. (2010) showed that those solvents with lower vapour pressure exfoliate and disperse SWNTs more effectively than those with a higher vapour pressure. More energy is required to induce cavitation in lower vapour pressure solvents, which in turn release more energy during bubble collapse. Better dispersion was also observed in higher viscosity solvents and those which had high surface tensions. High surface tension solvents and viscous solvents increase the cavitation threshold, but then the resulting cavitation effect is more pronounced.

The study of Cheng et al. (2010) demonstrated that the parameters with an effect on the ultrasonication process influenced the debundling and dispersion of the SWNTs, rather than the solvent solubility parameters as has been widely reported in several works reviewed (Hernandez et al., 2008, Hernandez et al., 2009, Coleman, 2012). Dispersion of the SWNTs was found to be influenced by the ultrasonication solvent parameters, particularly vapour pressure and viscosity. This study also showed that ultrasonication reduces the size of the SWNTs. Optimum sonication conditions are solvent dependent.

Yi et al. (2012) studied experimentally and through simulations the effect of vessel diameter (D) and liquid height (L) on the ultrasonication induced cavitation process and its scalability for few layer graphene production. Their study showed that the vessel diameter and liquid

height both change the cavitation volume and cavitation volume fraction. The cavitation volume fraction (the fraction of the liquid in which cavitation occurs) influenced the few layer graphene concentration and production efficiency. Few layer graphene (FLG) yield and power injected into the samples varied directly with cavitation volume and sample volume. From their study, the vessel diameter and liquid height should be designed to allow high cavitation volume fraction for high production efficiency. Higher yields of the FLG were only possible through high cavitation volumes which were obtained through a large D, L and sample volume. The study showed that enhanced cavitation intensity which entails high pressure amplitude was favourable to a high FLG production.

Yi and Shen (2015) highlighted that ultrasonication time and temperature affect the properties of the solvent medium used for ultrasonication, such as surface tension and viscosity thereby influencing cavitation. They point out that solvents can degrade if ultrasonication time is long or intensive.

Several studies showed that the intensity and distribution of ultrasonication induced cavitation is influenced by vessel dimensions and geometry and is often localized (Kojima et al., 1998, Asakura et al., 2008, Nanzai et al., 2009, Sutkar and Gogate, 2010). Studies on exfoliation of graphite using ultrasound have thus also observed that disperesed graphene concentration depended on vessel geometry and dispersion volume (Khan et al., 2010, Yi et al., 2012).

2.6.3. Graphite nanoplatelets from ultrasonication of exfoliated graphite

The delamination of exfoliated (expanded) graphite into graphite nanoplatelets using ultrasonication involves the application of ultrasound energy to dispersions of expanded graphite to obtain graphite nanosheets (Chen et al., 2004, Yu et al., 2007, Wei et al., 2009a, An et al., 2014, Carotenuto et al., 2012). This is akin to the exfoliation of graphite to graphene in various liquid media which has been widely studied as discussed earlier on (section 2.4.1.3). However, unlike pristine graphite, the interlayer spacing in expanded graphite has been significantly increased; hence the cohesive forces between the layers must be weakened.

Different groups have applied various sonication parameters and used different ultrasonication media to delaminate exfoliated graphite into graphite nanoplatelets. Carotenuto et al. (2012) recommended the use of horn type sonicators due to their ability to impart higher power. Carotenuto et al. (2012) also noted that the ultrasonication parameters time, temperature and power must be optimized in order to attain sufficient exfoliation. A study which investigated the ultrasonication parameters associated with cavitation and their effect on the delamination of expanded graphite into graphite nanoplatelets was yet to be encountered.

Effective liquid media for the exfoliation of expanded graphite into graphite nanoplatelets must wet, delaminate (exfoliate) and stabilize the dispersion (Wei et al., 2009a). Analogous to studies on the exfoliation of graphite into graphene reviewed earlier on, effective delamination media for expanded graphite into graphite nanoplatelets are those solvents with suitable solubility parameters and surface tensions close to that of graphite nanoplatelets; aqueous solutions with some surfactants and also some ionic liquids. Discussions from previous sections have shown that delamination of expanded graphite is effected by cavitation effects, and hence the media properties should enable sufficient acoustic cavitation under ultrasonication.

Various common solvents such as isopropanol, ethanol and acetone have been frequently used as ultrasonication media for the synthesis of GNPs (Fukushima, 2003, Lin and Chung, 2009, Chen et al., 2004, Yu et al., 2007, An et al., 2014). The solubility parameters of these solvents do not closely match those deemed ideal for the exfoliation of graphite (Hernandez et al., 2009). However, the effect of their properties on acoustic cavitation has not been reported.

Fukushima (2003) from Drzal's group utrasonicated expanded graphite in acetone at a frequency of 20 kHz and power of 100 W for 2 hours. The ultrasonication processor was not specified. He obtained graphite nanoplatelets with an average size of 14.5 μm which were further reduced in size by vibratory ball milling. Drzal's group has managed to commercialize this process to produce graphite nanoplatelets known as xGnP™ (Kalaitzidou et al., 2010). Lin and Chung (2009) also dispersed expanded graphite in acetone and utrasonicated it for 24 h at 100 W to obtain GNPs dispersions. Their nanoplatelets had lateral dimensions between 3-8 μm, and thicknesses in the nano-range. Yu, Ramesh & Itkis, 2007

utrasonicated expanded graphite for 24 h at power of 270 W in acetone, after initially dispersing it in the acetone by high speed shear mixing. Their study showed that the final thickness and lateral dimension of the graphite nanoplatelets were influenced by the temperature used to exfoliate the graphite. High exfoliation temperatures (800 °C) of the precursor GICs produced the thinnest graphite nanoplatelets (1.7 nm) with lateral dimensions of 0.35 μm. The thickness of 1.7 nm corresponded to the full exfoliation of a stage 4 graphite intercalation compound.

Chen et al. (2003) and Chen et al. (2004) utrasonicated a dispersion of expanded graphite in an aqueous solution of 65-70 % alcohol at a power of 100 W for various times using an ultrasonic bath. Sonication of expanded graphite for 8 hours resulted in graphite nanoplatelets with thicknesses between 30-80 nm and diameters of between 5-20 μm (Chen et al., 2003). The graphite nanoplatelets had an average diameter of 13 μm when a ultrasonication irradiation of 10 h was used (Chen et al., 2004). The average thickness of these nanoplatelets was estimated at 52 nm. The graphite nanoplatelets size decreased significantly with time when the dispersions where ultrasonicated for more than 10 h.

An et al. (2014) also used an alcohol, isopropyl alcohol, as the ultrasonication medium. They delaminated expanded graphite into graphite nanoplatelets with an ultrasonic wave generator at a frequency of 40 kHz and power of 700 W for 2 hours. The lateral size of their graphite nanoplatelets varied from 3-12 μm.

Some groups have however used special solvents with dispersants and even aqueous solutions with dispersants as ultrasonication media. For instance in the study by Wei et al. (2009a), they used a high molecular weight dispersant (BYK-163) and vinyl chloride-co-vinyl acetate resin to obtain a stable dispersion of graphite nanoplatelets in an organic solvent (ethylene glycol butyl ether acetate) by ultrasonication of expanded graphite in an ultrasonic bath for 12 h. They suggested that the dispersant facilitated the wetting and exfoliation of GNPs, and the resin stabilized the GNPs by stearic hindrance. Carotenuto et al. (2012) utrasonicated expanded graphite into graphite nanosheets in octane using high intensity ultrasound from a sonic horn at 1000 W. Choi et al. (2011b) ultrasonicated thermal plasma expanded graphite into graphite nanoplatelets in an aqueous solution with a dispersant. They used an intensity of 40 % using a sonicator with a 750 W power output and sonicated for 15-60 min. They obtained graphite nanoplatelets with lateral dimensions of up to 30 μm,

although averaging from 5-20 μm. Results from high-resolution scanning transmission electron microscopy and micro-Raman spectroscopy suggested that the nanoplatelets obtained were less than 10 graphene layers.

Chen et al. (2003) asserted that the stage of the precursor GIC used in synthesizing graphite nanoplatelets is a limiting factor which determines the thickness of the graphite nanoplatelets obtained. The thickness of a monolayer of graphite (graphene) is estimated at 0.5 nm (Chen et al., 2003). According to Carotenuto et al. (2012), precursor graphite intercalation compounds intercalated through a mild intercalation process produce graphite nanoplatelets with thicknesses in the range of 80-100 nm, whereas those GICs produced through deep intercalation processes produce platelets with thickness in the range of 10-20 nm.

The thickness of the graphite nanoplatelets produced after ultrasonication determines whether a stable or unstable colloidal suspension is obtained (Carotenuto et al., 2012). Concentrated colloidal suspensions are stable due the random orientation of graphite nanoplatelets, which prevents their sedimentation. Solvent removal from the colloidal suspensions produces a fragile aerogel (Carotenuto et al., 2012).

Chapter 3 Literature: Polymer composites

3.1 Introduction

A polymer composite is defined as a material consisting of at least one polymeric component and one or more components of different phase domains. The polymer forms the continuous phase domain (Work et al., 2004).

Additives used to fabricate polymer composites are categorized into reinforcements, fillers and reinforcing fillers (Xanthos, 2005). Xanthos (2005) reserved the term 'reinforcement' for long, continuous fibres or ribbons. The primary purpose of using reinforcements in polymers is to modify their mechanical properties. Reinforcements are stiffer and stronger than polymers. 'Reinforcing filler' describes discontinuous additives whose primary purpose is also the improvement of mechanical properties (Xanthos, 2005). The stiffness of inorganic reinforcing fillers is relatively high and they are characterized by relatively high aspect ratios. These are the length to diameter ratios for fibres and diameter to thickness ratio for platelets. The aspect ratio determines the surface area available for interaction between a polymer matrix and reinforcing filler (Xanthos, 2005).

Fillers are defined as solid particulate materials with various shapes used in relatively high concentrations in plastics. Fillers have been traditionally used as additives for the reduction of material costs by substituting the more expensive polymer, and also possibly reducing cycle times by increasing the thermal conductivity. However, fillers are multifunctional, although, they can be characterized by one primary function, hence the term functional filler. Xanthos (2005) has tabulated a number of functional fillers and their primary and secondary functions.

3.2 Electrically conductive composites

The absence of charge carriers and their limited mobility in polyolefins such as polyethylene inevitably makes them effective insulators with high volume and surface resistivities (volume resistivity $>10^{15}$ Ω cm) (Sun et al., 1993, Peacock, 2000). The build-up of static electricity on products from such polymers is a potential fire and explosion hazard which can occur through arc discharges (Strüempler and Glatz-Reichenbach, 1999, Wang et al., 2010a).

Electrostatically dissipative polymers continuously disperse electrostatic charges, preventing their build up and harmful discharges.

The International Electrotechnical Commission (IEC) standard IEC 61340-5-1, categorizes materials according to their electrical surface resistivities as being conductive, static dissipative or insulative. This classification is shown in Table 3-1 for packaging materials to be used in ESD applications.

Table 3-1 Classification of ESD materials (IEC 61340-5-1) (IEC: 2007).

Classification	**Required range: Surface resistance (R_s), Ω**
Insulator	$R_s \geq 1 \times 10^{11}$
Static dissipative	$1 \times 10^5 \leq R_s < 1 \times 10^{11}$
Conductive	$1 \times 10^2 \leq R_s < 1 \times 10^5$

Rosner (2001) discussed various methods in which polymers are rendered electrostatic dissipative. Non-particulate conductive additives are not suitable for some polymer forming processes such as rotational moulding due to thermal instability at the high temperatures used (~300 °C) and long cycle times which promote thermo-oxidative degradation (Dahman, 2003, Campbell and Tan, 1995, Ansari and Keivani, 2006). The alternative solution for such processes is electrically conductive polymer composites of polyolefins with conductive particulates for applications which need electrostatic dissipation. Due to its low electrical resistivity (50 μΩ cm) (Sengupta et al., 2011), graphite is one possible conductive filler. Traditional conductive fillers however require higher loadings of at least 15 wt.% to impart conductivity which has a negative impact on mechanical properties (Kim et al., 2010a).

3.2.1 Conduction mechanism and percolation theory

The electrical resistivity of a polymer composite consisting of an insulative polymer matrix filled with conductive particulates varies with the filler content according to a universal trend (Strüempler and Glatz-Reichenbach, 1999, Clingerman et al., 2002, Rosner, 2001). At low filler content, the polymer matrix entirely separates the conductive particles; they do not make contact with each other. The resistivity of the composites hardly decreases with an increase in the loading of conductive particles in this composition range. Beyond a critical

filler loading, the percolation threshold, sufficient conductive filler particles will be available such that a three-dimensional conductive network of touching conducting particles forms. At the percolation threshold the resistivity decreases abruptly by several orders of magnitude. Beyond the percolation threshold the resistivity decrease plateaus and adding more of the conductive filler makes insignificant difference.

The electrical resistivity of composites of insulating matrices containing conductive particulates can be described by numerous geometric, statistical and thermodynamic percolation models (Lux, 1993). However, the classical statistical percolation model originally proposed by Kirkpatrick & Zallen is often used to predict the resistivity of composites consisting of dispersed conductive particulates in insulating matrices (Lux, 1993). In this percolation model, the surface resistivity close to and above the percolation threshold is given as a power law (Sun et al., 1993):

$$\sigma_s = \sigma_f (V - V_c)^{-t} \qquad \textbf{(3-1)}$$

where σ_f is the resistivity of the conductive additive, V is the volume fraction of the conductive additive, t is a critical exponent of a universal character, V_c is the percolation threshold. The classical percolation model does not adequately describe experimentally observed results, although it forms the basis of most of the other models (Clingerman et al., 2002).

The inability of most percolation models to adequately predict the electrical resistivity of composites is due to their exclusion of several factors that affect the conductivity of composites. The electrical resistivity of composites is influenced by filler and matrix properties including the inherent conductivities of the filler and polymer matrix, the filler geometry and size, and also its surface properties (Strüempler and Glatz-Reichenbach, 1999, Clingerman et al., 2002). Low percolation thresholds are easily achieved with high aspect ratio fillers such as fibres or platelets, unlike spherical or irregular low aspect ratio fillers (Wang et al., 2010a, Kalaitzidou et al., 2010). The interfacial contact resistance at the interface of the filler and matrix significantly affects the effective conductivity of the composites, particularly in nanocomposites (Zeng et al., 2010).

3.3 Mechanical properties of composites

Effective reinforcement is the simultaneous enhancement of polymer matrix stiffness (modulus) and strength (Xanthos, 2005). The inclusion of rigid fillers into far less rigid polymer matrices enhances the modulus by virtue of the difference between the stiffness of the two components. Graphite has an in-plane tensile modulus of 1 TPa, whereas linear low density polyethylene has a tensile modulus of only up to few hundreds of MPa (Pierson, 1993). A larger difference in rigidity between the filler and polymer matrix results in more reinforcement with respect to stiffness. Significant reinforcement with respect to stiffness is observed in elastomers (Móczó and Pukánszky, 2008).

The filler size and geometry also have an effect on the composite stiffness. Large filler particles debond from polymer matrices with ease under load, resulting in premature failure of the composite (Móczó and Pukánszky, 2008). It has been shown that below a critical particle size which can only be determined experimentally, the modulus of particulate filled composites increase with a decrease in particle size (Fu et al., 2008). This particle size is apparently in the nanometre range. Smaller particles tend to agglomerate, which can be detrimental to the mechanical properties of composites.

For optimum reinforcement, the ratio of the filler surface area to its volume should be maximized (Xanthos, 2005). The surface available for interaction between the filler and the polymer matrix is determined by this ratio. The filler aspect ratio influences the surface area to volume ratio. Considering a constant volume, the surface area to volume ratio of spherical particles is fixed. However, that for anisotropic fillers such as graphite can be manipulated by varying the aspect ratio. The reinforcing effect of high aspect ratio fillers is therefore relatively superior.

It has been shown that the interfacial interaction at the filler/polymer interface does not have a significant effect on the composite stiffness (Fu et al., 2008). This was explained by considering that the Young's modulus was evaluated at relatively low deformations, which are insufficient to cause interfacial separation. However, the interfacial interaction between the polymer and the filler has an effect on the strength and toughness of the composite. The strength of the polymer composite is influenced by stress transfer between the filler and the matrix (Fu et al., 2008).

Effective stress transfer requires good interfacial adhesion, which in turn leads to high strength. Poor bonding between filler particles and polymer matrix leads to discontinuities in the form of debonding. As a result, the particles do not bear any load; their inclusion in the polymer matrix deteriorates its strength. Well bonded filler particles result in the enhancement of composite strength, particularly for nano particles which have large surface areas for polymer interaction (Fu et al., 2008). High aspect ratio fillers have larger surface areas available for interaction with the polymer, hence they possess a relatively high reinforcing effect with respect to the composite strength (Móczó and Pukánszky, 2008).

The strength of particulate filled composites also generally increases with decreasing filler particle size. Smaller filler particles have larger surface areas which enable more interaction with the polymer matrix and hence efficient stress transfer (Fu et al., 2008). However, filler agglomeration tends to limit the enhancement of strength when sub micrometre filler particles are included in the polymer matrices (Yasmin and Daniel, 2004).

The impact strength of particulate filled polymers is governed by de-wetting and crazing phenomena (Nielsen and Landel, 1994). Filler particles initiate crack formation in the polymer matrices and these are easily propagated in rigid polymers, causing a reduction on impact strength (Nielsen and Landel, 1994). Rigid fillers deteriorate the impact strength of elastomeric polymers (DeArmitt and Hancock, 2003). Rigid fillers can however improve the impact strength of rigid polymers by promoting crazing. The impact strength of rigid polymers can be improved by soft or rubbery fillers (Nielsen and Landel, 1994, DeArmitt and Hancock, 2003).

A prerequisite for the enhancement of impact strength is good interfacial adhesion between the filler and polymer matrix (Nielsen and Landel, 1994). Well-dispersed small filler particles are able to enhance the impact strength of particulate filled composites through a crack-pinning mechanism (DeArmitt and Hancock, 2003). The tendency of small particles to agglomerate will however deteriorate the impact strength at very small particles sizes (Nielsen and Landel, 1994). Filler particle agglomerates and large particles act as flaws (DeArmitt and Hancock, 2003).

The mechanical properties of particulate filled composites are also influenced by the composite structure. The composite structure is in turn influenced by homogeneity, filler attrition, aggregation and orientation of anisotropic fillers (Móczó and Pukánszky, 2008).

Improved mechanical properties are observed in composites with uniformly dispersed fillers. It was noted earlier on that filler agglomeration deteriorates all composite mechanical properties. Filler agglomeration occurs when the cohesive forces between filler particles are greater than the forces attempting to separate them (Móczó and Pukánszky, 2008). Filler agglomeration can be reduced by using shear mixing with a higher shear rate and also increasing the filler particle sizes. It can also be reduced by decreasing the surface tension and reversible work of adhesion of the polymer melts through surface treatments (Móczó and Pukánszky, 2008). Filler attrition changes the filler dimensions and geometry, which can influence the aspect ratio of the filler.

The alignment of anisotropic particles in a polymer composite relative to the direction of the applied load determines the mechanical properties of the composite. The orientation of the filler particles is influenced by flow patterns and shear forces developed during processing. The mechanical properties of a polymer composite can be enhanced by increased filler alignment (Móczó and Pukánszky, 2008).

The presence of voids in a particulate filled composite can deteriorate its mechanical properties (Verbeek and Focke, 2002). Inclusion of fillers in a polymer matrix can also alter its crystallization behaviour, thereby influencing its mechanical properties. The crystalline phase has a higher modulus compared to the amorphous phase. Hence if a change occurs in the degree of crystallinity it will be manifested in the mechanical properties.

3.4 Flame retardancy in polymer composites

The extensive use of polymers has increased the risk of fire hazards in the numerous environments in which they are in use, due to their high flammability. Flame retardant additives are often used in polymers in an attempt to extenuate these fire hazards. In a recent review, Laoutid et al. (2009) discussed the range of flame retardants applicable to polymers, together with their modes of operation.

The polyolefin sub-group of polymers which includes polyethylene presents challenges in applications which require flame retardancy due to their aliphatic nature. Polyolefins are non-charring and have high heats of combustion (Weil and Levchik, 2008). Flame retardants in use for polyolefins work in different ways, and their efficacy is usually polymer specific. Furthermore, they have advantages and disadvantages that warrant their use or non-use (Weil and Levchik, 2008).

Halogen-based flame retardants are still used extensively. However, owing to environmental concerns and the release of highly toxic and smoky effluents during combustion, their acceptability is deteriorating. They act through flame quenching reactions in the vapor phase, in which highly energetic free radicals are replaced by the more stable halogen radicals.

Alternatives to halogen based flame retardants include the metal hydrates, e.g. aluminum trihydrate and magnesium hydroxide. While these do not present any toxicological or environmental concerns, they require high loadings of up to 70 wt.% to be effective (Laoutid et al., 2009, Hull et al., 2011). They impart flame retardancy mainly by endothermic decomposition reactions that also release inert gases that dilute the combustible gas mixture. The high filler loadings required are detrimental to the mechanical properties of the polymer, although they reduce the amount of fuel presented by the polymer.

Several recent studies showed that expandable graphite, intumescent flame retardants and their synergistic combinations were effective in improving the fire behavior of polyethylene (Weil and Levchik, 2008, Qu and Xie, 2003, Xie and Qu, 2001). In section 2.3.2 it was elucidated how the exfoliation phenomenon of expandable graphite is exploited when it is used as a flame retardant. Intumescent additives cause the material to swell when exposed to high heat and form a carbonaceous foam residue that acts both as a heat insulator and a physical barrier to the transport of pyrolysis products (Camino et al., 1989, Wang and Chow, 2005, Lewin, 1999, Dasari et al., 2013)

The potential hazards which emanate from a fire are damage to property and death or injury to people or wildlife. Most deaths in a fire are caused by inhalation of smoke and toxic gases, with the exposure to excess heat also contributing (Irvine et al., 2000). The extent of these hazards can be quantified by the ease of ignition, amount and rate of heat evolved from the fire and smoke and toxic gases evolved.

Fires are dynamic and it is highly impractical to simulate all possible fire scenarios. The criteria used to characterize the flammability of polymers depend on the end use of the polymer product (Laoutid et al., 2009, Hull et al., 2011). None of the fire tests available are able to replicate the whole range of fire types or real fire scenarios because each particular fire is unique. However, the cone calorimeter test is widely used and accepted as a flammability test for polymers as it gives comprehensive parameters in a well-defined setup useful in design and use of polymers (Schartel and Hull, 2007). The cone calorimeter quantifies parameters pertinent to fire hazards. They include the time to ignition, heat release rate and total heat evolved and smoke released.

The fire growth rate (*FIGRA*) and the maximum average rate of heat emission (*MARHE*) are indices that may be used to interpret cone calorimeter data (Schartel and Hull, 2007, Sacristán et al., 2010). The *FIGRA* is an estimator for the fire spread rate and size of the fire whereas the *MARHE* estimates the tendency of a fire to develop (Sacristán et al., 2010). The *FIGRA* is defined as the maximum quotient of $HRR(t)/t$, i.e. the heat release rate up to a time t divided by this time.

3.5 Thermal conductivity of polymer composites

The thermal conductivity of particulate filled polymer composites is influenced by the inherent thermal conductivities of the components of the composite, the composition of the composite, the size, geometry, orientation and distribution of the filler particles, and the nature of the interface between the polymer matrix and the filler particles (Weber et al., 2003, Khodadadi et al., 2013).

Highly conductive fillers enhance the thermal conductivity of polymer composites more significantly compared to less conductive ones. However, (Bigg, 1995) showed that when the ratio of the filler thermal conductivity to matrix conductivity is above 100, the thermal conductivity of the composite essentially maintains a constant value.

High aspect ratio fillers result in polymer composites with enhanced thermal conductivities at lower loadings due to the ease of formation of conductive path ways within the polymer matrices compared to isotropic fillers (Agari et al., 1993). For anisotropic fillers, the thermal

conductivity is a maximum in the direction of filler alignment. For graphite filled composites, the highest conductivity is attained in the composites if the basal plane is aligned parallel to the direction of heat flow (Hill and Supancic, 2002). The study by Agari et al. (1991) showed that the thermal conductivity of particulate filled composites was higher in composites with dispersion states in which they can easily form conductive pathways.

Heat flow in solids is through lattice vibrations (phonons) and electron motion (Shenogin et al., 2004). The interfacial thermal resistance, also known as the Kapitza resistance or thermal boundary resistance is a resistance to heat flow which occurs at the interface of dissimilar materials due to the mismatch in the phonon spectra and poor interfacial adhesion (Shenogin et al., 2004). Poor interfacial interaction between the polymer and filler at the interface causes an increase in interfacial thermal resistance and therefore deterioration in conductivity (Dong et al., 2005). Improved interfacial interaction between the filler and polymer matrix enhances the thermal conductivity. Defects and pores contribute to interfacial thermal resistance though phonon scattering (Dong et al., 2005, Sumirat et al., 2006).

3.6 Nanoscale effect

3.6.1 Mechanical properties

Kalaitzidou et al. (2007) discussed the superiority of nanofillers compared to conventional fillers, with reference to their reinforcing capabilities. In their discussion, if material failure is considered to emanate from defects such as cracks, smaller materials such as nanofillers are stronger than their conventional micrometre sized counterparts. If a nanofiller is smaller than a critical crack length, it can reach its theoretical strength. Nanofillers are thus advantageous compared to conventional reinforcements as substantial matrix property enhancements occur at lower contents of nanofillers (Kalaitzidou et al., 2007). As a result it is possible to fabricate light weight nanocomposites which can be processed easily. The high surface area of nanofillers can enable efficient stress transfer if good adhesion is achieved at the nanofiller-matrix interface. The strength and toughness of composites is also improved as a result of longer crack propagation length due to larger surface areas (Kalaitzidou et al., 2007). However, the effective mechanical properties of nanocomposites are on the whole dependent on the level of nanofiller dispersion and the interfacial adhesion between the polymer matrix and nanofillers (Li and Zhong, 2011).

3.6.2 Electrical conductivity

The percolation threshold and electrical conductivity of polymer nanocomposites are mainly dependent on the method of fabrication which subsequently influences the degree of dispersion of the nanofiller. The nanofiller aspect ratio also significantly influences the nanocomposite electrical conductivity. This is particularly true for one dimensional nano fillers such as carbon nanotubes that easily form conductive pathways. These have reported percolation thresholds of less than 0.1 vol.%. Although the aspect ratio is also significant in the electrical conductivity of nanocomposites fabricated from two dimensional fillers such as graphite nanoplatelets, the number of platelets plays a pivotal role in the conductivity of such nanocomposites (Kalaitzidou et al., 2007).

3.6.3 Thermal conductivity

Simulation studies have shown that interfacial thermal resistance has a significant influence on the thermal conductivity of nanocomposites (Shenogin et al., 2004, Nan et al., 2004, Bui et al., 2011). The interfacial thermal resistance in nanocomposites is exacerbated by the high density of interfaces. The interfacial resistance can be reduced by stronger interfacial adhesion between the nanofiller and matrix. This can be achieved through covalent bonding of the matrix to the nanofiller. However, covalent attachments can reduce the intrinsic thermal conductivity by scattering phonons. The effective thermal conductivity of the nanocomposite can be enhanced by increasing the carbon filler aspect ratio. Phonon scattering by defects in the carbon nanofillers and contact resistance can also reduce the effective thermal conductivity of the nanocomposite (Shenogin et al., 2004, Shi et al., 2013, Yavari et al., 2011, Xiang and Drzal, 2011).

3.6.4 Thermal conductivity modelling

Progelhof et al. (1976) and Bigg (1995) extensively reviewed numerous mathematical models for predicting the thermal conductivity of two-phase composites. Nan et al. (1997) proposed a thermal conductivity model based on the Maxwell-Garnett-type effective medium approach for predicting the thermal conductivity of particulate composites. This model considers the interfacial thermal resistance between the particulates and matrix and also the particle geometry. The model is suitable for nanocomposites due to the significance of the interface densities in nanocomposites.

In the Nan model (Nan et al., 1997), for particulates in the form of oblate ellipsoids (which approximates graphite nanoplatelets) dispersed and oriented isotropically in a matrix with thermal conductivity λ_m, the effective thermal conductivity λ_c for the nanocomposite is given as:

$$\lambda_c = \lambda_m \frac{3+f[2\beta_{11}(1-L_{11})+\beta_{33}(1-L_{33})]}{3-f[2\beta_{11}L_{11}+\beta_{33}L_{33}]} \quad \textbf{(3-2)}$$

with

$$\beta_{11} = \frac{\lambda_{11}^g-\lambda_m}{\lambda_m+L_{11}(\lambda_{11}^g-\lambda_m)}, \qquad \beta_{33} = \frac{\lambda_{33}^g-\lambda_m}{\lambda_m+L_{33}(\lambda_{33}^g-\lambda_m)} \quad \textbf{(3-3)}$$

$$\lambda_{11}^g = \lambda_g/\left(1+\gamma L_{11}\,\lambda_g/\lambda_m\right), \qquad \lambda_{33}^g = \lambda_g/\left(1+\gamma L_{33}\,\lambda_g/\lambda_m\right) \quad \textbf{(3-4)}$$

$$L_{11} = \frac{p^2}{2(p^2-1)} + \frac{p}{2(1-p^2)^{3/2}}\cos^{-1}p\,, \quad L_{33} = 1-2L_{11} \quad \textbf{(3-5)}$$

where f is the volume fraction of graphite nanoplatelets, λ_g is the thermal conductivity of graphite nanoplatelets, λ_{11}^g and λ_{33}^g are the equivalent thermal conductivities along the transverse and longitudinal axes of a nanocomposite unit cell, which is defined as a graphite nanoplatelet coated with thin interfacial thermal barrier layer; $p = a_3/a_1$ is the aspect ratio for graphite nanoplatelets, which is defined as the ratio of the shortest radii to that of the longest radii for oblate ellipsoids which in this case becomes the ratio of the thickness to the diameter of GNPs; $\gamma = (1+2p)\alpha$, where $\alpha = a_k/a_3$ and $a_k = \lambda_m/G_k = R_k\lambda_m$ with a_k being the Kapitza radius, G_k the interfacial thermal conductance and R_k its reciprocal, the interfacial thermal resistance or Kapitza resistance. The model assumes complete coverage of the GNPs by the polymer matrix.

3.7 Polymer/Graphite nanoplatelets nanocomposites

The conventional methods of polymer/graphite nanoplatelet nanocomposites fabrication are direct mixing, solution mixing, in situ polymerization and melt mixing (Kalaitzidou et al.,

2007, Li and Zhong, 2011). Direct mixing is more suitable for low viscosity thermoset polymers. In solution mixing, the polymer is dissolved in a solvent in which the nanographite is disperesed thereafter. When mixing is completed the solvent is then evaporated. In in-situ polymerization a monomer is polymerized in the presence of the graphite nanoplatelets. Melt compounding makes use of twin screw extruders, two-roll mills or other types of mixers. Melt compounding is more suitable for polyolefins (Kalaitzidou et al., 2007).

Solution mixing and in-situ polymerization are able to disperse GNPs uniformly in polymer matrices and enable the fabrication of nanocomposites with low electrical conductivity thresholds and high conductivity after the threshold is reached. They are however undesirable due to the use of hazardous chemicals in polymerization or organic solvents in solution mixing (Chen et al., 2003, Kalaitzidou et al., 2010). Also these fabrication techniques typically produce low yields and are expensive, limiting their use in industry.

Melt mixing is still the fabrication technique of choice due to easy adaptation of pre-existing technology. Several studies have however shown that melt mixing is unable to sufficiently disperse GNPs, leading to high conductivity thresholds and poor mechanical properties (Kalaitzidou et al., 2010, Wang et al., 2010a, Jiang and Drzal, 2010, Jiang and Drzal, 2012). Melt mixing combined with other prior mixing techniques has however shown improved properties.

Prior mixing can be achieved in solution, melt or solid phase. For instance, Kalaitzidou et al. (2010) used a pre-coating method in which polypropylene was first coated with GNPs in isopropanol using ultrasonication, before melt compounding it. The method was more effective in reducing the threshold for conductivity and attaining higher conductivity values compared to solution mixing. The masterbatch technique and solid state shear pulverization are also prior mixing methods which have been combined with melt mixing to effectively disperse GNPs in polymer matrices, achieving conductivity at lower GNPs loading with good mechanical properties (Chen et al., 2007, Li and Chen, 2007, Wakabayashi et al., 2010, Jiang and Drzal, 2012).

Chapter 4 Literature: Rotational moulding

4.1 Process description

In principle, a predetermined amount of plastic powder (micro-pellets and liquids are also rotomoudable) is charged into one half of a metal mould and the mould is closed tight. The mould is rotated slowly biaxially and simultaneously heated. The plastic powder tumbles in the mould, forming a powder pool at the bottom of the mould as it heats up. Once the plastic powder begins to melt, it adheres to the mould surface. Successive layers of powder particles stick to each other where they touch through a sintering process, forming a three dimensional structure with voids which coat the mould surface. As heating continues the plastic densifies into a coherent melt forming a hollow part. However, the voids initially formed at the beginning of sintering process trap air and become air bubbles in the moulded part. Once the densification is finished, the moulding is subjected to a cooling processing, which is normally forced air cooling, water mist or water jet with the biaxial rotation still occurring. When the part has solidified and cooled to a safe enough temperature to be handled, the hollow part is de-moulded and downstream processes can take place (Crawford et al., 1996, Bellehumeur, 2005, Pick and Harkin-Jones, 2006). An illustration of the rotational moulding process is shown in Figure 4-1.

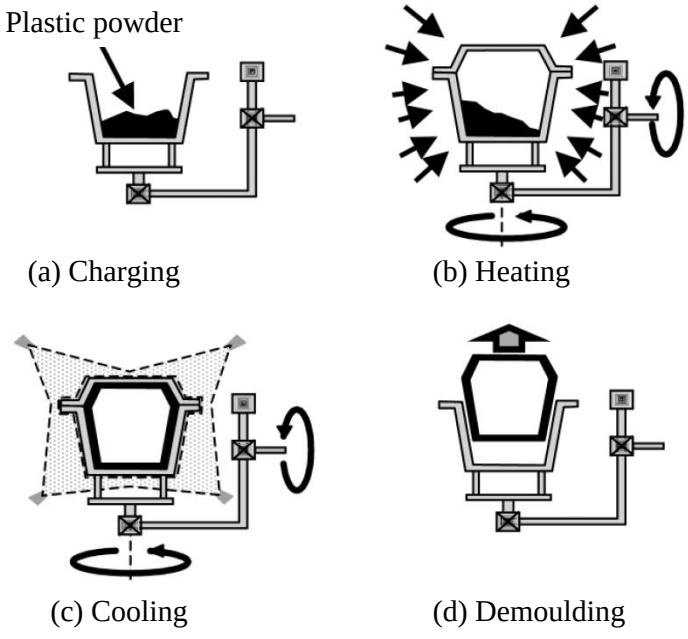

Figure 4-1 The rotational moulding process (Crawford and Throne, 2002).

4.2 Process characteristics

Compared to other polymer forming processes, rotomoulding is unique in several ways (Crawford et al., 1996, Siddhamalli and Lee, 1998, Bellehumeur, 2005, Yan et al., 2006). The temperature of the mould and plastic powder has to be raised from room temperature to the melting temperature of the powder and back to room temperature once the part is formed. The melting, shaping and cooling of the plastic occurs in the mould. As a result, cycle times are essentially higher compared to other forming processes. The plastic is subjected to long periods in which it is exposed to high temperatures and oxygen; oven temperatures are normally set around 300 °C. This makes the plastic susceptible to thermo-oxidative degradation more than in any other forming process. Thermal stabilization packages are a necessity, adding on to the cost of the process. The cost of resins is also relatively higher due to grinding costs. There is a limited range of material which can withstand long cycle times at high temperatures; hence polyethylene is the major rotomoulding material. Rotational moulding is also generally a labour intensive process although some automation had been developed.

Rotation speeds which are used in rotomoulding are very low, typically less than 20 rpm. As a result the process is essentially a pressure and shear stress free process, with no centrifugal forces involved as in casting. A benefit arising from this fact is that rotomoulded parts are essentially free of residual stresses. The moulds can also have thinner walls, are relatively inexpensive and have shorter lead times. Rotomoulded parts also have no weld lines or ejector pin marks, and essentially there is no material waste as all material is formed into a product. Short production runs of huge parts are possible, and the process offers greater flexibility and minimum design constrains. The wall thickness can be easily controlled by varying the relative rotation speeds. Rotomoulding also has relatively low cost tooling and capital costs compared to other processes (Crawford et al., 1996, Siddhamalli and Lee, 1998, Yan et al., 2006, Sharifi et al., 2012).

4.3 Relationship between processing conditions and part quality

Basically there are three process variables in the rotomoulding process, namely the oven time, oven temperature, and cooling rate (Crawford and Throne, 2002). Insufficient oven time or temperature results in incomplete melting and densification of the plastic powder. Hence

an undercured or undercooked part is formed which will exhibit poor mechanical properties particularly the impact strength and stiffness. If the plastic powder is subjected to very long oven times or very high oven temperatures, the polymer will undergo thermo-oxidative degradation. Thermo-oxidative degradation will also deteriorate the mechanical properties of the part. The cooling rate used has influence on the final structure of plastic part and its dimensional stability. Rotational moulding is unique because cooling occurs from outside of the mould only. Thus there is a temperature gradient across the part walls. Different cooling rates have the potential to introduce warpage in parts. The microstructure that the part assumes will differ depending on whether a faster or slow rate was used. Faster cooling rates result in parts with higher impact strength or toughness. This is vice versa for slow cooled parts.

4.4 Rotomoulded part quality

4.4.1 Traditional quality indicators

Due to the susceptibility to impact loading for most rotomoulded products, impact testing is the main quality control test method (Pick and Harkin-Jones, 2005). Mechanical properties of rotomoulded parts are commonly evaluated through falling weight impact tests because these tests are inexpensive to conduct and also due to the sensitivity of the impact resistance of rotomoulded parts to various aspects of the process (Kissick et al., 2011, Spence and Scott, 2003).

The Association of Rotational Moulders (ARM) International developed a standard for impact testing ‘Low Temperature Impact Test’. This test is similar to the ASTM standard test D 5628 ‘Standard Test Method for Impact Resistance of Flat, Rigid Plastic Specimens by Means of a Falling Dart (Tup or Falling Mass)’. The test is normally done at 20 °C or -40 °C. The test determines the mean failure energy of at least 10 samples subjected to a falling dart or tup with either different weights from the same height or with the same weight from different heights. The mode of failure viz. ductile or brittle failure is important in assessing the part quality with reference to processing conditions (Henwood et al., 2005, Spence and Scott, 2003). A part subjected to optimum moulding conditions i.e. optimum oven time and temperature exhibits acceptable impact strength and usually shows ductile impact behaviour.

The instrumented falling weight test is more advanced as data such force and duration of impact can be obtained (Kissick et al., 2011).

Liu et al. (2000) used the L'16 experimental matrix based on the Taguchi method to optimize impact strength of rotomoulded linear low density polyethylene. They found that oven time and temperature were the most significant factors affecting the impact strength, amongst the factors they considered.

Air bubbles and pinholes are a characteristic of rotomoulded parts in the cross-sections of part walls and on the outer surfaces, respectively (Crawford et al., 1996). The bubble density in the cross section of a part has also been traditionally used as an indicator to show whether the plastic densified to sufficient levels (Spence and Scott, 2003, Crawford and Throne, 2002). Undercured parts will have high bubble densities in their cross sections and they will exhibit poor impact properties (Liu et al., 2000, Spence and Scott, 2003). The absence of bubbles or presence of only a few shows that densification was complete. However, this could also mean that the polymer has degraded. Optimum impact properties are obtained with a few small diameter bubbles close to the inner surface. A total absence of bubbles might mean that degradation has occurred and actually reduce the impact properties (Liu et al., 2000, Spence and Scott, 2003).

The degree of densification attained by the polymer during rotomoulding is evaluated more quantitatively through density measurements. The final part density has significant influence on the mechanical properties of the rotomoulded part (Liu et al., 2000, Dodge and Perry, 2001, Crawford and Throne, 2002). The density of a rotomoulded part increases linearly with time as heating progresses. However, the final density of the part is governed by the number and size of air bubbles in the part (Liu, Lai & Tin, 2000). Density of the moulded parts can be evaluated through the use of density gradient columns (ISO 1183 or ASTM D-1505) (Dodge and Perry, 2001, Crawford and Throne, 2002). Gas pycnometry is now a common method to evaluate density of rotomoulded parts (López-Bañuelos et al., 2012). Low density values indicate that the part was undercured; the part will have too many bubbles and poor mechanical properties.

The quality of rotomoulded parts has also been widely evaluated by observing the appearance of their exterior and interior surfaces and also the smell of the interior surfaces (Spence and

Scott, 2003, Crawford and Throne, 2002). A rough or powdery interior surface is an indicator of incomplete melting and densification. A smooth surface would however show that the polymer densified completely. A high gloss, discolouration and acrid smell are signs that the polymer has been degraded as degradation starts form the inner surface due to the presence of oxygen and the high temperatures. The exterior surface may have a high density of pin holes or show incomplete filling especially on corners. This could be as a result of incomplete cure, poor resin choice or high moisture content (Spence and Scott, 2003, Crawford and Throne, 2002).

4.4.2 Analytical techniques

The influence of processing conditions used in the rotational moulding process on the microstructure, morphology and rheology of moulding materials and its subsequent effect on the part quality has been extensively studied by Crawford and his co-workers (Oliveira et al., 1996, Cramez et al., 1998b, Cramez et al., 2001, Oliveira and Cramez, 2001, Pick and Harkin-Jones, 2006). Several analytical techniques have been utilized to characterize the microstructure, morphology and rheology and correlate these to the apparent properties observed in the rotomoulded parts.

Observations of fractured cross sections of the moulded parts under a scanning electron microscope can show the occurrence of bubbles or voids in the cross sections (Cramez et al., 2001). The observation of thin sections of part walls under polarised light not only yields information on the bubble density and hence degree of cure, but also the morphology and microstructure developed as a result of the moulding and cooling conditions utilized (Oliveira et al., 1996, Oliveira and Cramez, 2001).

Rotomoulded polyethylene parts exhibit classical spherulitic structures in their crystal morphology. This is due to the absence of shear or pressure in the process, hence the absence of conditions to impart molecular orientation (Cramez et al., 2001). Polyethylene spherulites exhibit well-defined, characteristic Maltese crosses and regularly spaced bands (Oliveira and Cramez, 2001). The specific morphology which rotomoulded parts develop is directly related to the processing conditions used. For under cured polyethylene, a part will exhibit regular spherulitic morphology throughout the part cross section (Oliveira and Cramez, 2001). However, if degradation occurs, the morphology of the inner surface layer undergoes a

change that corresponds with the degree of degradation. This is because thermo-oxidative degradation of the plastic starts on the interior free surface which is exposed to a high temperature environment in the presence of oxygen (Oliveira and Cramez, 2001). The size and regularity of the spherulites deteriorates with polymer degradation, up to a point where the spherulites disappear from the inner surface, and a new layer of non birefringent material appears. A columnar or fibrous layer is sandwiched between this layer and spherulites in the bulk wall (Oliveira and Cramez, 2001, Cramez et al., 2001). As a result of the restriction with the wall, the spherulites on the surface in contact with the mould form transcrystalline structures (Oliveira et al., 1996, Pick and Harkin-Jones, 2006, Cramez et al., 2003).

The thermo-oxidative degradation of polyolefins such as polyethylene is an autocatalytic reaction which follows a free radical mechanism (Cramez et al., 2001, Tcharkhtchi and Verdu, 2004). The intermediate products are hydroperoxides that decompose into free radicals that initiate and sustain the chain reaction (Cramez et al., 2001, Tcharkhtchi and Verdu, 2004). Although chain scission reactions are also present in the termination reactions of the oxidative degradation of polyethylene, it is the cross-linking reactions which are dominant (Oliveira et al., 1996, Tcharkhtchi and Verdu, 2004). The non-volatile products of the oxidation of polyethylene are carbonyl, vinyl and hyroperoxide groups (Iring and Tüdő, 1990, Oliveira et al., 1996).

Fourier transform infrared spectroscopy (FTIR) can be used to determine if rotomoulded parts have undergone degradation and to what extent. Carbonyl species have infrared absorption between 1700-1750 cm^{-1} (Oliveira et al., 1996, Henwood et al., 2005). The carbonyl index is a measure of the extent of degradation by evaluating the concentration of carbonyl species formed (Hoàng et al., 2006). The double bonds of carbonyl and vinyl groups can also be detected when the rotomoulded part is viewed under a fluorescence microscope, providing a further analytical tool for analysing the degradation of rotomoulded polyethylene (Oliveira et al., 1996). The groups fluoresce under ultraviolet radiation when viewed under the fluorescence microscope (Oliveira et al., 1996). FTIR and fluorescence microscopy show that the degradation is limited to 30 µ thickness from the inner wall of rotomoulded parts (Oliveira and Cramez, 2001).

Evaluation of the rheology of material from the inner layer of rotomoulded parts is a further complementary technique which confirms if degradation had occurred. The rheology can be

used to identify the dominating degradation reactions (Oliveira and Cramez, 2001, Cramez et al., 2003, Henwood et al., 2005).

The cooling rate used has a substantial influence on the morphology of rotomoulded parts (Cramez et al., 2001, Pick and Harkin-Jones, 2006). Slow cooling rates result in coarse or large spherulites and high crystallinity (Pick and Harkin-Jones, 2006). Large spherulites evolve because of a lower nucleation density at higher temperatures. The inner surface will result in larger spherulites and higher crystallinity because this surface cools more slowly than outer surface in contact with the mould. Spherulites at the inner surface grow freely as they are not in contact with a mould wall. Fast cooling results in a variation in the sizes of the spherulites across the cross-section of a part due to uneven cooling across the part wall (Cramez et al., 2001). The plastic close to the mould wall will cool and solidify faster as cooling is done through the mould wall. It will result in spherulites with a fine texture. The cooling rate decreases towards the inner free surface, as a result of the plastic that cooled earlier acting as an insulator. Thus the spherulite size will also increase towards inner free surface. Uneven crystallinity occurs as a result, causing shrinkage which manifests itself through warping of the parts (Cramez et al., 2001).

The microstructure and morphology manifests itself in the apparent mechanical properties of rotomoulded parts. Low impact strength in rotomoulded polyethylene comes about as a result of either the presence of voids in the part wall thickness, poor cohesion of polymer particles or the presence of non-spherulitic textures due to degradation at the inner surface (Oliveira and Cramez, 2001, Tan et al., 2011). Undercured parts suffer brittle failure because of the presence of bubbles and the occurrence of insufficient sintering to have developed any impact strength (Henwood et al., 2005, Tan et al., 2011). The presence of bubbles also reduces the elongation to fracture (Pick and Harkin-Jones, 2006). Bubbles also prevent stresses applied on a part from being evenly distributed, resulting in the reduction of crack initiation energy and propagation. Bubbles can also act as stress concentrators. Crack initiation is encouraged by voids, inclusions, bubbles and imperfections (Pick and Harkin-Jones, 2006). Cross-linking due to degradation at the inner layer causes embrittlement of rotomoulded parts and the subsequent drastic loss of impact strength for over cured parts (Oliveira et al., 1996). At the commencement of crosslinking, the impact strength initially rises, before coming to a catastrophic drop (Henwood et al., 2005).

The morphology which results from the cooling rate used also has an influence on the mechanical properties. Pick and Harkin-Jones (2006) showed that the large spherulites and high crystallinity which emerge from slow cooling of rotomoulded parts deteriorate their strength. High crystallinity was shown to be synonymous with a shift in the β transition of the material to a higher temperature by using dynamic mechanical analysis, resulting in a higher brittle-ductile transition. Cramez et al. (2001) elucidated that inter-spherulitic boundary links transmit energy through the polymer, thereby imparting ductility to it. Large spherulites result in reduced inter-spherulitic boundary links and subsequently reduce its ductility. Crystallites also apparently act as stress concentrators and deteriorate the impact strength; hence high crystallinity causes a reduction in impact strength (Liu et al., 2000). Godinho et al. (1997) showed that the tensile and flexural properties of rotomoulded polyethylene increase linearly with crystallinity and spherulite size, whereas the impact strength deteriorates with an increase in crystallinity and spherulite size. In a study on four different rotomoulded polyethylenes by Harkin-Jones and Ryan (1996), the effect of crystallinity and spherulite size was not pronounced as was expected.

Fast cooling rates have been shown result in improved impact resistance of rotomoulded parts (Liu et al., 2000, Pick and Harkin-Jones, 2006). Fast cooling rates apparently yielded smaller spherulite sizes and reduced crystallinity. Fast cooling rates reduce crystallinity due to the occurrence of crystallization at lower temperatures and its obstruction, culminating reduced crystalline phases (Cramez et al., 2001). Ductility is enhanced by the increased flexible amorphous phase which contains a high amount of inter-lamellar and inter spherulitic tie-molecules that act as stress transducers (Cramez et al., 2001).

However, Cramez et al. (2001), observed that improved ductility in fast cooled rotomoulded polypropylene was limited to the layer close to the mould wall. This layer had the smallest spherulites and lowest crystallinity. The crystallinity was high in the bulk and close to the inner surface. The spherulite sizes increased away from the mould wall. This was due to the uneven cooling rates across the part wall which were introduced as the mould was cooled from outside only. They concluded that improved ductility of rotomoulded polypropylene can be obtained through fast cooling both sides of the parts. If fast cooling is applied to the mould wall only, it causes severe warpage as was explained in the earlier sections.

Discolouration is frequently used as an indicator for over cure and hence as a check for the occurrence for degradation of rotomoulded parts. For polymers with natural colours discolouration is observed as yellowing (Spence and Scott, 2003, Henwood et al., 2005). The yellowing effect is due to the sacrificial oxidation of phenolic antioxidants to chromophoric quinones as they protect the polymer (Sharifi et al., 2012). The yellowness is evaluated as a yellowness index (YIE) using a spectrophotometer (Henwood et al., 2005, Sharifi et al., 2012). A comparison of the yellowness index and carbonyl index with increase in oven time by Sharifi et al. (2012) showed that yellowing occurs before the onset degradation as detected by the formation of carbonyl compounds. They concluded that the discolouration was not a reliable indicator for thermo-oxidative degradation.

4.5 Process control and optimization

Process control of the rotomoulding process is made complex by the biaxially rotation of the mould and high temperatures used in the process (Crawford, 1996, Nugent et al., 1997). Until recently, process control and optimization was traditionally achieved by iterative trial and error methods and relied on the experience of the machine operators (Crawford, 1996, Liu et al., 2000, Cramez et al., 2002, Cramez et al., 2003). Work by Crawford's group established that the temperature of the air inside the mould was a key parameter which could be used for rotational moulding process control (Crawford and Nugent, 1992). Measurement of this temperature has become a standard procedure in determining the heating time that does not result in degradation of the plastic (Bellehumeur, 2005).

The temperature of the air inside the mould is close to that of the inner surface of the plastic during rotomoulding (Oliveira and Cramez, 2001, Crawford and Throne, 2002). Crawford and co-workers developed a device (Rotolog™) which is able to measure the temperature of the air inside the mould and transmit it to a control system in real time (Crawford and Nugent, 1992, Nugent et al., 1997). They showed that the temperature profile of the air inside the mould depicted all the stages of the rotomoulding process (Figure 4-2). This temperature profile is characteristic to the rotational moulding process (Bellehumeur, 2005).

Figure 4-2 shows an induction period from ambient temperature up to point A in which the temperature of the plastic powder rises as it tumbles in the mould. Between point A and B,

the powder undergoes a melting transition for semi-crystalline polymers and adheres to the mould. The voids which eventually become bubbles are trapped at this stage. During this period the mould air temperature does not rise fast as much of the heat is absorbed in the melting transition. The plastic layer coating the mould also forms an insulation barrier, contributing to the reduction in heat transfer to the inside air (Bellehumeur, 2005). Melting is complete at point B. From point B to C, sintering and densification occur. During this stage, the plastic layer thickness decreases as air is expelled from it. The resistance to heat transfer from the outside mould surface to the inside air is reduced (Crawford and Throne, 2002). Hence the temperature of the air inside the mould rises at a faster rate up to point C. Point C is commonly referred to as the peak internal air temperature (PIAT) (Bellehumeur, 2005). Crawford and Nugent (1992) pointed out that since degradation for the polymer emanates from the inner surface of the moulding, it is the temperature at point C, the PIAT, which governs product quality.

When the mould is removed from the oven, the temperature of the air inside the mould continues to rise momentarily (Crawford and Nugent, 1992, Oliveira et al., 1996). The overshoot in temperature depends on the thickness of the part wall. From point C to D, the plastic melt undergoes cooling, the temperature of the air inside the mould decreases at a rate dependant on the cooling method used. The plastic begins to solidify at point D. Semi-crystalline polymers such as polyethylene will solidify through an exothermic crystallization transition; hence the temperature of the air inside the mould will decrease at a reduced rate between point D and E. At point E, solidification is complete, the temperature of the air inside the mould drops at a faster rate up to the ambient temperature at which the product can be demoulded. It is feasible to use faster cooling rates for instance water spray once the plastic has solidified.

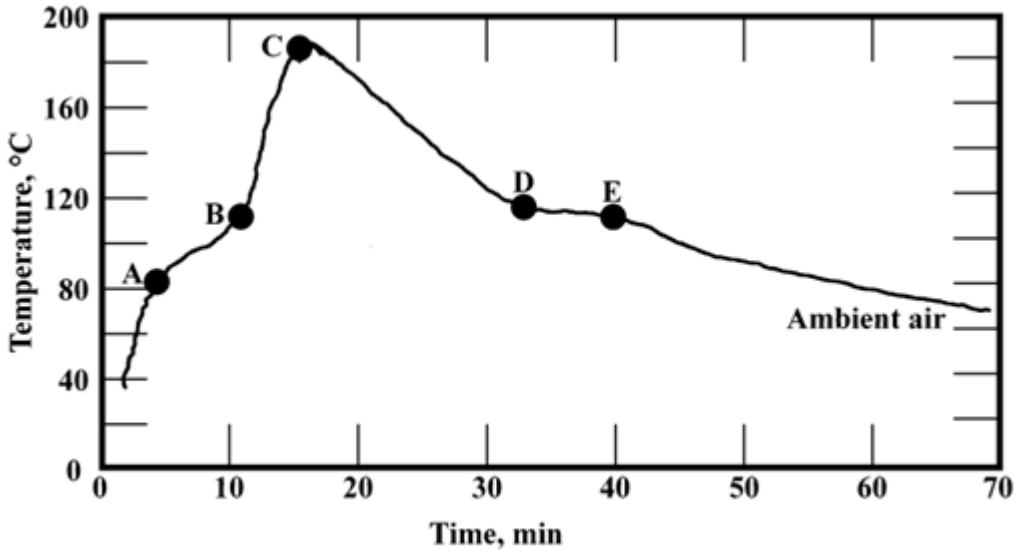

Figure 4-2 The anatomy of the rotomoulding cycle: Temperature trace of the mould air temperature (modified from Crawford and Throne (2002)).

The PIAT has been correlated with rotomoulded part properties and found to be a reliable control parameter for optimum part morphology and mechanical properties (Cramez et al., 1998b, Cramez et al., 2002, Oliveira and Cramez, 2001, Henwood et al., 2005). According to Crawford (1996), if a particular PIAT value specific to each polymer is attained, optimum mechanical properties will be attained. Crawford and Nugent (1992) reported that for polyethylenes, if a PIAT of 195±5 °C was maintained, a rotomoulded part with optimum and consistent mechanical properties would be obtained, independent of any other process variable. Low PIAT values result in under cured parts with high bubble densities and low part densities. The bubbles are trapped in the melt and are not able to escape before the polymer solidifies. Increasing the PIAT reduces the viscosity of the melt and allows them to escape (Oliveira and Cramez, 2001).

The mouldings that assume the morphology of under cured parts as described earlier on, have poor impact properties and fail in a brittle mode. Parts moulded at an optimum PIATs have satisfactory impact properties and fail in ductile mode. Work by Oliveira et al. (1996) and Cramez et al. (2001) showed that the optimum PIAT occurs just before the inception of degradation at the inner surface of the rotomoulded part. Above a critical PIAT, the plastic is overcured and degradation occurs. The mouldings will assume the morphology of overcured

plastic and have poor mechanical properties (Oliveira et al., 1996, Cramez et al., 2001, Oliveira and Cramez, 2001, Cramez et al., 2002, Henwood et al., 2005).

Recently, several workers highlighted the inadequacy of relying on the PIAT only as the control parameter in rotomoulding and proposed new methodologies (Spence and Scott, 2003, Cramez et al., 2002, Cramez et al., 2003). Cramez et al. (2002) pointed out that it is too simplistic to link the optimum cure of a plastic to one variable, the PIAT, because the melting and densification of the plastic depends on many factors such as the heating rate and time. The optimum PIAT is actually influenced by the heating rate and time (dependant on oven time and temperature and mould type), the atmosphere in the mould, antioxidant package, different wall thicknesses and different grades of same material (Cramez et al., 1998b, Cramez et al., 2002).

4.6 Melting and densification during rotational moulding

Melting and densification of the polymer powder into a homogeneous melt expends a significant part of the heating cycle in rotomoulding and has a major role in the properties of the rotomoulded part (Kontopoulou and Vlachopoulos, 2001, Chaudhary et al., 2001a). According to Bellehumeur (2005), melting and densification of the polymer powder particles into a homogenous melt in rotational moulding is governed by two bulk movements. These bulk movements are elucidated as the adhesion of polymer particles to the mould and between adjacent polymer particles; and melt densification which occurs by melting and collapse of the particulate structure. Melt densification is a two stage processes which involves polymer sintering and bubble dissolution (Kontopoulou and Vlachopoulos, 2001, Bellehumeur, 2005).

Polymer sintering is considered to be the fundamental and controlling mechanism in rotational moulding (Kontopoulou and Vlachopoulos, 2001). It is defined as the coalescence of polymer powder particles in contact with each other at an elevated temperature. A thermodynamic driving force exists between polymer particles in contact with each other at elevated temperatures to minimize their surface energy by reducing their total surface area (Chaudhary et al., 2001a, Kontopoulou and Vlachopoulos, 2001). The driving force for

coalescence is surface tension. Coalescence encounters resistance from viscosity (Chaudhary et al., 2001a, Kontopoulou and Vlachopoulos, 2001, Bellehumeur, 2005).

Several studies have been carried out on the sintering and densification behaviour of polymers and their role in rotational moulding (Bellehumeur et al., 1996, Bellehumeur et al., 1998, Kontopoulou and Vlachopoulos, 2001). Bellehumeur et al. (1996) studied the influence of various factors on sintering rates of polyethylene. They found that sintering rates increased as viscosity (zero shear viscosity) decreased. They also found that particle size was not a significant factor in the sintering rates except at the beginning of sintering. Particle geometry also did not have any significant effect on sintering rates. Bellehumeur et al. (1996) used mathematical models on coalescence that occurs by viscous flow and compared their experimental results with the predicted sintering times. The models of Frankel and that of Frankel corrected by Eshelby over predicted the coalescence times. However, the model by Hopper agreed well with experimental results.

Kontopoulou and Vlachopoulos (2001) studied the melt densification of thermoplastics. Their results showed that melt densification is a two stage process. The first stage is particle coalescence. Particle coalescence was governed by viscosity, surface tension and powder properties. The second stage involved the shrinkage and disappearance of bubbles which is was governed by diffusion. Models based on viscosity and surface tension adequately describe the densification process up to the point where bubbles formed. A model to describe bubble dissolution in the later stages was proposed.

The assessment of Bellehumeur (2005) was that on the basis of theoretical and experimental results, the material characteristics that are of importance in the coalescence of polymer particles in rotational were melt elasticity, melt viscosity and surface tension. The melt flow index is not particularly relevant to rotomoulding as it is a pressure and shear free process. The zero shear viscosity is a better alternative in assessing the coalescence characteristics of polymers (Bellehumeur, 2005).

Polymers with lower zero shear viscosities coalesce faster leading to shorter heating cycles during moulding (Bellehumeur et al., 1996). Low values of zero shear viscosity at lower temperatures are desirable as polymers coalesce at temperatures close to their melting points (Bellehumeur, 2005). Polymers with higher melt elasticities will coalesce at lower rates

(Bellehumeur et al., 1996, Bellehumeur et al., 1998). The molecular structure of a polymer will also influence its sintering rate (Bellehumeur, 2005). High molecular weight polymers have high viscosities therefore lower coalescence rates. Polymers with narrow molecular weight distribution have lower viscosities and melt elasticities, hence high coalescence rates. The melt surface energy is difficult to measure (Bellehumeur, 2005).

Chaudhary et al. (2001a) studied the use of low molecular weight additives mineral oil, glycerol monostearate and pentaerythntol monooleate as sintering enhancers for polyethylene. Their results show that the low molecular weight additives blended at 3 wt.% reduce the melt viscosity and/or elasticity of polyethylene at low shear rates. The reduction in the melt viscosity and elasticity of polyethylene blended with mineral oil was substantial. The low molecular weight additives resulted in faster coalescence in sintering studies of polyethylene. Melt densification and bubble removal occurred faster when mineral oil was used in rotational moulding. Reduced cycle times were obtained when polyethylene blended with mineral oil was rotomoulded. The impact strength of polyethylene blended with mineral oil was maintained at the same levels as that of neat polyethylene, showing that the addition of low molecular additives did not influence the mechanical properties.

Chaudhary et al. (2002) also investigated the effect of blending 10 wt.% of ethylene styrene interpolymer and ethylene vinyl acetate (EVA) as sintering and impact modifiers for rotomoulding polyethylene. They observed a marked improvement in the sintering rates with the use of the co-polymers in polyethylene. However, in this instance, the improvement in sintering rates was attributed to lower melting points of the co-polymers, rather than the melt viscosity or melt elasticity. The faster sintering rates resulted in faster bubble removal from the blends and subsequently reduced cycle times. The use of the co-polymers enhanced the impact strength. Kontopoulou and Vlachopoulos (2001) previously elucidated on the effect of melting points on sintering behaviour of polymers.

The size of air cavities which subsequently become air bubbles in the melt is influenced by the initial polymer powder particle size, the powder packing arrangement and the degree of coalescence achieved (Bellehumeur, 2005). Due to the relatively small bubble diameters and high polymer melt viscosities, bubbles remain stationary in the melt when they are formed (Kontopoulou and Vlachopoulos, 1999, Gogos, 2004, Bellehumeur, 2005). The shrinkage and

disappearance of bubbles is controlled by diffusion of air from the bubbles into the melt (Kontopoulou and Vlachopoulos, 2001, Gogos, 2004, Bellehumeur, 2005).

Spence and Crawford (1996) investigated the effect of a wide range of processing variables on the formation and removal of bubbles in the rotational moulding of polyethylene. Their study showed that the rate of bubble shrinkage was faster in low viscosity materials. They also showed that the polymer powder particle characteristics (shape, size and particle size distribution) had an effect on the size and density of bubbles. A higher amount of finer powder particles was observed to result in a high density of smaller bubbles. Overheating of the polymer was shown to be an efficient way of removing the bubbles, to the detriment of mechanical properties.

Kontopoulou and Vlachopoulos (1999) derived a bubble dissolution model on the basis of mass and momentum conservation equations. Their model took into account diffusion, viscosity and surface tension effects. In this model, bubble dissolution is diffusion controlled by the air concentration gradient between the bubble walls and the bulk polymer melt. The model predicts that bubble dissolution is dependent on the initial bubble size, surface tension and concentration of air in the melt, but not on the melt viscosity, particularly at the ranges of melt viscosities found in rotomoulding polymer grades. Their modelling and experimental results apparently contradict the observations of Spence and Crawford (1996), regarding the influence of viscosity on the dissolution of bubbles. However, the model predictions agreed well with experimental data for the diffusion of air in a medium density polyethylene melt at 190 °C under atmospheric pressure. The model also predicts that increased pressure will accelerate bubble dissolution, in agreement with their experimental results which show that bubble dissolution rates increase if pressure is applied after the melt has formed. Increased pressure was found to increase the driving force of diffusion. Gogos (2004) also derived a bubble dissolution model in the form of an analytical solution. His model fit well with the data of Spence and Crawford (1996) and also provides an explanation for the effect of mould pressurization.

Pick and Harkin-Jones (2006) postulated that the presence of smaller bubbles in rotomoulded parts could improve the impact strength of the parts by crack blunting and craze initiation mechanisms, which would relieve stress and enable shear yielding. Pick and Harkin-Jones (2006) also investigated the effect of using different pressure levels in the mould at various

stages of the moulding cycle on the amount of bubbles retained in the moulded part and their effect on the impact strength. It was shown that pressurizing the mould before the polymer is fully molten causes a significant increase in the bubble content which deteriorates the impact strength. However, pressure applied at different times after the polymer had molten and at different levels influenced the bubble content and size. Their results showed that in general the impact strength is deteriorated by an increase in the bubble content. However, a higher content of smaller bubbles improved the impact strength of rotomoulded polyethylene. The results also showed that the use of pressure reduces overall cycle times. Mould pressurization during the cooling stage was also shown to improve the impact properties as it cause smaller crystallites to be developed.

Bellehumeur (2005) summarized the variables that can influence the rate of bubble dissolution. These include the melt temperature and its diffusion characteristics, the initial size of the bubbles formed, surface tension of the melt, solubility characteristics of air into the melt and the saturation level of air in the melt.

4.7 Rotomoulding materials

From the preceding sections, it has been elucidated that the conventional rotomouldability of a material is highly dependent on its thermostability, sinterability and densification characteristics. Besides the various polyethylenes, other polymers traditionally considered for rotomoulding applications are polypropylene, polyvinyl chloride (PVC), polyamides 6, 11 and 12 and polycarbonate (Beall, 2000). Beall (1998) discussed properties of these polymers not found in polyethylene. Although polyethylene is widely used, it falls short in stiffness and heat distortion. It is also difficult to paint (Beall, 2000). Polyethylene is also is also highly flammable and a good electrical insulator, which makes it unsuitable for some applications (Sun et al., 1993).

Tcharkhtchi and Verdu (2004) discussed the relationships between the thermal stability and rotomouldability of polymers. They explained why some polymers can be more easily moulded than others. The difference between rotomoulding and other process is that the time which the polymer spends in the molten state simultaneously being exposed to oxygen is

significantly higher than in other processes, hence its susceptibility to thermal-oxidative degradation (Crawford, 1996, Oliveira and Cramez, 2001, Tcharkhtchi and Verdu, 2004).

According to Tcharkhtchi and Verdu (2004), a polymer is rotomoudable if the temperature above which it degrades is greater than the temperature at which it attains sufficient viscosity to be processable. They showed that the processing window for polyethylene is far wider compared to other commercial polymers such PVC, polyamides and polyethylene terephthalate (PET), due to its lower melting point and relatively high temperature beyond which it degrades. The use of stabilizers and an inert atmosphere has been shown to widen this processing window. The study by Greco et al. (2012) showed that polyamide 6 has a narrow processing window and thus was not suitable for rotomoulding. However, this could be altered by using a thermal stabilizer.

Material variables which influence sinterability and densification of a material were discussed in the previous sections. Although the rheology of polymers is commonly gauged through the melt flow index, this is not entirely relevant to rotomoulding. The appropriate melt viscosity is the zero shear viscosity as rotomoulding is basically a pressure and shear free process (Kontopoulou and Vlachopoulos, 1999, Crawford and Throne, 2002, Bellehumeur, 2005). The melt rheology at the zero shear stress conditions and temperatures utilized in rotomoulding has a significant effect on the sintering behaviour of polymers but not on their densification.

The majority of polymers used in the rotational moulding industry are pulverized or ground from pellets into a powder between rotating metal plates, although some liquid polymers are also rotomoudable (Crawford and Throne, 2002, Bellehumeur, 2005). The use of micro-pellets been demonstrated recently (Crawford and Throne, 2002, Kearns et al., 2006).

The quality of the polymer powder obtained from the grinding process is influenced by factors such as the size of the gap between the metal plates, grinding temperature, number of teeth on the metal plates and condition of the blades (Greco and Maffezzoli, 2004, Bellehumeur, 2005). In industry the quality of the powder is usually assessed through evaluation of the particle size distribution, the dry flow index and the bulk density (Crawford and Throne, 2002, Bellehumeur, 2005).

Large powder particles require a longer time to sinter, thereby increasing the cycle time. They result in the formation of bigger voids, which form big bubbles in the melt. They also result in poor surface finish. The initial bubble size influences their rate of dissolution. On the other extreme, heat transfer is enhanced by use of finer particles. They also give a good surface finish. However, the grinding of powder to finer particles is energy intensive. A high number of finer particles can be detrimental to heat transfer as they melt first preventing the rest of the polymer from melting (Chaudhary et al., 2001a, Greco and Maffezzoli, 2004).

The particle size recommended for rotomoulding is 35 mesh (500 μm) (Crawford and Throne, 2002, Bellehumeur, 2005). According to Bellehumeur (2005) a particle size distribution between 100-500 μm is a good compromise between the powder packing and flowing characteristics and the cost of grinding. Crawford and Throne (2002) recommended a narrow particle size distribution with particle sizes less than 500 μm. The dry flow determines the ease with which the powder distributes itself in the mould, giving insights into whether the polymer melt will reach all extents of complex mould shapes. To determine the dry flow, the time in which 100 g of powder flows through a standard funnel is measured (Crawford and Throne, 2002).

The bulk density determines the packing ability of the powder. As was discussed earlier on the packing arrangement influences the initial size of the cavities formed between particles and therefore the size of bubbles formed in the melt. The initial size of bubbles formed has an effect on their dissolution (Chaudhary et al., 2001a). Typical dry flow and bulk density values for rotational moulding LLDPE powders are 27 s and 320 kg m^{-3}, respectively (Crawford and Throne, 2002). Dry flow is a function of the shape and size of the powders, whereas the bulk density depends on the particle shape, particle size, and particle size distribution of the powder (Crawford and Throne, 2002).

Greco and Maffezzoli (2004) evaluated the effect of grinding polyethylene at three temperature ranges on the powder particle shapes and sizes produced. They further investigated the sintering characteristics of the powder using thermo-mechanical analysis (TMA). Their results showed that particles ground at lower temperatures were smaller in size and had irregular shapes and tails, in contrast to the larger and regular particle shapes with no tails obtained at higher temperatures. The bulk density of the powders increased with an increase in grinding temperature, as a result of the better packing of regular shapes obtained

at higher temperatures. However, in sintering studies the smaller particles obtained by grinding at lower temperatures sintered and densified more efficiently. Their results showed that sintering rates are dependent on the initial particle size. Large and more regular particles obtained by grinding at higher temperatures sintered at higher temperatures. Their study showed that an optimum grinding temperature can be obtained at which the powder will have good packing and sintering behaviour.

4.8 Recent developments and challenges in rotomoulding

4.8.1 Cycle time reduction

A major disadvantage of the rotational moulding process which makes it uncompetitive compared to other polymer forming processes and limits its growth is the long cycle times. Notable progress has been made in addressing this challenge. Abdullah et al. (2009) investigated several cycle reduction techniques which included using surface enhanced moulds, internally pressurizing the mould, using internal cooling, using water spray cooling, using higher oven flow rates, and a combination of these. Significant cycle time reductions of up to 70% were achieved by using a combination of these techniques. Pick and Harkin-Jones (2006) also observed significantly reduced cycle times when they used pressure in the mould.

The direct heating of the mould has also been investigated (Monzón et al., 2012). McQuay et al. (2013) demonstrated that cycle times could also be reduced by preheating the powder and the mould. Tan et al. (2011) reviewed internal cooling methods which can lead to significant reductions in cycle times and improved mechanical properties. Reductions in cycle times were also observed by Chaudhary et al. (2001b) when they blended polyethylene with low molecular weight additives.

4.8.2 Material limitations

The fact that polyethylene is the main rotomoulding material is a major constraint to the growth of the process. This is due to its property limitations which were discussed in section 4.7. Material properties necessary for a polymer to be processable by rotomoulding were also discussed in the preceding section 4.7. A significant number of polymers are excluded from the process due to their susceptibility to thermal oxidative degradation as rotomoulding exposes the polymers to oxygen at high temperatures during the long cycle times. A further

constraint on any potential rotomoulding material is the prerequisite for suitable sintering and densification characteristics at the zero shear stress conditions.

In an effort to widen the range of rotomoudable polymers, Greco and Maffezzoli (2004) characterized the suitability of bio-polymers poly-lactic acid (PLLA) and Mater-Bi for rotational moulding through sinterability studies using TMA and by rotomoulding prototypes. The processing window of PLLA was wider compare to that of Mater-Bi, showing its suitability to rotomoulding. Addition of a plasticizer improved the properties of the PLLA. However, there is still need for progress in this area.

4.9 Use of functional additives in rotomoulding

Additives are routinely added to polymers during their manufacture or processing to improve their intrinsic properties. The additives used in the polymer industry can be distinguished into three broad categories; processing aids, performance enhancers and modifiers (Andrews, 2011). Processing aids such as heat stabilizers, antioxidants and mould release agents facilitate the processing of the polymer. Performance enhancers introduce new functionalities to the polymer. These include fillers, reinforcements, antistatic agents, impact modifiers and flame retardants. Polymer modifiers change the physical or mechanical properties of the polymer, for instance plasticisers, blowing agents, nucleating agents, colorants (Andrews, 2011).

4.9.1 Stabilization: Antioxidants and UV stabilizers

The susceptibility of polymers to thermal oxidative degradation in rotomoulding due to long cycle times and exposure to oxygen at high temperatures is more pronounced compared to any other process. This necessitates the use of effective antioxidant/thermal stabilizers packages in order to widen the process window and produce good quality products (Oliveira and Cramez, 2001, Sharifi et al., 2012, Yu and Wallis, 2008). Rotomoulded parts are also susceptible to photo-oxidative degradation, particularly when they are used outdoors, which can lead to subsequent deterioration of properties (Steele and Davis, 2001).

Stabilization packages used in rotomoulding are usually composed of a combined hindered phenol/phosphite antioxidant and a hindered amine light stabilizer (HALS) (Steele and Davis,

2001, Yu and Wallis, 2008). The antioxidant imparts stability to the polymer during processing and fabrication, whereas the HALS provides protection from UV degradation during the life span of the product. Steele and Davis (2001) discussed the mechanism of protection afforded by the antioxidants and stabilizers.

4.9.2 Pigmentation

Rotomoulded parts are often available in a variety of colours (Nagy and White, 1996). However, the major rotomoulding material polyethylene is difficult to paint (Beall, 2000, Crawford and Throne, 2002). Colour is usually imparted to rotomoulded parts through the use of pigments (Nagy and White, 1996, Kearns and Crawford, 2003). Pigments used in rotational moulding are usually fine solid particulates, although the use of liquid pigments has been investigated recently (Nagy and White, 1996, Crawford and Throne, 2002, Kearns and Crawford, 2003).

Three methods for mixing the polymer and pigments have been distinguished in the literature. Dry blending or dry mixing utilizes low intensity mixers such as drum tumblers, ribbon blenders and vee mixers (Nagy and White, 1996, Crawford and Throne, 2002). The tumbling action induced by the rotomoulding machine can also be utilized in dry blending. Dry blending is frequently used in industry due to its favourable economics (Nagy and White, 1996, Crawford and Throne, 2002, Kearns and Crawford, 2003). Dry blending negates the need for stringent stock control as natural material can be bought in bulk and coloured as and when needed (Nagy and White, 1996, Crawford and Throne, 2002, Kearns and Crawford, 2003). Dry blending is however ineffective in dispersing and distributing pigments homogenously in the polymer as it is a low shear mixing process. Pigment agglomerates accumulate at particle interfaces during processing. Consequently, the rotomoulded part is sensitive to the amount and type of pigment and used. Dry blending also results in residual deposits on the mould (Nagy and White, 1996, Kearns and Crawford, 2003).

High speed mixers or turbo blenders are high intensity mixers which operate at relatively high speeds and shorter times compared to low intensity mixers (Nagy and White, 1996). These are paddle-type mixers which operate at relatively high temperatures due to frictional heating (Kearns and Crawford, 2003, Hanna et al., 2006). As a result of the relatively higher temperatures, the polymer powder softens and pigment particles adhere to it. This gives a

rotomoulding compound which does not leave residues on the mould (Crawford and Throne, 2002, Kearns and Crawford, 2003). Turbo blenders include Henschel type mixers (Nagy and White, 1996, Crawford and Throne, 2002). Material handling is improved by turbo blending as the rotomoulding compound is much cleaner. Better mixing is attained by turbo-blending but pigment agglomerates accumulate at particle interfaces during processing (Crawford and Throne, 2002).

Melt compounding in an extruder is the most effective mixing method of homogenizing the pigments in rotomoulding powders (Crawford and Throne, 2002, McCourt et al., 2005). Compounding the pigments imparts improved mechanical properties and consistent colours. Grinding costs are an additional expense when melt compounding is used. Melt compounding also limits flexibility as stock control over the required colours is necessary (Crawford et al., 1996, Nagy and White, 1996, Oliveira and Cramez, 2001).

The incorporation of pigments in rotational moulding powders by various methods and its effect on the properties of rotomoulded parts has been studied intensively (Nagy and White, 1996, Crawford et al., 1996, McCourt et al., 2005, Hanna et al., 2006). Nagy and White (1996) studied the effect of five different colour pigments on the properties of rotomoulded polyethylene. They used either dry blending, turbo mixing or melting compounding in an extruder and varied the concentration of the pigments from 0.11 to 0.36 wt.%. Their study showed that using a zinc stearate surfactant improved the colour quality and handling properties but caused shrinkage and warpage of the rotomoulded parts. Their results also showed that dry blending of pigments deteriorated the impact strength of the rotomoulded parts due to the pigments accumulating along the fusion lines of the polymer particles. However, the severity of reduction in impact properties was polymer and pigment specific and dependent on processing conditions used. Improved impact strength was possible with melt compounded samples or two layer parts with a pigmented layer and unpigmented inner layer.

Crawford et al. (1996) also investigated the effect of dry blending, turbo blending and melt compounding on the impact strength of rotomoulded polyethylene using various pigments and pigment concentration. Their study showed that turbo blending and dry blending (tumble mixing in the mould) reduced the impact strength of the rotomoulded parts in a similar manner. The reduction in impact performance with pigment content for parts with turbo

blended pigments was also observed by McCourt et al. (2005) and Hanna et al. (2006). Dry blending also resulted in a residue in the mould.

Results from the study by Crawford et al. (1996) showed that for some pigments, the impact strength was dependent on the pigment concentration whereas for the other pigments impact strength was maintained across the whole concentration ranges used. Similar to the subsequent observations of McCourt et al. (2005) and Hanna et al. (2006), in compounded samples, the inclusion of the pigments into polyethylene did not have significant influence on the impact properties. All the pigmented samples failed in a brittle mode, in contrast to the pigmented samples. The conclusion from this study was that it is not possible to generalise the effect of pigments on impact strength. However, lower levels of pigmentation (less than 0.15 wt.%) resulted in moulded parts with high levels of impact strength for all pigments used. Inorganic pigments apparently exhibited better impact properties than organic ones. The results also show that at low pigment concentration, turbo blending or dry blending can be as effective melt compounding.

Cramez et al. (1998b) studied the microstructure and mechanical properties of rotomoulded polyethylene pigmented with a nucleating and a non-nucleating pigment. Their study showed that prior thermo mechanical action results in a decrease in crystalline texture giving better mechanical properties. Microscopic techniques also show that turbo blended nucleating pigments concentrate on the fusion zones of the original polymer particles creating transcrystalline zones as was observed by Nagy and White (1996). The spherulite structure of parts produced from turbo blending the non-nucleating pigment was found to be similar to that of the virgin polymer. Turbo blending both types of pigments with polyethylene had no significant influence on the yield strength. However, the impact strength and elongation to break of the rotomoulded decreased with pigment addition for both pigments when they were turbo blended. This was apparently due to the concentration of pigment along the particle boundaries and the formation of transcrystalline structures at these boundaries. This poor dispersion resulted in stress concentration which weakened them.

When Cramez et al. (1998a) used extrusion compounding to disperse and mix both types of pigment, they found that they were well distributed and dispersed as in the other studies. The pigments produced finer spherulite structures which was more prominent with the nucleating pigment. Extrusion mixing improved the nucleating effect of the nucleating pigments as

shown by the increase in crystallization temperature and melt enthalpy, compared to turbo blending. Higher yield stresses were observed for the parts made by rotomoulding the powder mixed through extrusion mixing of the nucleating pigment and polyethylene due to the increased crystallinity and reduction of crystalline texture to a finer one. The influence of crystallinity on mechanical properties of rotomoulded parts was discussed in section 4.4.2.

In the study by Cramez et al. (1998a) extrusion mixing resulted in enhanced impact strength in comparison to turbo blending as in the other studies. However, the pigment type had no significant effect on the impact properties when extrusion mixing was used.

4.10 Rotomoulded composites: Fillers and reinforcements

The limitations prevalent in rotational moulding due to the dependency on polyethylene as the major rotomoulding material can be overcome by modifying polyethylene (Robert and Crawford, 1999). Polyethylene can be modified by developing rotomouldable composites with functional fillers. Several studies have been carried out on the rotational moulding of composites with reinforcements. The studies had mixed results. Rotomoulding presents challenges to the use of fillers and reinforcements because the absence of shear or pressure does not promote good mixing and adhesion. The likelihood of filler segregation and agglomeration is high (Robert and Crawford, 1999, Yan et al., 2006).

4.10.1 Fibre reinforced composites

The challenges that have encountered in reinforcing polymers for rotomoulding are filler/matrix segregation, lack of adhesion of the filler to the matrix and filler agglomeration (López-Bañuelos et al., 2012). The fact that the process is low shear means that there is no promotion of mixing between the fibres and matrix (Cramez et al., 1998b, Chang et al., 2011). Fibres have often been found lining the inner wall of the rotomoulded composite part as they will be heavier than the part (Wisley, 1999, Yuan et al., 2007, Chang et al., 2011, López-Bañuelos et al., 2012). Subsequently the fibres would not contribute to the enhancement of mechanical properties.

The dry blending method is particularly ineffective in preventing fibre/matrix segregation and fibre clustering (Wisley, 1999, Yuan et al., 2007). This leads to deterioration of mechanical

properties with inclusion of the fibres. However, in a study on polyethylene natural fibre reinforced composites processed by dry blending and rotomoulding, López-Bañuelos et al. (2012) found that an optimum fibre concentration of 10 wt.% resulted in a 65 % increase in tensile and flexural modulus. Raymond and Rodrigue (2013) also observed improvements in tensile and flexural modulus of rotomoulded polyethylene/ wood composites prepared by dry blending polyethylene and wood flour (maple) up to 20 wt.% wood particle content. However, the tensile strength of the composites in both studies deteriorated with fibre content. A study of the exterior and interior surfaces by López-Bañuelos et al. (2012) showed satisfactory dispersion of the fibres, although in higher fibre content composites the fibres were more prone to agglomeration or clustering. The impact strength of the composites deteriorated with an increase in fibre content. In the study by Raymond and Rodrigue (2013), poor adhesion between the hydrophobic polymer and hydrophilic wood filler was cited as the cause for the deterioration in tensile strength.

The multiple shot moulding procedure which results in multilayer moulding has been attempted as a solution for the fibre/matrix segregation (Wisley, 1999). In this procedure successive shots of polymer powder and fibres are introduced in the mould resulting in the fibres being sandwiched in-between polymer layers. Significant improvements in the mechanical properties have been observed using this method at the expense of disruptions in the process (Wisley, 1999, Torres and Aragon, 2006, Ortega et al., 2013, Chang et al., 2011).

Melt compounding the fibres and polymer matrix and subsequent grinding the composites extrudate into the powder prior to rotomoulding has been observed to produce composites with enhanced mechanical properties in most studies (Wisley, 1999, Yuan et al., 2007).

The improvement of the fibre/matrix adhesion through the use of compatiblizers and surface treatments has been shown to improve mechanical properties of fibre reinforced rotomoulded composites. Wisley (1999) observed improved mechanical properties in rotomoulded glass fibre reinforced polyethylene composites by using maleic anhydride grafted polyethylene compatiblizer. Yuan et al. (2007) used maleated polyethylene to improve the interfacial adhesion between wallastonite micro-fibres and polyethylene and achieve enhanced impact properties in wallastonite micro-fibre reinforced polyethylene composites. Raymond and Rodrigue (2013) improved the tensile strength of wood flour filled polyethylene composites

prepared by dry blending by treating the wood surface thereby enhancing the adhesion between the hydrophobic polymer matrix and hydrophilic filler.

4.10.2 Particulate reinforced composites

A comprehensive study by Yan et al. (2006) investigated the effects of mixing methods and particle sizes on the mechanical properties of particulate reinforced rotomoulded composites. They showed that an increase in the reinforcing effect with respect to the tensile modulus was possible with dry mixed larger particles (90-240 μm), up to 10 vol.% particulate content in polyethylene, thereafter deteriorating or remaining stable. Particulate agglomerates were observed using SEM beyond 10 vol.% particulate content which contributed to the demise of the modulus. Their study showed that marginal increases in modulus occurred only up to a particulate filler content of 2 vol.% when dry mixed small particulates (6.5-35 μm) were used in the rotomoulding of polyethylene. Thereafter the modulus deteriorated. In both cases the tensile strength deteriorated. However, it was more severe in the case of the small particulates.

Yan et al. (2006) emphasized that compared to larger particulates, smaller particulates needed more polymer to be wetted. The smaller particulates also had the tendency to agglomerate. The agglomerates apparently acted as defects deteriorating the mechanical properties. Their study showed that even distribution of the fillers was the prerequisite for the reinforcing effect to be achieved. Even filler distribution was achieved by dry manual mixing for bigger particles (90-240 μm) and melt compounding for smaller particles 6.5-35 μm. The size of the reinforcements had no significant effect on the modulus and strength if uniform distribution was achieved. Melt compounding of the smaller particles (6.5-35 μm) resulted in enhancement of the modulus up to 20 vol.%, and a less severe deterioration of tensile strength. Robert et al. (2000) had earlier on also obtained pronounced improvement in the tensile strength of melt compounded rotomoulded polyethylene with smaller mica particles (average diameter 3.5 μm) in comparison to the large mica particles (average diameter 30 μm). If even distribution of particulates is achieved, tensile modulus and tensile strength can be predicted by the Halpin-Tsai-Nielsen and Nicolais-Narkis models, respectively (Yan et al., 2006).

The study by Yan et al. (2006) followed on several earlier studies and subsequent studies which showed general trends in the mechanical properties of rotomoulded particulate reinforced composites. In these studies the composite modulus was mostly observed to increase up to a maximum particulate filler loading, deteriorating thereafter with any further filler addition (Wisley, 1999, Robert and Crawford, 1999, Robert et al., 2000, Yan et al., 2003, Kissick et al., 2011). The increase in modulus is due to the relative rigidity of the fillers compared to the polymer matrices and the interaction between the filler and polymer matrix which results in a reduced polymer molecular mobility (Wisley, 1999). Composites fabricated with higher aspect ratio particulate fillers showed better stiffness compared to those with lower aspect ratio fillers (Robert and Crawford, 1999, Robert et al., 2000).

However, the deterioration of the modulus results from filler particle agglomeration, uneven distribution of the fillers, particularly at high filler loadings, poor interfacial adhesion between the fillers and matrices and also the occurrence of a high density of voids or pores in the composite cross sections (Robert and Crawford, 1999, Yan et al., 2006, Baumer et al., 2014). The interfacial adhesion between the fillers and polymers has been improved by use of coupling agents, thereby improving the modulus through efficient stress transfer from the polymer matrix to the filler (Robert and Crawford, 1999). Higher bubble density suggests poor sinterability in the composites (Sae-Chieng and Kanokboriboon, 2007). The use of a slip agent in calcium carbonate filled rotomoulded polyethylene composites reduced the porosity slightly as it decreased the dry flow, improving the flowability and bulk density of the composite powders (Baumer et al., 2014).

In most of the studies on rotomoulded particulate reinforced composites the tensile and impact strength deteriorated severely with inclusion of the particulate fillers (Wisley, 1999, Robert and Crawford, 1999, Robert et al., 2000, Liu and Peng, 2010, Kissick et al., 2011, Baumer et al., 2014). In a few of the studies, marginal improvements in the tensile strength were observed (Robert and Crawford, 1999, Robert et al., 2000, Sae-Chieng and Kanokboriboon, 2007). Improvements in the impact strength of the composites were rare (Siddhamalli and Lee, 1998, Yan et al., 2003, Liu and Peng, 2010).

The impact strength of particulate reinforced composites deteriorates as a result of the rigidity of the fillers used, in comparison with the polymer matrices, making the polymer brittle (Wisley, 1999). Poor interfacial adhesion between the particulate fillers and the polymers has

frequently been shown to be the cause for poor impact and tensile strength of rotomoulded particulate reinforced polymers due to the de-wetting effect (Robert and Crawford, 1999, Liu and Peng, 2010). The lack of shear stress in rotomoulding does not promote adhesion between the polymer and filler (Wisley, 1999). Coupling agents such as maleic anhydride modified polyethylene have been used to promote adhesion between polyethylene and the fillers and improve the tensile and impact strength (Robert and Crawford, 1999, Robert et al., 2000, Yan et al., 2003). Rotomoulded composites with finer particles exhibited lesser deterioration in impact strength (Robert et al., 2000).

Some studies have shown that significant heat transfer enhancements occur in polymer matrices reinforced with thermally conductive fillers, resulting in reduced cycle times (Robert and Crawford, 1999). Some particulate fillers such as talc have a nucleating effect and promote the crystallization of polyethylene (Robert and Crawford, 1999). However, the tensile modulus and strength of rotomoulded particulate composites was shown to deteriorate with faster cooling rates, correlating well with the level of crystallinity observed in the composites (Liu and Peng, 2010). This was in contrast to the improvement in impact strength that was observed with an increase in the cooling rate. These observations are in agreement with what was discussed in section 4.4.2 about the effect of cooling rates on microstructure and mechanical properties of rotomoulded parts.

Vasudeo et al. (2001) prepared flame retardant polyethylene composites for rotomoulding containing flame retardants antimony trioxide and decabromodiphenyl oxide and an anti-drip agent talc and magnesium hydroxide. They made use of an elastomer to aid in the sintering of the composites. They prepared these composites by extrusion mixing. With respect to Underwriters Laboratories (UL) 94 fire ratings, the composites passed with various ratings. The flame retardant composites exhibited improved impact strength and flexural modulus compared to virgin polyethylene.

4.10.3 Nanocomposites

Formulations of polymer nanocomposites have also been extended to rotomoulding. Murphy et al. (2002) and Murphy et al. (2003) formulated polyethylene -organo-clay nanocomposites for rotomoulding. Planes et al. (2008) formulated ethylene-propylene co-polymer/graphite nanocomposites using expanded graphite. Their objective was to improve the thermal

conductivity of the co-polymer thereby reduce the rotomoulding cycle time. Chandran V and Waigaonkar (2015) formulated polyethylene-fumed silica nanocomposites for rotational moulding. Greco et al. (2012) studied the sinterability of polyamide 6/organo-modified montmorillonite nanocomposites formulated for rotomoulding using thermo-mechanical analysis. Their study showed that the nanocomposites had a narrow processing window and thus were not suitable for rotomoulding. However, the addition of a thermal stabilizer could widen this window.

None of the formulations discussed in the preceding paragraph were actually rotomoulded and the properties of the parts evaluated. Planes et al. (2008) reported that rotational moulding of polyolefin nanocomposites had not been tested. A limited number of studies in which nanocomposites formulations were rotomoulded are available in the literature.

In the study by Hanna et al. (2003) they prepared quaternary tallow ammonium chloride modified montmorillonite/polyethylene nanocomposites by melt compounding and subsequent rotomoulding. They investigated the mechanical properties of the nanocomposites at a fixed nano-clay concentration of 4 wt.% and varying maleic anhydride grafted polyethylene compatiblizer concentration. The tensile modulus and strength gradually decreased with increases in compatiblizer concentration. The impact strength of the nanocomposites was substantially lower at all compatiblizer concentrations, compared to that of the base polyethylene. The decrease in impact strength at 25 °C was severe at 6 and 10 wt.% of the compatiblizer, deteriorating by 94 %. SEM and XRD showed poor dispersion of the clay in the polymer matrix.

Chapter 5 Literature: Phase change materials for energy storage

5.1 Energy storage methods

Sharma et al. (2009) discussed the various methods which can be used to store energy. These include mechanical, electrical and thermal storage methods. Energy can be stored in mechanical form as gravitational energy or pumped hydropower storage, or compressed air energy storage and fly wheels. Electrical energy storage takes the form of batteries. Thermal energy storage occurs by changing the internal energy of a material as sensible heat, latent heat and thermochemical or a combination of these.

5.2 Energy storage through phase change materials

Latent heat is the energy absorbed or realised by a material undergoing a transition at a constant temperature. Phase change materials (PCMs) store and release energy by virtue of them undergoing phase changes at constant temperature in which they either absorb or release latent heat. Compared to sensible heat storage materials, latent heat storage can store up to 5-14 times more heat per unit volume at a constant temperature. Although solid-liquid phase changes have relatively lower latent heats of phase change compared to solid-gas and liquid-gas transitions, they involve lower volume changes which solve containment problems (Sharma et al., 2009). The energy stored by a PCM is evaluated using the equation (Sharma et al., 2009):

$$Q = \int_{T_i}^{T_m} mC_p \, dT + ma_m \Delta h_m + \int_{T_m}^{T_f} mC_p \, dT \quad \textbf{(5-1)}$$

$$Q = m\left[C_{sp}(T_m - T_i) + a_m \Delta h_m + C_{lp}(T_f - T_m)\right] \quad \textbf{(5-2)}$$

where Q is the amount of heat stored, T the temperature, T_i, T_m and T_f are the initial, melting and final temperatures, respectively, and m is the mass of the PCM. C_p, C_{sp} and C_{lp} are the specific heat capacity, average heat capacity between T_i and T_m and average specific heat capacity between T_m and T_f, respectively. a_m is the fraction of the PCM that actually melts and Δh_m the specific heat of fusion of the PCM.

PCMs that melt below 15 °C find applications in coolness storage in air conditioning applications, whereas those that melt above 90 °C can be used in absorption refrigeration. The PCMs which melt in between 15 °C and 90 °C have largely found application in solar heating and load levelling applications (Farid, Khudhair & Razack, 2004). Sharma et al. (2009) reviewed a wide range of solar heating and building applications in which PCMs have been applied.

5.3 Properties of phase change materials for energy storage

Several thermophysical and rheological properties determine the applicability of a material as a phase change material for energy storage (Farid et al., 2004, Sharma et al., 2009). The phase transitions of the material must occur in the desired application range. The materials must have high phase change enthalpy (latent heat) and thermal conductivity. High phase change enthalpy minimizes the size of storage systems. High thermal conductivity ensures good heat transfer, enabling fast charging and discharging rates. PCMs for energy storage must undergo congruent melting and exhibit minimum super cooling. Incongruent melting occurs if the material shows phase segregation accompanied with deterioration in latent heat when it undergoes successive melting and freezing cycles. Super cooling is undesirable as it interferes with proper heat extraction from the PCM. It has been reported that super cooling by more than 5 °C can prevent extraction totally (Sharma et al., 2009).

Phase change materials must also have high densities, undergo small volume change during their phase transitions and have low vapour pressures (Sharma et al., 2009). High densities will minimize the container sizes. Minimum volume changes during phase transitions and low vapour pressures reduce containment problems.

It is also desirable that phase change materials be non-toxic and have long term chemical and thermal stability as they undergo numerous melt/freeze cycles in their lifetime. Low flammability, cost effectiveness and abundant availability are the other important factors for a material to be considered as a phase change material for energy storage (Farid et al., 2004, Sharma et al., 2009).

5.4 Classification of phase change materials for energy storage

A wide range of materials can be used as phase change materials for thermal energy storage (Zalba et al., 2003, Farid et al., 2004, Sharma et al., 2009). Figure 5-1 shows a classification of phase change materials.

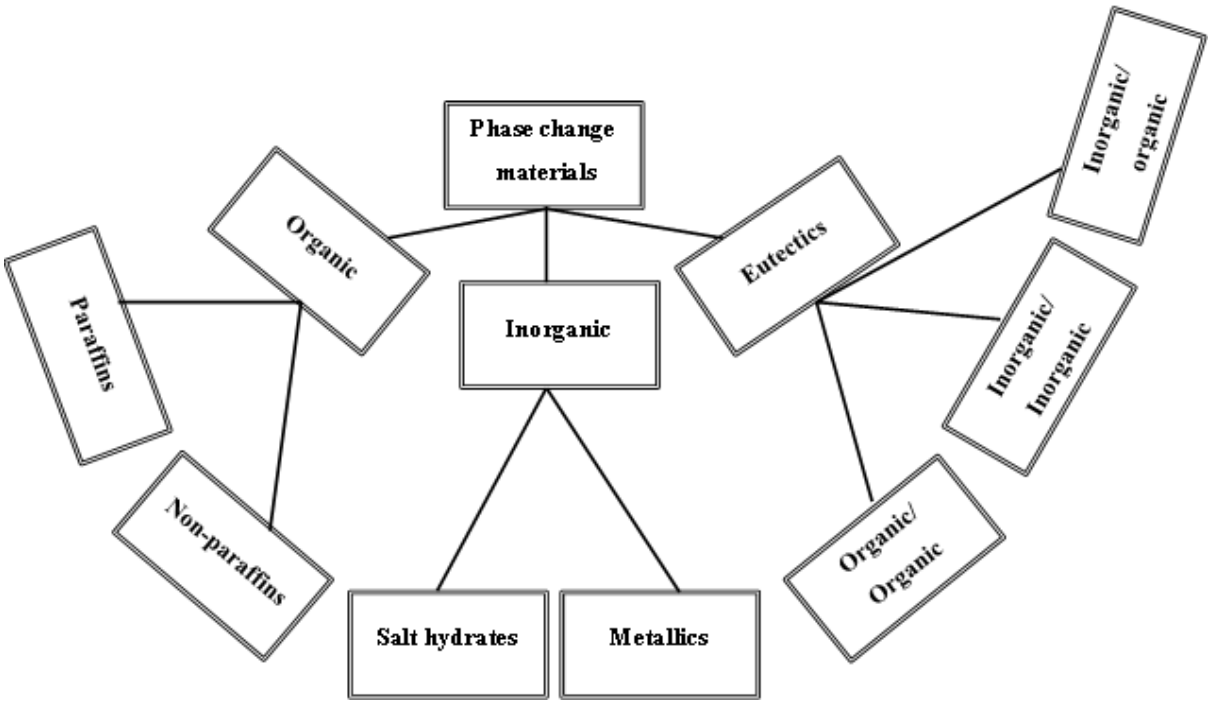

Figure 5-1 Classification of phase change materials for energy storage (adapted and modified from Sharma et al. (2009)).

5.5 Characterization of PCMs

Proper design of latent heat thermal energy storage (LHTES) systems dictates that the thermophysical and rheological properties of the PCMs be evaluated accurately as a function of temperature (Castellón et al., 2008, Lazaro et al., 2013). A significant error will result in the storage capacity of the PCM if the enthalpy as a function of temperature is determined incorrectly (Günther et al., 2009, Oró et al., 2012, Lazaro et al., 2013). However, reported thermophysical property data of phase change materials exhibit inconsistencies (Zalba et al., 2003, Oró et al., 2012).

Several techniques that include differential scanning calorimetry (DSC) and the T-history method have been used to evaluate the thermophysical property enthalpy as a function of

temperature for PCMs (Günther et al., 2009). When using these techniques thermodynamic equilibrium must be established in the sample in order to get comparable and well defined data (Mehling et al., 2006). Incorrect results are often obtained from the DSC due to the absence of thermodynamic equilibrium; a thermal gradient exists within the PCM sample dependent on the heating or cooling rate and also the mass used (Castellón et al., 2008). Until recently, there were no standards for the evaluation of thermophysical properties of phase change materials for energy storage (Mehling et al., 2006). *RAL Gütegemeinschaft PCM e.V.* (German Institute for Quality Assurance and Cerficiation E.V.) was formed in 2005 to set PCM quality assurance standards (Mehling et al., 2006). Since then, work to standardize the characterization of PCMs using DSC has been done (Lazaro et al., 2013, Gschwander et al., 2015). The uncertainty set for the successful design with PCMs is less than 10 % for the enthalpy of melting and less than 1 °C in the melting temperatures (Castellón et al., 2008, Günther et al., 2009).

Slow scanning rates and smaller masses of PCM can ensure thermodynamic equilibrium in the DSC. This can however be detrimental as slow scanning rates can result in a low signal to noise ratio and small samples might not be representative for an inhomogeneous PCM (Mehling et al., 2006). Castellón et al. (2008) and Günther et al. (2009) obtained high uncertainties in melting enthalpies and melting temperatures using the dynamic mode of the DSC with heating/cooling rates as low as 0.5 °C min^{-1}. However, inter-comparative work on the measurement of the enthalpy as a function of temperature for PCMs using the DSC gave rise to a calibration and measurement protocol to ensure reliable data (Lazaro et al., 2013).

The German Institute for Quality Assurance and Cerficiation E.V. (RAL) standard on PCMs, RAL-GZ 896 specifies that thermal conductivity of PCMs must be evaluated in the solid and liquid state with an accuracy of at least 5% in the thermal conductivity and 0.5 °C in the temperature of measurement.

The accelerated thermal cycling test is a widely used method used to evaluate whether the PCM will undergo many melt/freeze cycles without its properties deteriorating (Zuo et al., 2011a, Yuan et al., 2014). The German Institute for Quality Assurance and Cerficiation E.V. (RAL) standard on PCMs, RAL-GZ 896, classifies PCMs according to the number of complete melt/freeze cycles which they can withstand without their properties deteriorating. The standard classifies PCMs from category A-F depending on the number of melt/freeze

cycles they are intended to withstand without deteriorating, with A being the category with the highest number of melt/freeze cycles of ≥10000.

5.6 Fatty acids as phase change materials for energy storage

The properties of fatty alcohols which enable their exploitation as phase change materials for energy storage were mentioned in Chapter 1. Their relatively higher latent heats of fusion and crystallization were highlighted. The data collected by Yuan et al. (2014) shows that the melting enthalpy of saturated fatty acids increases with carbon chain length. This data also shows that for saturated fatty acids with a carbon chain length of at least 12 carbon atoms, the melting enthalpy was close to 200 J g^{-1}. The thermal stability of fatty acids with respect to the melting temperature has been shown to deterioate with successive melt/freeze cycles in a number of studies. The level of deterioration was however correlated with the purity of the fatty acids (Sarı, 2003, Sarı and Kaygusuz, 2003). The other undesirable properties of fatty acids as PCMs for energy storage are their mild corrosivity and bad odour (Sharma et al., 2009, Huang et al., 2013).

5.6.1 Stearic acid

Commercial stearic acid is a combination of approximately 55 % palmitic acid and 45 % stearic acid and other fatty acids (Tillotson, 1955). Palmitic acid and stearic acid are the trivial names of the fatty acids hexadecanoic acid and octadecanoic acid. These organic acids are aliphatic, straight chain and saturated mono-carboxylic acids with 16 and 18 carbon atoms, respectively (Gunstone et al., 2007).

Straight chain, saturated fatty acids (*n*-fatty acids) with even numbers of carbon atoms such as palmitic and stearic acid are known to exist in three polymorphs A, B and C. Another polyform E is a recent discovery (Garti et al., 1980, Kaneko et al., 1999, Gbabode et al., 2009). The most thermodynamically stable polyform is the C form. The C form can be obtained by solidification of the melt or crystallization from a polar solvent. The A form or a combination of the B and C forms are frequently obtained if crystallization is carried out in a non-polar solvent. The heating of the A and B forms irreversibly transforms them into the C form prior to melting. The measured melting point of these acids is thus that of the C form

(Garti et al., 1980, Gbabode et al., 2009). The B and E forms are only obtained by solution crystallization (Kaneko et al., 1999).

The enthalpies of the fatty acids are relatively high which makes them suitable as PCMs. The melting point and enthalpy of fusion of stearic acid as reported by Sato et al. (1990) are 69.6 °C and 61.3 kJ mol^{-1}, respectively. Gbabode et al. (2009) observed a melting point and enthalpy of 62.25 °C and 53.9 kJ mol^{-1}, respectively, for palmitic acid. However, as mentioned in section 5.6, the disadvantages of fatty acids as PMCs are a level of thermally instability due to thermal cycling, mild corrosiveness and pungent smells.

5.7 Fatty alcohols as phase change materials for energy storage

The properties of fatty alcohols which make them suitable candidates for PCMs for energy storage were introduced in Chapter 1. However, the polymorphism which they exhibit can affect heat storage and extraction when they are used as PCMs (Ventola et al., 2002).

n-Alkanols with between 12-20 carbons can exist as two monoclinic polymorphs β and γ at room temperature. The stable form for *n*-alkanols with an even number of carbon atoms is the γ form, whereas *n*-alkanols with an odd number of carbon atoms assume the β as their stable form (Ventola et al., 2002). Heating these ordered phases transforms them into the rotator phase, the α form, which subsequently melts. For *n*-alkanols with even numbered carbon atoms, the solid-solid transition $\gamma \rightarrow \alpha$ overlaps with the melting transition $\alpha \rightarrow liquid$ such that for purposes of heat storage the enthalpy from the two transitions can be considered to be occurring at the same temperature and summed up. However, for *n*-alkanols with odd numbered carbon atoms the solid-solid transition $\gamma \rightarrow \alpha$ occurs a few degrees before the melting transition (Ventola et al., 2002).

The *n*-alkanols crystallize into the α form when they are cooled. Negligible super cooling was observed for the transition $liquid \rightarrow \alpha$. However, significant super cooling is observed for the solid-solid transition $\alpha \rightarrow \beta$ and $\alpha \rightarrow \gamma$ (van Miltenburg et al., 2001). This super cooling is undesirable as it interferes with proper heat extraction from the PCM. Super cooling by more than 5 °C, can prevent extraction totally (Sharma et al., 2009).

5.7.1 Stearyl alcohol

Stearyl alcohol is the trivial name for the fatty alcohol 1-octadecanol. It is a saturated straight-chain primary alcohol with 18 carbon atoms and a hydroxyl functional group at the terminal carbon atom (Mudge, 2005).

The crystal structure and melting characteristic of stearyl alcohol has been reported on by van Miltenburg et al. (2001) and Ventola et al. (2002). As it is an *n*-alkanol with an even number of carbons (preceding section), the solid-solid transition $\gamma \rightarrow \alpha$ has been reported to overlap with the melting transition $\alpha \rightarrow liquid$ at around 331 K (57.85 °C) (Ventola et al., 2002). On cooling the crystallization transition exhibits negligible super cooling. Stearyl alcohol crystallizes into the rotator phase α. The crystallization transitions $liquid \rightarrow \alpha$ and solid-solid transition $\alpha \rightarrow \gamma$ from the rotator phase into the stable form γ are separated with the solid-solid transition displaying a super cooling of up to 5 °C. Van Miltenburg et al. (2001) and Ventola et al. (2002) reported typical enthalpies of close to 26 kJ mol^{-1} and 40 kJ mol^{-1} for the solid-solid transition and the melting transition, respectively, which when combined (since the transitions overlap) are relatively high.

5.8 Mixtures of stearyl alcohol and stearic acid as phase change materials

Previous studies on the phase diagrams of mixtures of *n*-alkanols and straight chain fatty acids showed that their eutectic mixtures do not exhibit the solid-solid transitions with super cooling (Gandolfo et al., 2003, Zeng et al., 2009). Mixing *n*-alkanols with fatty acids dilutes the odour of fatty acids and reduces their corrosivity. However, only a few of these mixtures have been studied as phase change materials for energy storage (Zeng et al., 2009, Zuo et al., 2011a, Zuo et al., 2011b, Huang et al., 2013). Gandolfo et al. (2003) studied the phase diagram of mixtures of stearic acid and stearyl alcohol and found that the eutectic composition occurred at a composition of 0.58 mol fraction stearyl alcohol and eutectic temperature of 50 °C. However, this mixture has not been studied as PCM.

5.9 Enhancing the thermal conductivity of PCMs

Several approaches for enhancing the thermal conductivity of PCMs have been studied. These include dispersion of highly thermally conductive particles into the PCMs such as

metallic particulates or graphite, the use of finned configurations or insertion of a metal matrix in the PCMs (Velraj et al., 1999). Another approach to enhance the conductivity of PCMs is the impregnation of PCMs into a highly thermally conductive material with a porous structure. Exfoliated graphite and other foams have been used as porous media (Sarı and Karaipekli, 2007). Use of porous materials also solves the leakage problem of PCMs by making them formstable.

Dispersion of traditional thermally conductive fillers into PCMs usually requires high loadings for appreciable enhancement in thermal conductivity to be realised (Mhike et al., 2012). High filler loadings limit the amount of PCM available for heat storage and results in weight penalties which make the system unviable. PCM/filler separation is also an undesirable effect when fillers are dispersed into PCMs as they can migrate to the bottom of the container during the melt/freeze cycles and not contribute in the enhancement of thermal conductivity. Finned configurations, metal matrices and metal insertions significantly enhance the heat transfer in LHTES systems (Velraj et al., 1999). However, the enhancement compromises the weight of the systems and inevitably increases costs. Fan and Khodadadi (2011) reviewed the thermal conductivity enhancement imparted by use of these structures.

Dispersion of nano-structured materials particularly nano carbon materials is a relatively new approach of enhancing the thermal conductivity of PCMs (Khodadadi et al., 2013). Nanoscale carbon materials such as carbon nanotubes, carbon nanofibres and graphene theoretically have high thermal conductivities and lower densities. Several studies have been conducted on the dispersion of carbon nanotubes, carbon nanofibres and graphene in PCMs (Elgafy and Lafdi, 2005, Cui et al., 2011, Yavari et al., 2011, Shi et al., 2013). Theoretical considerations predict that carbon nanofillers can enhance the thermal conductivity of PCMs by several orders of magnitude at low loadings due to their high thermal conductivities. However, marginal improvements in the thermal conductivity of the PCM nanocomposites frequently less than 100% were usually observed. This limited improvement is unexpected since the carbon nanofillers exhibit high thermal conductivities and high aspect ratios. However, as discussed in Chapter 4, the influence of the interfacial thermal resistance on the effective thermal conductivity is more pronounced in nanocomposites due to the higher density of interfaces which scatter phonons. The interfacial resistance in PCM/nanocomposites can be reduced by using nano fillers with high aspect ratios and

enhancing the interfacial adhesion between the PCM matrices and the nanofillers (Nan et al., 2004).

Shi et al. (2013) and Xiang and Drzal (2011) showed the effectiveness of graphite nanoplatelets in enhancing the thermal conductivity of paraffin wax PCMs. However, the dispersion of graphite nanoplatelets has not yet been extended to other PCM matrices such as stearic acid or stearyl alcohol. Due to the oxidative intercalation, the heat treatment and ultrasonication processes through which graphite nanoplatelets are produced, GNPs can have oxygen functional groups on their surfaces (Chen et al., 2003, Yi and Shen, 2015). These groups can interact with polar groups on stearyl alcohol/stearic acid through hydrogen bonding. This can result in improved interfacial adhesion between the nanofiller and the PCM which can subsequently reduce the interfacial resistance, resulting in an enhanced effective thermal conductivity of the PCM nanocomposites.

Chapter 6 Experimental

6.1 Synthesis of graphite nanoplatelets

Preliminary work was undertaken to establish a facile, efficient method to synthesize graphite nanoplatelets (GNPs). Two expandable graphite types were considered for the synthesis of graphite nanoplatelets. Traditional furnace exfoliation was compared to microwave radiation exfoliation. Four media were evaluated for their suitability in delaminating exfoliated graphite stacks into individual graphite nanoplatelets through ultrasonication assisted liquid phase exfoliation. Ultrasonication variables were kept constant, except the ultrasonication time which was initially varied until a suitable time was established.

6.1.1 Materials

Two grades of expandable graphite ES 250 B5 (exfoliation onset temperature 220°C) and ES170 300A (exfoliation onset temperature 300°C) were supplied by Qingdao Kropfmuehl Graphite (China). Natural Zimbabwean flake graphite was supplied by BEP Bestobell, Johannesburg. The ultrasonication media considered included two alcohols propan-2-ol (isopropanol) and 1-hexanol supplied by Merck. The other two ultrasonication media were two water-surfactant systems. The non-ionic surfactant polyethylene glycol sorbitan monolaurate with the brand name Tween 20 was supplied by ICI Surfactants. The anionic surfactant sodium dodecyl sulfate (SDS) was supplied by Sigma-Aldrich. Surfactant solutions were prepared with distilled water. Table 6-1 shows the ultrasonication media data relevant to acoustic cavitation for media used in this study and reference media.

Table 6-1 Ultrasonication media properties (Lide, 2005).

Ultrasonication media	Surface tension, mNm^{-1}	Vapour Pressure, KPa	Viscosity, mPa.s	Boiling point, °C
Water	71.99	2.33[a]	1.00[a]	100
Isopropanol	20.93	6.02	2.04	82
1-Hexanol	25.81	0.11	4.57	158
Cyclopentanone	32.80	1.55	-	131
NMP	40.10	0.04	-	202

[a]All values at 25 °C, except those for water, which are at 20 °C.

6.1.2 Graphite exfoliation and delamination

About 3.50 g of expandable graphite type ES 250 B5 or ES170 300A was exfoliated in either a preheated Thermopower furnace set at 600 °C or a Samsung Model ME9144ST microwave oven. The exposure time in the furnace was 5 minutes. The power setting on the microwave was 1 kW and the treatment time was 2 minutes. About 2 g of exfoliated graphite was then immersed in 300 mL of a particular exfoliation media present in a 600 mL beaker and placed in an ice bath. About 50 mg of each surfactant was used for 300 mL of distilled water. The same volume of exfoliation media and beaker size was maintained in order not to vary the cavitation volume. Ultrasonication was performed for 2 h at a power setting of 300 W using a Vibracell VC375 ultrasonic generator with a 12.5 mm solid tip horn. During this time the dispersion was agitated continuously with a magnetic stirrer.

Small portions of the colloidal dispersions of graphite nanoplatelets were deposited on microscopy slides and allowed to dry for observation with high resolution field emission scanning electron microscopy (HR FESEM) and Raman spectroscopy. After allowing the colloidal dispersions of graphite nanoplatelets to settle, part of the ultrasonication medium was decanted and the rest of the sample dried in a convection oven at 60 °C for 12 hours.

6.1.3 Characterization

6.1.3.1 Surface area and density

The Brunauer-Emmett-Teller (BET) specific surface area and apparent density of the exfoliated graphite was used to gauge the exfoliation efficiency of the two expandable graphites. The specific surface areas of the exfoliated graphite were determined using a Micrometrics TriStar BET in liquid N_2 at 77 K. Apparent density of the exfoliated graphite was determined using a graduated cylinder and an accurate balance. True densities of the various graphite forms were determined on a Micrometrics AccuPyc II 1340 helium gas pycnometer.

6.1.3.2 Morphology and particle size distribution (PSD)

To observe the extent of delamination into graphite nanoplatelets the morphologies and particle size distributions of the graphite were studied before and after ultrasonication. Graphite particle morphologies were studied using a JEOL JSM 5800LV scanning electron

microscope and an ultrahigh resolution field emission scanning electron microscope (HR FEGSEM Zeiss Ultra Plus 55) with an InLens detector. On the JEOL JSM 5800LV instrument an acceleration voltage of 20 kV was used whereas on the HR FEGSEM Zeiss Ultra Plus 55 instrument an acceleration voltage of 1 kV was used to ensure maximum resolution of surface detail. No electro-conductive coating was applied on the graphite particles. The graphite particle size distributions were determined with a MastersizerHydrosizer 3000 (Malvern Instruments, Malvern, UK). The GNPs were first dispersed in distilled water with Tween 20 and utrasonicated briefly for 5 minutes, before being fed into the instrument.

6.1.3.3 Structure and ordering

The crystal structure and ordering in the various graphite forms was observed using X-ray diffraction studies and Raman spectroscopy. X-ray diffraction (XRD) patterns of the various graphites were recorded using a Bruker D8 Advance powder diffractometer fitted with a Lynx eye detector. Measurements were performed in the 2θ range 5-90 ° with a 0.04 ° step size and counting time of 0.2 s. Raman spectra were recorded using a HORIBA Scientific, Jobin Yvon Technology T6400 series II triple spectrometer system. A 514.5 nm laser line of coherent Innnova®70 Ar^+ laser in the wavelength range 500-3500 cm^{-1} was used. The resolution of the laser was 2 cm^{-1}. An Olympus microscope attachment to the instrument recorded the spectra in back scattering configuration with a long working distance 100× objective. The detector used was liquid nitrogen cooled CCD detector and the laser power on the sample was 10 mW. An accumulation time of 120 s was utilized.

6.1.4 Preferred synthesis protocol

After the preliminary work the expandable graphite ES250 B5 was selected for subsequent work. Microwave exfoliation using the conditions stated in section 6.1.2 was adopted. After evaluation of the ultrasonication media, isopropanol was selected as the ultrasonication media for subsequent work. In the subsequent work, the graphite nanoplatelets were either used as dispersions as obtained in the ultrasonication media or as a dry, fluffy, highly friable graphite nanoplatelet aerogel. To obtain the aerogel, the colloidal dispersion of graphite nanoplatelets in the isopropanol was fed into a rotary evaporator (Büchi Rotavapor R-114) set at 100 °C.

The isopropanol was evaporated until a paste-like consistency was obtained. The paste was then dried for 12 h in a convection oven at set at 60 °C.

6.2 Rotomoulded polymer/graphite nanocomposites

6.2.1 Materials

Hexene comonomer-based linear low density polyethylene (LLDPE) rotomolding powder was supplied by Sasol Polymers (Grade HR 486: MFI 3.5 g (10 min)$^{-1}$ (190 °C (2.16 kg)$^{-1}$); density 0.939 g cm^{-3}; d_{90} particle size < 600 μm). Poly(ethylene-co-vinyl acetate) (EVA) was supplied by Affirm Marketing Services (Grade: AMS 3042: Vinyl Acetate content 18 %, MFI 1.7 g (10 min)$^{-1}$ (190 °C (2.16 kg)$^{-1}$); density 0.939 g cm^{-3}; d_{90} < 600 μm). Debco Technologies supplied the silicone-based mould release agent RM20. The dry, fluffy, highly friable graphite nanoplatelet aerogel was obtained from expandable graphite ES 250 B5 as described in the previous section 6.1.4.

6.2.2 Rotational moulding sample preparation

The mould was a stainless steel rectangular cuboid with interior dimensions of 200 × 150 × 100 mm. The rotomoulding machine was a modified Thermopower convection oven fitted with a biaxial mould rotating mechanism. Charge weights were determined following the protocol suggested by Crawford and Throne (2002). The charge volume was adjusted to ensure that all mouldings had the same wall thickness of 3 mm. For the neat polymer this amounted to 352 g. Moulding was conducted for 45 min at an oven temperature of 300 °C and a rotation speed of 20 rpm. This setting was chosen based on trials conducted at five different oven times, i.e. 30, 35, 40, 45 and 60 min. The cooling protocol was 20 minutes in the opened oven followed by 20 minutes in ambient air.

Dry-blended LLDPE/graphite nanocomposites were obtained by mixing the LLDPE powder and the graphite nanoplatelets in a 750 W grinder-mixer for 10 minutes. The graphite content was varied up to 2 wt.%. Dry-blended EVA/graphite nanocomposites were obtained in a similar manner except that the mixing time was reduced to 5 minutes to avoid melting of the polymer. Dry-blended LLDPE/expandable graphite composites for comparative fire tests

were prepared by mixing the LLDPE powder and expandable graphite ES 170 300A in the grinder mixer for 5 min.

Melt-compounded LLDPE-graphite nanocomposites were obtained as follows. First the LLDPE powder and the graphite nanoplatelets were mixed in the 750 W grinder-mixer for 10 minutes. These compositions were then melt compounded on a TX28P laboratory scale co-rotating 28 mm twin crew extruder with an L/D ratio of 18. The temperature profile, from hopper to die, was 140 °C/160 °C/180 °C/200 °C. The extruded strands were water-cooled, air-dried, and granulated into pellets. They were then milled into rotomoulding powder (< 600 μm) using a Pallmann 300 pulverizer.

Bilayer moulding was done by double dumping as follows. Two charges were prepared on the basis of a normally 1 mm thick exterior layer containing graphite and a 2 mm interior layer of LLDPE (231 g). A modified stainless steel mould was used for the double dumping experiments. The mould had the same interior dimensions but it was also fitted with a 28 mm diameter vent pipe that extended 50 mm into the mould cavity and 80 mm above the mould lid. The vent pipe had a screw cap that made double dumping possible. To produce a bilayer moulding, the mould lid was opened and charged with the shot for the outer layer. This layer was then rotomoulded for 30 min at 300 °C at a rotation speed of 20 rpm. After the first moulding cycle was completed, the second charge was fed via a funnel after removing the screw cap. Immediately after adding the second charge, the mould was rotated at 40 rpm to facilitate even distribution of the LLPDE powder. The second layer was then moulded for 30 min at 300 °C at a rotation speed of 20 rpm. Bilayer composites with an EVA outer layer were moulded in the same manner except that the moulding time was reduced to 15 min.

6.2.3 Characterization of the rotomoulded parts

6.2.3.1 Part density

The level of melt densification of the rotomoulded parts was quantified by measuring the density of 10 × 10 × 3 mm samples on the Micrometrics AccuPyc II 1340 helium gas pycnometer.

6.2.3.2 Morphology

The ultrahigh resolution field emission scanning electron microscope (HR FEGSEM Zeiss Ultra Plus 55) with an InLens detector was used observe fracture surfaces of the rotomoulded polyethylene cross sections obtained after immersion of the samples in liquid nitrogen at an acceleration voltage of 1 kV to ensure maximum resolution of surface detail. These samples were coated with carbon before viewing.

Cross sections of the rotomoulded nanocomposites were prepared using cryo-ultramicrotomy performed with a Leica EM UC6. Slices were cut at –80 °C using a glass knife at a speed 2.5 mm s^{-1}. Sections, with a nominal thickness set at 200 ± 10 nm, were mounted on a glass slide. They were observed under polarized light using a transmitted light microscope (Tokyo, Japan) with a Nikon DXM1200F digital camera (Tokyo, Japan).

6.2.3.3 Thermo-oxidative degradation

Fourier transform infrared spectroscopy (FTIR) was used to track thermo-oxidative degradation as a function of oven time. Spectra (based on the average of 32 scans) of the interior moulded surfaces were recorded with a Perkin Elmer FTIR fitted with an ATR attachment.

6.2.3.4 Surface resistivity

Composite surface resistivity was measured with a Vermason Analogue Surface Resistance Meter and the TB-7549 concentric ring probe. These measurements allowed categorization of the samples into conductive, static dissipative (antistatic) or insulative according to test method IEC 61340-2-3 (Commission, 2000).

6.2.3.5 Impact testing

Sheet specimens, measuring at least 70 × 70 × 3.0 mm, were cut from the moulding. Falling weight impact tests were performed at 25 °C on the rotomoulded composites according to test standard ASTM D 5628 (ASTM, 2010) using sample geometry FB. A weight of 2.5 kg was used for all the samples with the exception of the neat LLDPE moulded for 60 min which required a 5 kg weight. The sheet specimens were struck on the exterior side by the 25 mm

diameter tup. Failure was defined as the formation of a crack through which water can flow. At least 5 specimens were initially used to determine the approximate height at which a failure was likely to happen. Thereafter tests were conducted on ten specimens. The Bruceton up-and-down method was used to evaluate the mean failure energy normalised with respect to the average sample thickness.

6.2.3.6 Tensile tests

ASTM D638-08 Type IV dog bone specimens with a thickness of about 3.0 mm and gauge length of 25 mm were cut out of the mouldings for tensile tests. The tensile tests were conducted according to ASTM D 638-08 at 23 °C. A Lloyd Instruments LRX Plus machine fitted with a 5 kN load cell was used and the extension rate was set at 50 mm min^{-1}. At least six specimens were tested for each sample.

6.2.3.7 Fire testing

A Fire Testing Technology Dual Cone Calorimeter was utilized to perform fire tests on the rotomoulded nanocomposites according to the ISO 5660-1 standard. The specimens used had lateral dimensions of 100 × 100 mm and a thickness of 3.0 mm. The sheets were wrapped in aluminium foil and exposed horizontally to an external heat flux of 35 kW m^{-2}. A grid was placed on top of the sample to prevent the sample from expanding and touching the spark igniter. The outer layer was exposed to the radiant heat flux. At least two tests were conducted for each sample and average results are reported.

6.3 Phase change material/graphite nanocomposites

6.3.1 Materials

Stearyl alcohol (designated C_{18}-OH thereafter) was supplied by Merck. Stearic acid (designated C_{18}-Acid thereafter) was obtained from Pan Century Oleochemical SND BHD. Graphite nanoplatelets (GNPs) dispersions in isopropanol were obtained as described in section 6.1.4 from expandable graphite ES 250 B5 (exfoliation onset temperature 220°C) supplied by Qingdao Kropfmuehl Graphite (China).

6.3.2 Sample preparation

6.3.2.1 C_{18}-OH/C_{18}-Acid mixtures

Mixtures of C_{18}-OH and C_{18}-Acid with mole fractions ranging from 0.1 to 0.9 C_{18}-OH were prepared on the basis of 5 g C_{18}-OH by accurately weighing out the relevant masses into a glass beaker. The mixtures were melted on a hot plate controlled to a maximum temperature of 100 °C and simultaneously stirred with a magnetic stirrer for 5 min after melting. The mixtures were then allowed to cool and solidify before further analysis.

6.3.2.2 Phase change material/graphite nanoplatelets nanocomposites

A composition of mixtures of stearyl alcohol and stearic acid with single melting and crystallization peaks on its DSC data was selected as the phase change material (PCM). The mixture of C_{18}-OH/C_{18}-Acid with this composition was melted on a hot plate controlled to a maximum temperature of 100 °C and simultaneously stirred with a magnetic stirrer for 5 min after melting. The GNPs dispersion in isopropanol was briefly utrasonicated for 5 min, before subsequently pouring it into the molten mixture of C_{18}-OH/C_{18}-Acid in a fan extracted fume hood. The mixture was mildly stirred as the isopropanol evaporated, until it became a thick paste. The isopropanol in the PCM/GNPs nanocomposites was further evaporated in a convection oven for 12 hours at 60 °C. The PCM/GNPs nanocomposites were then left to cool and solidify at ambient conditions before further analysis. The PCM/GNPs nanocomposites were prepared at compositions ranging from 0 to 10 wt. % GNPs.

6.3.3 Characterization

6.3.3.1 Morphology

Fracture surfaces of the PCM/GNPs nanocomposites sections were obtained in liquid nitrogen and observed on the ultrahigh resolution field emission scanning electron microscope (HR FEGSEM Zeiss Ultra Plus 55) with an InLens detector at an acceleration voltage of 1 kV to ensure maximum resolution of surface detail. Optical microscopy images of pristine stearyl alcohol, stearic acid and their mixtures were obtained by placing a small amount of the sample onto the optical microscope stage and heating the sample using the Linkam CSS 450 platform and LinkSys32 software. Once molten, the sample was cooled at a rate of 0.5°C min^{-1} and images of the crystal structures that formed were captured using a Leica DFC420 digital camera.

6.3.3.2 Melting and crystallization characteristics

Melting and crystallization temperatures and enthalpy measurements of the mixtures of C_{18}-OH and C_{18}-Acid were performed on a Perkin Elmer DSC 4000 instrument. Temperature and enthalpy calibration measurements were done using n-octadecane (melting temperature 27.24 °C) and indium (melting temperature 156 °C) using a heating rate of 0.5 °C min^{-1} in nitrogen flowing at 50 mL min^{-1}. Baseline measurements were done with the reference crucible closed, with sample crucible empty with an open lid from 30 °C to 70 °C and a heating rate of 0.5 °C min^{-1}, with an isothermal segment at 30 °C and 70 °C in nitrogen flowing at 50 mL min^{-1}. Sample measurements were done in aluminium crucibles with sealed lids from 30 °C to 70 °C at 0.5 °C min^{-1} with an isothermal step at 30 °C and 70 °C in nitrogen flowing at 50 mL min^{-1}. Sample masses were maintained at ca. 5 mg throughout. This DSC calibration and measurement protocol for PCMs was based on the inter-comparative work which was done to ensure the reliability of thermophysical data (Lazaro et al., 2013). DSC curves with overlapping peaks were deconvoluted through the MagicPlot programme by using Lorentzian peaks.

6.3.3.3 Detection of the esterification reaction

Fourier Transform Infrared Spectroscopy (FTIR) was used to observe the possibility of sulphuric acid (residue sulphuric acid from the oxidative intercalation process) catalysed esterification of the C_{18}-OH/C_{18}-Acid PCM with GNPs at the temperatures used to prepare the PCM/GNPs nanocomposites. Spectra (based on the average of 32 scans) PCM/GNPs nanocomposites were recorded with a Perkin Elmer FTIR fitted with an ATR attachment.

6.3.3.4 Thermal conductivity: Molten state-70 °C

Thermal conductivity of the PCM/GNPs nanocomposites was measured using a Linseis THB100 Transient Hot bridge instrument. Samples were melted in 100 mL glass beakers on a hot plate at 100 °C and immersed in a temperature controlled water bath. Temperature was maintained at 70 °C. The THB6K/MFR sensor (42x22 mm) with a metal frame was completely immersed in the molten sample. Five measurements were obtained for each sample using a measurement time and current of 20 s and 80 mA, respectively.

6.3.3.5 Thermal conductivity: Solid state- 22 °C

PCM/GNPs nanocomposite samples were hot pressed into a 100 x100 x 3 mm sheets at a temperature of 60 °C and pressure of 20 MPa which were then cut into 100 x 50 x 3 mm pieces. Thermal conductivity was measured at 22 °C by sandwiching the THB6K sensor (42 x 22 mm) of the Linseis THB100 Transient Hot bridge instrument with two sample pieces. Three measurements were obtained for each sample using a measurement time and current of 25 s and 80 mA, respectively.

6.3.3.6 Thermal stability of the PCM/GNPs nanocomposites

The stability of the PCM/GNPs nanocomposites was evaluated through thermal cycling and settling tests. Thermal cycling of the PCM/GNPs nanocomposites was performed on a Perkin Elmer DSC 4000 instrument in air at a heating and cooling rate 10 °C min^{-1} from 30 °C to 80 °C for 100 melting and crystallization cycles. The sample size was ca. 5 mg in sealed aluminium pans. In the settling tests, the same mass of PCM/GNPs nanocomposites with compositions 0, 2.5, 5, and 10 wt. % was melted at 80 °C in glass vials. These were then placed in a preheated oven at 80 °C and observed for up to two months.

Chapter 7 Results and discussion: Synthesis of graphite nanoplatelets

7.1 Synthesis of graphite nanoplatelets

7.1.1 Expandable graphite properties

The particle characteristics of the two types of expandable graphite and their exfoliated forms used in this study are given in Table 7-1. The d_{50} particle sizes of both expandable graphites were above the threshold particle size (200 μm) for exfoliation as determined by Murdie et al. (1985). However, with a d_{50} particle size of 381 μm, the expandable graphite ES250 B5 was smaller than the expandable graphite ES170 300A by more than 25%. SEM micrographs of the expandable graphite flakes are shown in Figure 7-1. The densities of the two expandable graphite (Table 7-1) are slightly lower than that of pristine crystalline graphite (2.26 g cm^{-3}, Sengupta et al. (2011), conceivably due to the intercalation process which increased the graphite interlayer spacing. The BET surface area of expandable graphite ES250 B5 shown in Table 7-1 was marginally higher due to its smaller particle size, compared to the expandable graphite ES170 300A.

Table 7-1 Expandable and exfoliated graphite properties.

Graphite		Exfoliation	Particle size , μm			BET surface	Density
Type	**Form**	**method**	**d_{10}**	**d_{50}**	**d_{90}**	**Area m^2g^{-3}**	**g cm^{-3}**
ES170 300A	Expandable	-	322	521	811	2.09	2.23 ± 0.00
	Exfoliated	Furnace		-		14.8 ± 0.1	0.74 ± 0.01†
	Exfoliated	Microwave		-		37.9 ±2.2	0.011 ± 0.001†
ES250 B5	Expandable	-	144	381	642	2.40	2.08 ± 0.00
	Exfoliated	Furnace		-		22.4 ± 2.8	0.64 ± 0.03†
	Exfoliated	Microwave		-		40.7 ± 2.6	0.009 ± 0.001†

†Apparent density of the exfoliated graphite.

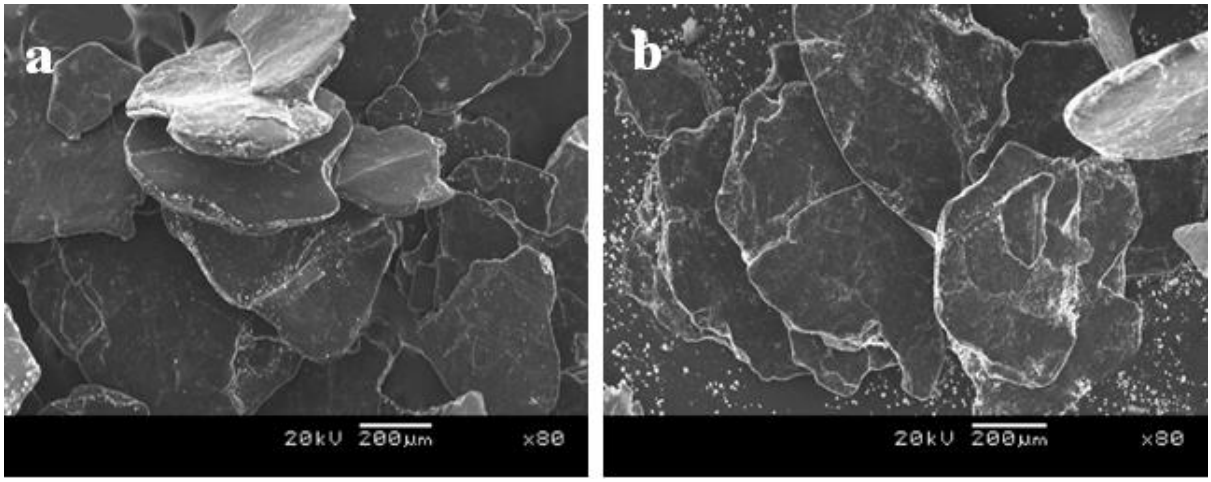

Figure 7-1 SEM pictures of expandable graphite (a) ES 250 B5 and (b) ES170 300A.

7.1.2 Exfoliation of graphite

Table 7-1 also shows the properties of the graphite in its exfoliated form. Based on the BET surface areas and apparent densities in Table 7-1, expandable graphite ES250 B5 exfoliates more efficiently than expandable graphite ES170 300A. The efficiency of microwave exfoliation compared to furnace exfoliation is also apparent in Table 7-1. The BET surface areas obtained using microwave exfoliation were higher compared to those found in the literature (Furdin, 1998, Chen et al., 2004, Kim et al., 2010a). A parameter used to evaluate the exfoliation efficiency is the expansion ratio, which is the reciprocal of the apparent density (Chen et al., 2003). It follows from the apparent densities of the exfoliated graphites in Table 7-1 that microwave exfoliated ES250 B5 and ES170 300 A had expansion ratios of 112 and 89 $cm^3 g^{-1}$, respectively, higher than the furnace expanded graphite.

The expandable graphite ES250 B5 was selected for the subsequent work due to its excellent exfoliation characteristics. Figure 7-2 shows an FESEM micrograph of the microwave exfoliated expandable graphite ES250 B5 which exhibits a worm like, accordion structure composed of stacks of graphene held together along the c-axis.

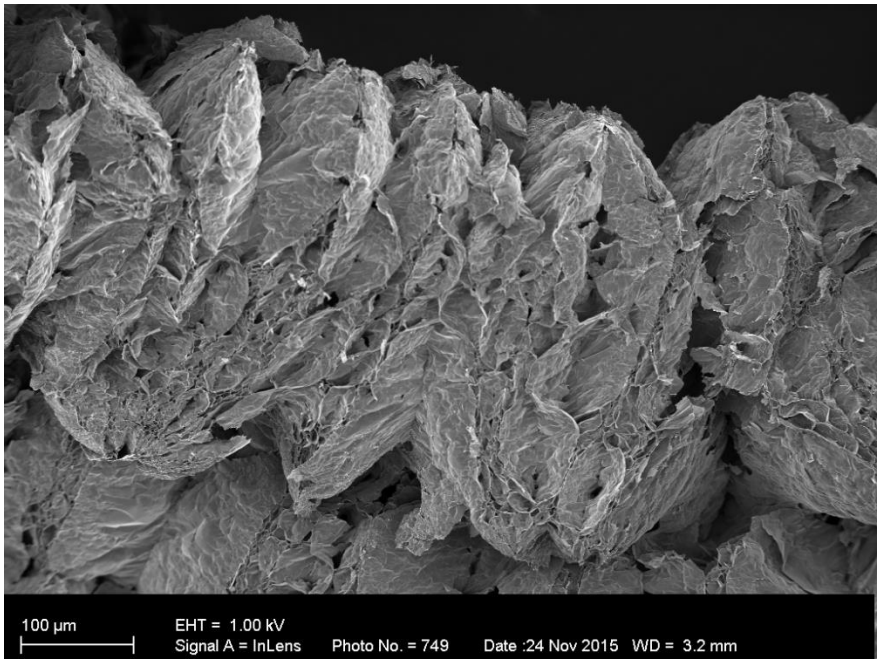

Figure 7-2 Microwave exfoliated graphite ES250 B5.

7.1.3 Graphite nanoplatelets delamination from exfoliated graphite

7.1.3.1 Morphology

Figures 7-3 to 7-5 show the FESEM micrographs of graphite nanoplatelets (GNPs) with crumpled morphology obtained from ultrasonication assisted liquid phase exfoliation with isopropanol, 1-hexanol or water with the surfactant Tween 20. GNPs from the water/SDS medium were excluded from the SEM analysis and further study due to the presence of exfoliated graphite particles (with the worm like structure) on top of the colloidal dispersions obtained after ultrasonication. This showed the inability of the water/SDS medium to efficiently delaminate the exfoliated graphite into graphite nanoplatelets. The FESEM micrographs in Figures 7-3 to 7-5 show that the thicknesses of the platelets obtained from all the ultrasonication media were apparently in the nano range, although lateral dimensions were in the micrometre range. The FESEM micrographs in Figure 7-4 for the GNPs utrasonicated in 1-hexanol appear to have some residue on their surface, in comparison to the GNPs produced in isopropanol and water/Tween 20 (Figures 7-3 and 7-5). It is apparent that the 1-hexanol cannot be easily removed from the GNPs. GNPs obtained from the ultrasonication media water/Tween 20 appeared to be mostly lying flat on top of each other (Appendix A), contrary to those obtained from isopropanol and 1-hexanol.

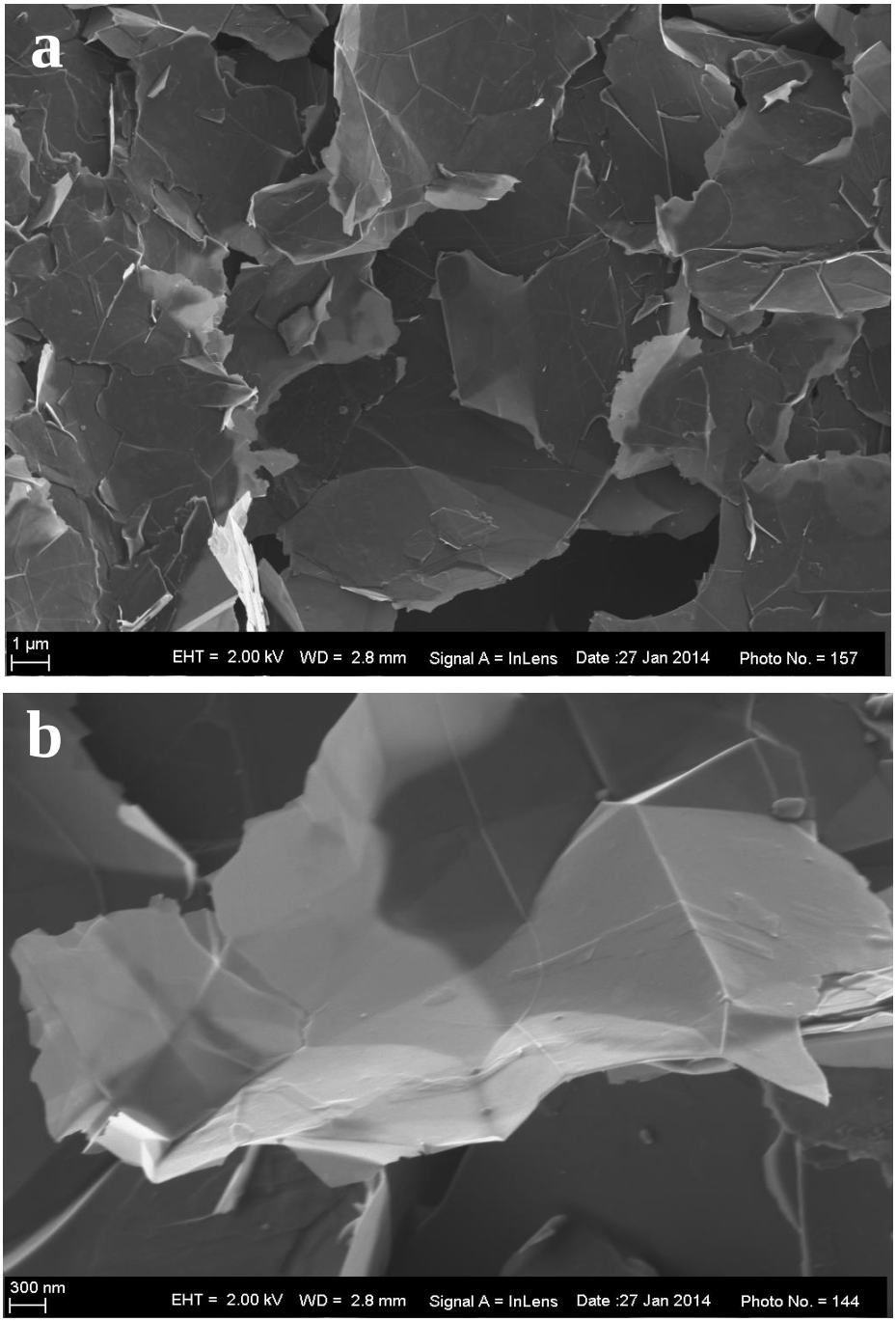

Figure 7-3 FESEM of graphite nanoplatelets obtained by ultrasonication-assisted liquid phase exfoliation of expanded graphite (Grade ES250 B5) in isopropanol. (a) Low magnification and (b) high magnification.

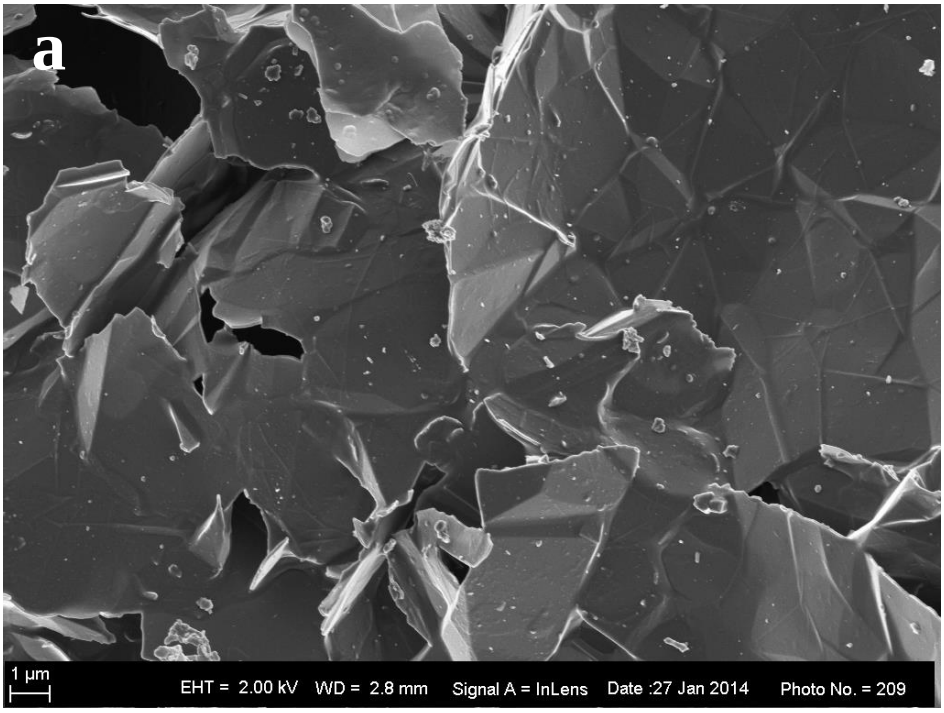

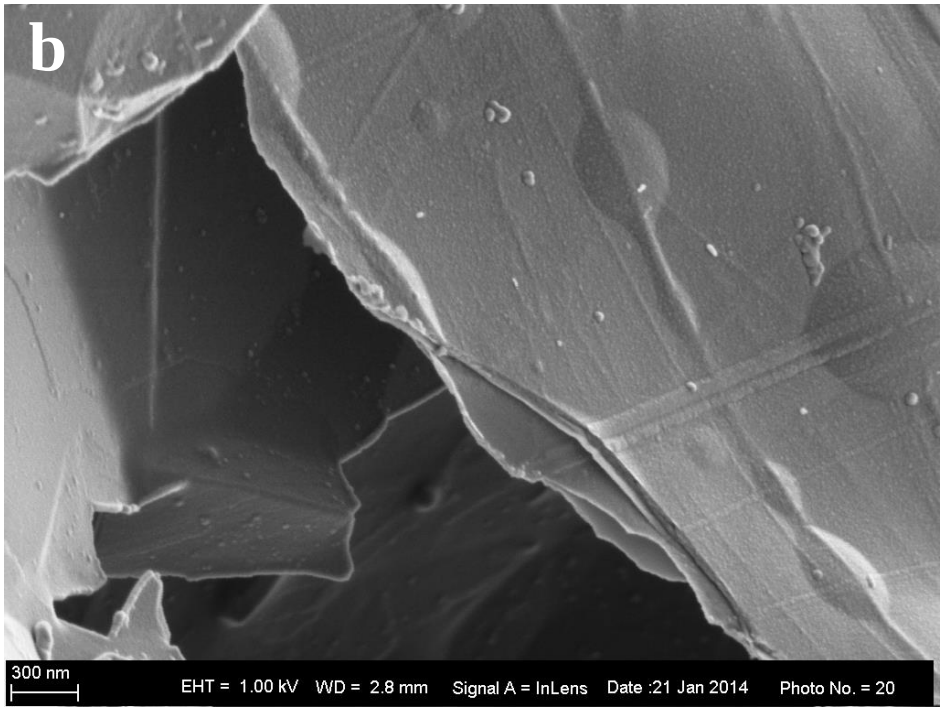

Figure 7-4 FESEM of graphite nanoplatelets obtained by ultrasonication-assisted liquid phase exfoliation of expanded graphite (Grade ES250 B5) in 1-hexanol. (a) Low magnification and (b) high magnification.

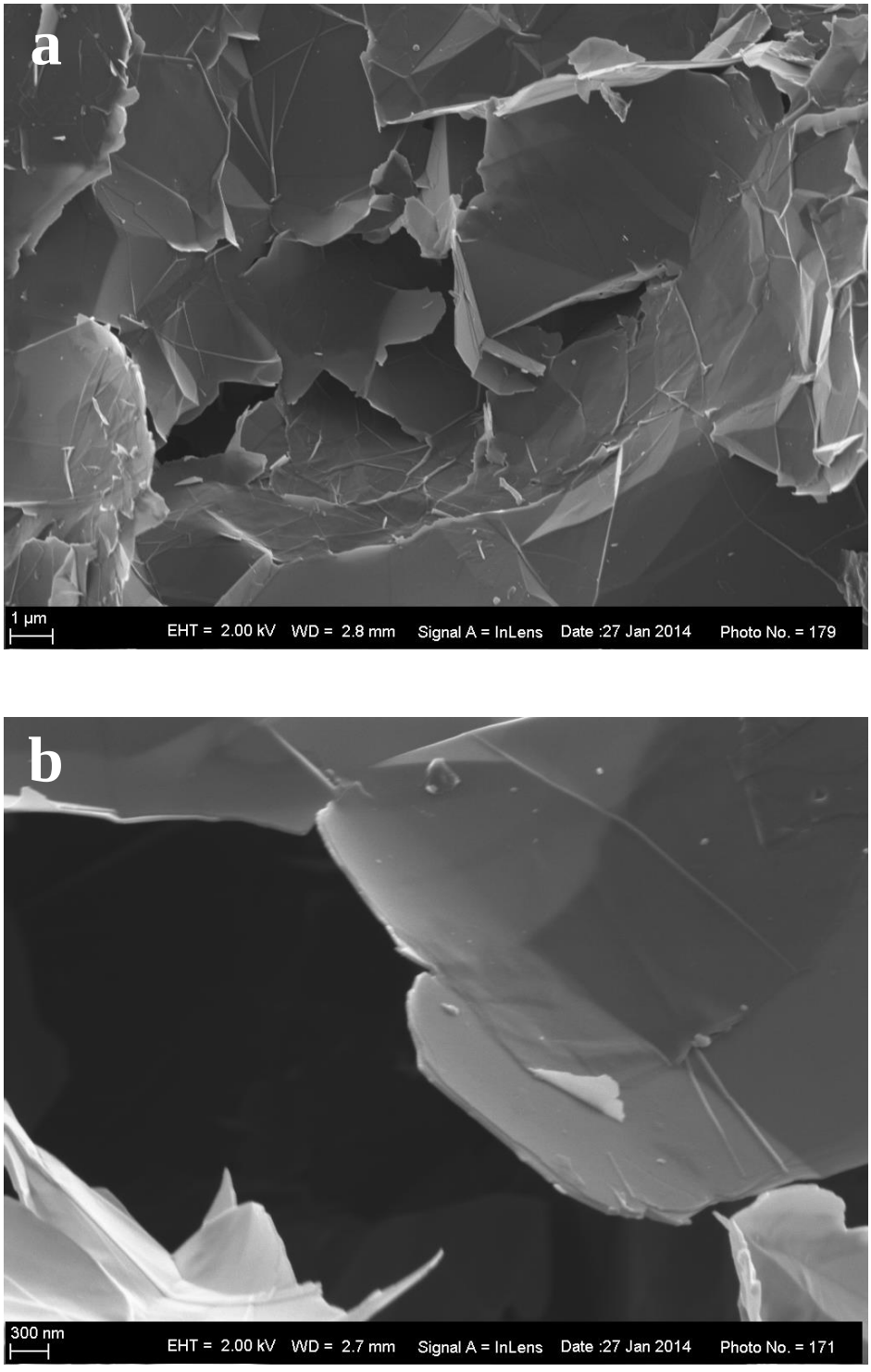

Figure 7-5 FESEM of graphite nanoplatelets obtained by ultrasonication-assisted liquid phase exfoliation of expanded graphite (Grade ES250 B5) in water with the surfactant Tween 20. (a) Low magnification and (b) high magnification.

7.1.3.2 PSD and surface area

Figure 7-6 shows the particle size distribution of the graphite nanoplatelets obtained from using isopropanol, 1-hexanol and water/Tween 20 as ultrasonication media compared to that of the initial expandable graphite ES250 B5. Table 7-2 lists the median particle sizes. Particle size analysis (Table 7-2) showed that at an average of 14 ± 1 μm, there was negligible difference between the d_{50} particle sizes of the obtained nanoplatelets. However, this was almost 30 times smaller than the precursor expandable graphite flakes. Ultrasonication is known to significantly reduce the particle size proportionally with the ultrasonication time until a critical size is reached (Chen et al., 2004). The d_{90} particle size of the obtained GNPs was consistent with SEM observations at 26-46 μm. Amongst the ultrasonication media considered, isopropanol was selected for subsequent work and used to delaminate microwave exfoliated expandable graphite ES250 B5 into graphite nanoplatelets.

The BET surface area of the GNP aerogel, after solvent removal, was 12 $m^2 g^{-1}$. This value is considerably lower than that for the exfoliated graphite shown in Table 7-1 (40.7 $m^2 g^{-1}$). The discrepancy is attributed to re-agglomeration of GNPs during solvent removal.

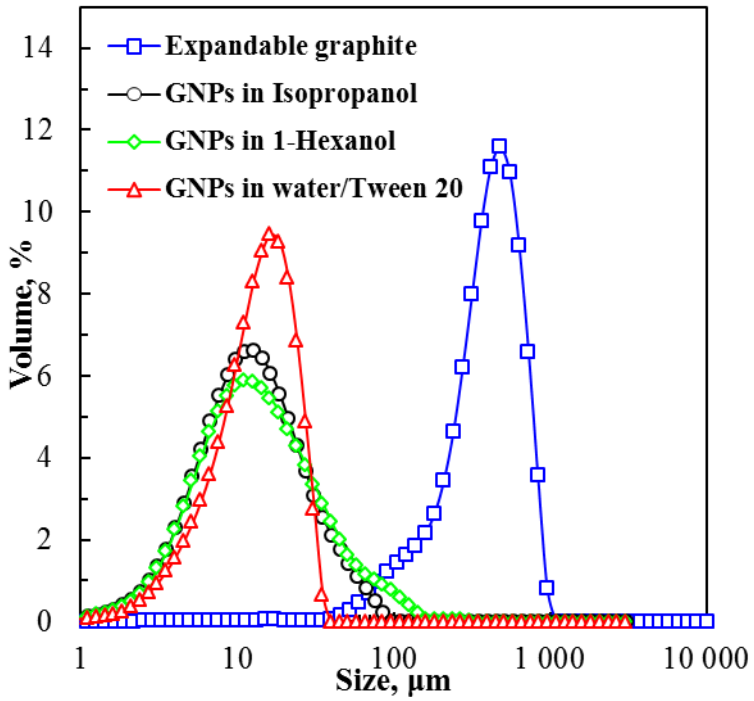

Figure 7-6 Particle size distribution of graphite nanoplatelets obtained from expandable graphite ES 250 B5 in isopropanol, 1-hexanol, and water with the surfactant Tween 20.

Table 7-2 Median particle sizes of graphite nanoplatelets obtained in various sonication media.

Graphite form	Ultrasonication medium	Particle size , µm		
		d_{10}	d_{50}	d_{90}
Expandable	-	144	381	642
Sonicated	Isopropanol	5	13	36
Sonicated	1-Hexanol	5	14	46
Sonicated	Water/Tween 20	6	15	26

7.1.3.3 Raman spectra, XRD and density

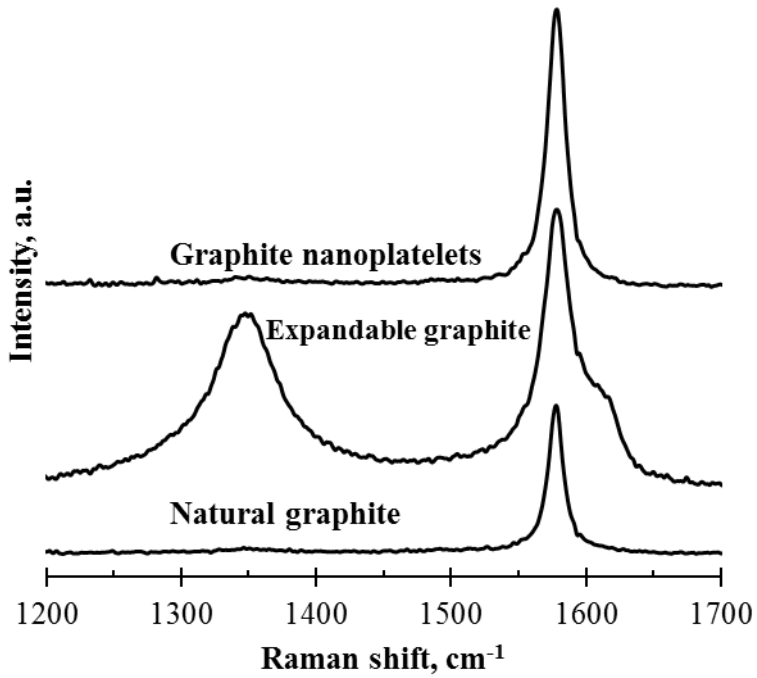

Figure 7-7 Raman spectra of the natural graphite, expandable graphite ES 250 B5 and the graphite nano platelets (GNPs) obtained from expandable graphite ES 250 B5.

The Raman spectrum of Figure 7-7 confirms the graphitic nature of the graphite nanoplatelets. The ratio of the peak intensities of the D (1350 cm^{-1}) to that of the G band (1582 cm^{-1}) (I_D/I_G) is a measure of imperfection in graphitic materials (Pimenta et al., 2007). The I_D/I_G ratios for the natural graphite, ES250 B5 and the graphite nanoplatelets synthesized

presently are given in Table 7-3. Relatively, the graphite nanoplatelets had the lowest (I_D/I_G) ratio. The measured density of the graphite nanoplatelets (2.26 g m^{-3}) was also is comparable to that of pure graphite.

Table 7-3 Raman (I_D/I_G) ratios and XRD *d*-spacing values of reference natural graphite, expandable graphite ES250 B5 and graphite nanoplatelets obtained from expandable graphite ES250 B5.

Graphite sample		Raman	XRD
Type	**Form**	(I_D/I_G)	***d* nm**
Natural		0.18	0.335
ES250 B5	Expandable	0.72	0.346*
			0.337†
	Nanoplatelets	0.15	0.337

† *d* spacing due to graphite peak,

**d* due to intercalation

Figure 7-8 shows XRD diffraction patterns of the expandable graphite ES250 B5 and the graphite nanoplatelets obtained from this graphite. These are compared to that of natural Zimbabwean flake graphite. The *d*-spacings in Table 7-3 were evaluated from the 2θ positions of the main peaks in the diffractograms using Bragg's equation:

$$n\lambda = 2d\sin\theta \qquad \textbf{(7-1)}$$

where θ is the diffraction angle, λ is the wavelength of the X-ray radiation used and n is an integer. The *d*-spacing of natural graphite was 0.335 nm. Expandable graphite ES 250 B5 exhibited two *d*-spacings at 2θ positions of 30.01 ° and 30.79 °. The peak position at 2θ 30.79 ° appears as a shoulder to the main peak at 30.01 ° and its *d*-spacing of 0.337 corresponds to that of natural graphite. The main peak which occurred at the 2θ position 30.01 ° had an increased *d*-spacing compared to that of graphite, showing evidence of intercalation. The fact that this peak was overlapping with that of pristine graphite shows that the expandable graphite was a high stage compound (Inagaki, 1966, Nakajima et al., 1988). The graphite nanoplatelets had a *d*-spacing similar to that of natural graphite

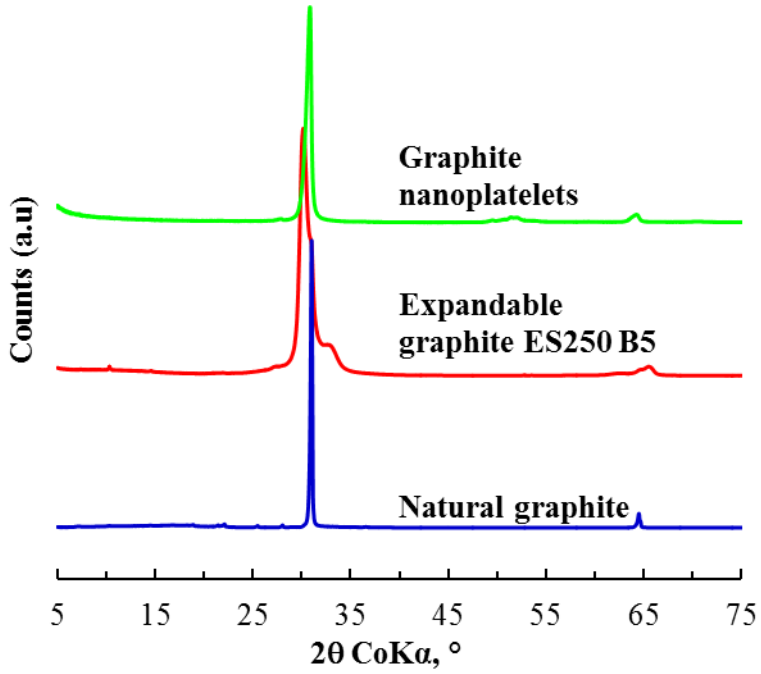

Figure 7-8 XRD patterns of the natural graphite, expandable graphite ES 250 B5 and the graphite nano platelets (GNPs) obtained from expandable graphite ES 250 B5.

7.2 Discussion

Furdin (1998) proposed that during exfoliation of expandable graphite there were two competing processes. The first process is boiling or explosion of the intercalate within the graphite particle which leads to exfoliation. The opposing process is desorption of the intercalate by evaporating through the graphite edges. Based on this premise, it is plausible that larger graphite particles exfoliates more efficiently due to a lower rate of intercalate desorption. It was thus expected that the expandable graphite ES170 300A would exfoliate much more efficiently than the expandable graphite ES250 B5 due to its larger particle size (Table 7-1). This was however contrary to observations.

Previous thermo-mechanical analysis (TMA) of expandable graphites ES250 B5 and ES 170 300A showed exfoliation onset temperatures of about 225 and 300 °C, respectively (Focke et al., 2014). These results also showed a higher expansion ratio for the expandable graphite ES250 B5. It was speculated that the better exfoliation of the expandable graphite ES250 B5 was as a result of the evolution of more gases from this particular expandable graphite, although it was smaller in size. It must be emphasized that as these are commercial

expandable graphites, the actual nature of processing is unknown. Hence such crucial factors as the initial stage of the graphite intercalation compound formed and the nature of the washing steps which determines the amount of intercalate remaining in the expandable graphite might also influence the exfoliation characteristics. XRD results in section 7.1.3.3 show that the expandable graphite ES250 B5 was a higher stage compound.

Analysis of the FESEM micrographs and particle size distributions showed that all the ultrasonication media considered for delaminating graphite nanoplates attained more or less the same level of exfoliation (Table 7-2, Figures 7-3 to 7-6), except the water/SDS medium.

Considering isopropanol which was eventually selected for subsequent work, it has a surface tension (20.93 mN m^{-1} at 25 °C) (Table 6-1), far from the surface energy of graphite (40 mN m^{-1}). However, its vapour pressure at 25 °C is 6.02 kPa (Table 6-1), which is higher compared to that of the best ranked exfoliation media for graphite into graphene, cyclopentanone, which is 1.55 kPa (Table 6-1). This means acoustic cavitation is easily induced in isopropanol compared to cyclopentanone.

However, cyclopentanone has the most suitable solubility parameters for graphite exfoliation into graphene, compared to those of isopropanol, according to the work of Coleman's group (Hernandez et al., 2009).

Higher viscosity and surface tension liquids require higher ultrasonication intensity to cavitate, but produce stronger cavitation effects, whereas higher vapour pressure liquids easily cavitate but produce weaker cavitation effects. The viscosity of 1-hexanol (4.6 mPa s at 25 °C) is particularly higher compared to that of water and isopropanol (1.0 and 2.0 mPa s, respectively, at 20 and 25 °C) (Table 6-1). However, some residues were observed on the GNPs obtained by using 1-hexanol for ultrasonication. Out of all the ultrasonication media considered, water has the highest surface tension (Table 6-1). The water/Tween 20 medium was effective, except for the manner in which the GNPs oriented after solvent removal, which suggested GNPs synthesised in this medium had a propensity for agglomeration (Appendix A). Amongst all the ultrasonication media considered, isopropanol had the lowest boiling point, meaning it is easily removed (Lide, 2005). Therefore, isopropanol was the most favourable media.

The aspect ratio of the graphite platelets obtained from delaminating exfoliated graphite ES250 B5 was estimated by comparing the BET surface area of their aerogel (12 $m^2 g^{-1}$) to that expected for a graphene monolayer, i.e. 2700 $m^2 g^{-1}$ (Chen et al., 2004). From this comparison the average GNP consisted of 227 graphene sheets and thus a thickness of 76 nm. Using the d_{50} particle size of 13 μm obtained for these GNPs resulted in an average aspect ratio of about w/t = 171. This is a relatively high aspect ratio.

Raman spectroscopy and XRD confirmed the crystal structure and ordering of the graphite nanoplatelets showing that the facile method adopted yielded good quality graphite nanoplatelets.

Chapter 8 Results and Discussion: Rotomoulded antistatic and flame retardant polymer/graphite nanocomposites

8.1 Rotational moulding process conditions

Figure 8-1 shows the variation of impact properties and tensile strength with oven time. The tensile strength of the rotomoulded LLDPE increased almost linearly with increase in oven time up to 45 min but deteriorated thereafter. The impact resistance was not affected by oven time up to 40 min but it increased above this heat exposure time. Parts moulded for 30 min or less featured pin holes in their exterior surfaces and porosity in the wall cross sections. These defects were not observed for samples moulded at oven times of 45 min or higher (Figure 8-2). According to Table 8-1, the density of the rotomoulded LLDPE parts increased with oven time and reached a plateau value at 45 min. This was also the oven time at which the highest tensile strength was realized.

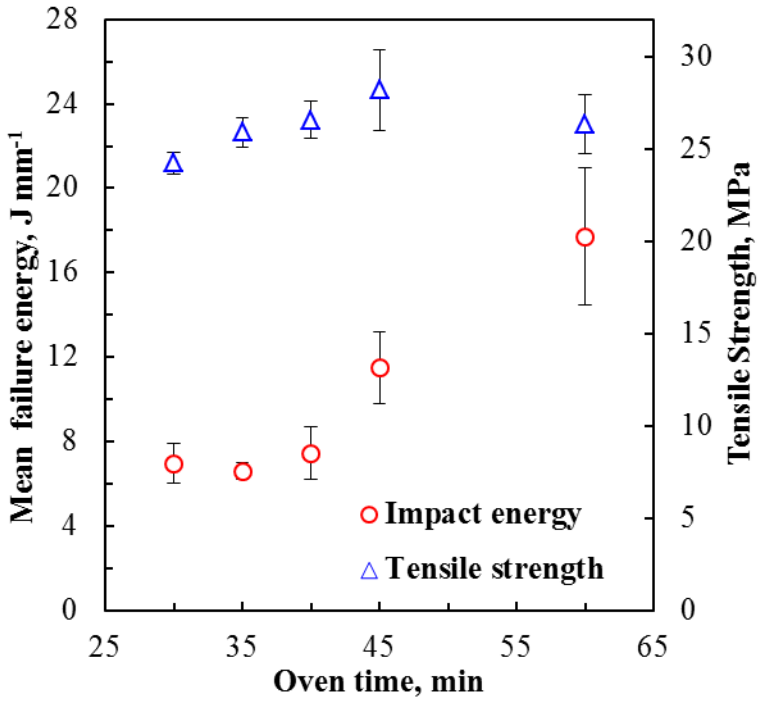

Figure 8-1 Effect of rotomoulding oven time on impact resistance (mean failure energy) and tensile strength.

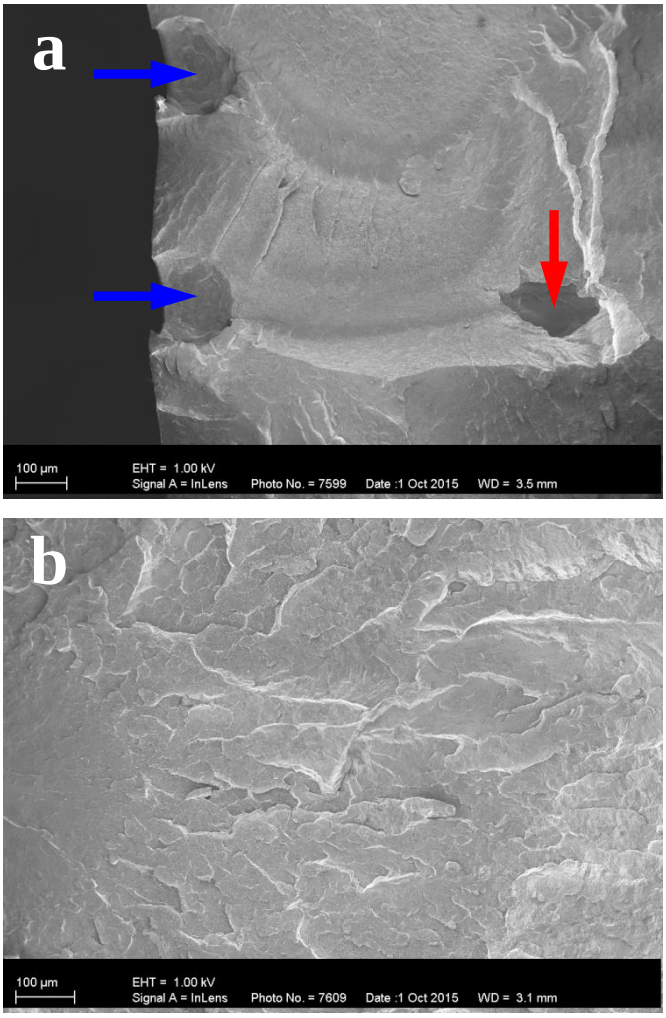

Figure 8-2 FESEM micrographs of cross-sections of (a) LLDPE rotomoulded at 30 min with pin holes on surface in contact with mould (blue arrows) and air bubbles (blue arrow) and (b) LLDPE rotomoulded at 45 min.

Table 8-1 Variation of LLDPE part density with rotomoulding oven time.

Oven time	**min**	30	35	40	45	60
Density	**g cm^{-3}**	0.918±0.005	0.923±0.004	0.929±0.001	0.932±0.001	0.933±0.006

The aesthetics of the parts moulded for 60 min were impaired as surface yellowing was evident. The discoloration probably arose from the sacrificial oxidation of the antioxidants to chromophoric quinones (Sharifi et al., 2012). Unlike parts moulded at lower temperatures, the FTIR spectra of the inner walls of these parts also featured a carbonyl peak at ca. 1717 cm^{-1} (Figure 8-3). This indicates that the onset of thermo-oxidative degradation had been reached.

During the early stages of oxidation the cross-linking reactions dominate in polyethylene (Oliveira et al., 1996). This effectively increases the molecular mass and provides an explanation for the continued increase in impact energy beyond 45 min. However, later on chain scission reactions will dominate and eventually catastrophic property loss will follow (Henwood et al., 2005).

Based on these observations, all further LLDPE-based mouldings were conducted using an oven time of 45 min.

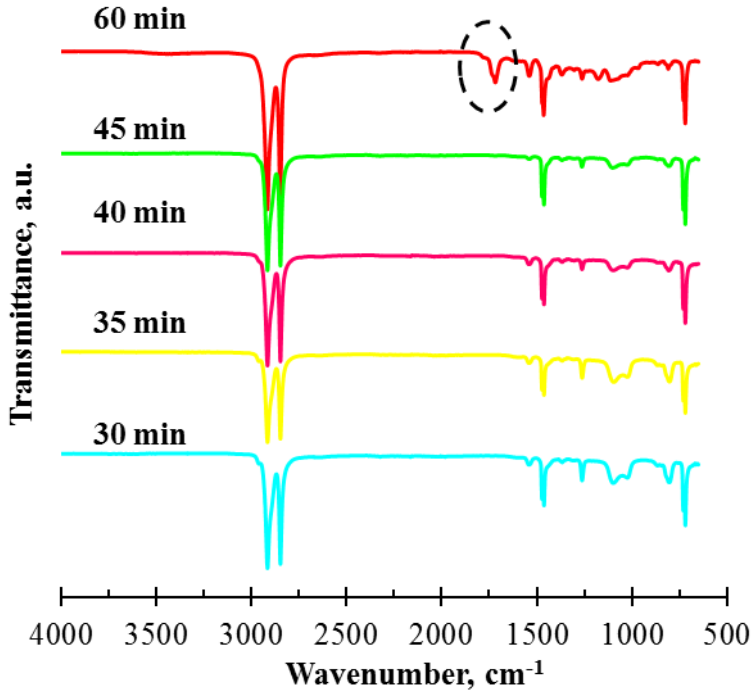

Figure 8-3 FTIR spectra of the interior of LLDPE rotomoulded at different oven times.

8.2 Rotomoulded nanocomposites properties

8.2.1 Morphology

8.2.1.1 FESEM

Figure 8-4 shows the FESEM micrographs of fractured nanocomposite sections at a graphite nanoplatelets content of 0.25 wt.%. Figure 8-4a revealed that, in the compounded samples, the nanoplatelets are uniformly dispersed and well separated. It is even difficult to discern them as the compounding process probably caused further crumpling into smaller particles.

In the sample obtained by dry blending random clusters of graphite nano platelets are clearly identified (Figure 8-4b). Apparently the platelets retained their flake-like shape and aggregated into larger domains. Away from these clusters, regions devoid of graphite particles are observed. Figure 8-5 is a FESEM micrograph of a fracture surface obtained from the cross-section of a dry blended nanocomposite containing 2.0 wt.% graphite nanoplatelets. This micrograph shows that the fracture surface is covered almost entirely with a tapestry of graphite nanoplatelets

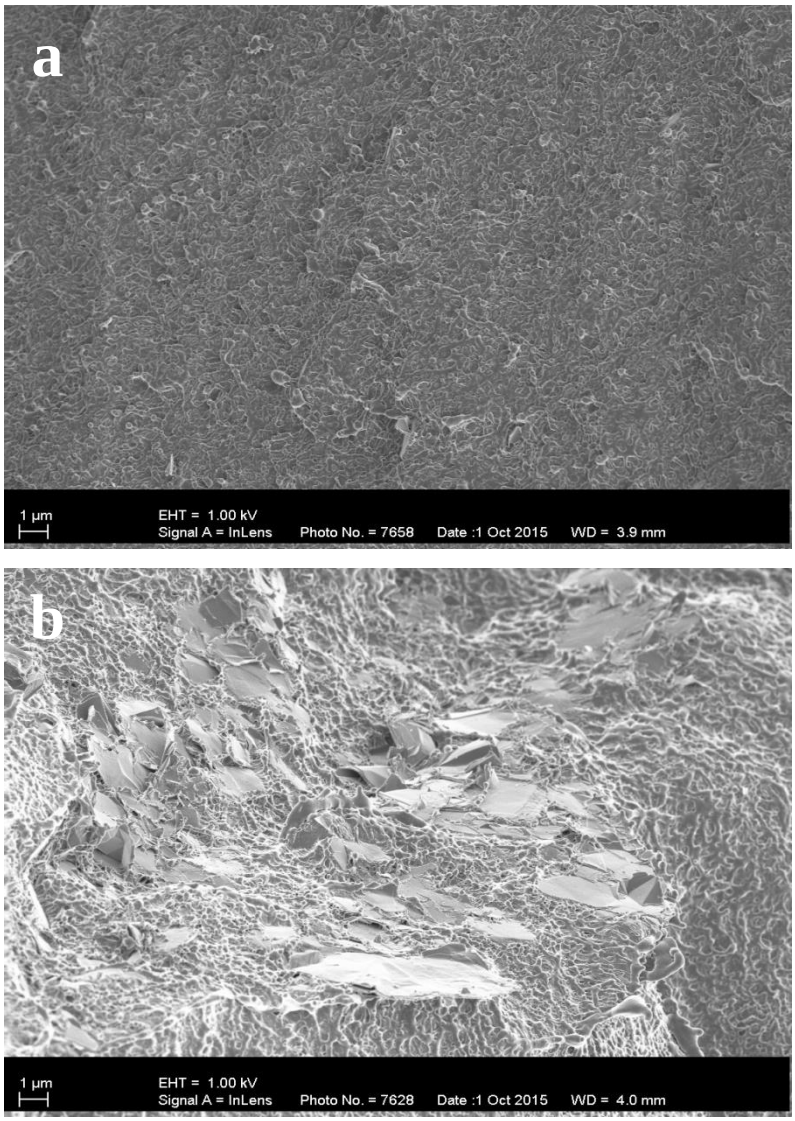

Figure 8-4 FESEM micrographs of rotomoulded LLDPE nanocomposites with 0.25 wt.% graphite nanoplatelets filler after (a) melt compounding and (b) dry blending.

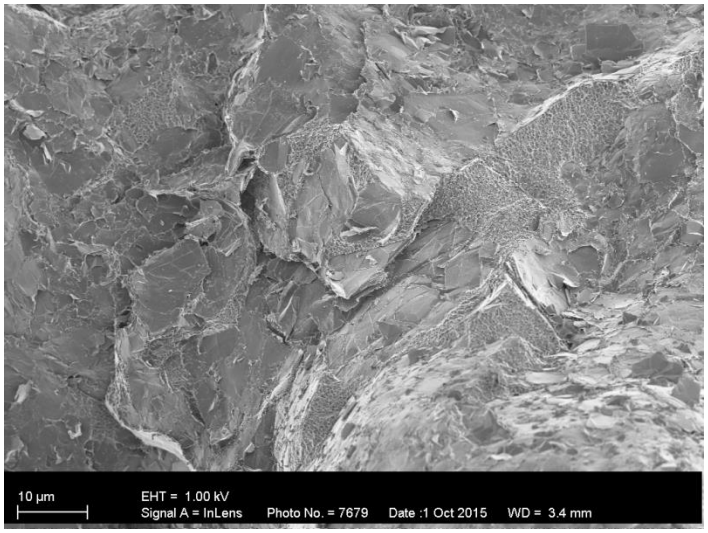

Figure 8-5 Scanning electron microscope image of a LLDPE fracture surface for a dry blended moulding containing 2.0 wt.% graphite nanoplatelets. The exposed surface is covered by a tapestry of graphite platelets.

8.2.1.1 Optical microscopy

Figure 8-6 shows an optical micrograph of part of a thin cross section of the rotomoulded nanocomposite wall. The dark fringes around large polyethylene domains are clearly visible. They are attributed to the presence of graphite platelets.

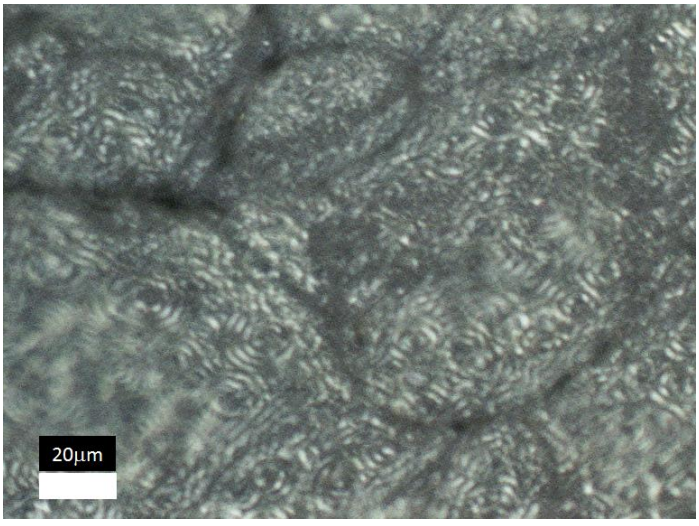

Figure 8-6 Optical microscopy image of a thin cross section of the part wall consisting of LLDPE containing 0.25 wt.% graphite nanoplatelets. The dark fringes represent spatially continuous graphite agglomerates.

8.2.2 Surface resistivity of melt compounded and dry blended nanocomposites

The resistivity of the neat polyethylene, and all the melt-compounded LLDPE nanocomposites considered presently, was outside the range of the instrument employed, i.e. $>10^{15}$ Ohms per square ($\Omega\ \square^{-1}$).

Figure 8-7 shows surface resistivity data for rotomoulded nanocomposite sheets obtained by dry blending. The surface resistivity decreased abruptly with increase in graphite content. At the lowest graphite loading used (0.25 wt.% or 0.10 vol.%), the surface resistivity of the polyethylene nanocomposites was $< 10^9\ \Omega\ \square^{-1}$, i.e. well into the static dissipative or antistatic classification region according to the specifications of the IEC 61340-2-3 standard. Further addition of graphite nanoplatelets decreased the surface resistivity into the conductive range. At 0.25 wt.% graphite content, the EVA nanocomposites were already in the conductive range, i.e. below $10^5\ \Omega\ \square^{-1}$. This implies that at 0.25 wt.%, the EVA nanocomposites had already reached the percolation threshold. Further addition of graphite nanoplatelets did not reduce the resistivity significantly.

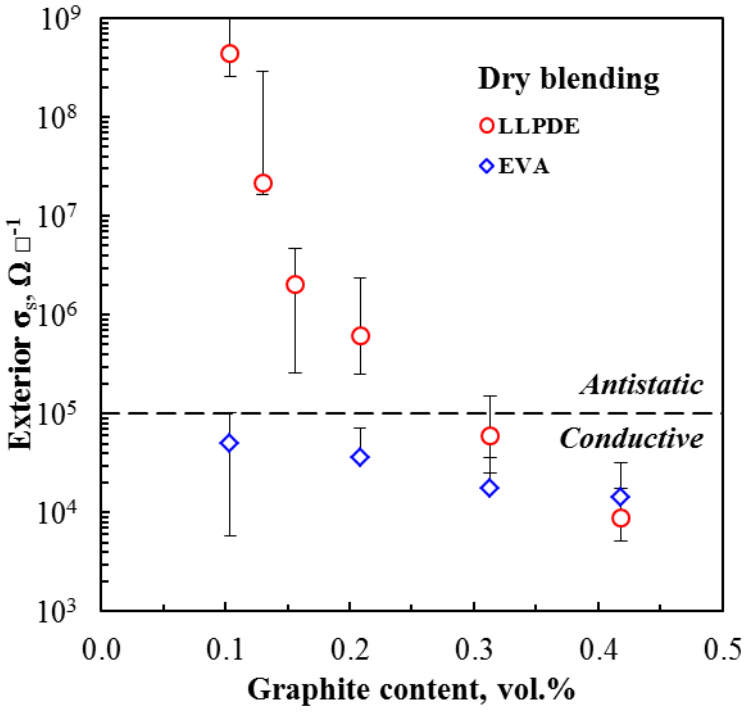

Figure 8-7 Surface resistivity of nanocomposite sheets prepared via dry blending neat polymer nanocomposites.

8.2.3 Surface resistivity of bilayer parts formed via double dumping

The double dumping procedure was used to rotomoulded nanocomposites that retained antistatic properties at the exterior surfaces. GNPs were included in the outer layer only. Figure 8-8 shows the surface resistivity of the bilayer nanocomposites obtained by double dumping. At 0.25 wt.% (0.10 vol.%) graphite nanoplatelet content in the outer layer both the LLDPE/LLDPE and EVA/LLDPE nanocomposites performed well into the antistatic range. The EVA/LLDPE nanocomposites showed little change in resistivity with an increase in graphite nanoplatelet content. However, the resistivity of the LLDPE/LLDPE nanocomposites decreased with an increase in nanographite content reaching into the conductive range, i.e. $<10^3\ \Omega\ \square^{-1}$.

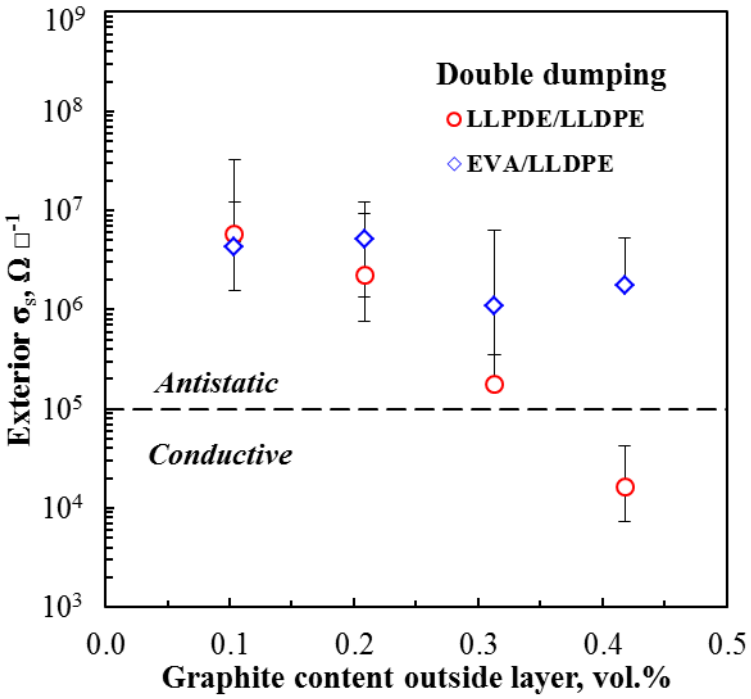

Figure 8-8 Surface resistivity of nanocomposite sheets prepared via dry blending neat polymer nanocomposites bilayer sheets made by double dumping.

8.2.4 Mechanical properties of dry blended and compounded nanocomposites

Impact resistance is a key indicator of rotomoulded part quality. Figure 8-9 compares the impact resistance and the tensile strength data at a graphite loading of 0.25 wt.%. Figure 8-10 shows the variation of the impact resistance with graphite nanoplatelet loading. Incorporation of GNPs by melt compounding at 0.25 wt.% decreased the impact resistance by only 31%.

However, that composite was not conductive. Even at a loading of 2 wt.% graphite the compounded samples retained the insulative character of polyethylene. Ductile failure was observed up to 0.50 wt.% and the impact resistance of the nanocomposites dropped by only 32%. However, beyond 0.50 wt.% graphite, mechanical properties deteriorated catastrophically.

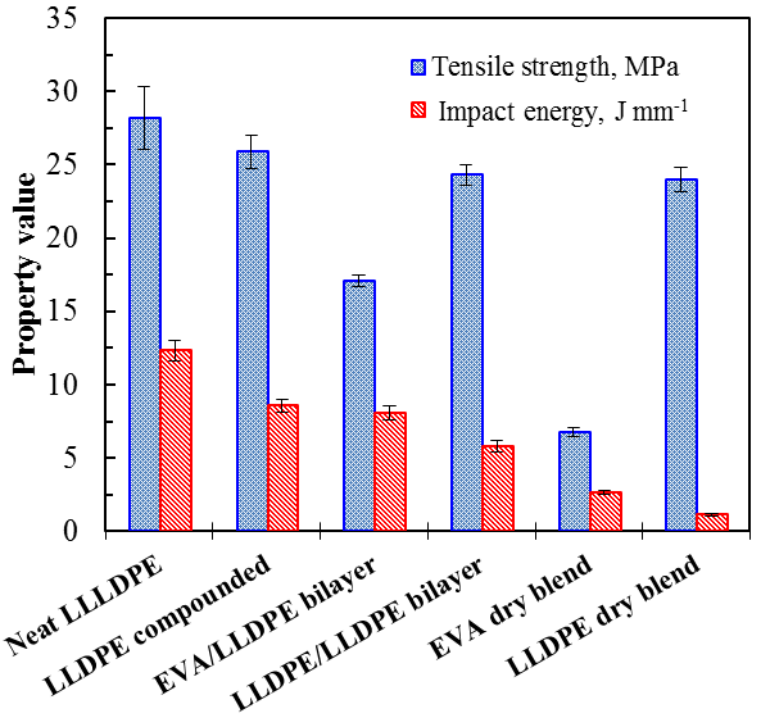

Figure 8-9 Impact resistance (J mm^{-1}) and tensile strength (MPa) of dry blended, compounded and double dumped nanocomposites containing 0.25 wt.% graphite nanoplatelets. In the bilayer sheets this corresponds to the concentration in the outer layer.

Considering dry blended LLDPE samples, the resistivity was already in the antistatic range at 0.25 wt.% GNP. However, impact resistance of the nanocomposite was four times lower compared to the virgin polyethylene. In fact, the nanocomposite exhibited a brittle failure mode even at this low graphite loading.

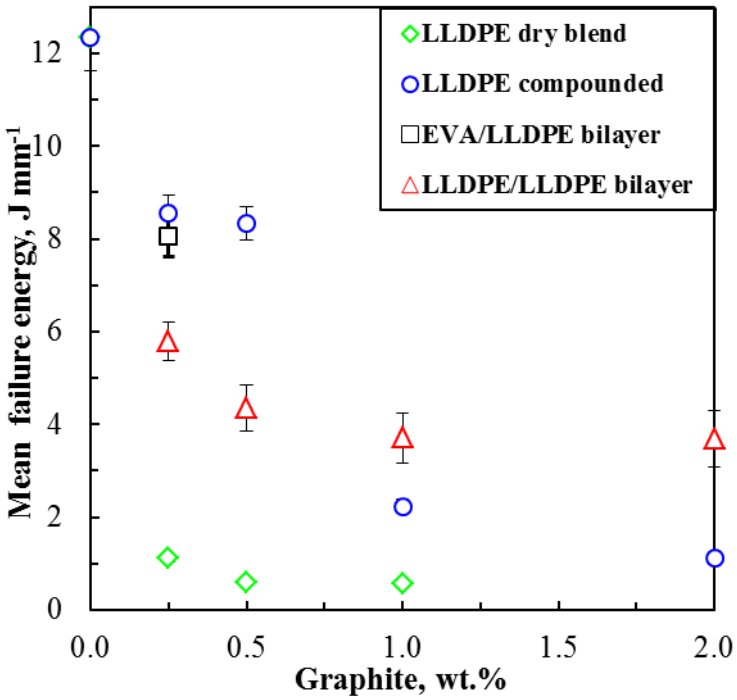

Figure 8-10 Variation of impact resistance (J mm^{-1}) with graphite nanoplatelet loading. In the bilayer sheets this corresponds to the concentration in the outer layer.

Changing to a bilayer structure resulted in significantly improved impact properties. Figure 8-9 shows the impact and tensile strength results when the outer layer (nominally 1 mm in thickness) was constructed of either LLDPE or EVA containing 0.25 wt.% GNP. The 2 mm inner LLDPE layer showed some level of ductility with the impactor making a deep-drawn dent in the samples before they failed. The impact energy appeared to have been absorbed through stress whitening in the LLDPE layer. Using EVA rather than PE as the outer graphite-containing layer improved the reduction in impact resistance compared to that of LLDPE. EVA is more flexible than LLDPE and thus able to absorb the impact energy more efficiently. The EVA layer together with the LLDPE exhibited some ductility, but the LLDPE layer failed first in most instances. The tensile strength was however compromised in the EVA-based nanocomposites.

8.2.5 Cone calorimeter fire test results

Nanofillers reportedly improve the fire properties of polymers at relatively low addition levels (Calò et al., 2012). Therefore the fire properties of the rotomoulded nanocomposites were evaluated at 1.0 wt.% GNP. Figure 8-11 compares the heat release rate (HRR) curves

for dry blended LLDPE and the bilayer LLDPE/LLDPE and EVA/LLDPE GNPs nanocomposites. Table 8-2 summarises the test results.

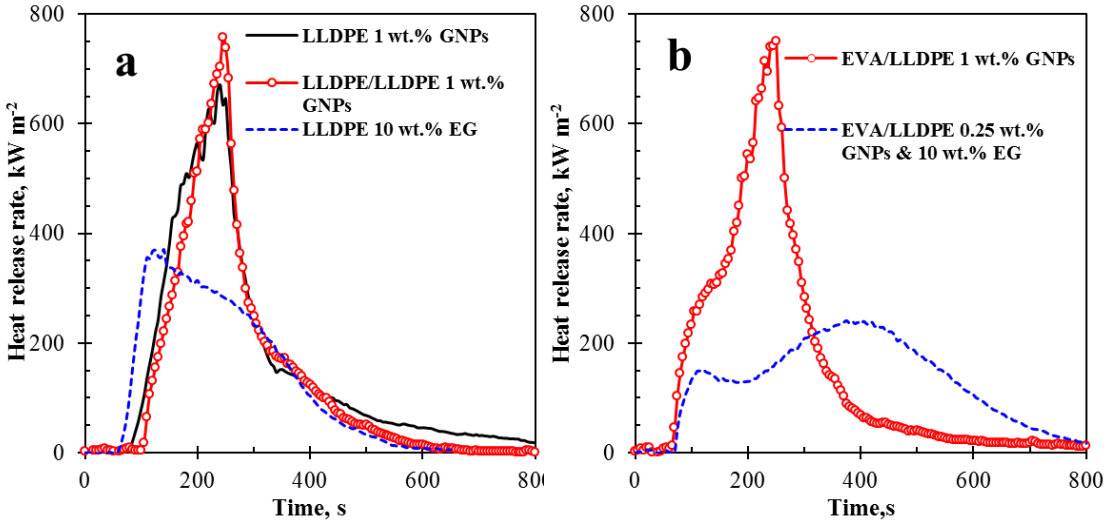

Figure 8-11 Heat release rate (HRR) curves of graphite-polyethylene composites. (a) LLDPE and LLDPE/LLDPE bilayer composites. (b) EVA/LLDPE bilayer composites. The graphite nanoplatelets (GNP) and expandable graphite (EG) fillers were only present in the outer layer of the bilayer composites.

The inclusion of the graphite nanoplatelets at a loading of 1.0 wt.% graphite nanoplatelets did not have a significant impact on the fire behaviour of the nanocomposites in cone calorimeter testing. The *HRR* curves for most of the nanocomposites featured a single sharp peak. This behaviour is characteristic of thermally thin samples that are pyrolyzed almost at once (Schartel and Hull, 2007). The peak heat release rate (pHRR) reached the highest value of 745 ± 18 kW m^{-2} and 714 ± 53 kW m^{-2} for the bilayer LLDPE/LLDPE and EVA/LLDPE structures, respectively. The corresponding value for a monolayer LLDPE sheet containing 1.0 wt.% GNP was ca. 667 ± 16 kW m^{-2}. This is only a marginal improvement.

The *HRR* curve for the expandable graphite composites that contained 10 wt.% expandable graphite featured a more flattened shape and a significantly lower *pHRR*. This attributed to a protective barrier layer that is formed at the top of the sample surface by the 'worm like' structures resulting from the endothermic expansion of the EG. This barrier slowed down heat transfer into the substrate during cone calorimeter testing. The *pHRR* was ca. 360 ± 10

kW m^{-2} for the monolayer LLDPE sheet containing 10 wt.% expandable graphite. This represents a significant improvement (Figure 8-11a). However, unexpectedly the EVA/LLDPE bilayer structure containing 0.25 wt.% graphite nanoplatelets and 10 wt.% expandable graphite in the outer EVA layer performed even better. In this case the pHRR was only about 259 ± 26 kW m^{-2} (Figure 8-11b).

Table 8-2 Cone calorimeter data summary.

Parameter	Units	LLDPE samples		
		Bilayer 1 wt.% GNP	**Monolayer 1 wt.% GNP**	**Monolayer 10 wt.% EG**
Time to ignition (t_{ign})	s	109 ± 6	77 ± 9	53 ± 6
Time to flame out	s	722 ± 110	859 ± 178	536 ± 27
Time to *pHRR*	s	273 ± 4	243 ± 6	123 ± 14
Peak heat release rate (*pHRR*)	kW m^{-2}	745 ± 18	667 ± 16	360 ± 10
Total heat release (*tHR*)	MJ m^{-2}	103 ± 8	114 ± 23	93 ± 7
FIGRA	kW $m^{-2}s^{-1}$	3.2 ± 0.1	2.79 ± 0.07	2.9 ± 0.3
MAHRE	kW m^{-2}	264 ± 6	291 ± 4	217 ± 5
$pHRR/t_{ign}$	kW $m^{-2}s^{-1}$	6.9 ± 0.6	8.7 ± 1.2	6.8 ± 0.6
Smoke release	m^2 m^{-2}	655 ± 23	706 ± 164	681 ± 12
Parameter	**Units**	**EVA/LLDPE bilayer samples**		
		1 wt.% GNP	**0.25 wt.% GNP & 10 wt.% EG**	
Time to ignition (t_{ign})	s	64.5 ± 3.5	72 ± 2	
Time to flame out	s	796 ± 112	926 ± 38	
Time to *pHRR*	s	235 ± 21	375 ± 0	
Peak heat release rate (*pHRR*)	kW m^{-2}	714 ± 53	259 ± 26	
Total heat release (*tHR*)	MJ m^{-2}	116 ± 10	109 ± 9	
FIGRA	kW $m^{-2}s^{-1}$	3.0 ± 0.0	1.34 ± 0.01	
MAHRE	kW m^{-2}	312 ± 12	160 ± 7.4	
$pHRR/t_{ign}$	kW $m^{-2}s^{-1}$	11.1 ± 0.2	3.6 ± 0.3	
Smoke release	m^2 m^{-2}	688 ± 565	792 ± 17	

The *FIGRA* is an estimator for the fire spread rate and size of the fire whereas the *MARHE* estimates the tendency of a fire to develop (Chapter 3, section 3.4). Table 8-2 also reports the *FIGRA* and *MARHE* indices. By far the lowest values (1.34 ± 0.01 kW $m^{-2}s^{-1}$ and 160 ± 7.4 kW $m^{-2}s^{-1}$, respectively) were recorded for the EVA/LLDPE bilayer structure containing 0.25 wt.% graphite nanoplatelets and 10 wt.% expandable graphite. This implies that this system offered the best fire protection as quantified by the cone calorimeter test. This bilayer nanocomposite also featured acceptable antistatic and mechanical properties. It had a surface resistivity of 10^6 Ω □$^{-1}$, i.e. within the antistatic range. The tensile strength was 16 MPa, a value comparable to the samples that contained only GNP as filler (17 MPa). The impact

resistance was 6 J mm^{-1}, a value similar to the impact resistance of the bilayer LLDPE/LLDPE nanocomposites with 0.25 wt.% GNPs in the outer layer.

8.3 Discussion

The properties of rotomoulded parts are strongly influenced by the oven time and temperature (Crawford and Throne, 2002). Optimum mechanical properties of rotomoulded parts are realised through properly cured parts. Insufficient oven time or too low a temperature results in incomplete melting and densification of the polymer powder. Undercured parts exhibit pin holes on the surface in contact with the mould wall and porous part cross sections. Such samples exhibit poor impact properties because these defects act as stress concentrators (Pick and Harkin-Jones, 2006). Over-curing parts result in thermo-oxidative degradation of the polymer with a concomitant deterioration in mechanical properties. Optimum part properties for rotomoulded polyethylene were obtained at an oven time and temperature of 45 min and 300 °C for the rotomoulding machine and polyethylene grade used in this study. Hence 45 min was used for subsequently moulding polyethylene.

The resistivity data in Figure 8-7 appears to follow the universal composition trend predicted by the percolation theory (Clingerman et al., 2002). Above a critical graphite volume fraction, corresponding to the percolation threshold, the concentration of graphite nanoplatelets is sufficient to ensure that a conductive network of touching particles is formed (Kalaitzidou et al., 2010). FESEM results of the fractured nanocomposites (Figure 8-4a) revealed that, in the compounded samples, the nanoplatelets are uniformly dispersed and well separated. It is even difficult to discern them as the compounding process probably caused further crumpling into smaller particles. Therefore their concentration in the matrix was too low to set up a conductive network. This is consistent with a previous study of polyethylene nanocomposites fabricated with GNPs which found percolation thresholds as high as 15 wt.% (Kim et al., 2009).

In the sample obtained by dry blending random clusters of graphite nanoplatelets are clearly identified (Figure 8-4b). Apparently the platelets retained their flake-like shape and aggregated into larger domains. Away from these clusters, regions devoid of graphite particles are observed. This morphology is attributed to the unique character of the dry-

blending and rotomoulding processes. During the blending action, in the high speed mixer-grinder, the graphite nanoplatelets are distributed over the surface of the much larger polyethylene powder particles. Apparently this accumulation at the periphery of the polyethylene domains largely persisted even after melting of the powder particles and the subsequent consolidation and freezing of the polymer phase. This means that the platelets essentially remained trapped in-between the original polyethylene powder particles. In this way they formed conductive pathways around the remnants of the original polymer powder particles that coalesced into a continuous matrix. This hypothesis explains the low percolation threshold and the severe loss in impact resistance.

Support for this hypothesis is provided by the FESEM image in Figure 8-5 and the optical microscope image in Figure 8-6 for LLDPE compounds containing 2.0 wt.% and 0.25 wt.% graphite, respectively. Figure 8-5 shows a fracture surface covered almost entirely with a tapestry of graphite nanoplatelets. Figure 8-6 is an image of part of a thin cross section of the moulded wall. The dark fringes around large polyethylene domains are clearly visible. They are attributed to the presence of graphite platelets.

Long range clustering of GNPs seen in the optical image and FESEM micrographs of dry blended composites enables the facile formation of a conductive network at low loadings, i.e. 0.25 wt.% graphite at the expense of mechanical properties. The GNPs particle clusters act as stress concentration points and also encourage crack formation, thereby weakening the nanocomposites (Pick and Harkin-Jones, 2006). At 0.25 wt.% the compounded composite exhibits better mechanical properties due to better dispersion (Figure 8-4), but they were not conductive.

Closer inspection of the FESEM images revealed that there was hardly any adhesion between the GNPs and LLDPE, with the basal planes of the GNPs mostly uncovered by the polymer Figure 8-4b, Figure 8-5). A mismatch in surface energies exists between graphite and the hydrophobic, non-polar polyethylene, hence the poor interfacial interaction (Planes et al., 2008). However, there is evidence of strong adhesion between the GNPs and LLDPE on the edges of some the GNPs (Appendix B).

Chapter 9 Results and Discussion: Phase change material/graphite nanocomposites

9.1 Stearyl alcohol/stearic acid (C_{18}-OH/C_{18}-Acid) mixtures

9.1.1 Melting and crystallization characteristics

Figure 9-1 shows the second heating and cooling DSC scans of stearyl alcohol and stearic acid. The heating curve of stearyl alcohol shows one endotherm with an onset temperature of 58.2 °C. The solid-solid transition from the monoclinic ordered γ phase into the α rotator phase which occurs when *n*-alkanols with an even number of carbon atoms are heated from room temperature is not apparent in the melting curve of stearyl alcohol as this transition overlaps with the melting transition hence it exhibits one endotherm (Ventola et al., 2002). The cooling curve of stearyl alcohol exhibits two exotherms. The first exotherm with an onset temperature of 57.8 °C exhibits negligible super cooling. The solid-solid transition $\alpha \rightarrow \gamma$ of stearyl alcohol exhibits super cooling of close to 5 °C, closer to the upper threshold for proper heat extraction from the PCM (Sharma et al., 2009).

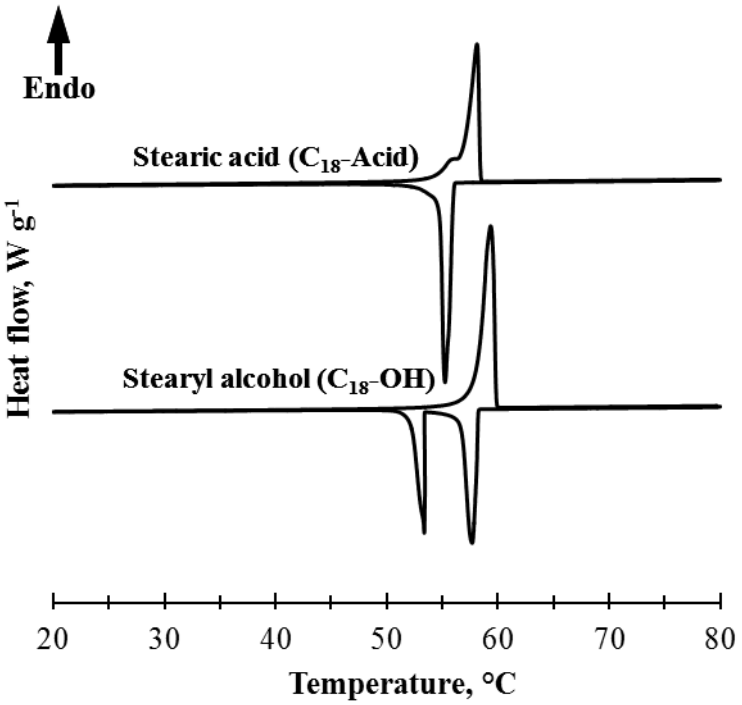

Figure 9-1 DSC heating and cooling scans for stearyl alcohol and stearic acid.

Commercial stearic acid is a combination of approximately 55 % palmitic acid (saturated fatty acid with 16 carbon atoms), 45 % stearic acid (saturated fatty acid with 18 carbons) and other fatty acids (Tillotson, 1955). In Table 9-1, the composition of the stearic acid used in this study as given by the supplier approximates the aforementioned composition. This composition was estimated to absolute values as shown in the last column in Table 9-1. In Figure 9-1, the heating and cooling curves of stearic acid feature single transitions; a melting endotherm and a crystallization endotherm. The melting endotherm however exhibits a shoulder. Mixtures of pure stearic acid and palmitic acid which constitute commercial stearic acid are known to exhibit eutectic behaviour (Tillotson, 1955). The melting temperature of the stearic acid (onset 56.8 °C, peak 58.1 °C) used in this study is lower than that of pure stearic acid (69.3 °C) but closer to that predicted in the phase diagram of mixtures of stearic acid and palmitic acid (Tillotson, 1955, Sato et al., 1990).

Table 9-1 Composition of palm triple pressed commercial stearic acid (Palmac 55-16).

Component	Composition (%)	Approximated Composition
C12	1.0 Maximum	1
C14	2.0 Maximum	2
C16	52.0-56.0	52
C18	42.0-47.0%	45
C18:1	0.5 Maximum	0
Others	1.0	0

Figure 9-2 shows the second DSC heating curves of the pseudo-binary mixtures of stearyl alcohol and the commercial stearic acid as a function of the stearyl alcohol (C_{18}-OH) mole fraction. Similar to previous studies on the mixtures of fatty alcohols and fatty acids, the curves feature multiple endotherms (Gandolfo et al., 2003, Zeng et al., 2009, Zuo et al., 2011a, Zuo et al., 2011b). However, between 0.1 and 0.7 mole fraction C_{18}-OH, the curves feature endotherms virtually at a constant temperature circa 47 °C. The endotherms which occur at higher temperatures appear to go through a minimum. This behaviour is characteristic of a eutectic system as observed in previous studies on mixtures of *n*-alkanols and straight chain fatty acids (Gandolfo et al., 2003, Zeng et al., 2009, Zuo et al., 2011a, Zuo

et al., 2011b). In a eutectic system there is miscibility in the liquid phase and demixing and segregation in the solid phase (Gandolfo et al., 2003). The constant temperature is the eutectic temperature and the temperature which goes through a minimum the solid-liquid equilibrium line (liquidus). At the eutectic composition, a single endotherm representing the melting transition should be observed in the DSC curves, whereas at any other composition, two endotherms should be observed, the first for the eutectic transition and the second the melting transition (Rycerz, 2013). In Figure 9-2, it is apparent that the eutectic composition is at 0.4 mole fraction stearyl alcohol.

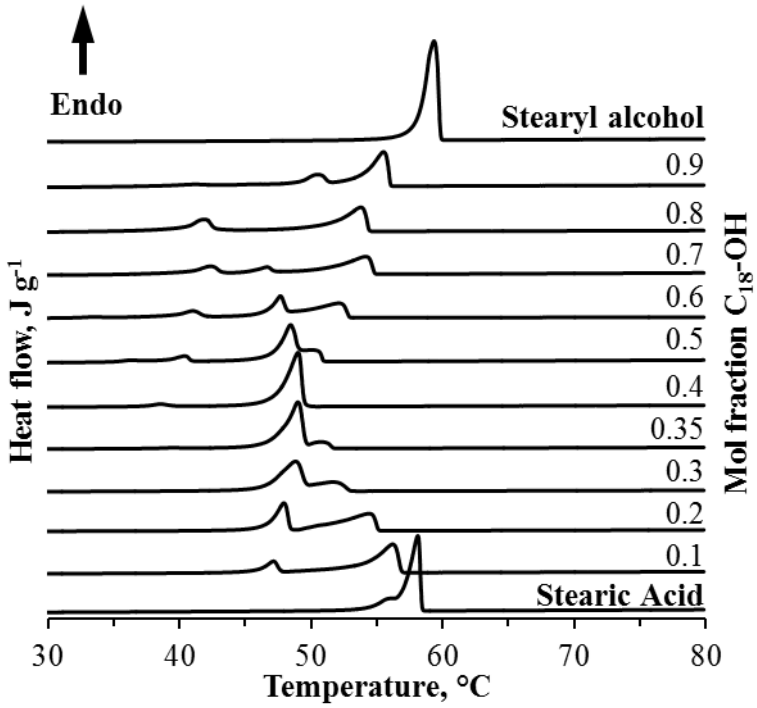

Figure 9-2 DSC heating curves for pseudo binary mixtures of stearyl alcohol and commercial stearic acid.

Between 0.4 and 0.9 mole C_{18}-OH fraction some endotherms appear before the eutectic temperatures. These were previously assigned to the effect of the solid transition in the alcohol (Gandolfo et al., 2003). It has been suggested that the alcohol could be partially miscible in the solid matrix of the acid (Gandolfo et al., 2003). Table 9-2 gives the transition temperatures and enthalpies of the transitions of the mixtures of stearyl alcohol (C_{18}-OH) and stearic acid (C_{18}-Acid) from the second DSC heating run. The phase diagram in Figure 9-3 for the pseudo-binary mixtures was constructed from the peak transitions temperatures of the

second DSC heating run (Table 9-2). According to Zuo et al. (2011a) the endotherm peak temperature gives a better representation of the transitions rather than the onset temperatures. The Schröeder-Van Laar equation also referred to as the van't Hoff freezing point relation, can be used to model the solid-liquid equilibrium (liquidus) line for ideal mixtures which are fully miscible in the liquid phase (Gandolfo et al., 2003, Zuo et al., 2011b). The equation is given as

$$\ln x_i = \frac{\Delta H_i}{R}\left(\frac{1}{T_i} - \frac{1}{T}\right) \qquad \textbf{(9-1)}$$

where x_i, ΔH_i and T_i are mole fraction, heat of fusion and melting temperature of pure compound i, respectively. R is the universal gas constant and T the melting temperature of the mixture. Zhao et al. (2014) showed that this empirical equation can also be applied to pseudo-binary mixtures. The predicted liquidus temperatures and eutectic temperature using the Schröeder-Van Laar equation are also shown in Figure 9-3. There is a reasonable agreement between the experimental data and the liquidus predicted by the Schröeder-Van Laar equation up to 0.7 mole fraction stearyl alcohol. Beyond this composition up to 100 % stearyl alcohol the Schröeder-Van Laar equation over predicted the liquidus.

A closer examination of the experimental data shows that the liquidus line goes through another minimum at around 0.8 mole fraction. This suggests that the present system exhibits two eutectic points. Mixtures which feature two eutectic compositions undergo co-crystallization and form co-crystals for compositions in-between the two eutectic compositions (Stahly, 2009).

Table 9-2 Transition temperatures and enthalpies for mixtures of stearyl alcohol and stearic acid from the second DSC heating run.

Mole fraction C_{18}-OH	Peak temperatures, °C				Enthalpies, J g^{-1}†			
	1st solid transition†	*2nd Solid transition*†	*Eutectic reaction*	*Melting*	*1st Solid transition*	*2nd Solid transition*	*Eutectic reaction*	*Melting*
0.00				58.11				177.42
0.10			47.13	56.19			22.46	169.59
0.20			47.93	54.45			61.66	120.41
0.30			48.81	51.83			121.47	50.09
0.35			48.99	50.95			141.19	24.33
0.40	38.70		49.01	49.01		16.52	197.02	
0.50	36.18	40.18	48.43	50.54	14.45	27.73	128.76	35.68
0.60	33.89	41.09	47.66	52.20	12.85	20.49	56.63	121.45
0.70	33.55	42.01	46.64	54.15	3.66	40.88	30.29	165.29
0.80		41.67		53.79		74.15	156.61	
0.90		41.39	50.53	55.51		20.00	2.43	234.78
1.00				59.33				246.86

†Data obtained after peak separation.

The Tamman diagram is a plot of the molar enthalpies of the DSC endotherms associated with the eutectic transition as a function of the mixture molar composition (Costa et al., 2009, Rycerz, 2013). A simple eutectic will exhibit a maximum in the molar enthalpies at the eutectic point, forming a triangular plot. The Tamman plot also shows the composition range in which solid solubility exists (Costa et al., 2009, Rycerz, 2013). The Tamman plot in Figure 9-4 verifies that the present pseudo-binary system is a bi-eutectic system with eutectic compositions at 0.40 and 0.80 mole fractions C_{18}-OH. Between these two compositions co-crystallization occurs.

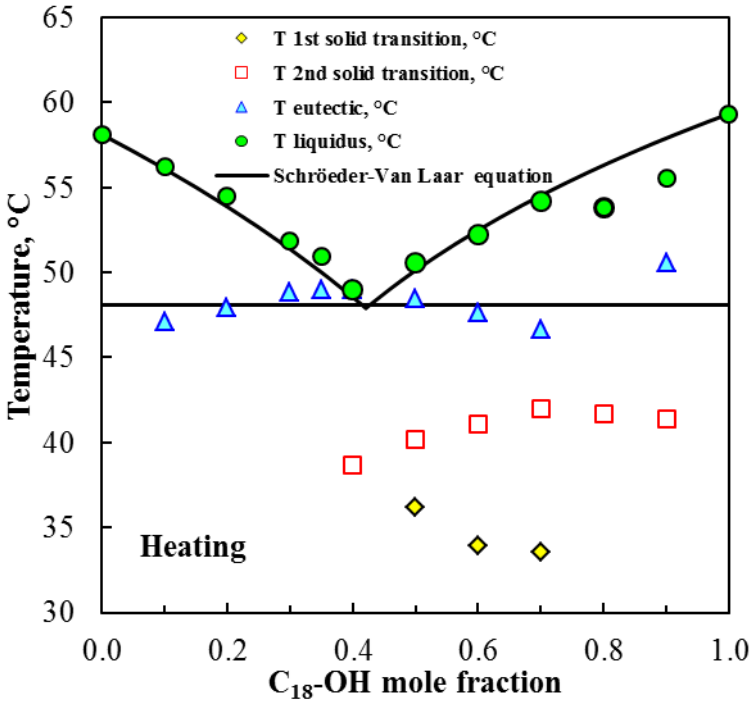

Figure 9-3 Phase diagram of the pseudo binary stearyl alcohol-commercial stearic acid mixtures.

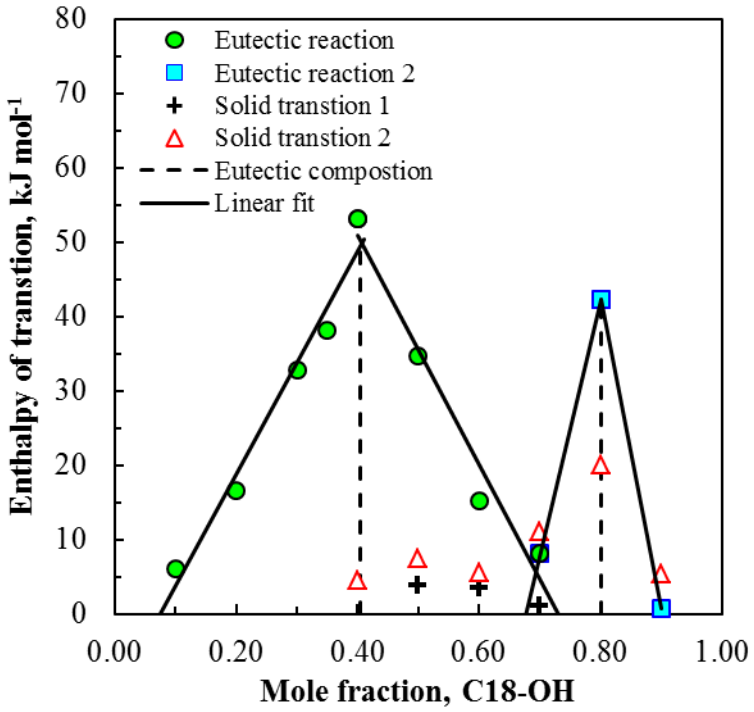

Figure 9-4 Tamman plot for pseudo binary mixtures of stearyl alcohol and commercial stearic acid.

At a composition of 0.35 mole fraction C_{18}-OH, close to the first eutectic point, the heating curve features a single endotherm with a small shoulder (Figure 9-2). The DSC cooling curves in Figure 9-5 showed that this composition had a single exotherm. This composition was selected as the PCM for further study.

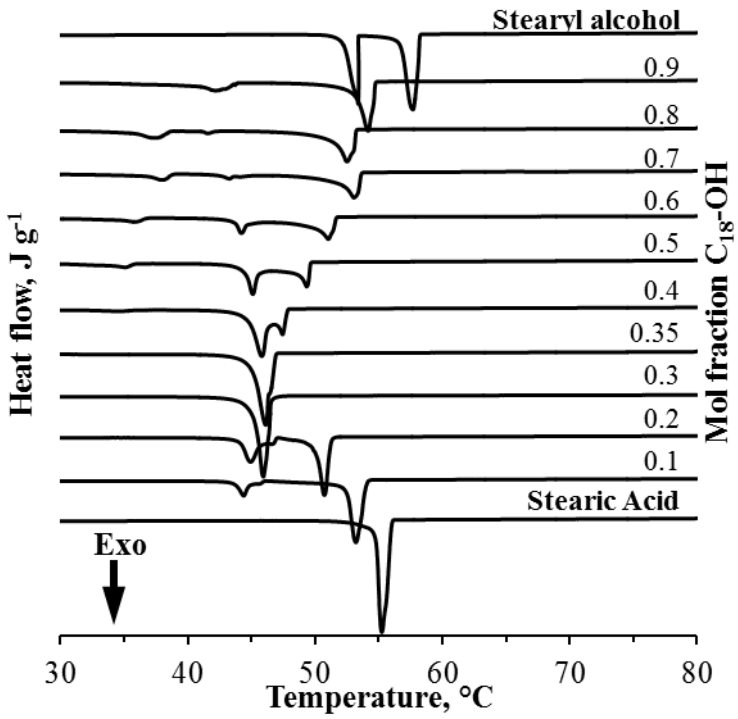

Figure 9-5 DSC cooling curves for pseudo binary mixtures of stearyl alcohol and commercial stearic acid.

Optical microscopy pictures acquired during crystallization of the stearyl alcohol, stearic acid and their mixtures at 0.35 mole fraction stearyl alcohol are shown in Appendix C. These showed that the mixture at 0.35 mole fraction C_{18}-OH had smaller crystals compared to the single components.Gandolfo et al. (2003) also previously observed smaller crystals for mixtures of stearyl alcohol and stearic acid. XRD studies by Schaink et al. (2007) showed that these where mixed crystals of stearyl alcohol and stearic acid.

9.2 PCM/GNPs nanocomposites

9.2.1 Morphology and structure

Figure 9-6 shows FESEM micrographs depicting the morphology of the PCM/GNPs nanocomposites. Figure 9-6a shows delaminated GNPs in the PCM with thicknesses less than 50 nm at loading of 2.5 wt.% GNPs. Figure 9-6b, shows that at 10 wt.%, the GNPs are randomly and well dispersed, forming an interconnected network between themselves which traps the PCMs in-between.

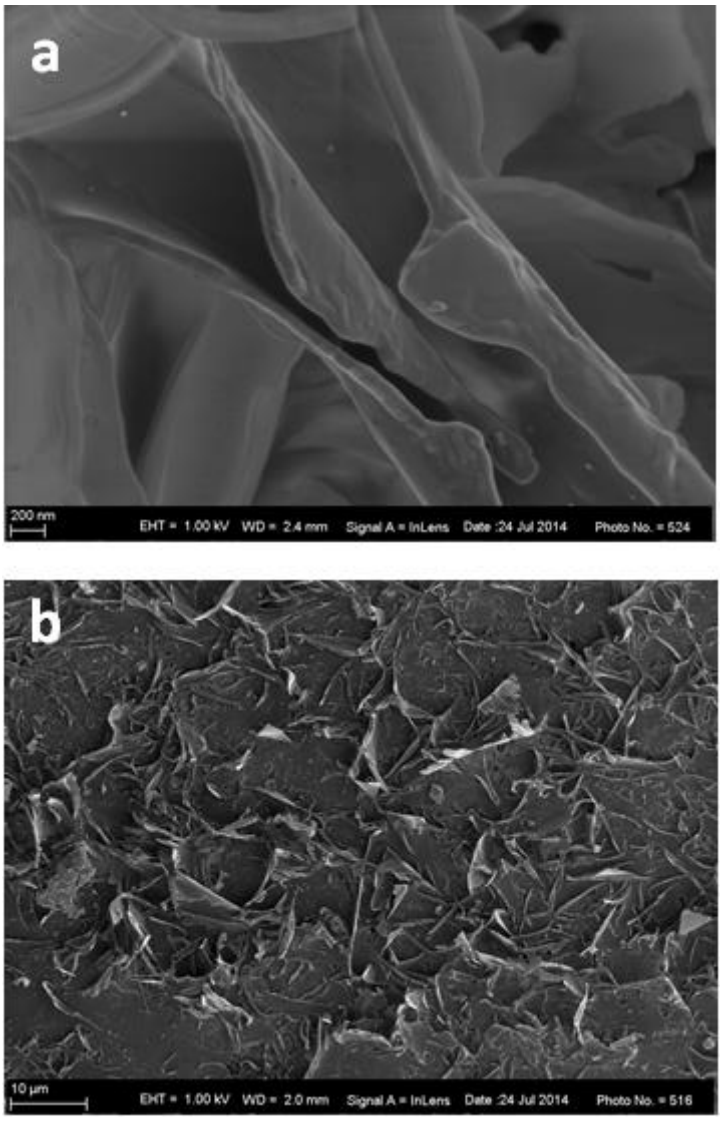

Figure 9-6 FESEM micrographs of stearyl alcohol/stearic acid PCM/GNPs nanocomposites at (a) 2.5 wt.% GNPs and (b) 10 wt.% GNPs.

9.2.2 Absence of the esterification reaction: FTIR

Figure 9-7 shows the FTIR spectra of stearyl alcohol, stearic acid and the phase change material (mixture of stearyl alcohol and stearic acid at 0.35 mol fraction stearyl alcohol) with 0 wt.% GNPs and 10 wt.% GNPs. The characteristic broad absorption band of bonded oxygen-hydrogen stretching vibrations which occurs for fatty alcohols and acids between 3230-3550 cm^{-1} and 2500 and 2700 cm^{-1}, respectively is apparent in the spectra in Figure 9-7 (Aydın, 2013). The carbonyl stretching vibrations which occur for fatty acids between 1700-1725 cm^{-1} can also be seen in the spectra (Aydın, 2013). The carbonyl stretching vibrations which are observed for acyclic saturated esters at around 1732 cm^{-1} were observed in the PCM/GNPs nanocomposites synthesized at 150 °C, as shown by the spectrum of 10 wt.% GNP in Figure 9-7.

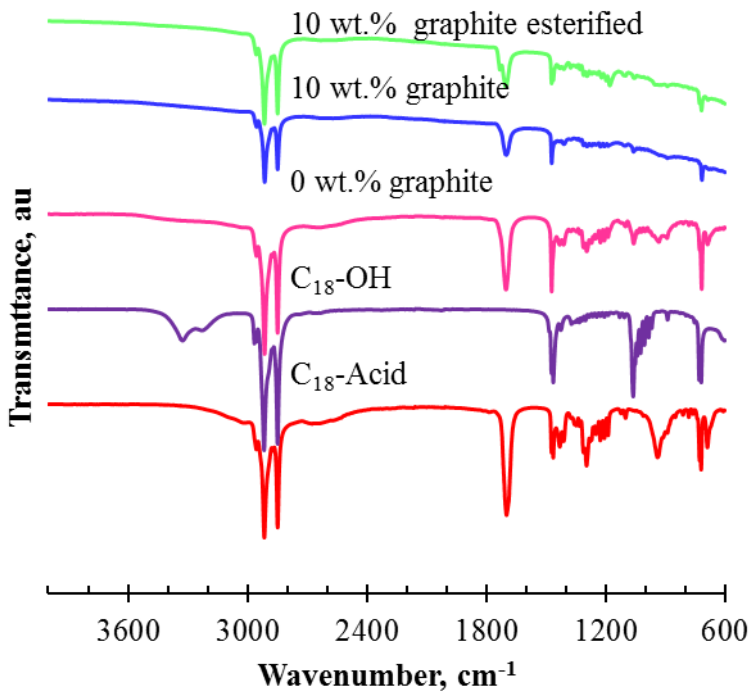

Figure 9-7 FTIR spectra of stearyl alcohol, stearic acid and the phase change material (mixture of stearyl alcohol and stearic acid at 0.35 mol fraction stearyl alcohol) with 0 wt.% GNPs and 10 wt.% GNPs. The PCM/GNPs nanocomposite which did not esterify was synthesized at 80 °C, whereas the PCM/GNPs nanocomposite which esterified was synthesized at 150 °C.

9.2.3 Melting and crystallization temperatures and enthalpies

Figure 9-8 shows the second DSC heating and cooling runs of the PCM/graphite nanocomposites. The onset and peak temperatures and enthalpies of melting derived from DSC runs are reported in Table 9-3. Figure 9-8 and Table 9-3 show that there was a decrease of more than 1 °C in the onset and peak melting temperatures with an increase in graphite content up to 10 wt.%. This was probably due to increased thermal conductivity in the PCM. Table 9-3 also shows that the melting and crystallization enthalpies normalized with respect to the mass of the organic phases of the PCM/graphite nanocomposites were similar to that of the PCM at 0 wt.% graphite nanoplatelets. Figure 9-8 and Table 9-3 also show that the PCM/graphite nanocomposites feature negligible super cooling.

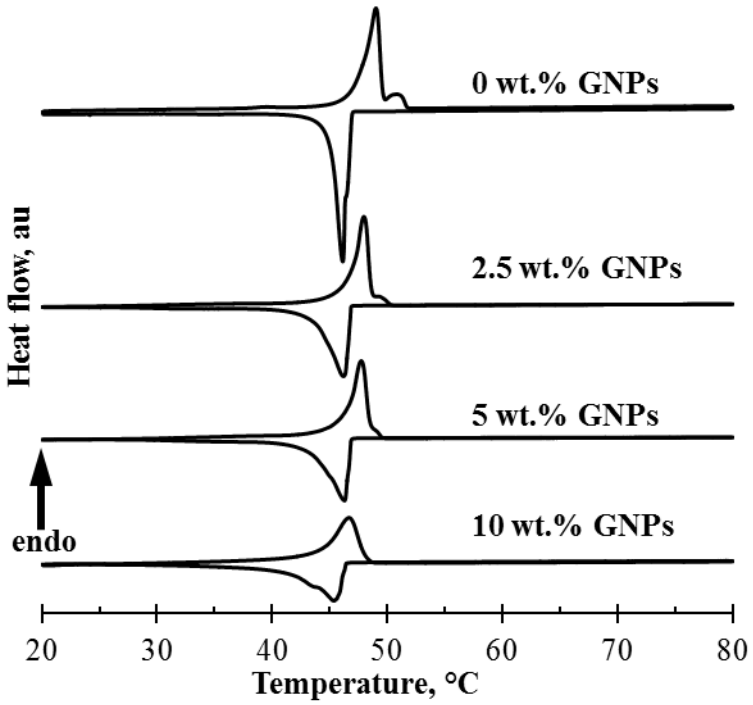

Figure 9-8 DSC heating and cooling curves of stearyl alcohol/stearic acid PCM/GNP nanocomposites.

Table 9-3 Melting and crystallization temperatures and enthalpies of the PCM/GNP nanocomposites from the DSC second heating cycle.

PCM Composition	Nanographite content, wt.%	Melting Onset T, °C	Melting Enthalpy, J g^{-1}	Peak Melting Temperature, °C
C_{18}-OH	0.0	58.1±0.1	248±1.1	59.4±0.1
C_{18}-Acid	0.0	56.8±0.0	179±1.6	58.1±0.0
0.35 mol/mol C_{18}-OH	0.0	47.4±0.1	161±9.7	49.0±0.1
0.35 mol/mol C_{18}-OH	2.5	46.8±0.1	156±15.3	48.3±0.3
0.35 mol/mol C_{18}-OH	5.0	46.4±0.3	163±20.1	48.2±0.3
0.35 mol/mol C_{18}-OH	10.0	45.8±1.2	150±12.9	47.8±0.9
PCM Composition	**Nanographite content, wt.%**	**Crystallization Onset T, °C**	**Crystallization Enthalpy, J g^{-1}**	**Crystallization Peak T, °C**
C_{18}-OH	0.0	58.3±0.1	245±0.7	57.6±0.0
C_{18}-Acid	0.0	56.1±0.1	185±1.8	55.2±0.0
0.35 mol/mol C_{18}-OH	0.0	46.6±0.0	158±7.9	46.0±0.1
0.35 mol/mol C_{18}-OH	2.5	46.9±0.1	154±16.1	46.0±0.2
0.35 mol/mol C_{18}-OH	5.0	47.0±0.3	164±16.8	46.3±0.4
0.35 mol/mol C_{18}-OH	10.0	46.6±0.3	145±12.9	45.8±0.3

9.2.4 Thermal conductivity

The thermal conductivity results of the PCM/GNPs nanocomposites are reported in Table 9-4. The results show that both in the solid state and molten state, the nanocomposite conductivity increases with graphite content. At 10 wt.% (4.2 vol.%) the conductivity is enhanced by approximately 600 % and 1200 % in the solid and liquid states, respectively.

Table 9-4 Thermal conductivity (W $m^{-1}K^{-1}$) of the PCM/graphite nanocomposites in the solid state (22 °C) and molten state (70 °C).

Graphite content		Solid state (22 °C) thermal conductivity, W $m^{-1} K^{-1}$	Molten state (70 °C) thermal conductivity, W $m^{-1} K^{-1}$
wt.%	vol.%		
0.0	0.0	0.252±0.002	0.177±0.014
2.5	1.0	0.565±0.001	0.359±0.014
5.0	2.0	0.833±0.003	0.614±0.024
10.0	4.2	1.687±0.009	2.311±0.027

9.2.5 Thermal stability

Figure 9-9 shows the accelerated thermal cycling melt/freeze cycles for the PCM/GNPs nanocomposite at 10 wt.% GNPs obtained using the DSC. All the PCM/GNPs compositions showed no deterioration in the melting and crystallization temperatures and enthalpies after 100 melt/freeze cycles. They also exhibited negligible super cooling.

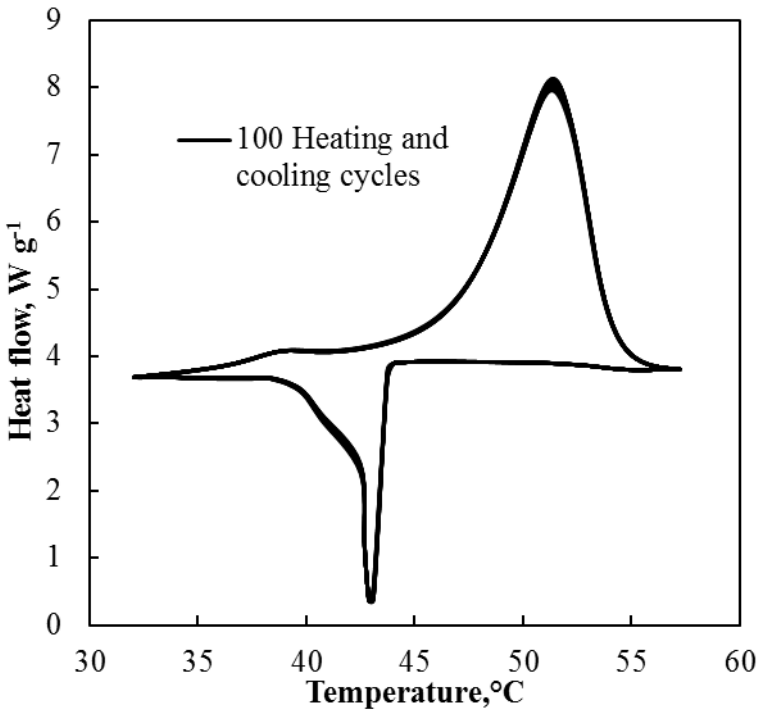

Figure 9-9 Thermal cycling stability: 100 accelerated melt/freeze cycles in the DSC at heating/cooling rates of 10 °C min^{-1}.

The settling tests results in Appendix D showed that after 60 days (1440 hours), the PCM/GNP nanocomposite with 10 wt.% GNPs exhibited no phase separation with the GNPs still well dispersed within the PCM matrices. However, at 5 wt.% and lower the PCM matrices and GNPs separated, with the GNPs settling at the bottom of the vial.

9.3 Discussion

To solve the super cooling problem exhibited by stearyl alcohol emanating from its solid-solid transition during cooling and also reduce the odour and mild corrosivity of stearic acid, mixtures of stearyl alcohol and stearic acid were prepared as a new PCM. The study by Gandolfo et al. (2003) on the phase diagram of mixtures of stearyl alcohol and stearic acid formed the basis of the work. However, because the commercial stearic acid used in this study was in actual fact a mixture of pure stearic acid and palmitic acid, the prepared mixtures were in reality ternary mixtures of stearic acid, palmitic acid and stearyl alcohol. The ratio of stearic acid and palmitic acid for the commercial stearic acid was fixed at 45/52; therefore the commercial stearic acid could be treated as a pseudo-single component, and the prepared mixtures as pseudo-binary mixtures of stearyl alcohol/commercial stearic acid (palmitic/stearic acid) (Zhao et al., 2014).

Analysis of the DSC data showed that the pseudo-binary mixtures formed a eutectic system with two eutectic points at 0.4 and 0.8 mole fraction stearyl alcohol. At 0.4 mole fraction stearyl alcohol, the mixtures exhibited single melting endotherms in the DSC curve (Figure 9-2). However, the cooling curve for this composition showed two exotherms overlapping with each other at this composition. Further analysis of the DSC curves showed that at a composition of 0.35 mole fraction stearyl alcohol, the DSC curves featured a single endotherm with a small shoulder in the heating run, and a single exotherm in the cooling run. This composition, which does not exhibit appreciable super cooling, is ideal for a phase change material for energy storage. Hence it was selected for further study.

Examination of the DSC data in Table 9-2 showed that the mixture with 0.35 mole fraction C_{18}-OH had a melting enthalpy lower than either stearyl alcohol or stearic acid. The smaller crystals observed in during crystallization of this mixture can explain the reduced enthalpy (Appendix C). The enthalpy is however relatively comparable to or better than several other

materials considered as PCMs for energy storage (Zalba et al., 2003, Sharma et al., 2009). This mixture also exhibits negligible super cooling (Table 9-3 and Figure 9-2), which solves the problem presented by the solid transition in stearyl alcohol.

The structure and thicknesses of the delaminated graphite nanoplatelets in the stearyl alcohol/stearic acid PCM/graphite nanocomposite shown in Figure 9-6a shows that ultrasonic assisted liquid phase exfoliation and the PCM/GNPs nanocomposites synthesis method used were efficient in delaminating and dispersing the nanoplatelets in the PCM. The GNPs in Figure 9-6a appear completely covered by the PCM, signifying good interfacial adhesion between the PCM and GNPs. It is known that the oxidative intercalation process utilized to obtain expandable graphite, the heat treatment used to exfoliate it and the ultrasonication process used in the delamination of the GNPs result in some oxygen functionalities on the GNPs. These can interact with the acid and alcohol groups through hydrogen bonding, resulting in improved interfacial adhesion. As the PCM/GNPs nanocomposite will undergo numerous melt/freeze cycles during its life time, it is important that the PCM does not form a separate phase from the GNPs. The morphology shown in Figure 9-6b suggests that the GNPs network will offer resistance to the flow of the PCM and hold it in place.

FTIR analysis was conducted on the stearyl alcohol/stearic acid PCM/ GNPs nanocomposites to confirm the absence of esters during the synthesis of the PCM/GNPs nanocomposites. At elevated temperatures residual H_2SO_4 from the oxidative intercalation of graphite can catalyse the esterification reaction between stearyl alcohol and stearic acid. Analysis of the FTIR spectra in Figure 9-7 showed that no ester was formed as evidenced by the absence of the absorption band at around 1732 cm^{-1} which shows carbonyl stretching vibrations for acrylic saturated esters. However, for PCM/GNPs nanocomposites synthesized at a temperature of 150 °C, the FTIR spectra shows evidence of ester formation as the absorption band around 1732 cm^{-1} was apparent. Hence all the PCM/GNPs nanocomposites where synthesized at 80 °C.

It is desirable to minimize the amount of conductive filler in the PCMs in order not to reduce the enthalpy of phase change and increase the weight of the PCM. The thermal conductivity results obtained in this study are substantial improvements when compared to several studies in which highly conductive nanofillers such as carbon nanotubes, carbon nanofibres and

graphene were dispersed in PCMs. In these studies marginal enhancements of the PCM nanocomposites of less than 100 % even at up to 10 wt.% nanofiller were reported, and in some instances carcinogenic solvents were necessary to disperse the nanofillers (Elgafy and Lafdi, 2005, Zeng et al., 2008, Cui et al., 2011, Wang et al., 2008, Shi et al., 2013). The results in this study in which a facile method was used to prepare the PCM nanocomposites are however comparable to those of Shi et al. (2013) and Xiang and Drzal (2011) who dispersed GNPs into paraffin waxes. Yavari et al. (2011) also obtained similar results with graphene (reduced graphene oxide) dispersed in stearyl alcohol.

In agreement with the results of Wang et al. (2008), the thermal conductivity of the PCM/GNPs (Table 9-4) is marginally higher in the solid state up to 5 wt.% GNPs. However, at 10 wt.%, the conductivity in the molten state is higher than in the solid state, which is an anomaly.

9.3.1 Thermal conductivity modelling

The thermal conductivity of PCM/dispersed conductive particulates nanocomposites is influenced by the inherent conductivity of the two separate phases, the composition of the composite, the size, geometry and distribution of the particulates and the interfacial nature between the PCM matrix and the nanoparticles (Khodadadi et al., 2013).

Nan et al. (1997) proposed a thermal conductivity model based on the Maxwell-Garnett-type effective medium approach for predicting the thermal conductivity of particulate composites. This model considers the interfacial thermal resistance between the particulates and matrix and also the particle geometry (Chapter 3).

The Nan et al. (1997) model was used to fit the room temperature (22 °C) solid state thermal conductivity data of the PCM nanocomposites obtained in this study. The d_{50} particle size of 13 μm was used as the GNPs diameter, and the estimated thickness of 76 nm as the GNP thickness. The graphite in-plane conductivity of 3000 W m^{-1} k^{-1} and through plane conductivity of 6 W m^{-1} k^{-1} where used for graphite. Figure 9-10 shows the room temperature experimental data and a fit of the Nan model. This fit was obtained with an interfacial thermal resistance of 4.03 x 10^{-8} m^2 K W^{-1} (equivalent to an interfacial thermal conductance of 25 MW m^{-2} K^{-1}) between the GNPs and the PCM matrix. The order of magnitude (10^{-8}

m^2 K W^{-1}) for the interfacial thermal resistance obtained by fitting the Nan model is similar to that obtained by Xiang and Drzal (2011) for paraffin PCM/GNPs nanocomposites. However, Xiang and Drzal (2011) fit a version of Nan's model (Nan et al., 2004), more applicable to carbon nanotube nanocomposites to their paraffin PCM/GNPs nanocomposites thermal conductivity data. They obtained a good fit with interfacial thermal resistance of 9 x 10^{-8} m^2 K W^{-1}, which is more than twice higher the value obtained in this study. Simulations by Nan et al. (2004), Clancy et al. (2010) and Xiang and Drzal (2011) showed that this difference has a significant impact on the enhancement of the thermal conductivity of the nanocomposites. In fact these studies showed that if the interfacial thermal resistance is beyond 10 x 10^{-8} m^2 K W^{-1}, no appreciable thermal conductivity enhancement will occur.

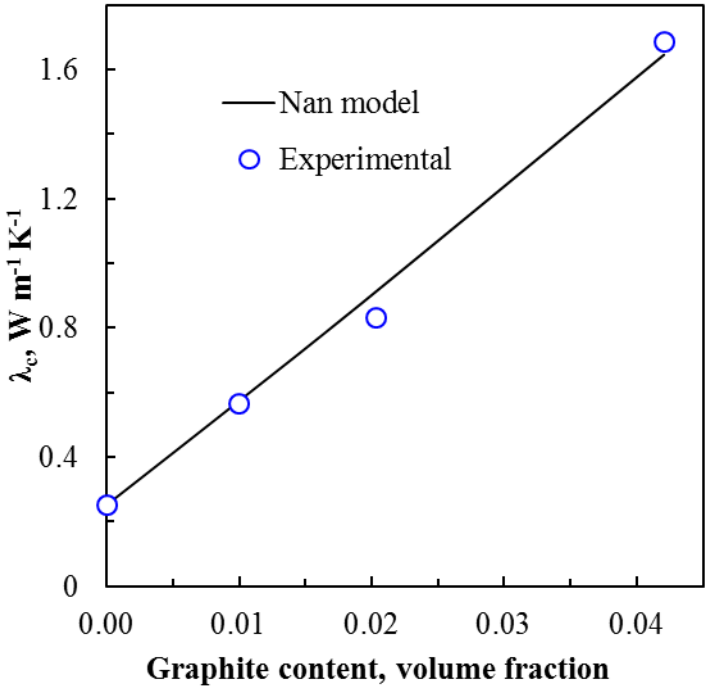

Figure 9-10 A fit of the Nan model to the Thermal conductivity data of stearyl alcohol/stearic acid PCM/GNPs nanocomposites.

The interfacial thermal resistance can be reduced by improving the interfacial interaction between the conductive fillers and the PCM matrix ideally through covalent bonding and also by increasing the aspect ratio of the GNPs. The FESEM micrograph in Figure 9-6a showed that the PCM matrix completely covered the GNPs, evidence of good interfacial interaction. It is known that the oxidative intercalation process used to produce GNPs introduces some

oxygen moieties on the GNPs. These could have possibly interacted with the carboxylic acid and alcohol groups on the PCM matrix through hydrogen bonding, resulting in improved interfacial adhesion.

9.3.2 Thermal stability of the PCM/Graphite nanoplatelets nanocomposites

The thermal stability of the PCM/GNP nanocomposites was evaluated through accelerated thermal cycling tests and settling tests of the PCM/GNPs nanocomposite in the molten state. PCM/GNPs nanocomposites in this study were subjected to 100 melt/freeze cycles in the DSC at a heating rate of 10 °C min^{-1}. The advantage of using the DSC for the cycling tests was that it could be directly observed if there was any deterioration in the melting and crystallization temperatures and enthalpies or if there any super cooling occurred with an increase in the number of cycles. The results in Figure 9-9 showed that the PCM/GNPs nanocomposites exhibited no deterioration for 100 melt/freeze cycles. Previous studies also showed high thermal stability for eutectic mixtures of a straight chain fatty acid and *n*-alkanol (Zuo et al., 2011a). This present study however also showed that the inclusion of the GNPs in the PCMs does not deteriorate their properties after 100 melt/freeze cycles. According to the standard RAL-GZ 896, the PCM/GNPs nanocomposites would be classified under the category E.

Phase separation between the GNPs and the PCM is undesirable as the GNPs will not contribute in the enhancement of the thermal conductivity. The settling tests therefore evaluated the long term stability of the PCM/GNPs nanocomposites. The results in Appendix D showed that only the PCM/GNPs nanocomposites at 10 wt.% GNPs was stable for at least 60 days, with separation occurring between the PCM matrix and GNPs in the other nanocomposites. The FESEM micrograph in Figure 9-6b shows that in the PCM/GNPs nanocomposites formed at a loading of 10 wt.% GNPs, the graphite nanoplates are aligned in a random manner forming a structure which prevents the PCMs from freely flowing and making a separate phase. At 10 wt.% GNPs, a formstable PCM/GNP nanocomposite is formed.

Chapter 10 Conclusions and Recommendations

Commercial expandable graphites exhibit different exfoliation efficiencies. Microwave radiation exfoliates expandable graphite more efficiently than furnace heating. Graphite nanoplatelets with thicknesses below 100 nm that retain lateral dimensions in the micrometre range can be conveniently prepared from expandable graphite by ultrasonic treatment of microwave-exfoliated material in isopropanol and several other media. Although the surface tension and solubility parameters of isopropanol are dissimilar to those recommended for the liquid exfoliation of graphite, its vapour pressure and viscosity are favourable for acoustic cavitation. Isopropanol also had the lowest boiling point for all liquid exfoliation media considered, hence easier recovery of the graphite nanoplatelets. Commercial expandable graphites are high stage compounds; hence they limit the thinness of graphite nanoplatelets obtained from them.

Rotomoulding blends of polyethylene powder with small amounts of graphite nanoplatelets yields antistatic and even conductive parts at graphite loadings below 0.5 wt.%. While the tensile strength of the base polymer is largely retained, the impact properties are significantly compromised. This problem can be partially overcome by moulding bilayer sheets using the double dumping rotomoulding technique with only the outer layer containing the filler. It is even possible to mould an antistatic part with bilayer structure that features both antistatic and good fire performance in cone calorimeter testing. This was achieved using a 1 mm outer EVA layer containing 0.25 wt.% graphite nanoplatelets together with 10 wt.% expandable graphite and a 2 mm inner layer of neat polyethylene. The outer surface resistance of the resultant sheet was $10^6\ \Omega\ \square^{-1}$, the tensile strength was 16 MPa, the impact resistance 6 J mm^{-1} and the cone calorimeter peak heat release rate ca. 259 kW m^{-2}. The corresponding values for polyethylene were $>10^{14}\ \Omega\ \square^{-1}$, 28 MPa, 12 J mm^{-1} and > 720 kW m^{-2}.

A pseudo binary stearyl alcohol-commercial stearic acid mixture with a single endotherm and exotherm at the melting and crystallization transitions, respectively, can be synthesized as a new phase change material for energy storage. Although the melting and crystallization enthalpies of the phase change material are lower than those of the stearyl alcohol and stearic acid, the PCM exhibits no super cooling. A facile synthesis method can be used to prepare stearyl alcohol-commercial stearic acid PCM/graphite nanoplatelets nanocomposites.

Addition of graphite nanoplatelets into this PCM matrix decreases the enthalpies marginally with an increase in graphite content. However, the PCM/GNPs nanocomposites feature reproducible melting and crystallization characteristics and exhibit no super cooling. Inclusion of the GNPs in to the PCM matrices nanocomposites results in substantial thermal conductivity enhancements of about 600 % and 1200 % in the solid and liquid state, respectively, at 10 wt.% GNPs loading. Thermal conductivity modelling shows that this high thermal conductivity is as a result of relatively lower interfacial thermal resistance between the PCM and GNPs. Thermal cycling tests shows that the PCM/GNPs nanocomposite are thermally cyclable for at least 100 melt/freeze cycles. Settling tests at 80 °C show that at a GNPs content of 10 wt.%, the PCM forms a structure which prevents phase separation between the GNPs and the PCM matrix.

In order to exercise control on the thickness and lateral dimensions of the final graphite nanoplatelets obtained, it is recommended that expandable graphite should be synthesized and characterized prior to exfoliating it, rather than using commercial expandable graphites of unknown treatment history.

It is also recommended that the prior mixing methods (pre-coating method, masterbatch technique and solid state shear pulverization) which have been used in fabricating polymer nanocomposites with graphite nanoplatelets be extended to rotomoulding nanocomposites. These methods, combined with melt compounding, were found to evenly disperse nanofillers and result in nanocomposites with excellent mechanical properties, low conductivity percolation thresholds and high conductivities at low filler loadings.

The poor impact properties exhibited by the rotomoulded polymer graphite nanocomposites could be as a result of poor sinterability. It is recommended that sinterability studies of the polymer graphite nanocomposite powders be carried out. The studies could also include the utility of sintering enhancers such as low molecular weight additives.

The utility PCM/GNPs nanocomposites fabricated in this study should be evaluated on a complete latent heat thermal energy storage (LHTES) unit to evaluate their effectiveness.

References

Abdullah, M. Z., Bickerton, S., Bhattacharyya, D., Crawford, R. & Harkin-Jones, E. 2009. Rotational molding cycle time reduction using a combination of physical techniques. *Polymer Engineering & Science,* **49,** 1846-1854.

Agari, Y., Ueda, A. & Nagai, S. 1991. Thermal conductivities of composites in several types of dispersion systems. *Journal of Applied Polymer Science,* **42,** 1665-1669.

Agari, Y., Ueda, A. & Nagai, S. 1993. Thermal conductivity of a polymer composite. *Journal of Applied Polymer Science,* **49,** 1625-1634.

Ambrosi, A., Chua, C. K., Bonanni, A. & Pumera, M. 2014. Electrochemistry of graphene and related materials. *Chemical Reviews,* **114,** 7150-7188.

An, J.-C., Kim, H. J. & Hong, I. 2014. Preparation of Kish graphite-based graphene nanoplatelets by GIC (graphite intercalation compound) via process. *Journal of Industrial and Engineering Chemistry*.

Anderson, S. & Chung, D. 1984. Exfoliation of intercalated graphite. *Carbon,* **22,** 253-263.

Andrews, S. 2011. Additives. In: Seidel, A. (Ed.) *Processing and finishing of polymeric materials* Hoboken, New Jersey, USA: John Wiley & Sons, Inc.

Ansari, R. & Keivani, M. 2006. Polyaniline conducting electroactive polymers thermal and environmental stability studies. *Journal of Chemistry,* **3,** 202-217.

Asakura, Y., Nishida, T., Matsuoka, T. & Koda, S. 2008. Effects of ultrasonic frequency and liquid height on sonochemical efficiency of large-scale sonochemical reactors. *Ultrasonics sonochemistry,* **15,** 244-250.

Ashokkumar, M. 2011. The characterization of acoustic cavitation bubbles – An overview. *Ultrasonics Sonochemistry,* **18,** 864-872.

Ashokkumar, M., Lee, J., Kentish, S. & Grieser, F. 2007. Bubbles in an acoustic field: an overview. *Ultrasonics Sonochemistry,* **14,** 470-475.

ASTM 2010. ASTM D5628 - 10 Standard Test Method for Impact Resistance of Flat, Rigid Plastic Specimens by Means of a Falling Dart (Tup or Falling Mass). West Conshohocken, PA: ASTM International.

Atchley, A. A. 1989. The Blake threshold of a cavitation nucleus having a radius-dependent surface tension. *The Journal of the Acoustical Society of America,* **85,** 152-157.

Aydın, A. A. 2013. Fatty acid ester-based commercial products as potential new phase change materials (PCMs) for thermal energy storage. *Solar Energy Materials and Solar Cells,* **108,** 98-104.

Bader, K. B., Raymond, J. L., Mobley, J., Church, C. C. & Gaitan, D. F. 2012. The effect of static pressure on the inertial cavitation threshold. *The Journal of the Acoustical Society of America,* **132,** 728-737.

Balandin, A. A. 2011. Thermal properties of graphene and nanostructured carbon materials. *Nature materials,* **10,** 569-581.

Barboza Neto, E. S., Coelho, L. A. F., Forte, M. M. d. C., Amico, S. C. & Ferreira, C. A. 2014. Processing of a LLDPE/HDPE pressure vessel liner by rotomolding. *Materials Research,* **17,** 236-241.

Baumer, M. I., Leite, J. L. & Becker, D. 2014. Influence of calcium carbonate and slip agent addition on linear medium density polyethylene processed by rotational molding. *Materials Research,* **17,** 130-137.

Beall, G. 1998. *Rotational Molding: Design, Materials, Tooling, and Processing,* Munich, Germany, Hanser Verlag.

Beall, G. 2000. The What, How and Why of Rotational Molding *Proceedings, ANTEC 2000 Plastics: The Magical Solution* Volume 1: Processing, May 7-11 2000 Orlando, Florida, USA. Society of Plastics Engineers.

Behabtu, N., Lomeda, J. R., Green, M. J., Higginbotham, A. L., Sinitskii, A., Kosynkin, D. V., Tsentalovich, D., Parra-Vasquez, A. N. G., Schmidt, J. & Kesselman, E. 2010. Spontaneous high-concentration dispersions and liquid crystals of graphene. *Nature nanotechnology,* **5,** 406-411.

Bellehumeur, C. 2005. Rotational Molding of Polymers. In: Sunggyu, E. (Ed.) *Encyclopedia of Chemical Processing.* New York, US: Taylor & Francis.

Bellehumeur, C., Bisaria, M. & Vlachopoulos, J. 1996. An experimental study and model assessment of polymer sintering. *Polymer Engineering & Science,* **36,** 2198-2207.

Bellehumeur, C. T., Kontopoulou, M. & Vlachopoulos, J. 1998. The role of viscoelasticity in polymer sintering. *Rheologica acta*, **37,** 270-278.

Bigg, D. 1995. Thermal conductivity of heterophase polymer compositions. *Advances in Polymer Science* **119,** 1-30.

Blake, P., Brimicombe, P. D., Nair, R. R., Booth, T. J., Jiang, D., Schedin, F., Ponomarenko, L. A., Morozov, S. V., Gleeson, H. F. & Hill, E. W. 2008. Graphene-based liquid crystal device. *Nano letters,* **8,** 1704-1708.

Boehm, H. P., Setton, R. & Stumpp, E. 1994. Nomenclature and terminology of graphite intercalation compounds (IUPAC Recommendations 1994). *Pure and Applied Chemistry,* **66,** 1893-1901.

Bourlinos, A. B., Georgakilas, V., Zboril, R., Steriotis, T. A. & Stubos, A. K. 2009a. Liquid-Phase Exfoliation of Graphite Towards Solubilized Graphenes. *Small,* **5,** 1841-1845.

Bourlinos, A. B., Georgakilas, V., Zboril, R., Steriotis, T. A., Stubos, A. K. & Trapalis, C. 2009b. Aqueous-phase exfoliation of graphite in the presence of polyvinylpyrrolidone for the production of water-soluble graphenes. *Solid State Communications,* **149,** 2172-2176.

Brownson, D. A., Kampouris, D. K. & Banks, C. E. 2012. Graphene electrochemistry: fundamental concepts through to prominent applications. *Chemical Society Reviews,* **41,** 6944-6976.

Bui, K., Duong4, H. M., Striolo, A. & Papavassiliou, D. V. 2011. Effective heat transfer properties of graphene sheet nanocomposites and comparison to carbon nanotube nanocomposites. *The Journal of Physical Chemistry C,* **115,** 3872-3880.

Calò, E., Massaro, C., Terzi, R., Cancellara, A., Pesce, E., Re, M., Greco, A., Maffezzoli, A., Gonzalez-Chi, P. & Salomi, A. 2012. Rotational molding of polyamide-6 nanocomposites with improved flame retardancy. *International Polymer Processing,* **27,** 370-377.

Camino, G., Costa, L. & Martinasso, G. 1989. Intumescent fire-retardant systems. *Polymer Degradation and Stability,* **23,** 359-376.

Camino, G., Duquesne, S., Delobel, R., Eling, B., Lindsay, C. & Roels, T. 2001. Mechanism of Expandable Graphite Fire Retardant Action in Polyurethanes. In: *Fire and Polymers.* American Chemical Society.

Campbell, R. W. & Tan, W. 1995. Use of static-safe polymers in automated handling equipment. *Proceedings, Electrical Overstress/Electrostatic Discharge Symposium,* Sept. 12-14 1995 Bordeaux, France. IEEE, 218-224.

Carotenuto, G., De Nicola, S., Palomba, M., Pullini, D., Horsewell, A., Hansen, T. W. & Nicolais, L. 2012. Mechanical properties of low-density polyethylene filled by graphite nanoplatelets. *Nanotechnology,* **23,** 485705.

Castellón, C., Günther, E., Mehling, H., Hiebler, S. & Cabeza, L. F. 2008. Determination of the enthalpy of PCM as a function of temperature using a heat-flux DSC—A study of different measurement procedures and their accuracy. *International Journal of Energy Research,* **32,** 1258-1265.

Chae, H. K., Siberio-Pérez, D. Y., Kim, J., Go, Y., Eddaoudi, M., Matzger, A. J., O'Keeffe, M. & Yaghi, O. M. 2004. A route to high surface area, porosity and inclusion of large molecules in crystals. *Nature,* **427,** 523-527.

Chandran V, G. & Waigaonkar, S. D. 2015. Rheological and dynamic mechanical characteristics of rotationally moldable linear low-density polyethylene fumed silica nanocomposites. *Polymer Composites***,** n/a-n/a.

Chang, W., Harkin-Jones, E., Kearns, M. & McCourt, M. 2011. Glass Fibre-Reinforced Polyethylene Composites in Rotational Moulding. *Proceedings, ANTEC 2011 Plastics: Annual Technical Conference Proceedings*, May 1-5 2011 Boston, Massachusetts, USA. Society of Plastics Engineers.

Chaudhary, B. I., Takacs, E. & Vlachopoulos, J. 2001a. Processing enhancers for rotational molding of polyethylene. *Polymer engineering and science,* **41,** 1731.

Chaudhary, B. I., Takacs, E. & Vlachopoulos, J. 2002. Ethylene copolymers as sintering enhancers and impact modifiers for rotational molding of polyethylene. *Polymer Engineering & Science,* **42,** 1359-1369.

Chaudhary, B. I., Takács, E. & Vlachopoulos, J. 2001b. Processing enhancers for rotational molding of polyethylene. *Polymer Engineering & Science,* **41,** 1731-1742.

Chen, G., Chen, X., Wang, H. & Wu, D. 2007. Dispersion of graphite nanosheets in polymer resins via masterbatch technique. *Journal of applied polymer science,* **103,** 3470-3475.

Chen, G., Weng, W., Wu, D. & Wu, C. 2003. PMMA/graphite nanosheets composite and its conducting properties. *European Polymer Journal,* **39,** 2329-2335.

Chen, G., Weng, W., Wu, D., Wu, C., Lu, J., Wang, P. & Chen, X. 2004. Preparation and characterization of graphite nanosheets from ultrasonic powdering technique. *Carbon,* **42,** 753-759.

Cheng, Q., Debnath, S., Gregan, E. & Byrne, H. J. 2010. Ultrasound-assisted SWNTs dispersion: effects of sonication parameters and solvent properties. *The Journal of Physical Chemistry C,* **114,** 8821-8827.

Cho, D., Lee, S., Yang, G., Fukushima, H. & Drzal, L. T. 2005. Dynamic Mechanical and Thermal Properties of Phenylethynyl-Terminated Polyimide Composites Reinforced With Expanded Graphite Nanoplatelets. *Macromolecular Materials and Engineering,* **290,** 179-187.

Choi, E.-Y., San Choi, W., Lee, Y. B. & Noh, Y.-Y. 2011a. Production of graphene by exfoliation of graphite in a volatile organic solvent. *Nanotechnology,* **22,** 365601.

Choi, S. Y., Mamak, M., Cordola, E. & Stadler, U. 2011b. Large scale production of high aspect ratio graphite nanoplatelets with tunable oxygen functionality. *Journal of Materials Chemistry,* **21,** 5142-5147.

Chung, D. 1978. Structural studies of graphite intercalation compounds. *Journal of Electronic Materials,* **7,** 189-210.

Chung, D. 2002. Review graphite. *Journal of materials science,* **37,** 1475-1489.

Chung, D. D. L. 1987. Exfoliation of graphite. *Journal of Materials Science,* **22,** 4190-4198.

Clancy, T. C., Frankland, S.-J. V., Hinkley, J. A. & Gates, T. S. 2010. Multiscale modeling of thermal conductivity of polymer/carbon nanocomposites. *International Journal of Thermal Sciences,* **49,** 1555-1560.

Clingerman, M. L., King, J. A., Schulz, K. H. & Meyers, J. D. 2002. Evaluation of electrical conductivity models for conductive polymer composites. *Journal of Applied Polymer Science,* **83,** 1341-1356.

Coleman, J. N. 2012. Liquid exfoliation of defect-free graphene. *Accounts of chemical research,* **46,** 14-22.

Commission, I. E. 2000. IEC 61340-2-3:2000 Electrostatics - Part 2-3: Methods of test for determining the resistance and resistivity of solid planar materials used to avoid electrostatic charge accumulation. International Electrotechnical Commission.

Costa, M. C., Rolemberg, M. P., Meirelles, A. J., Coutinho, J. A. & Krähenbühl, M. 2009. The solid–liquid phase diagrams of binary mixtures of even saturated fatty acids differing by six carbon atoms. *Thermochimica Acta,* **496,** 30-37.

Cramez, M., Oliveira, M. & Crawford, R. 1998a. Effect of pigmentation on the microstructure and properties of rotationally molded polyethylene. *Journal of materials science,* **33,** 4869-4877.

Cramez, M., Oliveira, M. & Crawford, R. 1998. Relationship between the Microstructure and the Properties of Rotationally Moulded Plastics. *Proceedings, ANTEC 1998 Plastics: Plastics on My Mind* Volume 1: Processing, April 26-30 1998b Atlanta, Georgia, US. Society of Plastics Engineers.

Cramez, M., Oliveira, M. & Crawford, R. 2001. Effect of nucleating agents and cooling rate on the microstructure and properties of a rotational moulding grade of polypropylene. *Journal of materials science,* **36,** 2151-2161.

Cramez, M., Oliveira, M. & Crawford, R. 2003. Optimization of the rotational moulding process for polyolefins. *Proceedings of the Institution of Mechanical Engineers, Part B: Journal of Engineering Manufacture,* **217,** 323-334.

Cramez, M. C., Oliveira, M. J. & Crawford, R. J. 2002. Optimisation of rotational moulding of polyethylene by predicting antioxidant consumption. *Polymer Degradation and Stability,* **75,** 321-327.

Cravotto, G. & Cintas, P. 2010. Sonication-Assisted Fabrication and Post-Synthetic Modifications of Graphene-Like Materials. *Chemistry – A European Journal,* **16,** 5246-5259.

Crawford, R. & Gibson, S. 2006. Rotationl molding: the basics for designers. *Rotoworld,* **March-April,** 60-66.

Crawford, R. & Nugent, P. 1992. A new process control system for rotational moulding. *Plastics rubber and composites processing and applications,* **17,** 23-31.

Crawford, R., Spence, A. & Silva, C. 1996. Effects of Pigmentation on the Impact Strength of Rotationally Moulded Polyethylene. *Proceedings, ANTEC 1996 Plastics: Plastics - Racing into the Future,* Volume 3: Special Areas, May 5-10 1996 Indianapolis, Indiana, US. Society of Plastics Engineers.

Crawford, R. J. 1996. Recent advances in the manufacture of plastic products by rotomoulding. *Journal of Materials Processing Technology,* **56,** 263-271.

Crawford, R. J. & Throne, J. L. 2002. *Rotational Molding Technology,* New York, US, Plastcis Desing Library/William Andrew Publishing.

Cui, Y., Liu, C., Hu, S. & Yu, X. 2011. The experimental exploration of carbon nanofiber and carbon nanotube additives on thermal behavior of phase change materials. *Solar Energy Materials and Solar Cells,* **95,** 1208-1212.

Dahman, S. J. 2003. All polymeric compounds: Conductive and dissipative polymers in ESD control materials. *Proceedings, Electrical Overstress/Electrostatic Discharge Symposium,* Sept. 12-14 2003 Bordeaux, France.

Dasari, A., Yu, Z. Z., Cai, G. P. & Mai, Y. W. 2013. Recent developments in the fire retardancy of polymeric materials. *Progress in Polymer Science,* **38,** 1357-1387.

DeArmitt, C. & Hancock, M. 2003. Filled Thermoplastics. In: Rothon, R. N. (Ed.) *Particulate-Filled Polymer Composites (2nd Edition).* Shrewsbury, UK: Smithers Rapra Technology Ltd.

Dodge, P. & Perry, J. 2001. Rotomolded Part Density and Its Relationship to Physical Properties. *Proceedings, ANTEC 2001 Plastics: The Lone Star* Volume 1: Processing, May 6-10 2001 Dallas, Texas. Society of Plastics Engineers.

Dong, H., Fan, L. & Wong, C. 2005. Effect of interface on thermal conductivity of polymer composite. *Proceedings*, 55th Electronic Components and Technology Conference, May 31- June 3 2005 Lake Buena Vista, Florida, US. IEEE, 1451-1454.

Dresselhaus, M. & Dresselhaus, G. 1981. Intercalation compounds of graphite. *Advances in Physics,* **30,** 139-326.

Du, W., Jiang, X. & Zhu, L. 2013. From graphite to graphene: direct liquid-phase exfoliation of graphite to produce single-and few-layered pristine graphene. *Journal of Materials Chemistry A,* **1,** 10592-10606.

Ebert, L. B. 1976. Intercalation compounds of graphite. *Annual Review of Materials Science,* **6,** 181-211.

Elgafy, A. & Lafdi, K. 2005. Effect of carbon nanofiber additives on thermal behavior of phase change materials. *Carbon,* **43,** 3067-3074.

Falcao, E. H., Blair, R. G., Mack, J. J., Viculis, L. M., Kwon, C.-W., Bendikov, M., Kaner, R. B., Dunn, B. S. & Wudl, F. 2007. Microwave exfoliation of a graphite intercalation compound. *Carbon,* **45,** 1367-1369.

Fan, L. & Khodadadi, J. 2011. Thermal conductivity enhancement of phase change materials for thermal energy storage: a review. *Renewable and Sustainable Energy Reviews,* **15,** 24-46.

Farid, M. M., Khudhair, A. M., Razack, S. A. K. & Al-Hallaj, S. 2004. A review on phase change energy storage: materials and applications. *Energy conversion and management,* **45,** 1597-1615.

Focke, W. W., Badenhorst, H., Mhike, W., Kruger, H. J. & Lombaard, D. 2014. Characterization of commercial expandable graphite fire retardants. *Thermochimica Acta,* **584,** 8-16.

Forsman, W., Dziemianowicz, T., Leong, K. & Carl, D. 1983. Graphite intercalation chemistry: an interpretive review. *Synthetic Metals,* **5,** 77-100.

Fu, S.-Y., Feng, X.-Q., Lauke, B. & Mai, Y.-W. 2008. Effects of particle size, particle/matrix interface adhesion and particle loading on mechanical properties of particulate–polymer composites. *Composites Part B: Engineering,* **39,** 933-961.

Fu, W., Kiggans, J., Overbury, S. H., Schwartz, V. & Liang, C. 2011. Low-temperature exfoliation of multilayer-graphene material from FeCl 3 and CH 3 NO 2 co-intercalated graphite compound. *Chemical Communications,* **47,** 5265-5267.

Fukushima, H. 2003. *Graphite nanoreinforcements in polymer nanocomposites.* PhD, Michigan State University, US.

Furdin, G. 1998. Exfoliation process and elaboration of new carbonaceous materials. *Fuel,* **77,** 479-485.

Gandolfo, F. G., Bot, A. & Flöter, E. 2003. Phase diagram of mixtures of stearic acid and stearyl alcohol. *Thermochimica acta,* **404,** 9-17.

Garti, N., Sarig, S. & Wellner, E. 1980. Determination of the composition of mixtures of fatty acid polymorphs by DTA. *Thermochimica Acta,* **37,** 131-136.

Gbabode, G., Negrier, P., Mondieig, D., Moreno, E., Calvet, T. & Cuevas-Diarte, M. À. 2009. Fatty acids polymorphism and solid-state miscibility: Pentadecanoic acid–hexadecanoic acid binary system. *Journal of Alloys and Compounds,* **469,** 539-551.

Geim, A. K. & Novoselov, K. S. 2007. The rise of graphene. *Nature materials,* **6,** 183-191.

Godinho, J. E. M. d. S., Cunha, J. & Crawford, R. J. 1997. *Property variations in polyethylene articles produced by a variety of moulding methods.* Queen's University of Belfast.

Gogos, G. 2004. Bubble removal in rotational molding. *Polymer Engineering & Science,* **44,** 388-394.

Greco, A. & Maffezzoli, A. 2004. Powder-shape analysis and sintering behavior of high-density polyethylene powders for rotational molding. *Journal of applied polymer science,* **92,** 449-460.

Greco, A., Maffezzoli, A., Calò, E., Massaro, C. & Terzi, R. 2012. An investigation into sintering of PA6 nanocomposite powders for rotational molding. *Journal of Thermal Analysis and Calorimetry,* **109,** 1493-1502.

Green, A. A. & Hersam, M. C. 2009. Solution phase production of graphene with controlled thickness via density differentiation. *Nano Letters,* **9,** 4031-4036.

Gschwander, S., Haussmann, T., Hagelstein, G., Sole, A., Cabeza, L. F., Diarce, G., Hohenauer, W., Lager, D., Ristic, A. & Rathgeber, C. 2015. Standardization of PCM Characterization via DSC. *Proceedings,* Greenstock 13th International Conference on Energy Storage, May 19-21 2015 Beijing, China.

Gu, W., Zhang, W., Li, X., Zhu, H., Wei, J., Li, Z., Shu, Q., Wang, C., Wang, K. & Shen, W. 2009. Graphene sheets from worm-like exfoliated graphite. *J. Mater. Chem.,* **19,** 3367-3369.

Guardia, L., Fernández-Merino, M., Paredes, J., Solis-Fernandez, P., Villar-Rodil, S., Martinez-Alonso, A. & Tascón, J. 2011. High-throughput production of pristine graphene in an aqueous dispersion assisted by non-ionic surfactants. *Carbon,* **49,** 1653-1662.

Gunstone, F. D., Harwood, J. L. & Dijkstra, A. J. 2007. *The lipid handbook with CD-ROM,* CRC press.

Günther, E., Hiebler, S., Mehling, H. & Redlich, R. 2009. Enthalpy of phase change materials as a function of temperature: required accuracy and suitable measurement methods. *International Journal of Thermophysics,* **30,** 1257-1269.

Hamilton, C. E., Lomeda, J. R., Sun, Z., Tour, J. M. & Barron, A. R. 2009. High-yield organic dispersions of unfunctionalized graphene. *Nano letters,* **9,** 3460-3462.

Hanna, P., McNally, G., Kassick, J., Kearns, M. & Murphy, W. 2006. The Effect of Polyethylene Catalyst Type and Pigment Concentration on Crystal Growth During Rotomoulding. *Proceedings, ANTEC 2006 Plastics: Annual Technical Conference Proceedings*, May 7-11 2006 Charlotte, North Carolina, US. Society of Plastics Engineers.

Hanna, P., McNally, M., Harkin-Jones, E. & McMillian, P. 2003. Mechanical Properties of Rotationally Moulded Nanocomposites. *Proceedings, ANTEC 2003 Plastics: Annual Technical Conference* Volume 1: Processing, May 4-8 2003 Nashville, Tennessee, US. Society of Plastics Engineers.

Harkin-Jones, E. & Ryan, S. 1996. The effect of process and material parameters on the morphology and mechanical properties of rotatlonally moulded polyethylene. *Proceedings, ANTEC 1996,* Volume 2: Materials, May 5-10 1996 Indianapolis,Indiana, US.

Harkin-Jones, E. & Crawford, R. 1996. Mechanical properties of rotationally molded nyrim. *Polymer Engineering & Science,* **36,** 615-625.

Harvey, G., Gachagan, A. & Mutasa, T. 2014. Review of high-power ultrasound-industrial applications and measurement methods. *IEEE Transactions on Ultrasonics, Ferroelectrics, and Frequency Control,* **61,** 481-495.

Haznedar, G., Cravanzola, S., Zanetti, M., Scarano, D., Zecchina, A. & Cesano, F. 2013. Graphite nanoplatelets and carbon nanotubes based polyethylene composites: electrical conductivity and morphology. *Materials Chemistry and Physics,* **143,** 47-52.

Hennig, G. 1952. The Properties of the Interstitial Compounds of Graphite. II. The Structure and Stability of Graphite Residue Compounds. *The Journal of Chemical Physics,* **20,** 1438-1442.

Hennig, G. 1955. Properties of Graphite Compounds. *Proceedings, Carbon 1955*, June 1955 Buffalo, New York,US.

Henwood, N., Roberts, M., Quaratino, A., Collins, S., Sharifi, P., Liauw, C. & Lees, G. 2005. Removing the Mystery from Rotomoulding. *Proceedings, ANTEC 2005 Plastics: Annual Technical Conference* Volume 1: Processing, May 1-5 2005 Boston, Massachusetts, US. Society of Plastics Engineers.

Hernandez, Y., Lotya, M., Rickard, D., Bergin, S. D. & Coleman, J. N. 2009. Measurement of multicomponent solubility parameters for graphene facilitates solvent discovery. *Langmuir,* **26,** 3208-3213.

Hernandez, Y., Nicolosi, V., Lotya, M., Blighe, F. M., Sun, Z., De, S., McGovern, I. T., Holland, B., Byrne, M., Gun'Ko, Y. K., Boland, J. J., Niraj, P., Duesberg, G., Krishnamurthy, S., Goodhue, R., Hutchison, J., Scardaci, V., Ferrari, A. C. & Coleman, J. N. 2008. High-yield production of graphene by liquid-phase exfoliation of graphite. *Nat Nano,* **3,** 563-568.

Hill, R. F. & Supancic, P. H. 2002. Thermal Conductivity of Platelet-Filled Polymer Composites. *Journal of the American Ceramic Society,* **85,** 851-857.

Hoàng, E. M., Allen, N. S., Liauw, C. M., Fontán, E. & Lafuente, P. 2006. The thermo-oxidative degradation of metallocene polyethylenes: Part 2: Thermal oxidation in the melt state. *Polymer degradation and stability,* **91,** 1363-1372.

Huang, J., Lu, S., Kong, X. & Liu, S. 2013. Form-stable phase change materials based on eutectic mixture of tetradecanol and fatty acids for building energy storage: preparation and performance analysis. *Materials,* **6,** 4758-4775.

Hull, T. R., Witkowski, A. & Hollingbery, L. 2011. Fire retardant action of mineral fillers. *Polymer Degradation and Stability,* **96,** 1462-1469.

Inagaki, M. 1966. On the formation and decomposition of graphite-bisulfate. *Carbon,* **4,** 137-141.

Inagaki, M., Iwashita, N. & Kouno, E. 1990. Potential change with intercalation of sulfuric acid into graphite by chemical oxidation. *Carbon,* **28,** 49-55.

Inagaki, M., Rouillon, J., Füg, G. & Delhaes, P. 1977. Physical properties of graphite-nitrate residue compound. *Carbon,* **15,** 181-185.

Inagaki, M., Tashiro, R., Washino, Y.-i. & Toyoda, M. 2004. Exfoliation process of graphite via intercalation compounds with sulfuric acid. *Journal of Physics and Chemistry of solids,* **65,** 133-137.

Iring, M. & Tüdő, F. 1990. Thermal oxidation of polyethylene and polypropylene: Effects of chemical structure and reaction conditions on the oxidation process. *Progress in polymer science,* **15,** 217-262.

Irvine, D. J., McCluskey, J. A. & Robinson, I. M. 2000. Fire hazards and some common polymers. *Polymer Degradation and Stability,* **67,** 383-396.

Jang, B. Z. & Zhamu, A. 2008. Processing of nanographene platelets (NGPs) and NGP nanocomposites: a review. *Journal of Materials Science,* **43,** 5092-5101.

Jiang, X. & Drzal, L. T. 2010. Multifunctional high density polyethylene nanocomposites produced by incorporation of exfoliated graphite nanoplatelets 1: Morphology and mechanical properties. *Polymer Composites,* **31,** 1091-1098.

Jiang, X. & Drzal, L. T. 2012. Multifunctional high-density polyethylene nanocomposites produced by incorporation of exfoliated graphene nanoplatelets 2: Crystallization, thermal and electrical properties. *Polymer Composites,* **33,** 636-642.

JojoTanks. 2016. *Vertical tanks* [Online]. http://www.jojotanks.co.za/index.php/products/vertical-tanks. [Accessed April 7 2016].

Jorio, A., Dresselhaus, M. S., Saito, R. & Dresselhaus, G. 2011. *Raman spectroscopy in graphene related systems*, John Wiley & Sons.

Kalaitzidou, K., Fukushima, H. & Drzal, L. T. 2007. A new compounding method for exfoliated graphite–polypropylene nanocomposites with enhanced flexural properties and lower percolation threshold. *Composites Science and Technology,* **67,** 2045-2051.

Kalaitzidou, K., Fukushima, H. & Drzal, L. T. 2010. A route for polymer nanocomposites with engineered electrical conductivity and percolation threshold. *Materials,* **3,** 1089-1103.

Kalyoncu, R. S., Taylor, H. A. & by Staff, U. 2005. Natural Graphite. In: Seidel, A. (Ed.) *Kirk-Othmer Encyclopedia of Chemical Technology*. Hoboken, New Jersey, US: John Wiley & Sons, Inc.

Kaneko, F., Tashiro, K. & Kobayashi, M. 1999. Polymorphic transformations during crystallization processes of fatty acids studied with FT-IR spectroscopy. *Journal of crystal growth,* **198,** 1352-1359.

Kang, F., Zheng, Y.-P., Wang, H.-N., Nishi, Y. & Inagaki, M. 2002. Effect of preparation conditions on the characteristics of exfoliated graphite. *Carbon,* **40,** 1575-1581.

Kearns, M. & Crawford, R. J. 2003. *Practical Guide to Rotational Moulding*, Smithers Rapra Press.

Kearns, M., McCourt, M. & Ervik, R. 2006. The Effect of Pigment on Rotomoulded Polyethylene Powder and Micropellets. *Proceedings, ANTEC 2006 Plastics: Annual Technical Conference Proceedings,* 7-11 May 2006 Charlotte, North Carolina, US. Society of Plastics Engineers.

Khan, U., O'Neill, A., Lotya, M., De, S. & Coleman, J. N. 2010. High-Concentration Solvent Exfoliation of Graphene. *Small,* **6,** 864-871.

Khodadadi, J., Fan, L. & Babaei, H. 2013. Thermal conductivity enhancement of nanostructure-based colloidal suspensions utilized as phase change materials for thermal energy storage: a review. *Renewable and Sustainable Energy Reviews,* **24,** 418-444.

Kim, S., Do, I. & Drzal, L. T. 2009. Multifunctional xGnP/LLDPE nanocomposites prepared by solution compounding using various screw rotating systems. *Macromolecular Materials and Engineering,* **294,** 196-205.

Kim, S., Seo, J. & Drzal, L. T. 2010a. Improvement of electric conductivity of LLDPE based nanocomposite by paraffin coating on exfoliated graphite nanoplatelets. *Composites Part A: Applied Science and Manufacturing*, **41,** 581-587.

Kim, S., Sergiienko, R., Shibata, E., Hayasaka, Y. & Nakamura, T. 2010b. Production of graphite nanosheets by low-current plasma discharge in liquid ethanol. *Materials transactions*, **51,** 1455-1459.

Kissick, J., Clarke, A., McNally, M. & Hanna, P. 2011. Inital Investigation into the Use of Silicon Dioxide as a Filler in Rotational Moulding of Polyethylene. *Proceedings, ANTEC 2011 Plastics: Annual Technical Conference Proceedings*, 2011 Boston, Massachusetts,US. Society of Plastics Engineers.

Kojima, Y., Koda, S. & Nomura, H. 1998. Effects of sample volume and frequency on ultrasonic power in solutions on sonication. *Japanese journal of applied physics*, **37,** 2992.

Kontopoulou, M. & Vlachopoulos, J. 1999. Bubble dissolution in molten polymers and its role in rotational molding. *Polymer Engineering & Science*, **39,** 1189-1198.

Kontopoulou, M. & Vlachopoulos, J. 2001. Melting and densification of thermoplastic powders. *Polymer Engineering & Science*, **41,** 155-169.

Laoutid, F., Bonnaud, L., Alexandre, M., Lopez-Cuesta, J. M. & Dubois, P. 2009. New prospects in flame retardant polymer materials: From fundamentals to nanocomposites. *Materials Science and Engineering: R: Reports*, **63,** 100-125.

Lazaro, A., Peñalosa, C., Solé, A., Diarce, G., Haussmann, T., Fois, M., Zalba, B., Gshwander, S. & Cabeza, L. F. 2013. Intercomparative tests on phase change materials characterisation with differential scanning calorimeter. *Applied Energy*, **109,** 415-420.

Lee, C., Wei, X., Kysar, J. W. & Hone, J. 2008. Measurement of the elastic properties and intrinsic strength of monolayer graphene. *science*, **321,** 385-388.

Leighton, T. 1995a. 9 The principles of cavitation. *Ultrasound in food processing***,** 151.

Leighton, T. 1995b. Bubble population phenomena in acoustic cavitation. *Ultrasonics Sonochemistry,* **2,** S123-S136.

Leonelli, C. & Mason, T. J. 2010. Microwave and ultrasonic processing: now a realistic option for industry. *Chemical Engineering and Processing: Process Intensification,* **49,** 885-900.

Leong, T., Ashokkumar, M. & Kentish, S. 2011. The fundamentals of power ultrasound—a review. *Acoust. Aust,* **39,** 54-63.

Lewin, M. 1999. Synergistic and catalytic effects in flame retardancy of polymeric materials - an overview. *Journal of Fire Sciences,* **17,** 3-19.

Li, B. & Zhong, W.-H. 2011. Review on polymer/graphite nanoplatelet nanocomposites. *Journal of materials science,* **46,** 5595-5614.

Li, X., Zhang, G., Bai, X., Sun, X., Wang, X., Wang, E. & Dai, H. 2008. Highly conducting graphene sheets and Langmuir–Blodgett films. *Nature nanotechnology,* **3,** 538-542.

Li, Y., Liang, J., Zhang, W., Qi, W., Su, M. & Liu, C. 2007. Study on processs and impact strength for a rotationally molded truck fender. *Journal of materials processing technology*, **187,** 492-496.

Li, Y. C. & Chen, G. H. 2007. HDPE/expanded graphite nanocomposites prepared via masterbatch process. *Polymer Engineering & Science*, **47,** 882-888.

Lide, D. R. 2005. *CRC Handbook of Chemistry and Physics,* Boca Raton, Florida, US, CRC Press.

Lin, C. & Chung, D. 2009. Graphite nanoplatelet pastes vs. carbon black pastes as thermal interface materials. *Carbon*, **47,** 295-305.

Liu, N., Luo, F., Wu, H., Liu, Y., Zhang, C. & Chen, J. 2008. One-step ionic-liquid-assisted electrochemical synthesis of ionic-liquid-functionalized graphene sheets directly from graphite. *Advanced Functional Materials,* **18,** 1518-1525.

Liu, S. J., Lai, C. C. & Lin, S. T. 2000. Optimizing the impact strength of rotationally molded parts. *Polymer Engineering & Science,* **40,** 473-480.

Liu, S. J. & Peng, K. M. 2010. Rotational molding of polycarbonate reinforced polyethylene composites: Processing parameters and properties. *Polymer Engineering & Science,* **50,** 1457-1465.

Liu, W., Wang, J. & Wang, X. 2012. Charging of unfunctionalized graphene in organic solvents. *Nanoscale,* **4,** 425-428.

López-Bañuelos, R., Moscoso, F., Ortega-Gudiño, P., Mendizabal, E., Rodrigue, D. & González-Núñez, R. 2012. Rotational molding of polyethylene composites based on agave fibers. *Polymer Engineering & Science,* **52,** 2489-2497.

Lorimer, J. & Mason, T. 2002. Applied Sonochemistry: Uses of power ultrasound in chemistry and Processing. *Federal Republic of Germany: Wiley-VCH.*

Lotya, M., Hernandez, Y., King, P. J., Smith, R. J., Nicolosi, V., Karlsson, L. S., Blighe, F. M., De, S., Wang, Z. & McGovern, I. 2009. Liquid phase production of graphene by exfoliation of graphite in surfactant/water solutions. *Journal of the American Chemical Society,* **131,** 3611-3620.

Lotya, M., King, P. J., Khan, U., De, S. & Coleman, J. N. 2010. High-concentration, surfactant-stabilized graphene dispersions. *ACS nano,* **4,** 3155-3162.

Lux, F. 1993. Models proposed to explain the electrical conductivity of mixtures made of conductive and insulating materials. *Journal of Materials Science,* **28,** 285-301.

Ma, Z., Yu, J. & Dai, S. 2010. Preparation of inorganic materials using ionic liquids. *Advanced Materials,* **22,** 261-285.

McClure, J. 1957. Band structure of graphite and de Haas-van Alphen effect. *Physical Review,* **108,** 612.

McCourt, M., McNally, G., Kearns, M., McConnell, D., Martinez-Cobler, M. & Murphy, W. 2005. The Effect of Pigmentation on Crystal Growth during Rotomoulding. *Proceedings, ANTEC 2005 Plastics: Annual Technical Conference* Volume 1: Processing, May 1-5 2005 Boston, Massachusetts, US. Society of Plastics Engineers.

McQuay, G., Fischer, J. & Muller, B. Rotational Molding Cycle Reduction by Preheating the Mold and the Polymer Powder. *Proceedings, ANTEC 2013 - Proceedings of the Technical Conference & Exhibition,* April 22-24 2013 Cincinnati, Ohio, USA Society of Plastics Engineers.

Mehling, H., Ebert, H. & Schossig, P. 2006. Development of standards for materials testing and quality control of PCM. *Proceedings,* 7th IIR Conference on Phase Change Materials and Slurries for Refrigeration and Air Conditioning, Sept. 13-15 2006 Dinan, France.

Mhike, W., Ferreira, I. V., Li, J., Stoliarov, S. I. & Focke, W. W. 2015. Flame retarding effect of graphite in rotationally molded polyethylene/graphite composites. *Journal of Applied Polymer Science,* **132**.

Mhike, W. & Focke, W. W. 2013. Surface resistivity and mechanical properties of rotationally molded polyethylene/graphite composites. *Journal of Vinyl and Additive Technology,* **19,** 258-270.

Mhike, W., Focke, W. W., Mofokeng, J. & Luyt, A. S. 2012. Thermally conductive phase-change materials for energy storage based on low-density polyethylene, soft Fischer–Tropsch wax and graphite. *Thermochimica Acta,* **527,** 75-82.

Móczó, J. & Pukánszky, B. 2008. Polymer micro and nanocomposites: structure, interactions, properties. *Journal of Industrial and Engineering Chemistry,* **14,** 535-563.

Monzón, M. D., Bordón, P., Benítez, A. N., Kearns, M., Hernández, P. M. & Marrero, M. D. 2012. Global efficiency of innovative rotational mold directly heated by thermal fluid. *Polymer Engineering & Science,* **52,** 1998-2005.

Morozov, S., Novoselov, K., Katsnelson, M., Schedin, F., Elias, D., Jaszczak, J. & Geim, A. 2008. Giant intrinsic carrier mobilities in graphene and its bilayer. *Physical review letters,* **100,** 016602.

Mudge, S. M. 2005. Fatty alcohols-a review of their natural synthesis and environmental distribution. *The Soap and Detergent Association,* **132,** 1-141.

Murdie, N., Edwards, I. & Marsh, H. 1985. Intercalation of natural flake graphites. *Journal of Materials Science,* **20,** 171-181.

Murphy, M., Martin, D., Truss, R. & Halley, P. 2002. Improving Polyethylene Performance - The Use of Nanocomposites in Ziegler-Natta Polyethylene for Rotational Moulding *Proceedings, ANTEC 2002 Plastics: Annual Technical Conference,* Volume 1: Processing, May 5-9 2002 San Francisco, California, US. Society of Plastics Engineers.

Murphy, M., Truss, R., Halley, P., Martin, D. & Ang, C. 2003. Polyethylene Nanocomposites - Investigating the Tensile Properties of Polyethylene Nanocomposites for Rotational Moulding. *Proceedings, ANTEC 2003 Plastics: Annual Technical Conference* Volume 1: Processing, May 4-8 2003 Nashville, Tennessee. Society of Plastics Engineers.

Nagy, T. & White, J. L. 1996. The effect of colorants on the properties of rotomolded polyethylene parts. *Polymer Engineering & Science,* **36,** 1010-1018.

Nakajima, T., Mabuchi, A. & Hagiwara, R. 1988. A new structure model of graphite oxide. *Carbon,* **26,** 357-361.

Nan, C.-W., Birringer, R., Clarke, D. R. & Gleiter, H. 1997. Effective thermal conductivity of particulate composites with interfacial thermal resistance. *Journal of Applied Physics,* **81,** 6692-6699.

Nan, C.-W., Liu, G., Lin, Y. & Li, M. 2004. Interface effect on thermal conductivity of carbon nanotube composites. *Applied Physics Letters,* **85,** 3549-3551.

Nanzai, B., Okitsu, K., Takenaka, N., Bandow, H., Tajima, N. & Maeda, Y. 2009. Effect of reaction vessel diameter on sonochemical efficiency and cavitation dynamics. *Ultrasonics sonochemistry,* **16,** 163-168.

Nielsen, L. E. & Landel, R. F. 1994. *Mechanical properties of polymers and composites,* New York, US, Marcel Dekker.

Noel, M. & Santhanam, R. 1998. Electrochemistry of graphite intercalation compounds. *Journal of Power Sources,* **72,** 53-65.

Novoselov, K. S., Fal, V., Colombo, L., Gellert, P., Schwab, M. & Kim, K. 2012. A roadmap for graphene. *Nature,* **490,** 192-200.

Novoselov, K. S., Geim, A. K., Morozov, S. V., Jiang, D., Zhang, Y., Dubonos, S. V., Grigorieva, I. V. & Firsov, A. A. 2004. Electric Field Effect in Atomically Thin Carbon Films. *Science,* **306,** 666-669.

Nugent, P., Peev, G. & Little, E. 1997. The Use of Non-Contact Temperature Sensing in Extending Process Control for Rotational Molding. *Proceedings, ANTEC 1997 Plastics: Plastics Saving Planet Earth,* Volume 3: Special Areas, April 27-May 2 1997 Totonto, Ontario, Canada.

Nuvoli, D., Valentini, L., Alzari, V., Scognamillo, S., Bon, S. B., Piccinini, M., Illescas, J. & Mariani, A. 2011. High concentration few-layer graphene sheets obtained by liquid phase exfoliation of graphite in ionic liquid. *Journal of Materials Chemistry,* **21,** 3428-3431.

Oliveira, M. & Cramez, M. 2001. Rotational molding of polyolefins: processing, morphology, and properties. *Journal of Macromolecular Science, Part B,* **40,** 457-471.

Oliveira, M., Cramez, M. & Crawford, R. 1996. Structure-properties relationships in rotationally moulded polyethylene. *Journal of Materials Science,* **31,** 2227-2240.

Oró, E., De Gracia, A., Castell, A., Farid, M. & Cabeza, L. 2012. Review on phase change materials (PCMs) for cold thermal energy storage applications. *Applied Energy,* **99,** 513-533.

Ortega, Z., Monzón, M., Benítez, A., Kearns, M., McCourt, M. & Hornsby, P. 2013. Banana and abaca fiber-reinforced plastic composites obtained by rotational molding process. *Materials and Manufacturing Processes,* **28,** 879-883.

Park, S. & Ruoff, R. S. 2009. Chemical methods for the production of graphenes. *Nature nanotechnology,* **4,** 217-224.

Paton, K. R., Varrla, E., Backes, C., Smith, R. J., Khan, U., O'Neill, A., Boland, C., Lotya, M., Istrate, O. M. & King, P. 2014. Scalable production of large quantities of defect-free few-layer graphene by shear exfoliation in liquids. *Nature materials,* **13,** 624-630.

Peacock, A. 2000. *Handbook of polyethylene: structures: properties, and applications*, CRC Press.

Pick, L. & Harkin-Jones, E. 2005. An investigation of the relationship between thermal relaxations and the impact performance of rotationally moulded linear low density polyethylenes. *Proceedings of the Institution of Mechanical Engineers, Part L: Journal of Materials Design and Applications,* **219,** 1-10.

Pick, L. & Harkin-Jones, E. 2006. Effect of mould pressurisation on impact strength of rotationally moulded polyethylenes. *Plastics, rubber and composites,* **35,** 324-330.

Pierson, H. O. 1993. *Handbook of carbon, graphite, diamonds and fullerenes: processing, properties and applications*, Park Rudge, NJ, US, William Andrew/Noyes.

Pimenta, M., Dresselhaus, G., Dresselhaus, M. S., Cancado, L., Jorio, A. & Saito, R. 2007. Studying disorder in graphite-based systems by Raman spectroscopy. *Physical chemistry chemical physics,* **9,** 1276-1290.

Planes, E., Duchet, J., Maazouz, A. & Gerard, J.-F. 2008. Characterization of new formulations for the rotational molding based on ethylene–propylene copolymer/graphite nanocomposites. *Polymer Engineering & Science,* **48,** 723-731.

Progelhof, R., Throne, J. & Ruetsch, R. 1976. Methods for predicting the thermal conductivity of composite systems: a review. *Polymer Engineering & Science,* **16,** 615-625.

Qu, B. & Xie, R. 2003. Intumescent char structures and flame-retardant mechanism of expandable graphite-based halogen-free flame-retardant linear low density polyethylene blends. *Polymer international,* **52,** 1415-1422.

Randviir, E. P., Brownson, D. A. & Banks, C. E. 2014. A decade of graphene research: production, applications and outlook. *Materials Today,* **17,** 426-432.

Raymond, A. & Rodrigue, D. 2013. Wood Plastics Composites Produced by Rotomolding. *Proceedings, ANTEC 2013 - Proceedings of the Technical Conference & Exhibition*, April 22-24 2013 Cincinnati, Ohio, US. Society of Plastics Engineers.

Ren, W. & Cheng, H.-M. 2014. The global growth of graphene. *Nature nanotechnology,* **9,** 726-730.

Restolho, J., Mata, J. L. & Saramago, B. 2009. On the interfacial behavior of ionic liquids: Surface tensions and contact angles. *Journal of colloid and interface science,* **340,** 82-86.

Robert, A. & Crawford, R. 1999. The Effect of Fillers on the Properties of Rotationally Molded Polyethylene *Proceedings, ANTEC 1999 Plastics: Bridging the Millennia* Volume 1: Processing, May 2-6 1999 New York City, New York, US Society of Plastics Engineers.

Robert, A., Orr, J. & Crawford, R. 2000. Influence of Mica and Talc Fillers on the Properties of Rotationally Moulded LLDPE. *Proceedings, ANTEC 2000 Plastics: The Magical Solution* Volume 1: Processing, May 7-11 2000 Orlando, Florida, US. Society of Plastics Engineers.

Rosner, R. B. 2001. Conductive materials for ESD applications: an overview. *Device and Materials Reliability, IEEE Transactions on,* **1,** 9-16.

Rüdorff, W. 1959. Graphite intercalation compounds. *Advances in Inorganic Chemistry and Radiochemistry,* **1,** 223-266.

Rüdorff, W., Stumpp, E., Spriessler, W. & Siecke, F. 1963. Reactions of Graphite with Metal Chlorides. *Angewandte Chemie International Edition in English,* **2,** 67-73.

Rycerz, L. 2013. Practical remarks concerning phase diagrams determination on the basis of differential scanning calorimetry measurements. *J Therm Anal Calorim,* **113,** 231-8.

Sacristán, M., Hull, T. R., Stec, A. A., Ronda, J. C., Galià, M. & Cádiz, V. 2010. Cone calorimetry studies of fire retardant soybean-oil-based copolymers containing silicon or boron: Comparison of additive and reactive approaches. *Polymer Degradation and Stability,* **95,** 1269-1274.

Sae-Chieng, W. & Kanokboriboon, A. 2007. An Investigation on the Effects of a Fine-Particulate Filler on the Properties of a Rotomolding-Grade Polyethylene. *Proceedings, ANTEC 2007 Plastics: Annual Technical Conference Proceedings*, May 1-5 2007 Boston, Massachusetts, US. Society of Plastics Engineers.

Santos, H. M., Lodeiro, C. & Capelo-Martínez, J.-L. 2009. The Power of Ultrasound. In: *Ultrasound in Chemistry.* Weinheim, Germany: Wiley-VCH Verlag GmbH & Co. .

Sarı, A. 2003. Thermal reliability test of some fatty acids as PCMs used for solar thermal latent heat storage applications. *Energy Conversion and Management,* **44,** 2277-2287.

Sarı, A. & Karaipekli, A. 2007. Thermal conductivity and latent heat thermal energy storage characteristics of paraffin/expanded graphite composite as phase change material. *Applied Thermal Engineering,* **27,** 1271-1277.

Sarı, A. & Kaygusuz, K. 2003. Some fatty acids used for latent heat storage: thermal stability and corrosion of metals with respect to thermal cycling. *Renewable Energy,* **28,** 939-948.

Sato, K., Yoshimoto, N., Suzuki, M., Kobayashi, M. & Kaneko, F. 1990. Structure and transformation in polymorphism of petroselinic acid (cis-. omega.-12-octadecenoic acid). *Journal of Physical Chemistry,* **94,** 3180-3185.

Schaink, H., Van Malssen, K., Morgado-Alves, S., Kalnin, D. & Van der Linden, E. 2007. Crystal network for edible oil organogels: possibilities and limitations of the fatty acid and fatty alcohol systems. *Food Research International,* **40,** 1185-1193.

Schartel, B. & Hull, T. R. 2007. Development of fire-retarded materials—Interpretation of cone calorimeter data. *Fire and Materials,* **31,** 327-354.

Schniepp, H. C., Li, J.-L., McAllister, M. J., Sai, H., Herrera-Alonso, M., Adamson, D. H., Prud'homme, R. K., Car, R., Saville, D. A. & Aksay, I. A. 2006. Functionalized single graphene sheets derived from splitting graphite oxide. *The Journal of Physical Chemistry B,* **110,** 8535-8539.

Selig, H. & Ebert, L. B. 1980. Graphite intercalation compounds. *Adv Inorg Chem Radiochem,* **23,** 281-327.

Sengupta, R., Bhattacharya, M., Bandyopadhyay, S. & Bhowmick, A. K. 2011. A review on the mechanical and electrical properties of graphite and modified graphite reinforced polymer composites. *Progress in Polymer Science,* **36,** 638-670.

Sharifi, P., Henwood, N., Liauw, C., Lees, G. & Quaratino, A. 2012. Studies of Degradation Effects during Rotational Molding. *Proceedings, ANTEC 2012 Plastics: Annual Technical Conference Proceedings,* April 2-4 2012 Orlando, Florida, US. Society of Plastics Engineers.

Sharma, A., Tyagi, V., Chen, C. & Buddhi, D. 2009. Review on thermal energy storage with phase change materials and applications. *Renewable and Sustainable energy reviews,* **13,** 318-345.

Shenogin, S., Xue, L., Ozisik, R., Keblinski, P. & Cahill, D. G. 2004. Role of thermal boundary resistance on the heat flow in carbon-nanotube composites. *Journal of Applied Physics,* **95,** 8136-8144.

Shi, J.-N., Ger, M.-D., Liu, Y.-M., Fan, Y.-C., Wen, N.-T., Lin, C.-K. & Pu, N.-W. 2013. Improving the thermal conductivity and shape-stabilization of phase change materials using nanographite additives. *Carbon,* **51,** 365-372.

Siddhamalli, S. K. & Lee, V. W. 1998. The influence of rotational molding cycle on the morphology and physical properties of FR-LLDPE. *Journal of Vinyl and Additive Technology,* **4,** 222-228.

Singh, V., Joung, D., Zhai, L., Das, S., Khondaker, S. I. & Seal, S. 2011. Graphene based materials: past, present and future. *Progress in materials science,* **56,** 1178-1271.

Slonczewski, J. & Weiss, P. 1958. Band structure of graphite. *Physical Review,* **109,** 272.

Smith, R. J., Lotya, M. & Coleman, J. N. 2010. The importance of repulsive potential barriers for the dispersion of graphene using surfactants. *New Journal of Physics,* **12,** 125008.

Spence, A. & Crawford, R. 1996. Removal of pinholes and bubbles from rotationally moulded products. *Proceedings of the Institution of Mechanical Engineers, Part B: Journal of Engineering Manufacture,* **210,** 521-533.

Spence, A. & Scott, R. 2003. Rotational Molding Process Control. *Proceedings, ANTEC 2003 Plastics: Annual Technical Conference* Volume 1: Processing, May 4-8 2003 Nashville, Tennessee, US. Society of Plastics Engineers.

Stahly, G. P. 2009. A survey of cocrystals reported prior to 2000. *Crystal Growth & Design,* **9,** 4212-4229.

Stankovich, S., Dikin, D. A., Piner, R. D., Kohlhaas, K. A., Kleinhammes, A., Jia, Y., Wu, Y., Nguyen, S. T. & Ruoff, R. S. 2007. Synthesis of graphene-based nanosheets via chemical reduction of exfoliated graphite oxide. *Carbon,* **45,** 1558-1565.

Stankovich, S., Piner, R. D., Chen, X., Wu, N., Nguyen, S. T. & Ruoff, R. S. 2006. Stable aqueous dispersions of graphitic nanoplatelets via the reduction of exfoliated graphite oxide in the presence of poly (sodium 4-styrenesulfonate). *Journal of Materials Chemistry,* **16,** 155-158.

Steele, T. & Davis, L. 2001. A gran of prevention: Additives for rotomolded parts. *Plastics engineering,* **57,** 36-36.

Stoller, M. D., Park, S., Zhu, Y., An, J. & Ruoff, R. S. 2008. Graphene-based ultracapacitors. *Nano letters,* **8,** 3498-3502.

Strüempler, R. & Glatz-Reichenbach, J. 1999. Feature article conducting polymer composites. *Journal of Electroceramics,* **3,** 329-346.

Subrahmanyam, K., Panchakarla, L., Govindaraj, A. & Rao, C. 2009. Simple method of preparing graphene flakes by an arc-discharge method. *The Journal of Physical Chemistry C,* **113,** 4257-4259.

Sumirat, I., Ando, Y. & Shimamura, S. 2006. Theoretical consideration of the effect of porosity on thermal conductivity of porous materials. *Journal of Porous Materials,* **13,** 439-443.

Sun, J.-S., Gokturk, H. S. & Kalyon, D. M. 1993. Volume and surface resistivity of low-density polyethylene filled with stainless steel fibres. *Journal of Materials Science,* **28,** 364-366.

Suslick, K., Doktycz, S. & Flint, E. 1990. On the origin of sonoluminescence and sonochemistry. *Ultrasonics,* **28,** 280-290.

Suslick, K. S. 2003. Sonoluminescence and Sonochemistry. In: Meyers, R. A. (Ed.) *Encyclopedia of Physical Science and Technology.* New York: Academic Press.

Suslick, K. S., Didenko, Y., Fang, M. M., Hyeon, T., Kolbeck, K. J., McNamara, W. B., Mdleleni, M. M. & Wong, M. 1999. Acoustic cavitation and its chemical consequences. *Philosophical Transactions of the Royal Society of London A: Mathematical, Physical and Engineering Sciences,* **357,** 335-353.

Sutkar, V. S. & Gogate, P. R. 2010. Mapping of cavitational activity in high frequency sonochemical reactor. *Chemical Engineering Journal,* **158,** 296-304.

Talanov, V., Melezhik, A. & Chuiko, A. 1993. X-ray photoelectron study of the surface of expanded and expandable graphite. *Theoretical and Experimental Chemistry,* **28,** 273-276.

Tan, S., Hornsby, P., McAfee, M., Kearns, M. & McCourt, M. 2011. Internal cooling in rotational molding—A review. *Polymer Engineering & Science,* **51,** 1683-1692.

Tcharkhtchi, A. & Verdu, J. 2004. Structure-Processibility Relationships During Rotational Moulding of Plastics. *Advanced Engineering Materials,* **6,** 983-992.

Thompson, L. & Doraiswamy, L. 1999. Sonochemistry: science and engineering. *Industrial & Engineering Chemistry Research,* **38,** 1215-1249.

Thomy, A., Ousset, J., Furdin, G., Pelletier, J. & Vannes, A. 1987. Exfoliation du Graphite Par Traitement Laser D'un Composé Intercalaire. *Le Journal de Physique Colloques,* **48,** C7-115-C7-118.

Tillotson, C. 1955. Some physical chemical properties of stearic acid. *Journal of the society of cosmetic chemists,* **6,** 9.

Torres, F. & Aragon, C. 2006. Final product testing of rotational moulded natural fibre-reinforced polyethylene. *Polymer testing,* **25,** 568-577.

Tryba, B., Morawski, A. W. & Inagaki, M. 2005. Preparation of exfoliated graphite by microwave irradiation. *Carbon,* **43,** 2417-2419.

van Miltenburg, J. C., Oonk, H. A. & Ventola, L. 2001. Heat capacities and derived thermodynamic functions of 1-octadecanol, 1-nonadecanol, 1-eicosanol, and 1-docosanol between 10 K and 370 K. *Journal of Chemical & Engineering Data,* **46,** 90-97.

Vasudeo, Y., Kapadia, J., Rangaprasad, R. & Purav Marg, V. 2001. Rotational Moulding of Flame Retardant Linear Low Density Polyethylene (FR-LLDPE) Compounds *Proceedings, ANTEC 2001 Plastics: The Lone Star* Volume 3: Special Areas, May 6-10 2001 Dallas, Texas, US. Society of Plastics Engineers.

Velraj, R., Seeniraj, R., Hafner, B., Faber, C. & Schwarzer, K. 1999. Heat transfer enhancement in a latent heat storage system. *Solar energy,* **65,** 171-180.

Ventola, L., Ramirez, M., Calvet, T., Solans, X., Cuevas-Diarte, M., Negrier, P., Mondieig, D., Van Miltenburg, J. & Oonk, H. 2002. Polymorphism of n-alkanols: 1-Heptadecanol, 1-octadecanol, 1-nonadecanol, and 1-eicosanol. *Chemistry of materials,* **14,** 508-517.

Verbeek, C. & Focke, W. 2002. Modelling the Young's modulus of platelet reinforced thermoplastic sheet composites. *Composites Part A: Applied Science and Manufacturing,* **33,** 1697-1704.

Viculis, L. M., Mack, J. J., Mayer, O. M., Hahn, H. T. & Kaner, R. B. 2005. Intercalation and exfoliation routes to graphite nanoplatelets. *Journal of Materials Chemistry,* **15,** 974-978.

Wakabayashi, K., Brunner, P. J., Masuda, J. i., Hewlett, S. A. & Torkelson, J. M. 2010. Polypropylene-graphite nanocomposites made by solid-state shear pulverization: Effects of significantly exfoliated, unmodified graphite content on physical, mechanical and electrical properties. *Polymer,* **51,** 5525-5531.

Wallace, P. R. 1947. The band theory of graphite. *Physical Review,* **71,** 622.

Wang, J., Xie, H. & Xin, Z. 2008. Thermal properties of heat storage composites containing multiwalled carbon nanotubes. *Journal of applied physics,* **104,** 113537.

Wang, J., Zhu, M., Outlaw, R. A., Zhao, X., Manos, D. M. & Holloway, B. C. 2004. Synthesis of carbon nanosheets by inductively coupled radio-frequency plasma enhanced chemical vapor deposition. *Carbon,* **42,** 2867-2872.

Wang, J. Q. & Chow, W. K. 2005. A brief review on fire retardants for polymeric foams. *Journal of Applied Polymer Science,* **97,** 366-376.

Wang, L., Hong, J. & Chen, G. 2010a. Comparison study of graphite nanosheets and carbon black as fillers for high density polyethylene. *Polymer Engineering & Science,* **50,** 2176-2181.

Wang, X., Fulvio, P. F., Baker, G. A., Veith, G. M., Unocic, R. R., Mahurin, S. M., Chi, M. & Dai, S. 2010b. Direct exfoliation of natural graphite into micrometre size few layers graphene sheets using ionic liquids. *Chem. Commun.,* **46,** 4487-4489.

Weber, E. H., Clingerman, M. L. & King, J. A. 2003. Thermally conductive nylon 6, 6 and polycarbonate based resins. II. Modeling. *Journal of applied polymer science,* **88,** 123-130.

Wei, T., Fan, Z., Luo, G., Wang, S. & Song, L. 2009a. Dispersibility and stability improvement of graphite nanoplatelets in organic solvent by assistance of dispersant and resin. *Materials Research Bulletin,* **44,** 977-983.

Wei, T., Fan, Z., Luo, G., Zheng, C. & Xie, D. 2009b. A rapid and efficient method to prepare exfoliated graphite by microwave irradiation. *Carbon,* **47,** 337-339.

Weil, E. D. & Levchik, S. V. 2008. Flame Retardants in Commercial Use or Development for Polyolefins. *Journal of Fire Sciences,* **26,** 5-43.

Wisley, B. 1999. The Rotational Molding of Glass Fibre Reinforced Polyethylene *Proceedings, ANTEC 1999 Plastics: Bridging the Millennia,* Volume 1: Processing, May 2-6 1999 New York City, New York, US. Society of Plastics Engineers.

Wissler, M. 2006. Graphite and carbon powders for electrochemical applications. *Journal of power sources,* **156,** 142-150.

Work, W., Horie, K., Hess, M. & Stepto, R. 2004. Definition of terms related to polymer blends, composites, and multiphase polymeric materials (IUPAC Recommendations 2004). *Pure and applied chemistry,* **76,** 1985-2007.

Xanthos, M. 2005. Polymers and Polymer Composites. In: *Functional Fillers for Plastics.* Wiley-VCH Verlag GmbH & Co. KGaA.

Xiang, J. & Drzal, L. T. 2011. Investigation of exfoliated graphite nanoplatelets (xGnP) in improving thermal conductivity of paraffin wax-based phase change material. *Solar Energy Materials and Solar Cells,* **95,** 1811-1818.

Xie, R. & Qu, B. 2001. Synergistic effects of expandable graphite with some halogen-free flame retardants in polyolefin blends. *Polymer degradation and stability*, **71,** 375-380.

Yan, W., Lin, R. J., Bhattacharyya, D. & Bickerton, S. Rotational moulding of particulate reinforced polymeric shell structures. *Proceedings*, *Materials Science Forum,* 437, 2003. Trans Tech Publ, 235-238.

Yan, W., Lin, R. J. T. & Bhattacharyya, D. 2006. Particulate reinforced rotationally moulded polyethylene composites – Mixing methods and mechanical properties. *Composites Science and Technology,* **66,** 2080-2088.

Yaroshenko, A., Savos' kin, M., Magazinskii, A., Shologon, V. & Mysyk, R. 2002. Synthesis and properties of thermally expandable residual graphite hydrosulfite obtained in the system HNO3-H2SO4. *Russian journal of applied chemistry,* **75,** 861-865.

Yasmin, A. & Daniel, I. M. 2004. Mechanical and thermal properties of graphite platelet/epoxy composites. *Polymer,* **45,** 8211-8219.

Yavari, F., Fard, H. R., Pashayi, K., Rafiee, M. A., Zamiri, A., Yu, Z., Ozisik, R., Borca-Tasciuc, T. & Koratkar, N. 2011. Enhanced thermal conductivity in a nanostructured phase change composite due to low concentration graphene additives. *The Journal of Physical Chemistry C,* **115,** 8753-8758.

Yi, M. & Shen, Z. 2015. A review on mechanical exfoliation for the scalable production of graphene. *Journal of Materials Chemistry A*, **3,** 11700-11715.

Yi, M., Shen, Z., Zhang, X. & Ma, S. 2012. Vessel diameter and liquid height dependent sonication-assisted production of few-layer graphene. *Journal of Materials Science,* **47,** 8234-8244.

Yoon, G., Seo, D.-H., Ku, K., Kim, J., Jeon, S. & Kang, K. 2015. Factors Affecting the Exfoliation of Graphite Intercalation Compounds for Graphene Synthesis. *Chemistry of Materials,* **27,** 2067-2073.

Yoshida, A., Hishiyama, Y. & Inagaki, M. 1991. Exfoliated graphite from various intercalation compounds. *Carbon,* **29,** 1227-1231.

Yu, A., Ramesh, P., Itkis, M. E., Bekyarova, E. & Haddon, R. C. 2007. Graphite Nanoplatelet−Epoxy Composite Thermal Interface Materials. *The Journal of Physical Chemistry C,* **111,** 7565-7569.

Yu, J. & Wallis, E. 2008. Recent Additive Development for Rotational Molding. *Proceedings, ANTEC 2008 Plastics: Annual Technical Conference Proceedings*, May 4-8 2008 Milwaukee, Wisconsin, US. Society of Plastics Engineers.

Yuan, X., Easteal, A. J. & Bhattacharyya, D. 2007. Mechanical performance of rotomoulded wollastonite-reinforced polyethylene composites. *International Journal of Modern Physics B,* **21,** 1059-1066.

Yuan, Y., Zhang, N., Tao, W., Cao, X. & He, Y. 2014. Fatty acids as phase change materials: a review. *Renewable and Sustainable Energy Reviews,* **29,** 482-498.

Zalba, B., Marín, J. M., Cabeza, L. F. & Mehling, H. 2003. Review on thermal energy storage with phase change: materials, heat transfer analysis and applications. *Applied thermal engineering,* **23,** 251-283.

Zeng, J., Cao, Z., Yang, D., Xu, F., Sun, L., Zhang, L. & Zhang, X. 2009. Phase diagram of palmitic acid-tetradecanol mixtures obtained by DSC experiments. *Journal of thermal analysis and calorimetry,* **95,** 501-505.

Zeng, J., Liu, Y., Cao, Z., Zhang, J., Zhang, Z., Sun, L. & Xu, F. 2008. Thermal conductivity enhancement of MWNTs on the PANI/tetradecanol form-stable PCM. *Journal of Thermal Analysis and Calorimetry,* **91,** 443-446.

Zeng, Y., Liu, P., Du, J., Zhao, L., Ajayan, P. M. & Cheng, H.-M. 2010. Increasing the electrical conductivity of carbon nanotube/polymer composites by using weak nanotube–polymer interactions. *Carbon,* **48,** 3551-3558.

Zhao, P., Yue, Q., He, H., Gao, B., Wang, Y. & Li, Q. 2014. Study on phase diagram of fatty acids mixtures to determine eutectic temperatures and the corresponding mixing proportions. *Applied Energy,* **115,** 483-490.

Zhong, Y. L., Tian, Z., Simon, G. P. & Li, D. 2015. Scalable production of graphene via wet chemistry: progress and challenges. *Materials Today,* **18,** 73-78.

Zhou, M., Tian, T., Li, X., Sun, X., Zhang, J., Cui, P., Tang, J. & Qin, L.-C. 2014. Production of graphene by liquid-phase exfoliation of intercalated graphite. *Int. J. Electrochem. Sci,* **9,** 810-820.

Zuo, J., Li, W. & Weng, L. 2011a. Thermal performance of caprylic acid/1-dodecanol eutectic mixture as phase change material (PCM). *Energy and Buildings,* **43,** 207-210.

Zuo, J., Li, W. & Weng, L. 2011b. Thermal properties of lauric acid/1-tetradecanol binary system for energy storage. *Applied Thermal Engineering,* **31,** 1352-1355.

Publications

Journal Articles

Mhike, W., Ferreira, I.V., Li, J., Stoliarov, S.I. and Focke, W.W., 2015. Flame retarding effect of graphite in rotationally molded polyethylene/graphite composites. *Journal of Applied Polymer Science*, ***132***(7).

Mhike, W., Asante, J.K.O., Manyala, N.I. and Focke, W.W. Rotomolded antistatic and flame retarded polyethylene-graphite nanocomposites. Submitted to: *Journal of Thermoplastic Composite Materials.*

Mhike, W., Mackenzie, J., Mills, E.J. and Focke, W.W., Nanocomposites of pseudo binary mixtures of stearyl alcohol/commercial stearic acid and graphite nanoplatelets as phase change materials for energy storage. Manuscript to be submitted to the journal *Thermochimica Acta*.

Conference Papers Presented

Mhike, W., Ferreira, I.V., Li, J., Stoliarov, S.I. and Focke, W.W., 2015. Flame Retarding Effect of Graphite Polyethylene, *Proceedings*: Carbon 2015, July 12-17, 2015, Dresden, Germany.

Mhike, W. and Focke, W.W., 2015. Antistatic and Flame Retardant Rotomouldable Polymer Graphite Nanocomposites, *Proceedings*: 13th Annual Unesco/IUPAC Workshop and Conference on Macromolecules & Materials, September 7-10, Port Elizabeth, South Africa.

Appendices

Appendix A Graphite nanoplatelets obtained in water with the surfactant Tween 20

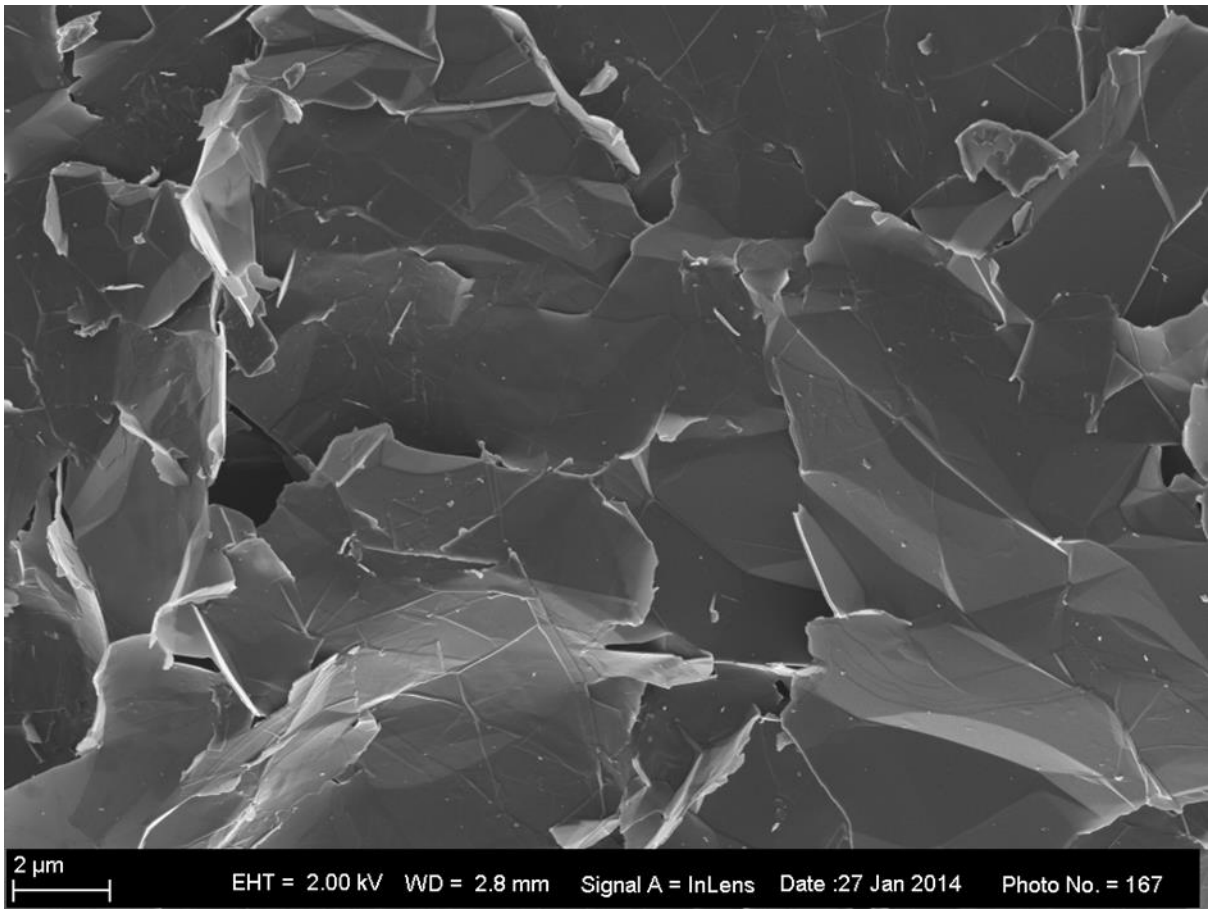

Figure A1 FESEM of graphite nanoplatelets obtained by ultrasonication-assisted liquid phase exfoliation of expanded graphite (Grade ES250 B5) in water with the surfactant Tween 20.

Appendix B Graphite nanoplatelets edge interaction with polyethylene

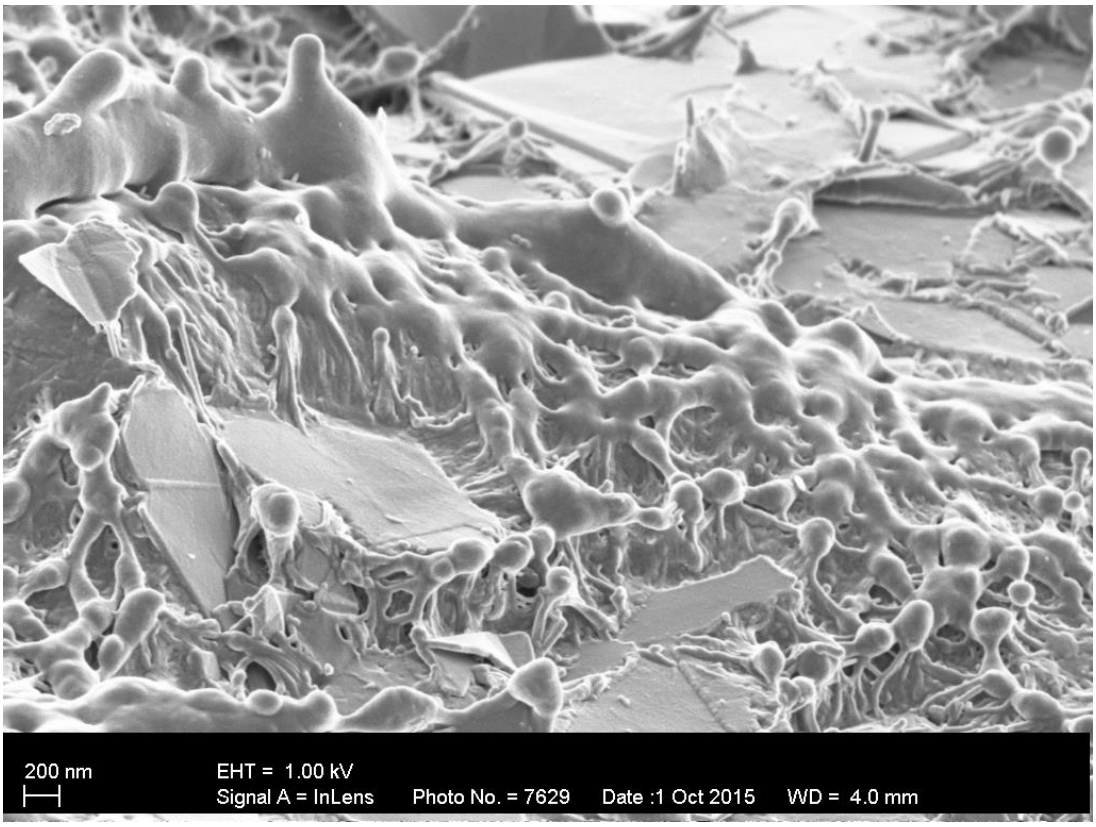

Figure B1 FESEM micrograph of LLDPE/ GNPs nanocomposites rotomoulded after dry blending LLDPE with 0.25 wt.% GNPs at higher magnification showing the existence of edge interaction of graphite with LLDPE.

Appendix C Optical microscopy micrographs of the crystallization of stearyl alcohol, stearic acid and their mixtures

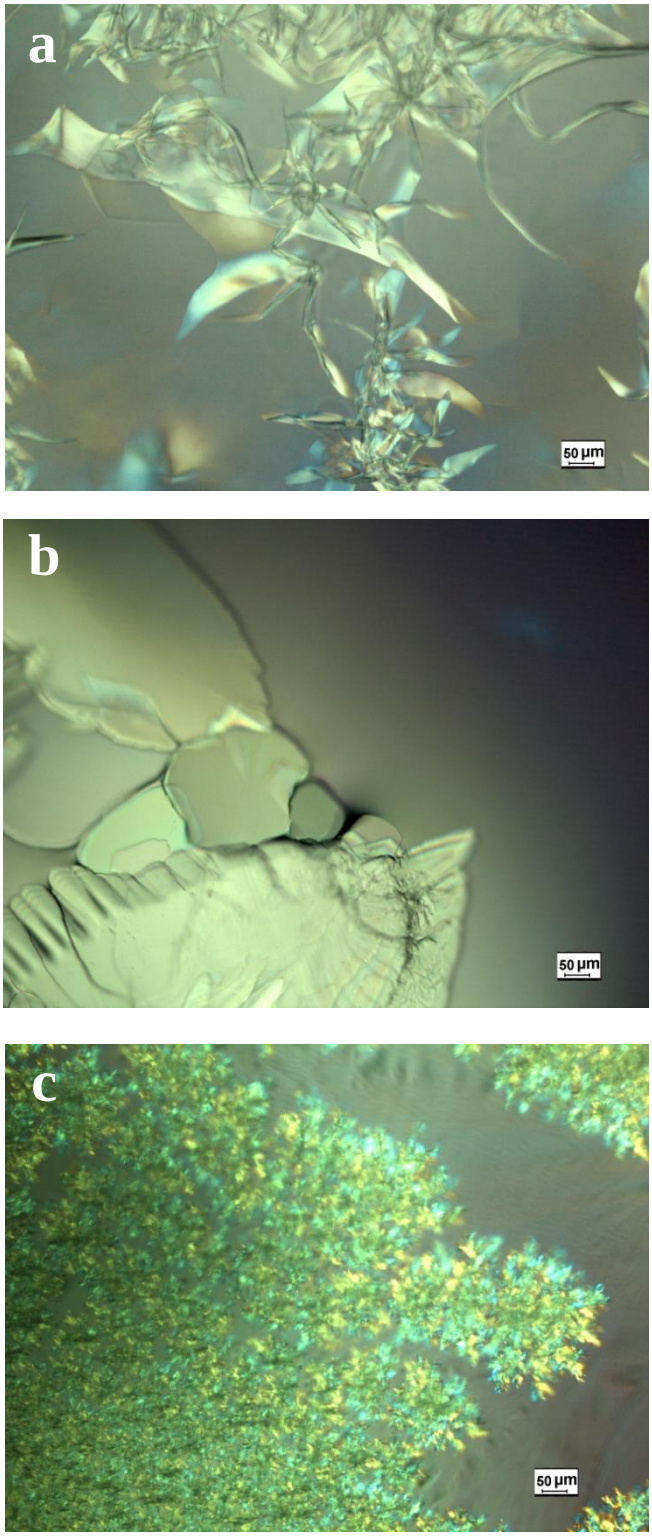

Figure C1 Optical microscopy micrographs showing crystallization of (a) Stearyl alcohol, (b) Stearic acid and (c) mixture of stearyl alcohol and stearic acid with 0.35 mole fraction stearyl alcohol at x10 magnification.

Appendix D Settling tests for PCM/graphite nanocomposites

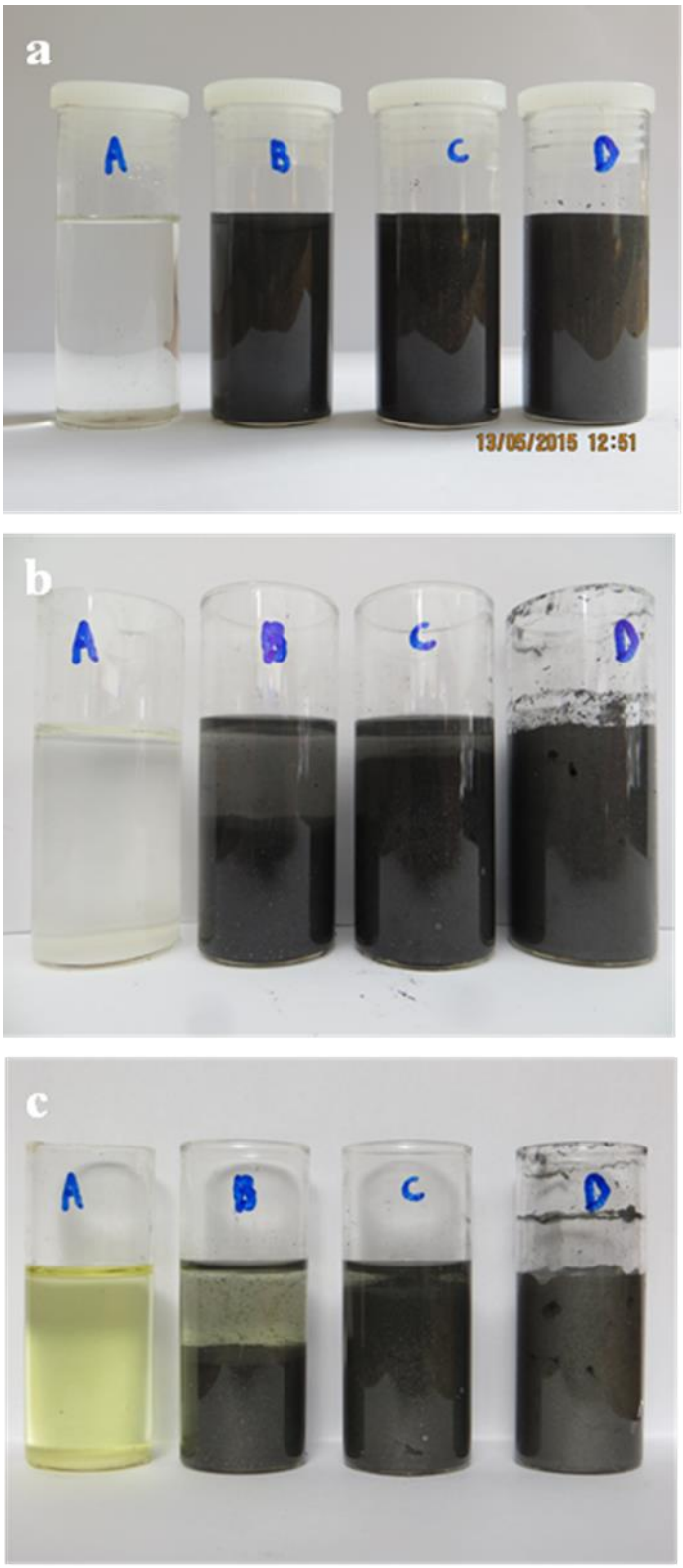

Figure D1 Thermal stability: Settling tests. A: 0 wt.% GNPs, B: 2.5 wt.% GNPs, C: 5 wt.% GNPs and D:10 wt.% GNPs. a) Day 1, b) Day 5, and c) after 2 months.